Technische Universität Berlin

Schriftenreihe

KUNSTSTOFF-FORSCHUNG

Herausgegeben von Manfred H. Wagner

81

From Linear to Long-Chain Branched Poly(ethylene terephthalate) – Reactive Extrusion, Rheology and Molecular Characterization

Matthias Kruse

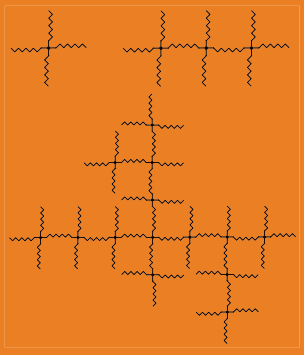

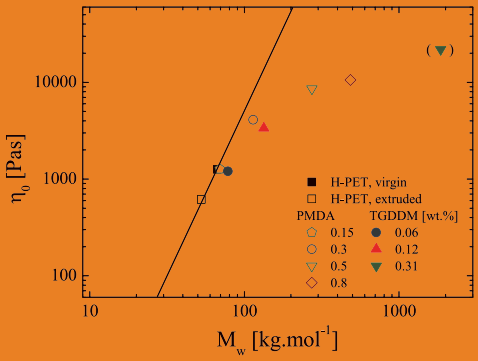

Polymertechnik / Kunststofftechnikum
Berlin 2017

Matthias Kruse

From Linear to Long-Chain Branched Poly(ethylene terephthalate) – Reactive Extrusion, Rheology and Molecular Characterization

Prof. Manfred H. Wagner studierte Physik und Physikalische Chemie an der Universität Stuttgart und der Oregon State University, Corvallis/USA. Nach der Promotion zum Dr.-Ing. (1976) an der Universität Stuttgart auf dem Gebiet der rheologisch-thermodynamischen Modellbildung in der Kunststoffverarbeitung war er bis 1979 wissenschaftlicher Assistent am Institut für Polymere der Eidgenössischen Technischen Hochschule Zürich. Danach folgte eine neunjährige Industrietätigkeit bei der damaligen Hoechst-Tochter SIGRI GmbH (heute SGL Carbon AG) in der Elektrographitentwicklung mit vielfältigen internationalen Aufgaben. Daneben war er Lehrbeauftragter der Universität Erlangen-Nürnberg für das Fachgebiet Rheologie der Polymerschmelzen.

1988 wurde er an die Universität Stuttgart auf die Professur für Numerische Strömungsmechanik/Rheologie berufen. In Stuttgart beschäftigte sich Prof. Wagner mit der Entwicklung von numerischen Verfahren zur Simulation von Deformations- und Strömungsvorgängen in hochviskosen newtonschen und nicht-newtonschen Flüssigkeiten und mit der Entwicklung rheologischer Stoffgesetze für makromolekulare Flüssigkeiten, wie sie in der Polymererzeugung und -verarbeitung, aber auch in der Bio- und Medizintechnik auftreten. 1998–99 war er Dekan der Fakultät Verfahrenstechnik und Technische Kybernetik der Universität Stuttgart. 1999 folgte er einem Ruf der TU Berlin und leitet seitdem das Fachgebiet Polymertechnik/Polymerphysik des Instituts für Werkstoffwissenschaften und -technologien.

Zahlreiche Publikationen auf so verschiedenen Fachgebieten wie Festkörperphysik, Numerische Strömungsmechanik, Rheologie polymerer Schmelzen, Kunststoff-verarbeitung, Medizintechnik, Kunstkohle und Elektrographit belegen seine vielfältigen wissenschaftlichen Aktivitäten. Von 1991 bis 2003 war Prof. Wagner Vorsitzender der Deutschen Rheologischen Gesellschaft. Von 1996 bis 2005 war er Sekretär der Europäischen Rheologischen Gesellschaft, 2005 bis 2009 war er deren Präsident. Seit 2004 ist er Geschäftsführer des International Committee on Rheology. 1981 erhielt Prof. Wagner den Annual Award der British Society of Rheology, 2002 den Swinburne Award des Institute of Materials, London, und 2011 den Weissenberg Award der European Society of Rheology. Die East China University of Science and Technology, Shanghai, ernannte ihn 2002 zum “Guest Professor”.

Schriftenreihe Kunststoff-Forschung | 81

Matthias Kruse

From Linear to Long-Chain Branched Poly(ethylene terephthalate) – Reactive Extrusion, Rheology and Molecular Characterization

Universitätsverlag der TU Berlin

Bibliografische Information der Deutschen Nationalbibliothek
Die Deutsche Nationalbibliothek verzeichnet diese Publikation in der Deutschen Nationalbibliografie; detaillierte bibliografische Daten sind im Internet über http://dnb.dnb.de abrufbar.

Universitätsverlag der TU Berlin, 2017
http://verlag.tu-berlin.de

Fasanenstr. 88, 10623 Berlin
Tel.: +49 (0)30 314 76131 / Fax: -76133
E-Mail: publikationen@ub.tu-berlin.de

Zugl.: Berlin, Techn. Univ., Diss., 2017
Gutachter: Prof. Dr.-Ing. Manfred H. Wagner
Gutachter: Prof. Dr.-Ing. Rainer Schnabel
Die Arbeit wurde am 2. Dezember 2016 an der Fakultät III unter Vorsitz von Prof. Dr. Walter Reimers erfolgreich verteidigt.

Druck: docupoint GmbH
Satz/Layout/Umschlagbild: Matthias Kruse

ISBN 978-3-7983-2891-4 (print)
ISBN 978-3-7983-2892-1 (online)

ISSN 0174-4003 (print)
ISSN 2197-814X (online)

Zugleich online veröffentlicht auf dem institutionellen Repositorium der Technischen Universität Berlin:
DOI 10.14279/depositonce-5683
http://dx.doi.org/10.14279/depositonce-5683

Für Víctor

Vorwort

Diese Promotionsschrift entstand während meiner Tätigkeit als wissenschaftlicher Mitarbeiter am Fachgebiet Polymertechnik/Polymerphysik der Technischen Universität Berlin. Die Möglichkeit, an einem Forschungsprojekt über eine Dauer von fünf Jahren unabhängig von Finanzierung und wirtschaftlichen Interessen arbeiten zu dürfen, hat mir große Freude bereitet und mich sehr dankbar gemacht. Eine wissenschaftliche Arbeit entsteht nicht im Alleingang - zumindest nicht in meinem Falle. Dabei haben mich viele Menschen tatkräftig mit ihren Händen und Köpfen unterstützt.

Mein Doktorvater Professor Manfred H. Wagner besitzt neben einer außergewöhnlichen Fachkompetenz vor allem eine ausgeprägte wissenschaftliche Neugier. Er hat mich immer ermutigt und eingenordet: „Herr Kruse, das Wichtigste ist Ihre Arbeit.“ Ich denke, ich spreche für seine vielen Absolventen und Absolventinnen, wenn ich den Rückhalt durch Professor Wagner betone.

Professor Rainer Schnabel hat das Zweitgutachten erstellt, obwohl sich viele Pensionäre sicherlich angenehmere Aufgaben suchen. Sein Einsatz, der ein übliches Pflichtbewusstsein übertrifft, ist mir ein Vorbild. Gleiches gilt für den Vorsitzenden der Prüfungskommission Professor Walter Reimers, dessen Engagement weit über den Bereich der Metalle hinaus reicht.

Eine umfangreiche Arbeit lebt von vielen verlässlichen Daten und ihrer Diskussion. Sie verdanke ich unter anderem Cécile Barthet, Carla Isabel Pinilla Ducreux, Yu Liu, Thi Thu Trang Nguyen, Rajas Sudhir Shah, Rongcheng Xu und ganz besonders Peng Wang. Bei technischen Problemen war Christian Wyrwich immer eine große Stütze, wofür ich sehr dankbar bin.

Weitere fachliche Unterstützung bekam ich durch Falk Rohnstock und Oliver Löschke, deren Freundschaft mir nicht weniger hilfreich war und die die Zeit am Fachgebiet besonders wertvoll werden ließen.

Die eigentliche Projektidee und der erfolgreiche DFG-Projektantrag stammten von Dr. habil. Víctor Hugo Rolón Garrido. Die Gründe, warum er mich ausgesucht und vorbehaltlos unterstützt und gefördert hat, habe ich nie ganz zu fassen bekommen. Er war für mich ein wissenschaftliches und moralisches Vorbild und echter Freund. Er verstand es, in mir einen brüderlichen Ehrgeiz zu wecken, der selbst heute noch in mir hervortritt und dabei wundervolle Erinnerungen weckt. Víctor verdanke ich das meiste.

Von der freiheitlichen aber auch verantwortungsbewussten Erziehung meiner Eltern Harry und Anita habe ich auch während meiner Promotion profitiert.

Ohne den Pioniergeist und die Unterstützung meiner Schwester Diana wäre ich wohl nicht auf die Universität gegangen.

Meiner lieben Lene habe ich viel mehr zu verdanken als die unzähligen Redigate. In den letzten fünf Jahren hat sie mich feinfühlig abgelenkt, wenn ich stagnierte, und motiviert, wenn ich zerstreut war. Dass wir eine Vergangenheit und eine Zukunft teilen, macht mich sehr glücklich. Ihr gehört meine Liebe.

Berlin, den 22.02.2017 Matthias Kruse

Abstract

Poly(ethylene terephthalate) is one of the most widely used polymers in packaging industry, due to its high mechanical strength, chemical resistance, and barrier functions. However, its processing is determined by degradation and low viscosity. In particular, foaming and film blowing is restricted by the linear structure of the molecule and low melt strength.

The stability of three linear commercial PET grades produced by different synthesis routes with different molar masses is analyzed in regards of processing at industrial scale. Subsequently, reactive processing with three multifunctional chain extenders (pyromellitic dianhydride, PMDA, tetraglycidyl diamino diphenyl methane, TGDDM, and triphenyl phosphite, TPP) is conducted to create large and long-chain branched (LCB) molecules. The mechanical and molecular properties in melt state are analyzed by linear and non-linear viscoelastic rheology, modeling by the molecular stress function (MSF) theory and size-exclusion chromatography (SEC) with light scattering measurements.

Thermal stability measurements in the linear viscoelastic regime revealed degradation and a reduction of the storage modulus in air atmosphere, and, besides thermal degradation, an enhancement of the modulus in nitrogen atmosphere, due to polycondensation (Kruse et al., 2013). Fitting by an exponential function leads to the reconstruction of the initial state of the sample at zero-loading time and to a time constant, which reveals clear relations between stability and molar mass for all three PET grades in both atmospheres. High molar mass PET is more stable in nitrogen and less stable in air environment, and vice versa, depending on OH end group concentration and synthesis route. The analysis by means of time-resolved mechanical spectroscopy allows the observations of moduli and complex viscosity at a fixed time, a wide range of angular frequencies, and at different atmospheres, and revealed: (i) a plasticizer effect induced by small molecules from thermal and thermo-oxidative degradation, (ii) cross-linking leading to yield stress, (iii) diffusion influencing polycondensation reaction, (iv) slipping due to deposition of side products, and (v) an enhanced shear thinning regime (Kruse and Wagner, 2016).

The extrusion of neat PET with a twin-screw extruder at industrial scale leads to strong reduction of viscosity mainly due to shearing. The impact of thermo-oxidative degradation is comparably small.

The reactive processing of the three PET grades with the three chain extenders leads to the conclusion that the tri-functional TPP is not a useful chain

extender due to rapid degradation and toxicity. The two tetra-functional chain extenders, PMDA and the epoxy-based TGDDM, lead to strong viscosity increase, increasing strain hardening effect, and increasing thermal stability with increasing chain extender concentration as confirmed by loss- and storage modulus, phase angle, activation energy of flow, and elongational viscosity. The MSF model predictions show good agreement with data measured, and allowed a quantitative analysis of the branching structure and of the stretch of the molecules by both non-linear MSF parameters, β and f^2_{max}. In comparison to the high molar mass PET with an apparent comb-like structure at high PMDA concentrations, the two initially low molar mass grades show a higher molar mass after processing with PMDA and seem to have a tree-like structure, which can be explained by the hydroxyl end group concentration of these two PET grades. The extensive use of TGDDM leads to a hyperbranched and gel-like structure. The fracture analysis from uniaxial elongation experiments reveals a limiting stress value for high PMDA concentrations and a limiting strain value for high TGDDM concentrations due to formation of a covalent network.

The molecular analysis by SEC with triple detection of the high molar mass PET, which was reacted with PMDA and TGDDM, shows a strong increase of the average molar masses, polydispersity, radius of gyration, and hydrodynamic radius and confirms the molar mass increase observed by the rheological measurements. The branching was confirmed by a decreasing Mark-Houwink exponent with increasing chain extender concentration. Further, the analysis of the contraction of the molecule revealed a more star-like structure at low concentrations for both chain extenders. With increasing concentration, the structure changed to more comb-like for PMDA and random tree-like or hyperbranched for TGDDM as was also observed by non-linear viscoelastic measurements. PMDA revealed to be an excellent coupling agent which induces reproducibly either a star-like, comb-like, or tree-like structures depending on the concentration of coupling agent added and the hydroxyl concentration of the PET employed.

Kurzfassung

Polyethylenterephthalat (PET) zeichnet sich durch hervorragende mechanische Eigenschaften, sowie chemische Beständigkeit und Barriereeigenschaften aus und findet insbesondere in der Verpackungsindustrie Verwendung. Die Neigung zur Degradation und die wegen der linearen Kettenmoleküle geringe Viskosität schränken jedoch die Verarbeitbarkeit von PET wie beispielsweise das Schäumen und Folienblasen erheblich ein.

In der vorliegenden Arbeit wird der Einfluss der thermischen Stabilität während der Verarbeitung von drei linearen industriellen PET-Typen untersucht, die sich durch Molmasse und Herstellungsverfahren unterscheiden. Des Weiteren wird langkettenverzweigtes PET (LCB-PET) durch reaktive Verarbeitung mit drei verschiedenen multifunktionalen Kettenverlängerern, Pyromellitsäuredianhydrid (PMDA), Tetraglycidyl-Diamino-Diphenyl-Methan (TGDDM) und Triphenylphosphit (TPP), hergestellt und charakterisiert. Durch die experimentelle Bestimmung der linearen und nichtlinearen rheologischen Eigenschaften der Schmelze und ihre Beschreibung mit Hilfe des sogenannten "Molecular Stress Function" (MSF) Modells gelingt eine quantitative Analyse des Materialverhaltens. Die molekulare Analyse wird zusätzlich durch die Ergebnisse von Gelpermeationschromatographie (GPC bzw. SEC) in Verbindung mit Lichtstreumessung gestützt.

Die Untersuchungen der thermischen Stabilität von linearem PET im linear viskoelastischen Bereich zeigen einen abnehmenden Speichermodul und somit ein thermo-oxidatives Degradationsverhalten in Luftatmosphäre. In inerter Stickstoffatmosphäre tritt hingegen nur thermische Degradation auf, gleichzeitig führt jedoch eine Polykondensationsreaktion zu einem Ansteigen des Moduls (Kruse et al., 2013). Mit einem exponentiellen Regressionsansatz kann der anfängliche Zustand des Moduls in beiden Atmosphären zum Zeitpunkt Null, der dem Einbringen der Probe in das Rheometer entspricht, rekonstruiert werden. Die sich aus diesem Ansatz ergebende Zeitkonstante erlaubt es, quantitative Zusammenhänge zwischen der thermischen Stabilität der drei PET-Sorten und deren Molmasse sowie dem Herstellungsverfahren der PET-Typen aufzuzeigen. So weist hochmolekulares PET eine höhere Stabilität in Stickstoff und eine geringere Stabilität in Luft auf und umgekehrt. Hauptursache für dieses Verhalten ist die unterschiedliche Konzentration an Hydroxylendgruppen, die je nach Molmasse und Herstellungsmethode der jeweiligen PET-Typen variiert.

Mit Hilfe der "Time-Resolved Mechnical Sprectroscopy" konnte die sich ändernde Viskosität über ein weites Frequenzspektrum und zu einer beliebigen Messzeit in beiden Atmosphären bestimmt werden. Wesentliche Ergebnisse dieser Untersuchung sind der Nachweis des Auftretens von (i) einem Weichmachereffekt bedingt durch die thermische und thermo-oxidative Degradation und den daraus resultierenden Oligomeren, (ii) dreidimensionaler Vernetzung mit der Ausbildung einer Fließgrenze, (iii) Diffusionsprozessen, die Einfluss auf die Polykondensationsreaktion haben, (iv) Wandgleiten, bedingt durch die Ablagerung von Nebenprodukten auf den Platten des Rheometers und (v) einem verbreiterten Scherverdünnungbereich (Kruse and Wagner, 2016).

Die Extrusion von linearem PET mit einem Doppelschneckenextruder unter industriellen Bedingungen führt zu einer starken Abnahme der Viskosität, die hauptsächlich durch Scherung und weniger durch thermo-oxidativen Abbau verursacht wird.

Bei der reaktiven Verarbeitung der drei PET-Typen mit den drei verschiedenen Kettenverlängerern erwies sich das dreifunktionale TPP auf Grund von Toxizität und Lagerinstabilitäten als unbrauchbar. Die Verarbeitung der beiden vierfunktionalen Kettenverlängerer, PMDA und das epoxidhaltige TGDDM, führt zu erhöhter Viskosität, erhöhter Dehnverfestigung und erhöhter thermischer Stabilität mit zunehmender Konzentration des jeweiligen Kettenverlängerers. Das beschriebene Verhalten zeigt sich sowohl am Speicher- und Verlustmodul und dem daraus abgeleiteten Verlustwinkel, als auch an der Fließaktivierungsenergie und der Dehnviskosität. Dabei lassen sich die gemessenen Dehnviskositäten sehr präzise mit dem MSF-Modell beschreiben und die beiden nichtlinearen Modelparameter, β und f^2_{max}, ermöglichen eine quantitative Analyse der Verzweigungsstruktur und der Molekülstreckung. So zeigt die Modifiziereng von hohen PMDA-Konzentrationen und dem hochmolekularen PET eine mehr kammartige Struktur im Vergleich zu den beiden niedermolekularen PET-Typen, die eine baumartige Molekülstruktur und eine höhere Molmasse nach der reaktiven Extrusion aufweisen. Beide Effekte können mit der höheren OH-Endgruppenkonzentration der beiden niedermolekularen PET-Typen erklärt werden. Zu hohe Zusätze von TGDDM führen zu einem hochverzweigten und gelartigen Polymer.

Das Bruchverhalten bei der uniaxialen Dehnung von mit einem hohen Zusatz von PMDA hergestellten langkettenverzweigten PET wird von einer limitierenden Bruchspannung bestimmt. Demgegenüber bestimmt eine maximale Dehnung das Bruchverhalten des mit einem hohen TGDDM-Zusatz hergestellten LCB-PET, verursacht durch ein kovalent gebundenes Polymernetzwerk.

Die SEC Messungen mit drei Detektoren wurden an LCB-PET durchgeführt, das auf Basis der hochmolekularen PET-Type hergestellt wurde. Die molekulare Analyse der mit PMDA und TGDDM modifizierten Proben zeigt eine deutliche Zunahme der mittleren Molmassen, Molmassenverteilungsbreite,

des Gyrationsradius und des hydrodynamischen Radius und bestätigt somit die rheologischen Ergebnisse. Das Auftreten von Verzweigungen wird außerdem durch den abnehmenden Mark-Houwink-Exponenten bei zunehmender Additivkonzentration verdeutlicht. Eine genauere Betrachtung weist auf eine sternartige Molekülstruktur bei geringer Zugabe beider Kettenverlängerer hin. Bei erhöhter Zugabe hingegen tritt eine kammartige Struktur bei PMDA und eine baumartige oder hochverzweigte Struktur bei TGDDM auf, wie auch aus den nichtlinearen viskoelastischen Messungen zu schließen ist. Insbesondere PMDA erweist sich als hervorragender Kettenverlängerer, der bei reaktiver Extrusion reproduzierbar eine sternartige, kammartige oder baumartige Molekülstruktur in Abhängigkeit von der verwendeten PET-Type und der PMDA-Konzentration ermöglicht und so das Verarbeitungsspektrum von PET auf neue Anwendungsgebiete erweitert.

Contents

1 Introduction

Today's tasks of polymer research and development involve both progression of novel properties and the sustainability of the material. The demand on poly(ethylene terephthalate) (PET) increased continuously in the last decades, since the rigid and transparent[1] character benefits applications like packaging. However, the processing of the polymer is limited due to low viscosity. A modification of the molecular properties, e.g. a higher molar mass or a branched structure, would facilitate and improve the processability, such as film blowing or foaming (Münstedt et al., 2006). The second aspect, the sustainability of polymers, is strongly connected to the potential of recycling. Although the production of polymers increases, the landfilling amount recently declines[2]. In particular, the pre-selection of poly(ethylene terephthalate) bottles promotes a second use of the polymer. Nowadays, 20% of the recycled PET bottles fulfill high technical and U.S. Food and Drug Administration requirements and can be used for beverage bottles again. However, the majority of PET waste undergoes a downcycling to produce thermoformed films and fibers (Plastics Europe, 2015). This is mainly because poly(ethylene terephthalate) in liquid state is a rather complex and delicate material.

1.1 Poly(ethylene terephthalate) in Liquid State

A polymer in solution or melt state is essentially affected by the correlations between time, temperature and intermolecular forces governing the flow behavior. Consequently, it is worth examining the constitution of the PET molecule in more detail, or in specific terms, the ester group. The most general way to obtain a polyester is the reaction of an alcohol with an acid group by separation of water (Ravve, 2012). Since the reaction is reversible, it should be obvious that water can harm the molecule (Coltelli et al., 2007). Unfortunately, an ester group includes two oxygen atoms leading to a polar polymer that absorbs water molecules. Marshall and Todd (1953) were one of the first who reported on the degradation of PET and its impact on melt viscosity. In addition to hydrolysis from moisture, a thermo-oxidative (in air) and a purely thermal degradation (in nitrogen) at the ester linkage was observed.

[1] If the size or amount of crystals exceeds a certain value, PET appears in non-transparent white.

[2] The landfilling of polymers reduced by 40% in Europe during 2006 and 2012 (Plastics Europe, 2015).

The molecular structure of a polymer is determined by the molar mass (M), the molar mass distribution (MMD)[3], and the molecular architecture, i.e. linear or different types of branching (Dealy and Larson, 2006). The structure of PET depends on the polycondensation reaction and occurs as esterification or transesterification, which is a new arrangement of the functional group. A typical consequence of this step polymerization is reflected by the moderate Schulz-Zimm MMD (Mori and Barth, 1999). However, the range from the smallest to the very longest molecule essentially influences the rheological behavior, e.g. a broader distribution would extend the shear thinning behavior. In particular, a higher molar mass leads to a higher entanglement density and higher viscosities. This effect is reflected by the relation between the zero-shear viscosity η_0 and the molar mass, which governs a 3.4 power-law (Dealy and Larson, 2006). This empirical rule can be predicted by the reptation model of de Gennes (1971) with a molar mass dependence of M^3. Later, Doi (1983) presented a more precise explanation based on the tube model (cf. Chapter 2). Unfortunately, the increase in molar mass is limited in the reactor. The accompanied increase of viscosity prohibits a thoroughly stirring and evaporating of the side products. An increased temperature would lower the viscosity, but leads to homolytic scission. A commercial way out of the dilemma is the treatment of PET grades by solid state polymerization (SSP) to satisfy high technical applications. The SSP is conducted in an inert atmosphere at about $40°C$ below the melting point up to $24h$ (Ma et al., 2003). Once more the transesterification changes molecular properties.

Besides the composition, the role of catalysts has to be considered. In particular, different combinations of two catalysts needed for the polycondensation were reported to either decrease or increase the solution viscosity of PET during the reaction over long periods of time (Zimmermann, 1984). Traces of these metal compounds can later affect the processing of PET. Consequently, the idea that the polymer reveals an ongoing enhancement of molar mass in melt state should be considered. In sum, PET is a versatile polymer, but its reactivity can be also convenient for recycling or to induce new material properties during processing.

1.2 Reactive Processing

In 1928, six years after Hermann Staudinger introduced the concept of macromolecules, Wallace H. Carothers started to investigate the polycondensation of polyesters at *DuPont*. Eventually, his work helped to prove Staudingers theory, since Carothers was able to polymerize cumulative to a molar mass of $12 kg.mol^{-1}$. With this fairly long molecules he was able to pull fibers out of

[3]Also called polydispersity index (PDI).

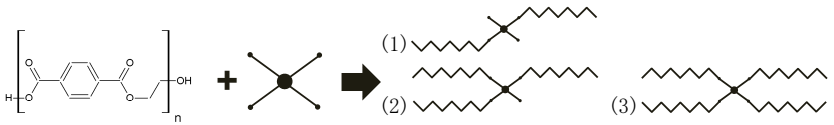

Figure 1.1: Tetra-functional chain extender reacting with two (1), three (2) or four (3) PET chains to a linear or branched molecule.

melt. Additionally, Carothers oriented fibers in solid state and called it *cold drawing*. Based on his work, J.R. Whinfield and J.T. Dickson submitted the first patent on poly(ethylene terephthalate) in 1941 (McIntyre, 2003).

Today's PET applications still include fibers, as woven textiles or high-strength yarns for tyre cords (Awaja and Pavel, 2005). Not least due to Carothers observation on forced stretching, *DuPont* began to develop the blow molding of hollow PET parts in the 1970s. The PET bottle and packaging applications have become the main demands by far (Plastics Europe, 2015). Besides blow molding, extrusion and injection molding are the most often applied processing operations (Assadi et al.). The two latter are conducted at temperatures above $255°C$, which leads to strong degradation of the molecule. The decomposition can be even more pronounced due to impurities in recycled grades (Awaja and Pavel, 2005). One, although expensive, solution is the compensation of degradation during recycling by SSP (Karayannidis et al., 1993, 1995).

In the recent past, reactive processing of PET is becoming more attractive since it allows to modify chain properties without an additional process (Xanthos, 1992). The idea consists in adding small functional molecules to the process which react with the end groups of the backbone. In fact, the extruder is employed as a reactor and the coupling agent is called chain extender. Due to its high reactivity, a bi-functional molecule would bond two single PET chains and increase the molar mass. Recycled poly(ethylene terephthalate) can be up-cycled and high linear PET molecules can be generated. Multi-functional chain extenders can be employed to achieve a branched structure and consequently fully new properties (Figure 1.1), as long-chain branched (LCB) polymers are known to have a higher melt strength compared to linear polymers (Wagner et al., 2001; Gabriel and Münstedt, 2003). Since these polymers can withstand higher stresses in melt state, thin and stable films can be blown, and foams can be expanded (Japon et al., 2000b; Xanthos et al., 2004; Coccorullo et al., 2009).

1.3 Role of Rheology

Rheology is the science of flow of matter and encloses the engineering and structural analysis of polymers. It is able to describe the processing of polymer melts and shows large sensitivity to molecular properties. Polymers consists of large macromolecules with viscoelastic properties, i.e. a combined solid and liquid material behavior. A main influence on the linear viscoelastic behavior is the free volume, which decreases with increasing molar mass to a certain extend. As a consequence, the friction and relaxation times enlarge, which leads to an increase of moduli and viscosity (Ferry, 1980). Both are also drastically affected by the number of entanglements which act as a temporary network, as will be discussed in Chapter 2. Dynamic measurements allow a distinction between the entropy driven elastic and the dissipative viscous part. The corresponding storage and loss modulus can be expressed as loss angle, which represents a more solid or liquid material behavior at different observation times or frequencies. This phase shift allows structural predictions including branching (Trinkle et al., 2002) and gelation (Winter and Chambon, 1986). Additionally, linear viscoelastic analysis can be employed to study the reaction kinetics of polymers, even during the measurement (Mours and Winter, 1994), and the diffusion of additives (Cassagnau et al., 2007).

The non-linear measurements, which occur at high deformations or deformation rates, are able to detect very precisely LCB. In particular, uniaxial elongation experiments are able to analyze the melt strength (Wagner et al., 1998). Further, it has been shown that the elongational properties largely determine the processability of polymers, e.g. during film blowing and thermoforming (Münstedt et al., 2006), which are of great importance in PET processing.

By constitutive equations, the physical response of the polymer bulk can be related to molecular features. The parameter β and f^2_{max} of the molecular stress function (MSF) model analyzed in this study are such parameters, which are capable to emphasize the branching (Wagner et al., 2004) and the stretch of the molecule (Wagner et al., 1998).

1.4 Motivation for This Work

Already Carothers took advantage of a certain melt strength, which enabled him to draw fibers. Enhanced elongation properties would improve film blowing or facilitate new applications like foaming of PET, even on recycled PET grades (Coccorullo et al., 2009), which cannot be achieved by common techniques nowadays (Scheirs, 2004).

The objective of this work is to create and analyze different grades of long-chain branched poly(ethylene terephthalate). The structure that has been pro-

duced by reactive processing, should be evaluated by means of rheology and molecular characterization.

Although the investigations of linear PET melt has been of common interest since decades, a research on current studies led to differing conclusions. Therefore, a thorough analysis for three different linear PET grades in regards of thermal and thermo-oxidative degradation, reaction kinetics and preparation method is necessary to understand further processing.

LCB PET can be achieved by reactive extrusion, but the processing of even neat material can effect the molecular properties. Hence, the analysis of the extrusion process in regards of thermal, thermal-oxidative, and shear degradation is a fundamental task.

Possible differences of the branched PET can be related either to different PET grades or chain extenders used. The aim of this study is to compare the reactive processing of three different PET grades with three different chain extenders by variation of the concentration of the additive. Additionally, the capability of industrial applications should be analyzed, which is realized by reactive processing at industrial scale.

The evaluation of the produced PET grades by linear and non-linear viscoelastic analysis is the main interest of this study. Therefore, the molecular stress function model and the two non-linear parameter β and f_{max}^2 can be used for a quantitative analysis of the molecular structure. Additionally, the understanding of melt fracture is of interest for polymer processing.

Finally, the rheological findings can be compared to the molecular characterization by light scattering and size exclusion chromatography to get more insight of the relation between structure and flow behavior.

2 Molecular Structure and Flow Behavior

The present study considers only polymer properties in liquid state. As will be shown in the following chapter, the similarities between polymers in solution and in melt state are numerous. Furthermore, the quantities of a single chain, e.g. size, molar mass, and branching, determine the behavior of the bulk, but the understanding of the interactions between the molecules are a challenging task. Consequently, the three-dimensional arrangement of a single polymer chain will be introduced in the first section of the chapter. The second section describes continuum mechanics, which can be used as a tool to analyze the macroscopic behavior. Finally it will be emphasized how the bulk approach can be related to the single chain properties by means of rheology and constitutive equations.

2.1 Properties of a Single Chain

The appearance or conformation of macromolecules in polymers is determined by statistics. It was Flory (1953), who described the chain properties theoretically, e.g. the molar mass distribution, but also related the statistical approaches to experimental results. The concept of the freely jointed chain is such a theoretical approach, which can be confirmed experimentally and be related to the size of the molecule by light scattering (Strobl, 2007). Additionally, branching can be analyzed in combination with *size-exclusion chromatography* (SEC) with triple detection. As will be shown, the shape and the mass of the polymer largely influence the dynamics of the molecule.

2.1.1 The Freely Jointed Chain

Polymers consist of single units which are arranged in chains. From a chemical point of view, these units are defined by monomers, which provide unified properties for each polymer. Besides the constitution of the molecule, the conformation of the chain largely influences the physical behavior. The conformation is the geometric appearance, which is defined by rotational angles. Usually, the rotational angle and the corresponding arrangement of two carbon atoms are restricted by repulsive forces between the hydrogen atoms. However, due to the low potential energy of the so-called trans and two gauche positions, the rotation of a few conjoint atoms can be considered as quasi free. Not least,

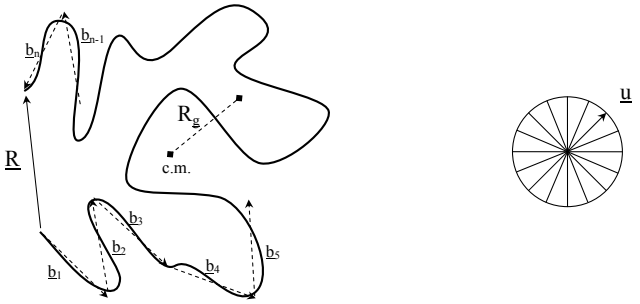

Figure 2.1: Illustration of conformation of an ideal chain with end-to-end vector $\underline{R}$, segment vectors $\underline{b}_i$, and radius of gyration $\underline{R}_g$. On the right, the representatives of unit vectors $\underline{u}$ in the undeformed relaxed state are depicted.

since the difference of potential energy vanishes at high temperature (Boyd and Phillips, 1996). The freely jointed chain, as illustrated in Figure 2.1, can be separated by chain segments with length b, which are not restricted by the correlation between two adjacent segments and the rotational angles (Hu, 2013). The sum of the corresponding vectors $\underline{b}_i$ defines the end-to-end vector with the components R_x, R_y, and R_z:

$$\underline{R} = \sum_{n=0}^{N} \underline{b}_i \tag{2.1}$$

Kuhn (1934) rejected the idea of a stiff, rod-like chain. He postulated a fiber-forming molecule, and divided the chain into units or segments of length b_k, which are related to the fully expanded chain R_{max} and the mean square end-to-end distance $\langle R^2 \rangle$:

$$b_k = \frac{\langle R^2 \rangle}{R_{max}} \tag{2.2}$$

The randomly arranged chain with a coil shape possesses a segment length between 5 and 12 carbon atoms which is a measure of the chain stiffness (Rubinstein and Colby, 2003). The notation $< ... >$ describes an ensemble average. The end-to-end distance of an ideal chain R_0 should be expressed as mean square, since the sum of orientation vectors $\underline{u}$ of segments $b \ll R_{max}$ is zero (Figure 2.1). With the length and number N of segments, the mean square end-to-end distance of an ideal chain is expressed as:

$$\langle R_0^2 \rangle = Nb^2 \tag{2.3}$$

Due to the stiffness of the monomers and hindered self-interaction, the end-to-end vector based on the segmental approach can deviate from an ideal end-to-

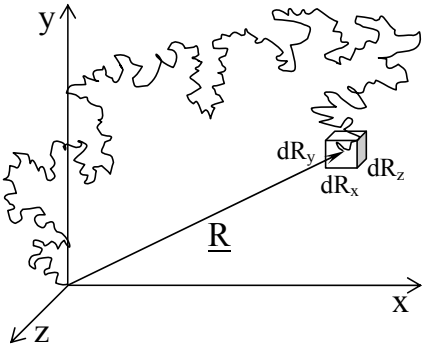

Figure 2.2: Conformation of an ideal chain with end-to-end vector $\underline{R}$, pointing in volume element dR_x, dR_y, and dR_z.

end vector, assuming fully free bond rotations. The characteristic ratio defines the difference between actual radii of a polymer and a theoretical value of free bond rotation:

$$C_\infty = \frac{\langle R^2 \rangle}{n b_b^2} \tag{2.4}$$

with length b_b and number n of bonds. If the segments are equal or larger than the Kuhn length, but smaller than the fully expanded chain R_{max}, the freely rotated chain with no excluding volume can by described by a random walk. The random walk, or flight for a three dimensional description, describes the relation between the initial and the end position after N arbitrary steps. Due to the large number of segments, such binomial probability function can be represented by a Gaussian distribution for a three-dimensional coil (Rubinstein and Colby, 2003):

$$\Psi(\underline{R}) d^3R = \left(\frac{3}{2\pi N b^2} \right)^{\frac{3}{2}} exp \left(\frac{3 \langle R^2 \rangle}{2 N b^2} \right) dR_x dR_y dR_z \tag{2.5}$$

This function describes the probability that the end-to-end vector $\underline{R}$ points into a volume element dR_x, dR_y, and dR_z, as can be noted by Figure 2.2. The ideal freely jointed chain is assumed to occur in melt or in theta solutions. Since the monomer concentration in melt is constant, the chain does not tend to expand. The so-called theta solution states that the attractive and repulsive forces between chain and solvent are in equilibrium. Consequently, the second viral coefficient A_2 vanishes at low concentrations (Strobl, 2007).

2.1.2 Characterization of Structure and Branching

A real chain cannot be characterized directly by the introduced quantities since the molecule is too small to measure the trajectory and define the end-to-end

distance. Additionally, ring or branched chains cannot be defined distinctly by R. A second measure of the dimension of a molecule is given by the radius of gyration R_g. The mean square of R_g and the end-to-end vector for a Gaussian chain are related by:

$$\left\langle R_g^2 \right\rangle = \frac{\left\langle R^2 \right\rangle}{6} \tag{2.6}$$

The radius of gyration is based on a consideration that the size can be described by a mean square average of magnitudes of vectors, pointing from the center of mass to single mass points, e.g. monomers (cf. Figure 2.1) (Boyd and Phillips, 1996). R_g can be expressed by:

$$\left\langle R_g^2 \right\rangle = \frac{1}{N} \sum_{i=1}^{N} \left\langle |\underline{r}_i - \underline{r}_{c.m.}|^2 \right\rangle \tag{2.7}$$

Since the definition of the center of mass is difficult, especially in permanent moving systems, R_g can be also determined by the difference between segments:

$$\left\langle R_g^2 \right\rangle = \frac{1}{N^2} \sum_{i=1}^{n} \sum_{j=1}^{n} \left\langle (\underline{r}_i - \underline{r}_j)^2 \right\rangle \tag{2.8}$$

The number of mass points is directly related to the molar mass, and since the radius of gyration describes the distances between the mass points, it is a measure of the coil size. The distribution of segments can be described by the relation between pairs. The pair correlation function of a Gaussian chain relates the number of monomers m to the radius r:

$$m \propto \left(\frac{r}{b}\right)^2 \tag{2.9}$$

The self-similarity of the ideal chain is expressed in Equation 2.9 by a fractal dimension of 2. The pair correlation function states the probability to find a monomer in a unit volume:

$$g(r) = \frac{3}{\pi r b^2} \tag{2.10}$$

It can be seen that the probability of finding a monomer decreases with distance. A further substitution of the pair distribution into the Debye structure function relates R_g to the number of monomers of a linear chain and Equation 2.6 can be derived (Strobl, 2007).

Light scattering is not only sensitive to the mass points, additionally, it can infer the size and conformation based on the pair distribution. If a molecule, or in particular the respective electrons, are perturbed by an oscillating electric field of a light beam, a dipole moment is induced which leads to an emission of photons (Boyd and Phillips, 1996). The scattering vector $\underline{q}$, as illustrated in

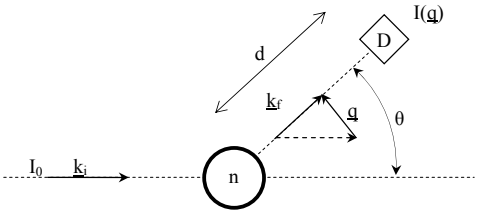

Figure 2.3: Sketch of light scattering on particle with respective scattering vector $\underline{q}$ and angle θ.

Figure 2.3, is the subtraction of wave vectors of scattered $\underline{k}_f$ and the incident plane wave $\underline{k}_i$.

$$\underline{q} = \underline{k}_f - \underline{k}_i \tag{2.11}$$

The scattering vectors from different monomers emerge and can be expressed as angle θ. The relation between scattering vector and angle $\theta$is a function of the wave length λ_0 and the refractive index of the solvent n_0 for polarized light:

$$\underline{q} = \frac{4\pi n_0}{\lambda_0} sin\frac{\theta}{2} \tag{2.12}$$

A more common way is the analysis of the radius of gyration by the Rayleigh ratio $R(\underline{q})$ or $R(\theta)$, which is the ratio between the intensity of scattering light $I(\underline{q})$ to the intensity of incident light I_0:

$$R(\underline{q}) = \frac{1}{V}\frac{I(\underline{q})d^2}{I_0} \tag{2.13}$$

with the distance d between particle and detector, and the volume of the scattered solution V (Strobl, 2007). The Rayleigh ratio is of practical relevance, e.g. by multi-angle light scattering (MALS). MALS in combination with a concentration detector is an absolute measurement of the molar mass and allows the determination of the radius of gyration (Podzimek, 2011). The particle scattering function includes the theoretical pair distribution function (Equation 2.10), and can be determined as:

$$P(\theta) = \frac{R_\theta}{R_0} \tag{2.14}$$

with the intensity of radiation at angle θ and at angle zero, the size and molar mass can be obtained independently from the source. As illustrated in Figure 2.4, by extrapolation to zero concentration c_0 the molar mass is given by the intersection with the ordinate and R_g is represented by the slope at different scattering angles (Zimm, 1948). A more detailed discussion of the light scattering is covered in Chapter 6.

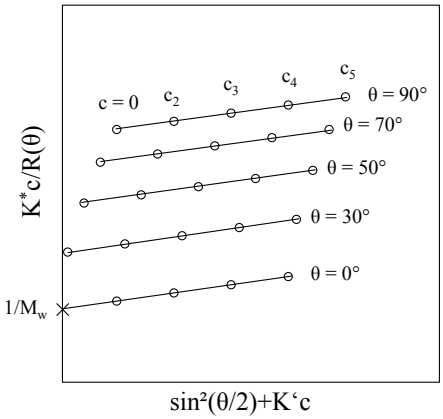

Figure 2.4: Zimm plot as representation of Rayleigh ratio $R(\theta)$ over the the scattering angle as $sin^2(\theta/2)$ as reciprocal of the molar mass at zero angle and R_g as slope of the scattering function with concentration c and optical constant K^*.

Branching

Due to a large number of possible end-to-end distances, it is more difficult to define a branched molecule by a quantity compared to a linear. A theoretical description is given by the Kramer theorem which considers of splitting an ideal branched molecule of N freely jointed Kuhn segments into two tree-like chains with N_1 and $N - N_1$ segments. If all possibilities of dividing the chain into two molecules are considered, the radius of gyration will be given as:

$$\left\langle R_g^2 \right\rangle = \frac{b^2}{N} \left\langle N_1(N - N_1) \right\rangle \tag{2.15}$$

By combinatorics a fractal dimension of 4 is expressed (Rubinstein and Colby, 2003), which emphasizes that a randomly branched polymer possesses a higher monomer density.

Zimm and Stockmayer (1949) derived a similar relation based on a numerical analysis of a randomly branched molecule consisting of branch units with 3 and 4 arms and a star polymer. They defined a coil contraction factor g, which relates the mean square radius of gyration of a linear to a branched molecule with equal molar mass:

$$g = \frac{\left\langle R_{g,br}^2 \right\rangle}{\left\langle R_{g,lin}^2 \right\rangle} \tag{2.16}$$

The upper limit is restricted to 1 by definition and contractions to 0.1 are reported (Podzimek, 2011).

With this numerical approach different contraction factors can be calculated leading to a degree of branching m, i.e. branch points per molecule. The following equations show the relations between contraction and branching for

star molecules with f arms of equal length (g_s) and tri- and tetra-functional (g_3 and g_4) branch units:

$$g_s = \frac{3f-2}{f^2} \tag{2.17}$$

$$g_3 = \left[\left(1+\frac{m}{7}\right)^{\frac{1}{2}} + \frac{4m}{9\pi}\right]^{-\frac{1}{2}} \tag{2.18}$$

$$g_4 = \left[\left(1+\frac{m}{6}\right)^{\frac{1}{2}} + \frac{4m}{3\pi}\right]^{-\frac{1}{2}} \tag{2.19}$$

A second verification of the coil contraction factor is given by the intrinsic viscosity. Similar to the coil contraction based on the radius of gyration, a factor g' is defined by the intrinsic viscosity $[\eta]$. The comparison between a linear and a branched molecule with equal molar mass is expressed as (Zimm and Kilb, 1959)

$$g' = \frac{[\eta_{br}]}{[\eta_{lin}]} \tag{2.20}$$

The advantage of g' is that it can be obtained for small molecules, since the detection of R_g is restricted to values larger than $10nm$. Both factors can be related by a power law, which allows conclusions of the structure with an exponent ε (Berry, 1968, 1988; Podzimek, 2013).

$$g' = g^{\varepsilon} \tag{2.21}$$

From the degree of branching, a branching frequency λ per 1000 repeated units can be calculated. Both the radius of gyration and the intrinsic viscosity can be performed by batch test without separation of size. However, the molar mass can be expressed by different moments leading to a number-average:

$$M_n = \frac{\sum_i n_i M_i}{\sum_i n_i} \tag{2.22}$$

weight-average

$$M_w = \frac{\sum_i n_i M_i^2}{\sum_i n_i M_i} = \frac{\sum_i w_i M_i}{\sum_i w_i} = \sum_i \frac{c_i}{c} M_i \tag{2.23}$$

and z-average

$$M_z = \frac{\sum_i n_i M_i^3}{\sum_i n_i M_i^2} = \frac{\sum_i w_i M_i^2}{\sum_i w_i M_i} = \frac{\sum_i c_i M_i^2}{\sum_i c_i M_i} \tag{2.24}$$

with the number fraction n_i, weight fraction w_i, concentration fraction c_i and the molecular mass distribution (MMD) or polydispersity index (PDI) is given as:

$$PDI = \frac{M_w}{M_n} \tag{2.25}$$

Consequently, a polymer with broad molar mass distribution should be analyzed by fractionated specimens, in order to get more insight of the physical response under deformation and the polymer structure. The SEC is the common technique to separate a diluted polymer by the hydrodynamic radius. The triple detection, i.e. the combination of MALS, concentration and viscosity detector, is capable to define an absolute molar mass, M_n, M_w, M_z, the radius of gyration and the intrinsic viscosity, which can be distinguished from a linear chain by the Mark-Houwink equation:

$$[\eta] = KM^a \tag{2.26}$$

with K depending on polymer, solvent and temperature and a, on the chain structure, additionally.

2.1.3 Microscopic Dynamics

A freely jointed chain obeys Brownian motions as long as no external constrains affect the mobility of the molecule. Consequently, it is plausible to include some thermodynamic considerations when analyzing microscopic behavior of a single chain. Based on the first law of thermodynamics a retractive force $\underline{f}$ as a function of the Helmholtz free energy F by a change of length dl at constant temperature and volume can be defined:

$$\underline{f} = \left(\frac{\partial F}{\partial l}\right)_{T,V} \tag{2.27}$$

$$= \left(\frac{\partial U}{\partial l}\right)_{T,V} - T\left(\frac{\partial S}{\partial l}\right)_{T,V} \tag{2.28}$$

$$= \underline{f}_e - \underline{f}_s \tag{2.29}$$

with internal energy U, temperature T, entropy S, and f_e as the energy and f_s the entropy contribution to the force. Above a certain temperature[1], the physical interactions between the amorphous chains are negligible ($f_e = 0$) and the force is purely entropic (Boyd and Phillips, 1996). The maximum entropy will occur, if the chain bond rotation is quasi free. The Boltzmann constant k relates the entropy to the probability of microstates of the molecule:

$$S = k\, ln\Psi \tag{2.30}$$

The possible states are given by Equation 2.2 and depend on the end-to-end vector $\underline{R}$. In other words, if the end-to-end distance is constrainted by a force into a less preferred length, the amount of free microstates and entropy declines.

[1] Thermal inversion point.

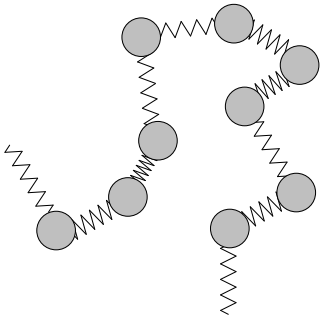

Figure 2.5: Rouse model as illustration of beads which are connected by different spring elements.

By assuming that all conformations have the same internal energy $U = const.$, the force in Equation 2.28, leads to the retractive force of an ideal chain $\underline{K}$, which is needed to separate chain ends:

$$\underline{f} = \underline{K} = \left(\frac{\partial F}{\partial \underline{R}}\right)_{T,V} = \frac{3kT}{Nb^2}\underline{R} \tag{2.31}$$

The term in front of $\underline{R}$ is the entropic spring constant, which decreases with decreasing number and length of segments and increases with increasing temperature. The force increases by stretching due to less possible conformation of the chain, but the linear dependence does not hold for large elongations, where $\underline{R}$ approaches R_{max} (Rubinstein and Colby, 2003).

Rouse Model
Whether solvent or melt, the diffusion of a particle in a surrounding fluid is controlled by the fluctuation and collisions of adjacent molecules. The force needed to drag the particle through the liquid with constant velocity $\underline{v}$ depends on a friction coefficient ζ which is proportional to a solvent viscosity[2]:

$$\underline{f} = \zeta \underline{v} \tag{2.32}$$

The friction coefficient can be related to the diffusion coefficient D by the Einstein relation (Einstein, 1905), which states how fast a molecule can move:

$$D = \frac{kT}{\zeta} \tag{2.33}$$

Rouse developed the first model that was able to describe the dynamics of a polymer chain. As can be seen in Figure 2.5, he separated the chain into n beads which are connected by springs with end-to-end distance b. If the chain is

[2]A velocity and shear rate dependence on the liquid is not considered here.

dragged through a freely draining solvent, each bead undergoes a single friction and the total contribution is given by (Rubinstein and Colby, 2003):

$$\zeta_R = n\zeta \tag{2.34}$$

and with Equation 2.33 the diffusion coefficient of a Rouse chain becomes:

$$D_R = \frac{kT}{n\zeta} \tag{2.35}$$

Since the chain consists of different segments, a differential equation of motion based on Equation 2.32 leads to different modes. The longest relaxation time, i.e. the first mode, is usually referred as Rouse relaxation time (Rouse, 1953):

$$\tau_R = \frac{\zeta b^2}{6\pi^2 kT} n^2 \tag{2.36}$$

It can be noted by Equation 2.36 that the inverse entropic spring constant (Equation 2.31) determines the movement of the chain. It was shown that the model undergoes limitations in a diluted system, due to the lack of hydrodynamic interaction, which are included in the Zimm model (Rubinstein and Colby, 2003). Nevertheless, the Rouse model can describe the behavior of an unentangled polymer chain in melt state (Bueche, 1954). As will be demonstrated later, this characteristic time is a determining property of the relaxation modulus of polymeric systems, i.e. single chains, colloids, rubber material, and entangled melts. However, the description of such bulk material requires a capable macroscopic mechanical approach.

2.2 Fundamentals of Continuum Mechanic

The most basic description in mechanics is given by the relation between the load and the deformation of a material. For a wide range of solids the response of the material follows a linear constant, i.e. the shear or Youngs modulus, known as Hookes law. Polymers are viscoelastic materials and possess a large time and deformation dependent response. A stress σ, i.e. a force per area, is given by an intrinsic material property G and a deformation:

$$\sigma \propto G \cdot S \tag{2.37}$$

The deformation can be expressed in different form, due to the time dependence. The general strain measure S is either correlated to a dimensionless deformation gradient[3], an orientation tensor[4] or a deformation rate[5]. The time dependent

[3] E.g. elongation strain ε, Cauchy tensor $\underline{\underline{C}}$.
[4] $\underline{\underline{S}}$.
[5] E.g. shear rate $\dot{\gamma}$, deformation rate tensor $\underline{\underline{D}}$.

material property G is usually a modulus[6], the viscosity or the memory function m, which includes the deformation history. Either G or S is expressed as time derivative to include the former deformation or deformation rate dependence[7]. Generally, the constitutive equation is either a differential-type or an integral-type, as will be considered in this study. Equation 2.37 reflects only a proportional relation between the properties. In particular, a non-linear parameter in regards to entanglements and stretch of the molecules needs to be added to achieve a fully developed equation. The necessary parameters are introduced in this chapter, and are still a current concern in polymer research (Narimissa and Wagner, 2016a,b).

The linear and non-linear viscoelastic behavior of polymers is largely deformation and motion dependent, due to the relaxation properties and interactions of the macromolecules. For such bulk materials, continuum mechanics can describe the forces and motions in regards of their spatial behavior as long as the quantities are larger than those of the individual particles. An advantage of this approach is the application of field theory, which can be employed as long as a homogeneous distribution of matter is given in space. This allows a characterization of matter by scalar, vector and tensor values, in the forms of mass density, velocity distribution or stress tensors depending on time and space (Leigh, 1968; Haupt, 2002).

2.2.1 The Spatial Stress

An applied stress on a three-dimensional body acts from the surface to the inside, which can be understood by an interaction of infinitesimal cubes, as can be seen in Figure 2.6 (a). A complete description is given by the stress tensor and by nine Cartesian components σ_{ij} with i as plane and j as direction indices:

$$\underline{\underline{\sigma}} = \begin{bmatrix} \sigma_{xx} & \sigma_{xy} & \sigma_{xz} \\ \sigma_{yx} & \sigma_{yy} & \sigma_{xz} \\ \sigma_{zx} & \sigma_{zy} & \sigma_{zz} \end{bmatrix} = \begin{bmatrix} \sigma_{xx} & \tau_{xy} & \tau_{xz} \\ \tau_{yx} & \sigma_{yy} & \tau_{xz} \\ \tau_{zx} & \tau_{zy} & \sigma_{zz} \end{bmatrix} \tag{2.38}$$

The components with equal indices are defined as normal stresses σ and the components, which are parallel to the corresponding plane as shear stresses τ. Due to a balance of angular momentum, the tensor is symmetric and opposed shear stresses are equal, i.e. $\tau_{xy} = \tau_{yx}$, $\tau_{xz} = \tau_{zx}$ and $\tau_{yz} = \tau_{zy}$ (Münstedt and Schwarzl, 2014). With this, a force $\underline{f}$ acting on a plane with any orientation,

[6] E.g. shear modulus G, elastic modulus E.
[7] m or $\underline{\underline{D}}$.

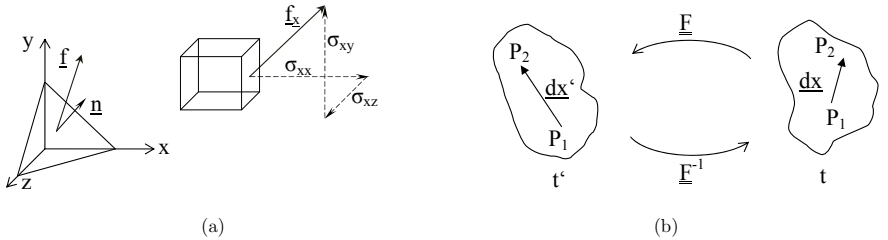

Figure 2.6: Extra stress tensor (a) and deformation of two arbitrary points (b).

which is characterized by a normal vector $\underline{n}$, can be described:

$$\underline{f} = \underline{n} \cdot \underline{\underline{\sigma}} \tag{2.39}$$

$$\underline{f}_i = \underline{n}_j \cdot \underline{\underline{\sigma}}_{ij} \tag{2.40}$$

An isostatic pressure acts as normal stresses in negative direction on the material. Due to the assumption that polymer melts are incompressible, the pressure can be seen as scalar component, which changes the absolute boundary conditions, but not the flow behavior. Therefore the normal stresses are usually denoted as differences. The stress tensor introduced here is equal to the so-called extra stress tensor, neglecting the isostatic pressure (Macosko, 1994).

2.2.2 Deformation

At small deformations, it is sufficient to know the displacement of two adjacent points from a relaxed state $\underline{x}_0$ at $t = 0$ to a deformed state $\underline{x}$ at a time t. If the changes in all directions are known, the Cauchy-Green deformation tensor can be expressed and a distinct relation to the stress tensor can be found. Other than usual deformations of solids, polymer melts undergo large strains during processing. The relative deformation of two adjacent points P_1 and P_2 (Figure 2.6 (b)) with vector $\underline{dx}$ at the observation time and $\underline{dx}'$ at the past can be related by a partial derivative with respect to the present position:

$$\underline{dx}' = \frac{\partial \underline{x}'}{\partial \underline{x}} \underline{dx} \tag{2.41}$$

The components of the displacement lead to the the relative deformation gradient tensor $\underline{\underline{F}}_{t,t'}(t, t')$ with regards to the time of observation t:

$$\underline{\underline{F}}_{t,t'}(t, t') \equiv \frac{\partial \underline{x}'}{\partial \underline{x}} = \begin{bmatrix} \frac{\partial x'}{\partial x} & \frac{\partial x'}{\partial y} & \frac{\partial x'}{\partial z} \\ \frac{\partial y'}{\partial x} & \frac{\partial y'}{\partial y} & \frac{\partial y'}{\partial z} \\ \frac{\partial z'}{\partial x} & \frac{\partial z'}{\partial y} & \frac{\partial z'}{\partial z} \end{bmatrix} \tag{2.42}$$

The expression as a gradient allows a uniform description of the deformation of adjacent points. Since it is not easy to define a fully relaxed state t_0 of viscoelastic materials, the observations of the relative deformation concern a deformed state t' between 0 and t. The use of Lagrangian coordinates allows a perspective which follows the motion of the material. This simplifies the boundary values, since an initial state is obsolete and the past motion can be described as Equation 2.42. This prediction goes back in time and the relative inverse deformation gradient tensor refers to the time of observation, with $F_{ij}^{-1} = \partial x_i / \partial x'_j$:

$$\underline{\underline{F}}^{-1}_{t,t'}(t,t') \equiv \frac{\partial \underline{x}}{\partial \underline{x}'} \tag{2.43}$$

Since rotation of the material does not lead to a change of distance between two points concerned, the emerging stress would be unaffected. The rotation can be discarded by the product of the tensor and its transposed, leading to the relative Cauchy tensor $\underline{\underline{C}}_{t,t'}(t,t')$ and its inverse, the Finger tensor $\underline{\underline{C}}^{-1}_{t,t'}(t,t')$ (Leigh, 1968; Bird et al., 1987; Münstedt and Schwarzl, 2014):

$$\underline{\underline{C}}_{t,t'}(t,t') = \underline{\underline{F}}^{T}_{t,t'}(t,t') \cdot \underline{\underline{F}}^{-1}_{t,t'}(t,t') \tag{2.44}$$

$$\underline{\underline{C}}^{-1}_{t,t'}(t,t') = \underline{\underline{F}}^{-1}_{t,t'}(t,t') \cdot \underline{\underline{F}}^{T}_{t,t'}(t,t') \tag{2.45}$$

2.2.3 Shear and Extensional Flow

A constraint deformation induces an opposed force as a consequence of entropic elasticity, as derived in Section 2.1.3. However, the Brownian motion and an entropic driven resistance are largely time dependent. Therefore, it is necessary to study the flow by the rate of the relative deformation, expressed as the velocity gradient tensor (Haupt, 2002):

$$\underline{\nabla v} = \frac{\partial}{\partial t} \underline{\underline{F}}^{-1}_{t,t'}(t,t') \tag{2.46}$$

or written in components $\underline{\nabla v} = \partial v_j / \partial x_i$ (Bird et al., 1987). It can also be written as $\underline{\underline{\kappa}}$ and decomposed into the sum of a symmetric and an antisymmetric tensor:

$$\underline{\nabla v} = \underline{\underline{\kappa}} = \underline{\underline{D}} + \underline{\underline{W}} \tag{2.47}$$

with $\underline{\underline{D}}$ representing the deformation rate tensor and $\underline{\underline{W}}$ the rotation deformation or vorticity tensor. This separation is useful since the rotation is not always of interest in studying the flow behavior[8]. The tensors are defined as:

$$\underline{\underline{D}} = \frac{1}{2}\left(\underline{\nabla v} + (\underline{\nabla v})^T\right) \tag{2.48}$$

$$\underline{\underline{W}} = \frac{1}{2}\left(\underline{\nabla v} - (\underline{\nabla v})^T\right) \tag{2.49}$$

[8]Simple elongation possesses no rotation components in contrast to shear flow.

An effective way to simplify the boundary conditions is the use of well defined flows. Simple shear and uniaxial extensional flow possess the advantage to be analyzed by both experimental and theoretical approaches.

Simple Shear Flow
A simple shear flow can be achieved by two parallel confining plates, where the lower is fixed and the upper moves with a velocity $\underline{v}_x$, as can be seen in Figure 2.7. If the fluid possesses wall adhesion, the shear deformation $\gamma(t, t')$ and the corresponding rate can be expressed as:

$$\gamma(t, t') = \frac{dx}{y} \tag{2.50}$$

$$\dot{\gamma}(t, t') = \frac{d\gamma}{dt} \tag{2.51}$$

The time dependence is omitted for the following strains, $\gamma = \gamma(t', t)$. The shear deformation defines the displacement in x-direction, as $x = x' + \gamma y$, and with no displacement in y and z direction, the relative deformation gradient tensor is given as:

$$\underline{\underline{F}}^{-1}_{t,t'}(t, t') = \begin{bmatrix} 1 & \gamma & 0 \\ 0 & 1 & 0 \\ 0 & 0 & 1 \end{bmatrix} \tag{2.52}$$

The velocity of deformation in x-direction can be expressed with the shear rate as $\underline{v}_x = \dot{\gamma} y$, and with zero velocity in the y- and z-direction, the velocity gradient becomes:

$$\underline{\nabla v} = \begin{bmatrix} 1 & \dot{\gamma} & 0 \\ 0 & 1 & 0 \\ 0 & 0 & 1 \end{bmatrix} = \underline{\underline{D}} + \underline{\underline{W}} = \frac{1}{2} \begin{bmatrix} 0 & \dot{\gamma} & 0 \\ \dot{\gamma} & 0 & 0 \\ 0 & 0 & 0 \end{bmatrix} + \frac{1}{2} \begin{bmatrix} 0 & \dot{\gamma} & 0 \\ -\dot{\gamma} & 0 & 0 \\ 0 & 0 & 0 \end{bmatrix} \tag{2.53}$$

As can be seen by Equation 2.53, simple shear is determined only by a scalar value, and the shear stress can be expressed by $\tau_{xy} = \eta\dot{\gamma}$ (Phan-Thien, 2002).

Simple Extensional Flow
Uniaxial or simple elongation is the change of shape under normal stresses. Equibiaxial and planar elongation are not discussed here. The strain or extension ratio of each direction i is given by the ratio of the present length l to the former length l' (Macosko, 1994):

$$\lambda_i(t, t') = \frac{l_i(t)}{l_i(t')} \tag{2.54}$$

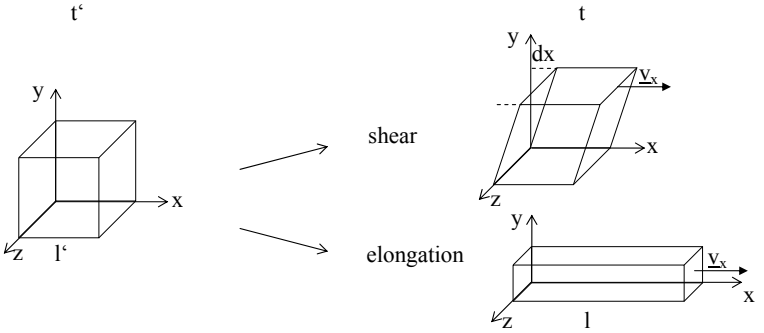

Figure 2.7: Shear and elongation deformation.

For simplicity, the direction and time dependence is not denoted further. A common description for the strain is given by the engineering strain as:

$$\varepsilon_E = \frac{l - l'}{l'} \tag{2.55}$$

By assuming an incompressible fluid the volume is constant, leading to:

$$\lambda_1 \cdot \lambda_2 \cdot \lambda_3 = 1 \tag{2.56}$$

At large deformation, it is convenient to use an infinitesimal change of the current length by a differential analysis, which leads to the so-called Hencky strain:

$$d\varepsilon = \frac{dl}{l} \rightarrow \quad \varepsilon = ln\lambda \tag{2.57}$$

A strain can be expressed as inverse deformation gradient tensor:

$$\underline{\underline{F}}^{-1}_{t,t'}(t,t') = \begin{bmatrix} \lambda & 0 & 0 \\ 0 & \lambda^{-\frac{1}{2}} & 0 \\ 0 & 0 & \lambda^{-\frac{1}{2}} \end{bmatrix} = \begin{bmatrix} e^{\varepsilon} & 0 & 0 \\ 0 & e^{-\frac{1}{2}\varepsilon} & 0 \\ 0 & 0 & e^{-\frac{1}{2}\varepsilon} \end{bmatrix} \tag{2.58}$$

The Hencky strain rate $\dot{\varepsilon}$ is the time derivative of ε and the velocity gradient tensor is given as:

$$\underline{\nabla v} = \frac{1}{2} \begin{bmatrix} \dot{\varepsilon} & 0 & 0 \\ 0 & -\frac{1}{2}\dot{\varepsilon} & 0 \\ 0 & 0 & -\frac{1}{2}\dot{\varepsilon} \end{bmatrix} = \underline{\underline{D}} \tag{2.59}$$

Since no rotation occurs in simple elongation, the vorticity vector is zero.

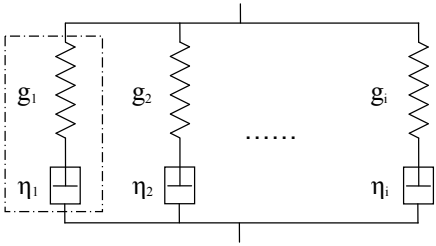

Figure 2.8: Maxwell model (dashed box) and generalized Maxwell model with different modes.

2.3 Linear Viscoelasticity

The complete description of the material function Equation 2.37 is given by a entirely known material behavior. In regards of the extend or rate of deformation, a linear and a non-linear response need to be distinguished. A creep or a relaxation experiment under shear is a simple arrangement to observe the linear viscoelastic behavior of a material. As long as the applied constant stress or deformation is small, a compliance $J(t)$ or relaxation modulus $G(t)$ describes the material sufficiently. The time dependent behavior can be analyzed by models.

2.3.1 Generalized Maxwell Model

The Maxwell model describes the relaxation behavior of an idealized polymer, which is governed by an elastic (spring) and viscous (dashpot) contribution (dashed box in Figure 2.8). The differential Equation 2.60 describes the relation between shear rate $\dot{\gamma}$, relaxation time λ, shear stress τ and viscosity η.

$$\eta\dot{\gamma} = \lambda\dot{\tau} + \tau \tag{2.60}$$

The characteristic value of the material is given by the relaxation time as the ratio of the viscous (η) and elastic (G) contributions:

$$\lambda = \frac{\eta}{G} \tag{2.61}$$

The solution of the differential equation leads to (Ferry, 1980):

$$\tau(t) = \int_{i=1}^{N} G e^{-\frac{t-t'}{\lambda}} \dot{\gamma}(t,t')dt' \tag{2.62}$$

An idealized polymer consists of chains with uniform length, leading to a molar mass distribution of 1. Usually, polymers have a broad MMD and even narrow distributed polymers possess different molar masses. The general Maxwell

model, as can be seen in Figure 2.8, is an approximation of the behavior of real polymers by different modes i. Single spring and dashpot elements representing different fraction of molecules with a characteristic relaxation time λ_i and modulus g_i arranged to an array. The single modes describe single stresses which can be added as Carreau et al. (1997):

$$\sigma = \sum_{i=1}^{N} \sigma_i \tag{2.63}$$

This sum is known as Boltzmann superposition principle, which is given when a stress or deformation on a body can be added and a linear proportional response emerges. By including Equation 2.63 into Equation 2.62, the generalized Maxwell model for any spacial deformation can be described:

$$\underline{\underline{\sigma}}(t) = 2 \int_{i=-\infty}^{t} \sum_{i=1}^{N} g_i e^{-\frac{t-t'}{\lambda_i}} \underline{\underline{D}}_{t,t'}(t,t')dt' \tag{2.64}$$

with the discrete relaxation spectrum as

$$G(t-t') = \sum_{i=1}^{N} g_i e^{-\frac{t-t'}{\lambda_i}} \tag{2.65}$$

In the linear viscoelastic regime a fully known relaxation modulus leads to a complete description of the stress and the strain.

Although a complete stress relaxation curve can be achieved from a step strain test, the precision at long relaxation times is limited due to physical limits of the instrument. An oscillatory rotational measurement is not only a precise and convenient technique, but also, it allows to examine relaxation phenomena at different frequencies. Based on the generalized Maxwell model a substitution of the strain with a complex sinusoidal strain:

$$\gamma(t) = \gamma_0 \cdot sin(\omega t) \tag{2.66}$$

$$\gamma^*(t) = \gamma_0 \cdot e^{i\omega t} \tag{2.67}$$

lead to a complex shear modulus

$$G^* = G'(\omega) + iG''(\omega) \tag{2.68}$$

with $G'(\omega)$ as storage and $G''(\omega)$ loss modulus.

$$G'(\omega) = \sum_{i=1}^{N} g_i \frac{(\omega\lambda_i)^2}{1+(\omega\lambda_i)^2} \tag{2.69}$$

$$G''(\omega) = \sum_{i=1}^{N} g_i \frac{\omega\lambda_i}{1+(\omega\lambda_i)^2} \tag{2.70}$$

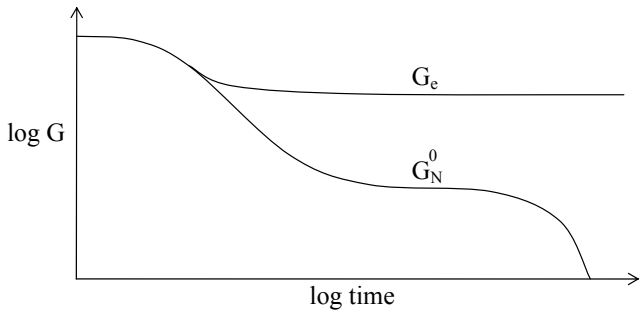

Figure 2.9: Time dependence of relaxation modulus with plateau value G_N^0 of an entangled polymer and an equilibrium modulus G_e of a cross-linked polymer.

The elastic and viscous response are shifted by a phase angle δ. The absolute complex viscosity can be expressed as:

$$|\eta^*| = \frac{\sqrt{G'(\omega)^2 + G''(\omega)^2}}{\omega} \tag{2.71}$$

From the numerators in Equation 2.69 and 2.70 it can be noticed that G' and G'' depend on the angular frequency with ω^2 and ω at small values of ω. This dependence is expressed by a slope of 2 and 1 in a double logarithmic plot for a Maxwell fluid, indicating the terminal regime.

Although the discrete relaxation spectrum (λ_i and g_i) possesses no physical meaning (Dealy and Larson, 2006), it allows a complete description of the storage and the loss moduli and hence, the linear viscoelastic behavior. The relaxation modulus can be calculated from the discrete spectrum by different analytic or numerical approaches (Schwarzl, 1975; Baumgaertel and Winter, 1989). If infinitesimal modes are known, a continuous relaxation spectrum $H(\lambda)$ would be expressed (Goodwin and Hughes, 2000), which is of particular importance for the expression of the compliance and the analysis of creep experiments. A typical evolution of the relaxation modulus with time for an entangled thermoplastic with broad MMD and a cross-linked polymer is illustrated in Figure 2.9. The double logarithmic plot reveals a drastic drop of the modulus to a plateau G_N^0 which is governed by the entanglements of the strands, as will be discussed in Section 2.4.2. Further, the final decrease corresponds to the terminal behavior with the aforementioned frequency dependence of G' and G''. Polymers with additional cross-linking like rubbers exhibit a similar relaxation at first, but also a remaining elastic component G_e, which depends on the amount of network cross-links.

2.3.2 Dependence on Temperature, Molar Mass, and Branching

The measurement of the relaxation modulus is strongly dependent on time, since the duration of relaxation can exceed to very long measurement times, e.g. during a step strain experiment. However, the relaxation time can be reduced by higher temperature since at low temperature the behavior is more glassy and at high temperature more rubbery and viscous. Therefore, the relaxation modulus in Figure 2.9 and the storage and loss moduli can be obtained at different temperatures and shifted along the time or frequency axis to a master curve. The main assumption is that the relaxation phenomena possesses the same temperature dependence (Ferry, 1980) and can be shifted by a single parameter a_T:

$$\lambda_i(T) = a_T(T)\,\lambda_i(T_r) \tag{2.72}$$

If the temperature is more than $100K$ above the glass transition temperature T_g, an Arrhenius type equation can be used to relate the shift to the reference temperature T_r:

$$a_T = \exp\left[\frac{E_A}{\mathcal{R}}\left(\frac{1}{T} - \frac{1}{T_r}\right)\right] \tag{2.73}$$

where $\mathcal{R}$ is the universal gas constant. A change of flow activation energy E_A is known to depend more significantly on branching than on the molar mass of a molecule (van Gurp and Palmen, 1998). As soon as the observed temperature is close to T_g, the WLF equation can be used, which is based on an assumption that the free volume changes with temperature linearly. Beside the horizontal shift, a vertical shift b_T can be necessary, which can be explained by variation of density ρ with temperature (Ferry, 1980):

$$b_T \equiv \frac{T_r \rho_r}{T \rho} \tag{2.74}$$

Rouse related the vertical shift to a change of the friction coefficient with free volume effects (Rouse, 1953), leading to a shift of the relaxation modulus. Additionally, experimental artifacts can be compensated by a vertical shift (Macosko, 1994). If both factors are not sufficient to create a master curve, the material is said to be thermo-rheologically complex [Schwarzl and Staverman 1952].

A material with LCB structure often exhibits thermo-rheological complexity, since the free volume dependence is more sophisticated, although star-like chains are mostly found to be simple (Dealy and Larson, 2006). A method to analyze such behavior is the *van Gurp-Palmen plot* (van Gurp and Palmen, 1998; Trinkle and Friedrich, 2001; Trinkle et al., 2002), which relates the complex modulus to the phase angle. Since such an illustration contains no time and

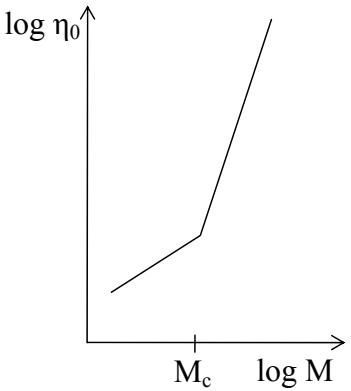

Figure 2.10: Relation between zero-shear viscosity and molar mass for entangled and non-entangled molecules.

temperature information, a rheological simple material should superimpose. A further advantage of the analysis is a molar mass independent plotting, leading to the predictions of the structure in terms of molar mass distribution and branching. The method is discussed in detail in Section 5.1.3.

The most significant and widely analyzed correlation between molecular structure and linear viscoelastic response of the material is provided by the zero-shear viscosity η_0 (Münstedt, 1980). If a shear rate is low enough, a liquid polymer possesses no rate dependence and the Boltzmann superposition principal is valid. Based on a large number of experiments, a relation between the molar mass and η_0 can be represented as Figure 2.10. The first section of the graph is restricted by a critical molar mass M_c and reveals a slope of 1 in the double logarithmic plotting. The region is governed by the Rouse time, which increases linear with the molar mass (cf. Section 2.1.3). Regardless of a diluted or melt state, the friction coefficient acts like a spring constant and the relaxation time and zero-shear viscosity increase linear, as long as no entanglements exits. From a critical value M_c, which is in the range of $2M_e$, the entanglements dominate the viscosity and the slope changes (Münstedt and Auhl, 2005). The origin of the behavior is discussed in the next section. As shown in the literature, the exponent changes slightly with the polymer and different numbers are reported on this question (Ferry, 1980; Dealy and Larson, 2006; Münstedt et al., 2006). The 3.4 power law used in this study can be seen as a empirical tradition.

$$\eta_0 = K M_w^{3.4} \qquad M_w \geq M_c \tag{2.75}$$

The parameter K and M_c depend on the polymer and temperature (Dealy and Larson, 2006; Rubinstein and Colby, 2003). This power law is only valid for linear polymers. Deviations were observed at equal molar mass for highly branched molecules leading to lower viscosities and single LCB polymers like

star-like structures, which exhibit a higher zero-shear viscosity at constant molar mass (Larson, 1988; Münstedt et al., 2006). This phenomenon was analyzed by an exponential function by (McLeish and Milner, 1999). It was also found that small amounts of high molar mass increase the zero-shear viscosity, although thought to be independent of MMD (Kheirandish, 2005).

Indeed, the linear viscoelastic measurement is capable to distinguish different topologies of polymer (Van Ruymbeke et al., 2002). The zero viscosity is very sensitive to changes in molar mass, and the activation energy to LCB. The phase angle can be analyzed by the van Gurp-Palmen plot and broad MMD and LCB can be concluded. Unfortunately, a large amount of reference measurements is necessary and an absolute prediction can not be drawn. Therefore, non-linear rheological characterization should be employed for secured information (Dealy and Larson, 2006).

2.4 Non-Linear Viscoelasticity

In this section the non-linear phenomena in shear and elongational flow are described. Different theories were developed in the last decades to model the deformation behavior. Molecular features, in particular, helped to improve the performance and the realistic description of the models and are discussed in the following.

2.4.1 Non-Linear Phenomena

Non-linearity between stress and strain will occur if the strain or the strain rate exceeds a critical value. In other words, when shearing occurs with a low rate or low deformation, the molecules are able to compensate the constrains by relaxation.

The two main origins of this behavior are the entanglements and the stretch of the molecules. The former can be observed by the shear thinning effect, which occurs when the recoiling of the chains cannot follow the deformation rate. Consequently, disentanglement emerges and the viscosity decreases. Different models were developed[9], quantifying the shear thinning and include the offset partially (Macosko, 1994). Since the phenomena originates in the entanglement density, it is affected by the chemical consistency, temperature, molar mass and polymer structure.

However, since an oscillatory response of liquid material depends also on the entanglement density, it reveals a change from Newtonian to non-terminal behavior, too. Cox and Merz (1958) observed that the onset and magnitude of

[9] Ostwald/de Waele, Carreau/Yasuda, Herschel/Bulkley.

the shear thinning effect will superimpose, if steady shear and dynamic shear data are compared:

$$\eta(\dot{\gamma}) = |\eta^*|(\omega); \qquad with \qquad \dot{\gamma} = \omega \tag{2.76}$$

This empirical rule is widely used in polymer research for all kinds of polymers. However, due to the usual logarithmic illustration, the observed difference of 25% vanishes apparently (Dealy and Larson, 2006).

The second effect, the stretching, can also be observed during a steady state experiment and is of great practical relevance. If a converging flow appears, e.g., from an extruder barrel into a die, a pure shear dissipation is enhanced by a stretch contribution. As demonstrated in Chapter 4, a capillary flow needs to be corrected to achieve true data. Cogswell (1972, 1978, 1981) derived Equation 2.77, that allows to distinguish between shear and elongational contribution, and gives an elongation viscosity as a function of the strain rate $\dot{\varepsilon}$:

$$\eta_E = \frac{9}{32}\frac{(n+1)^2}{\eta}\left(\frac{P_O}{\dot{\gamma}}\right)^2 \tag{2.77}$$

η is the shear viscosity, $\dot{\gamma}$ the shear rate, P_O the pressure drop of an orifice die and n the shear power law index.

Both effects need to be included in a constitutive equation like Equation 2.37 to achieve a complete description valid for all types of deformation. The disentanglement effects were analyzed by the *damping function* (Wagner, 1976), which describes a survival property of entanglements (cf. Rolón-Garrido and Wagner (2009)). The second contribution, in particular, can be observed during simple elongation. The *molecular stress model* was introduced by Wagner and Schaeffer (1992, 1993) to describe the stretching effect and the impact on the rheological behavior based on molecular features. The model is based on the *tube model* and a brief overview of its evolution is given in the following sections.

2.4.2 The Rubber-Like Liquid and Tube Model

In the beginning of the 1940s, a theory of elasticity for a cross-linked network was introduced independently by different researchers (Larson, 1988). The *rubber elasticity* is based on network strands, which are connected by permanent cross-links and possess N_k Kuhn segments. At the undeformed state, it is assumed that each strand is defined by an end-to-end vector $\underline{R}$ and a Gaussian distribution $\Psi_0(\underline{R})d^3\underline{R}'$, as can be noted in Figure 2.11. By assuming an even spaced arrangement of strands, an affine deformation λ, lead to a deformed $\underline{R}$ and new probability $\Psi(\underline{R})d^3\underline{R}$ of microstates. The two states are related by the affine strain, i.e. the same relative deformation of the strands as imposed on macroscopic network (Rubinstein and Colby, 2003):

$$\underline{R}_i = \underline{R}'_i\lambda_i \tag{2.78}$$

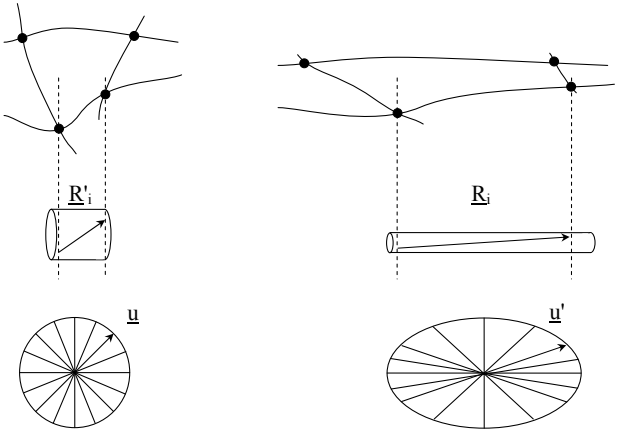

Figure 2.11: Rubber elasticity with affine deformation.

Equation 2.39 relates the stress to a unit area depending on a force $\underline{f}$. Therefore, a spacial stress can be related to the network strands per unit volume v, each possessing a respective retractive forces $\underline{K}$:

$$\underline{\underline{\sigma}} = v \left\langle \underline{R}\, \underline{K} \right\rangle = \frac{3kTv}{Nb^2} \left\langle \underline{R}^2 \right\rangle \tag{2.79}$$

The classical rubber elasticity equation for an incompressible material is expressed by the relative Finger tensor as:

$$\underline{\underline{\sigma}} = G_e \, \underline{\underline{C}}^{-1}_{t,t'}(t,t') = vkT \begin{bmatrix} \lambda_x^2 & 0 & 0 \\ 0 & \lambda_y^2 & 0 \\ 0 & 0 & \lambda_z^2 \end{bmatrix} \tag{2.80}$$

with the equilibrium shear moduls of the permanent network G_e (Ferry, 1980; Larson, 1988)[10]:

$$G_e = vkT \tag{2.81}$$

Rubber-Like Liquid

The Rouse relaxation time and the rubber elasticity are the fundamental equations in polymer mechanics, although they do not include entanglement and

[10] Two different notations are common in the literature. If the Boltzmann constant is expressed as gas constant, the strand density would be in molar units.

deformation rate of the material. Green and Tobolsky (1946) transformed the idea of rubber elasticity into a transient network model by replacing the cross-links by temporary junctions. A survival property P of isotropic distributed entanglements during a deformation between t' and t can be related to a relaxation time λ:

$$\frac{d}{dt}P_{t',t} = -\frac{1}{\lambda}P_{t',t} \tag{2.82}$$

If only a single relaxation process occurs, a material could be characterized by one relaxation time. A decade later, Lodge (1956) refined the idea by adding multiple relaxation processes. By assuming a constant number of v_i strands per volume with λ_i relaxation times, Equation 2.80 can be expressed as:

$$\underline{\underline{\sigma}}(t) = \int_{i=-\infty}^{t} m(t-t')\,\underline{\underline{C}}_t^{-1}(t,t')dt' \tag{2.83}$$

and subtitution of the memory function:

$$m(t-t') = \sum_i \frac{g_i}{\lambda_i} e^{-\frac{t-t'}{\lambda_i}} = \frac{dG(t-t')}{dt'} \tag{2.84}$$

The memory function describes the survival probability regarding the intrinsic material properties and can be determined experimentally from Equation 2.65. The strand density in Equation 2.81 can be replaced by an entanglement density v_e, which leads to the plateau modulus of a high molecular liquid material:

$$G_N^0 \;=\; v_e \mathcal{R}T = \frac{\rho \mathcal{R}T}{M_e} \tag{2.85}$$

with a molar mass of entanglements M_e and the density ρ:

$$M_e \;\equiv\; \frac{\rho}{v_e} \tag{2.86}$$

$$\tag{2.87}$$

The plateau modulus of a rubber and rubber-like liquid material (cf. also G_e and G_N^0 in Figure 2.9) are unique polymer properties and can be determined experimentally. Equation 2.83 is able to predict the first normal stress difference and strain hardening behavior, although overpredicted.

The expression by Lodge considers the motion of the molecules, but neglects the survival probability due to deformation included by Wagner (1976), and the *damping function* $h(I_1, I_2)$, with $0 \leq h \geq 1$. I_1 and I_2 being the first and second invariants of the Finger tensor. This results in a scalar, which adjusts the overpredictions from the the memory function by separation into a strain and

time dependent behavior (Wagner, 1976, 1978). The modified Lodge equation is:

$$\underline{\underline{\sigma}}(t) = \int_{i=-\infty}^{t} m(t-t')\, h(I_1, I_2)\, \underline{\underline{C}}^{-1}(t,t')dt' \tag{2.88}$$

The most important feature of a model is the application to different scenarios. The rubber-like liquid theory allows predictions of shear and elongation with the corresponding deformation gradient Equation 2.52 and 2.58 and Cauchy tensor, respectively. The Trouton ratio relates a transient shear $\eta_S^+(t)$ to an uniaxial elongation viscosity $\eta_E^+(t,\dot{\varepsilon})$ (Dealy and Larson, 2006):

$$\lim_{\dot{\varepsilon}\to 0} \eta_E^+(t,\dot{\varepsilon}) = 3\,\eta_s^+(t) \tag{2.89}$$

A further progression of the rubber elasticity theory was introduced as K-BKZ equation [Kaye-Bernstein, 62,63], which considered the free energy of the history integral, leading to a time-strain separability. Nevertheless, the presented models consider solely a continuum approach and neglect the molecular features.

Tube Model

The breakthrough of a molecular based description began with the *tube model* of Doi and Edwards (Doi and Edwards, 1978; Doi, 1983; Doi and Edwards, 1986). The model is based on considerations of chain motion, which were introduced by de Gennes (1971). In de Gennes perception, a single free chain in a surrounding cross-linked gel undergoes worm-like motion, which in analogy to movements of a snake or a lizard is called *reptation*. Two characteristic times of chain motion were introduced that control the reptation, which lead to $\lambda \propto M^3$. Doi and Edwards transformed the idea into an entangled high concentrated solution or melt, where the obstacles and tube geometry are defined by entanglements, as can be seen in Figure 2.12. The tube can be separated into segments with diameter and segment length a. The chain is meandering through the tube and each segment possesses an end-to-end vector $\underline{R}$, assuming a freely jointed chain. Reptation is the diffusion controlled motion of the chain into a new tube. If an imposed load on the chain ends is released after a deformation, two relaxation times dominate. The first is related to the Rouse time τ_R, which leads to an equilibrium in each segment from retraction. The tension is equal to the equilibrium state:

$$|\underline{K}| = \left|\underline{K_{eq}}\right| = \frac{3kT}{a_0} \tag{2.90}$$

The second relaxation process is a disengagement time τ_d which occurs due to Brownian motion, leading to disentanglements by chain fluctuations at both tube ends. The latter includes further processes like double reptation, which

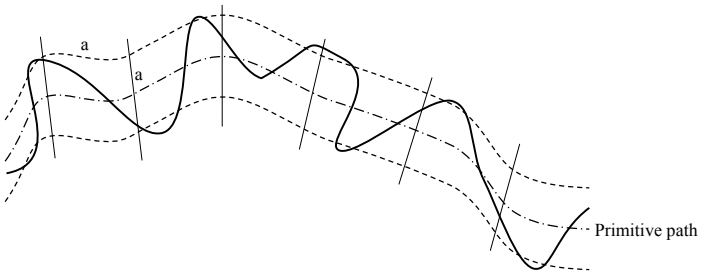

Figure 2.12: Doi Edwards tube model, with segment length a, and primitive path.

takes into account the release of confining chains and their reptation. A more complex phenomenon based on the reptation of the surrounding chains is the constraint release mechanism (Section 2.4.3). The disengagement time is of particular interest in the present work, since it is the longest process and strongly influences the rheological behavior. This contributions still explains solely a M^3 dependents of the relaxation processes. Doi expanded the theory by the contour length fluctuation to explain a slope of 3.4 in the molar mass and zero-shear viscosity relation (Doi, 1983). The basic concept is that the tube ends become fuzzy and friction enhances. If the fuzzy end segments become small compared to the entire tube length, M^3 should be the dominating correlation. A second consequence of the end fluctuation is an enhanced relaxation time of branched molecules with long side arms as star-like molecules. McLeish reported on a restricted backbone relaxation, which can only occur if the entire side arms are in close neighborhood to the backbone (McLeish and Milner, 1999)

The molecular approach of the tube model allows an expression of a strain as a change from an unoriented into a oriented conformation. The single tube segments can be described by tangent vectors $\underline{u}$ and an affine deformation leads to the deformed orientation vector $\underline{u}' = \underline{u}'(t, t')$ from the equilibrium state $\underline{u}$:

$$\underline{u}' = \underline{\underline{F}}^{-1}(t, t')\,\underline{u} \tag{2.91}$$

If creation and vanishing of entanglements are in balance, the dyadic product of the deformed unit vector leads to the orientation tensor. Through a negligible correlation between adjacent segments, assuming each segment in its equilibrium state leading to a constant tube diameter (with $\underline{R}' = R\underline{u}'$ and $\underline{R} = R\underline{u}$), the second order orientation tensor with independent alignment assumption is given as:

$$\underline{\underline{S}}^{IA}_{DE} = 5\left\langle \frac{\underline{u}'\underline{u}'}{u'^2} \right\rangle = 5\underline{\underline{S}} \tag{2.92}$$

with $< ... >$ as an integral over an isotropic distribution of unit vectors over an unit surface by angle Ω:

$$\langle ... \rangle = \frac{1}{4\pi} \int < ... > d\Omega \tag{2.93}$$

The factor 5 allows a correct prediction of the linear viscoelastic limit. Hence, the Doi-Edwards model is expressed as:

$$\underline{\underline{\sigma}}(t) = \int_{-\infty}^{t} m(t-t') \underline{\underline{S}}_{DE}^{IA}(t,t') dt' \tag{2.94}$$

which possesses the advantage of separable integrals and allows the description of the linear viscoelastic start-up. The affine strain of a polymer network can be also expressed by a dyadic product of $\underline{u}'$ (Wagner and Geiger, 1997):

$$\underline{\underline{C}}_{t,t'}^{-1} = 3 \langle \underline{u}' \underline{u}' \rangle \tag{2.95}$$

Therefore the Lodge Equation 2.83 is a function of affine deformation. The disadvantage of the tube model is an overprediction of the shear thinning, and the normal stress overshoot is not predicted. Although Doi and Edwards were able to introduce the chain orientation into description, the model assumes a constant tube diameter, and phenomena like strain hardening cannot be modeled.

2.4.3 Molecular Stress Function Model

Wagner and Schaeffer (1992) introduced an equation which considers the stretch of the molecule as contribution to an emerging stress, i.e. the *molecular stress function* (MSF) model (Wagner and Schaeffer, 1993). Based on the tube model, the stretch of the molecule would lead to a stretch of the tube and the tube diameter is reduced with increasing deformation:

$$a = a(\langle u' \rangle) \tag{2.96}$$

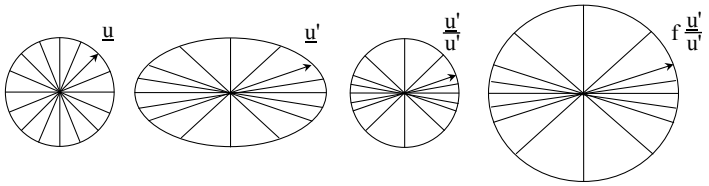

Figure 2.13: Undeformed, affine deformation, DE and MSF orientation.

Thus, the stretch $f(t,t')$ can be expressed as reciprocal of the decreasing tube diameter with respect to the initial size a_0 at equilibrium:

$$f(t,t') = \frac{a_0}{a(t,t')} \tag{2.97}$$

The MSF theory leads to a new strain measure of the Doi-Edward independent alignment assumption orientation tensor, which is enhanced by the non-linear scalar parameter $f > 1$:

$$\underline{\underline{S}}_{MSF} = f^2 \, \underline{\underline{S}}^{IA}_{DE} \tag{2.98}$$

The constitutive equation for the stress is given as:

$$\underline{\underline{\sigma}}(t) = \int_0^\infty m(t-t') \, \underline{\underline{S}}_{MSF}(t,t') dt' \tag{2.99}$$

Since the actual tube geometry is not known, an energy consideration can be used to describe the changes (Marrucci and Grizzuti, 1983). The entropic force introduced by the molecule on a tube segment at equilibrium state will change, if a stretch occurs and tube diameter decreases:

$$|\underline{K}| = \frac{3kT}{a} = \frac{a_0}{a(\langle u' \rangle)} |\underline{K}_{eq}| = f(\langle u' \rangle) |\underline{K}_{eq}| \tag{2.100}$$

The change of diameter and force leads to a change in free energy of a segment w_{MSF}. The derivation of the model can be found in the literature (Rolón-Garrido, 2014). For the present study, it should be emphasized that an evolution equation is necessary to describe the stretch with respect to the deformation rate tensor:

$$\frac{\partial f^2}{\partial t} = f^2 \left[(\underline{\underline{\kappa}} : \underline{\underline{S}}) - \frac{CR}{f^2 - 1} \right] \tag{2.101}$$

The tube stretch depends on the observation time and the strain history. As seen, the reptation of the confining molecules leads to a reduced stress of the deformed molecule. The constraint release (CR) occurs, as entanglements renew during the motion (Marrucci and Grizzuti, 1983; Wagner et al., 2001). Consequently the chain is able to relax in absence of entanglements. This dissipative process is determined by two parameters, $a_1 \geq 0$ and $a_2 \geq 0$ (Wagner, 2006):

$$CR = a_1 (f^2 - 1)^2 \sqrt{\underline{\underline{D}}^2 : \underline{\underline{S}}} + a_2 (f^2 - 1)^2 \sqrt{|\underline{\underline{W}} \, \underline{\underline{D}} : \underline{\underline{S}}|} \tag{2.102}$$

The factor $a_2 \geq 0$ needs to be considered for simple shear flow, where a rotational component emerges, but it is irrelevant for uniaxial elongation where $\underline{\underline{W}} = 0$ (cf. Section 2.2). The evolution equation for uniaxial flow for a linear polymer is:

$$\frac{\partial f^2}{\partial t} = \dot{\epsilon} f^2 \left(S_{11} - \frac{1}{2} S_{22} - \frac{1}{2} S_{33} - a_1 (f^2 - 1) \sqrt{S_{11} + \frac{1}{4} S_{22} + \frac{1}{4} S_{33}} \right) \tag{2.103}$$

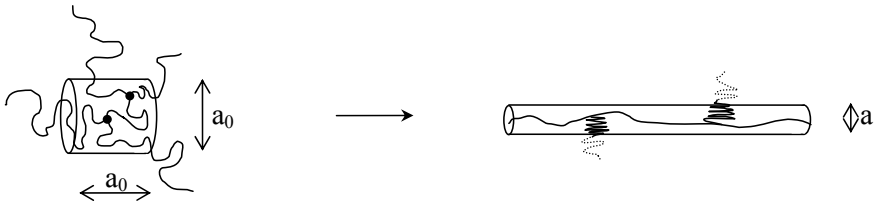

Figure 2.14: Sketch of an branched molecule in a tube segment at undeformed and deformed state.

The prefactors of the components of the orientation tensor S_{ii} are valid only for uniaxial deformation and not for equibiaxial or planar elongation. The boundary value of the equation is set to the maximum reduction of the tube segments, which is a measure of the maximum of storable energy. It is assumed that at large strains $f = f^2_{max}$ when $\partial f^2/\partial t = 0$ and a_1 can be expressed by:

$$a_1 = \frac{1}{f^2_{max} - 1} \tag{2.104}$$

Figure 2.13 demonstrates orientation of an undeformed and affine deformed case, the normalization by the Doi-Edwards orientation, and the impact of the stretch from the MSF model which enhances the amount of orientation by stretch weighted.

The MSF model was shown to predict linear polymer melts with high accuracy in melt and solution for narrow and broad distributed polymers (Wagner et al., 2005). However, the molecular motion of branched deviates from linear structures. The stretch and the friction contribution increases, and an enhanced strain hardening behavior can occur due to the topology (Wagner et al., 2000). Wagner et al. (2003) proposed an assumption that side chains are compressed during the tube stretch, as can be seen in Figure 2.14, and contribute to the energy balance of the segments. Consequently, the branching factor β can be introduced into the evolution equation:

$$\frac{\partial f^2}{\partial t} = \frac{\beta f^2}{1 + \frac{\beta - 1}{f^4}} \left[(\underline{\underline{\kappa}} : \underline{\underline{S}}) - \frac{CR}{f^2 - 1} \right] \tag{2.105}$$

A quantitative description of the parameter is given as (Wagner et al., 2004):

$$\beta = \frac{M_n}{M_{n,bb}} \tag{2.106}$$

where the number average molar mass of the backbone $M_{n,bb}$ is related to the molar mass of the entire branched molecule M_n.

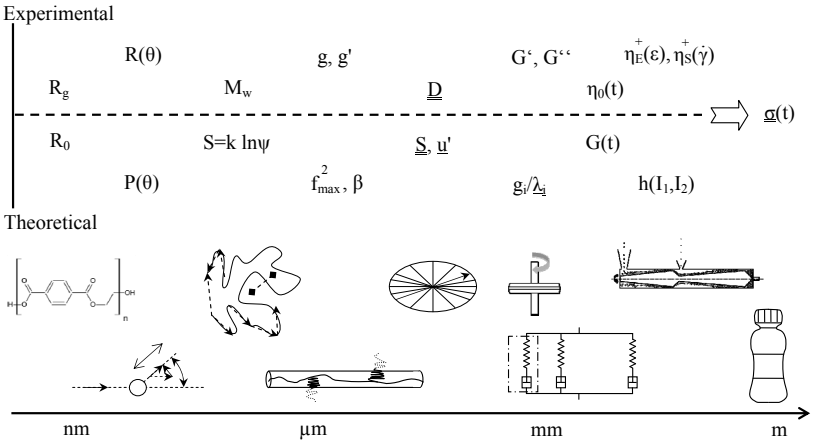

Figure 2.15: Interactions between experimental and model parameters from micro- to macroscale (cf. Nomenclature).

2.5 Conclusions

It was shown that the behavior of a single molecule and the behavior of a macroscopic bulk can be related by different quantities and model parameters. The most important feature of a model parameter is that it can be attributed to a physical origin and can be verified experimentally.

Figure 2.15 illustrates the correlations and interaction between the quantities that can be measured and those that are based on theoretical approaches.

The use of statistics and field approaches are necessary to correlate the microstate with the macrostate. The freely jointed chain and the end-to-end vector R_0 based on a random walk can be determined by measuring the radius of gyration R_g. The particle scattering function $P(\theta)$ allows to determine the theoretical monomer distribution, which can be measured by the Rayleigh ratio R_θ and the radius and molar mass can be achieved. The different microstates Ψ determine the entropy S and hence the retraction force $|\underline{\underline{K}}|$ and entropic spring constant. Consequently, the stretch of a molecule f_{max}^2 can be calculated by a change of the force and free energy w, respectively. Additionally, the branching is represented by β and can be determined experimentally by the coil contraction factor g or g'. The transition to the macrostate can be accomplished by the orientation $\underline{u}'$ of the deformed molecule, which can be included in the strain measure $\underline{\underline{S}}$. By means of the Maxwell model and a discrete relaxation spectrum with g_i and λ_i, the relaxation modulus $G(t)$ can be determined and an entire description of the material behavior is given by the stress evolution $\underline{\underline{\sigma}}(t)$.

3 Properties of PET in Melt State

In Chapter 1 the key role of the ester group and the impact of synthesis on possible molecular alterations were emphasized. The following chapter concerns about polymerization of PET by introducing the three PETs investigated. Subsequently, the experimental method and thermal stability of poly(ethylene terephthalate) are described and analyzed, respectively. This involves the role of surrounding atmosphere (air or nitrogen), which has to be considered by interpreting the data. Based on the G' data analyzed, an extrapolation of the initial unaffected condition of the polymer is realized. The changes during the characterization occurred in a rapid manner, consequently, time-resolved mechanical spectroscopy (TRMS) is conducted, which includes an observation of the frequency dependence. This findings are crucial for analyzing the viscosity. Finally a comparison of linear dynamic, steady and rotational flow measurements is conducted to verify the validity of the Cox-Merz rule.

3.1 Materials

This section covers the three different grades of PET used in this study. The different chain extenders employed to modify the polymer structure are introduced in Section 4.3.1.

The polycondensation of poly(ethylene terephthalate) consists of mainly two reactions as shown in Figure 3.1. The first leads to the intermediate product bis(2-hydroxyethyl) terephthalate (BHET) and the second condensation reaction into the PET macromolecule. Commercially, the synthesis routes starts either form dimethyl terephthalate (DMT) or purifed terephthalic acid (TPA) as initial material. DMT and monoethylene glycol (MEG) reacts to BHET and methanol as side products, and the latter has to be removed by vacuum (Ravve, 2012). The methane end groups of the DMT are attached to the benzene ring by an ester group. Consequently, this first reaction is a transesterification. However, the polycondensation from the initial TPA is an esterification. The reaction with ethylene glycol and the separation of water is becoming more common (Rieckmann and Völker, 2004), since the production of highly purified terephthalic acid progressed. The first step is processed at relatively low

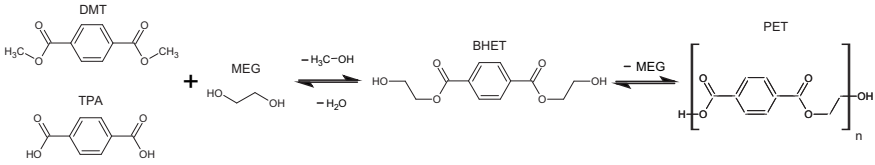

Figure 3.1: Polycodnesation of PET from dimethyl terephthalate (DMT) and purifed terephthalic acid (TPA) as initial material with monoethylene glycol (MEG). Bis(2-hydroxyethyl) terephthalate (BHET) is an intermediate product and water, methane and MEG are side products with respect to the synthesis routine.

Table 3.1: Specifications of the producer for H-PET, L-PET, and l-PET.

	Initial product	$[\eta]$ $[dl/g]$[1]	DEG $[wt\%]$	Carboxyl end groups $[meq/kg]$
H-PET	DMT	0.82-0.88	<0.80	<25
L-PET	DMT	0.652-0.678	<1.0	22-32
l-PET	TPA	0.643-0.647	<1.1	22-28

temperatures from 150-250°C (Ravve, 2012), whether it is a trans- or an esterification. The side products emerged, i.e. water and methanol, can be neglected with regards to the processing of PET. Due to the subsequent temperature increase and the applied vacuum, the concentration converges to zero during the second step (Scheirs and Long, 2004). The second reaction is a transesterification of BHET into the final PET, and accompanied by a separation of MEG at around 270-285°C. The high temperature ensures a lower viscosity, which leads to an improved processability and a thoroughly stirring of the melt (Ravve, 2012). Only an extensive mixing promotes the side product, in this case ethylene glycol, to evaporate from the polymer. Otherwise the reversible reaction inhibits a higher molar mass (Scheirs and Long, 2004). Additionally, diethylene glycol (DEG) or other derivatives can affect the melt properties (Zimmermann, 1984), if MEG remains in the resin produced.

The grades selected for this work cover a broad variety of properties. This enables an analysis of melt properties and degradation mechanisms, and different molecular structures induced by the chain extension, which are discussed in Chapter 5 and 6. The three poly(ethylene terephthalate) investigated are linear, titanium free homopolymers as confirmed by Invista. The specifications of the producer are shown in Table 3.1. The preceding letter refers to the syn-

[1]Intrinsic viscosity in 1% solution of dichloroacetic acid

Table 3.2: DSC results for virgin for H-PET, L-PET, and l-PET.

	T_g $[°C]$		T_m $[°C]$		T_{cc} $[°C]$		$\triangle H_m$ $\left[J.g^{-1}\right]$	
H-PET	80.7	±0.20	254.2	±0.36	173.4	±1.70	29.3	±0.94
L-PET	80.0	±0.42	254.5	±0.43	168.5	±0.39	27.2	±0.66
l-PET	79.4	±0.15	253.6	±0.65	171.6	±2.78	36.0	±1.18

thesis route of the corresponding PET, i.e. the capital H and L denote DMT and uncapitalized l, TPA as base material. Another distinction is given by the molar mass of the grades. From the Mark-Houwink Equation 2.26, the intrinsic viscosity is proportional to the molar mass. The letter H represents the high, and L and l the low and even lower molar mass of the grades.
The enhancement of molar mass in the reactor is limited, but the intrinsic viscosity of H-PET reveals a 30% higher value compared to the other grades, which results from the solid-state polycondensation. During the annealing of the SSP, the transesterification continues and a crystallization process occurs (Toda et al., 1995), and additionally volatile products diminish, as can be noted by a reduction of the diethylene glycol content.

The thermal properties and a relation to molecular differences were investigated. Dynamic scanning calorimetry (DSC) was conducted with a Mettler Toledo DSC 822e at heating and cooling rates of $10Kmin^{-1}$ and a mass of around $5mg$. Table 3.2 reveals a decreasing glass temperature T_g from H-PET to l-PET. The higher mobility of shorter chains enables a molecular movement at lower temperatures, where less free volume exists. Fox and Flory (1950) derived Equation 3.1, where T_g is related to the inverse of the molar mass:

$$T_g = T_{g,\infty} - \frac{K}{M} \tag{3.1}$$

$T_{g,\infty}$ is the transition temperature of an infinitely long molecule and K a constant including thermal expansion, density and impurities from the chain ends (Lechner et al., 2014). The impact on T_g is known to be small above a critical molar mass (Cowie and Toporowski, 1968), which has a strong correlation to M_c denoted in Figure 2.10 (van Krevelen and te Nijenhuis, 2009). The observed tendency is small and within an experimental error. The comparison of the melt and cold crystallization temperature (T_m and T_{cc}) and the enthalpy of fusion $\triangle H_m$ are not strictly correlated with the molar mass. Catalysts or different residuals of side reactions from the synthesis influence the crystallization behavior, e.g. as nuclei, but the overall differences are small.

3.2 Experimental Conditions for Shear Viscosity Measurements

When a strain applied on a melt exceeds a certain value, the material reacts non-linear. However, since the rheometer is limited by its physical resolution, a deformation reasonably close to the non-linear response is favorable, which allows an observation of material properties at low frequencies. A strain amplitude of $\gamma_0 = 10\%$ was obtained valid for all grades (Incarnato et al., 2000), by an amplitude sweep measurement at a fixed angular frequency $\omega = 10s^{-1}$ (Daver et al., 2008). The dynamic measurements were conducted with an *Anton Paar MCR301* stress-controlled rheometer with parallel plate geometry of $25mm$. The advantage of this geometry is a convenient handling, e.g. since the gap size can be adjusted, and even high viscous polymer melts, as the modified PET, can be analyzed (Macosko, 1994). Therefore, the experimental setting is nearly the same throughout this work. Additionally a $50mm$ parallel plate and a cone and plate geometry of $25mm$ were used to validate the data and to perform the rotational experiments. The melting temperature was determined at approximately $255°C$. Measurements around $258°C$ revealed a tendency to shear crystallization. However, with respect to elongation experiments and a possible sagging effect, a low temperature is required to analyze even low elongation viscosities. The temperatures applied are 265, 272, 280 and $288°C$ by an *Anton Paar CTD 450* convection heating chamber by nitrogen or dried air supply. The frequency sweep, steady rotational and TRMS experiments were performed by variation of angular frequency or shear rate between 0.05 to $500s^{-1}$ with 5 points per decade (5, 7.92, 12.6, 19.9 and 31.5). The capillary flow measurements were conducted from 50 to $3150s^{-1}$ with the same interval.

The most important feature to characterize a time dependent alteration is a reliable reference. To minimize structural changes before the data collection, pellets were loaded directly between the plates, squeezed after softening, molten for two minutes, compressed to approximately $1mm$ gap size and trimmed. The time between loading and the start of the measurement was always recorded. Additionally, samples prepared by heated compression molding in air and in a mold with N_2 atmosphere, which was specially made for the occasion, were investigated to study the effect of preparation. The produced sheets with an area about $400cm^2$ possess a thickness between 0.5 and $0.8mm$. The moisture content of the pellets was reduced by thoroughly drying in a vacuum oven at $130°C$ for $24h$ (Utracki et al., 1982; Hatzikiriakos et al., 1997) to achieve a water content below $0.02wt\%$ (Scheirs, 1998).

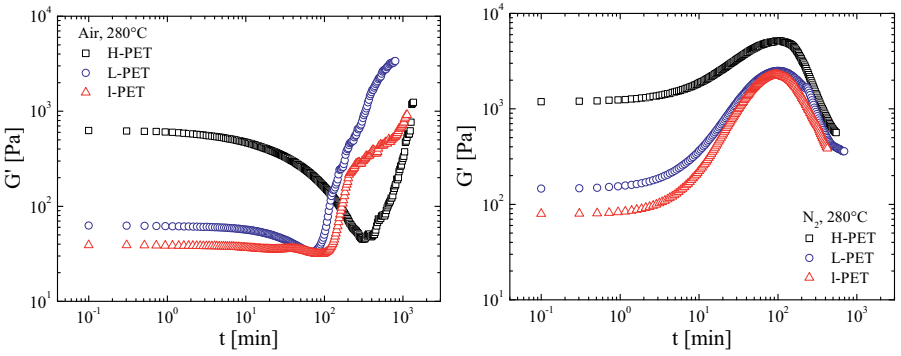

Figure 3.2: Storage modulus as time-dependent function for H-PET (square), L-PET (circle) and l-PET (triangle) of virgin pellets in air (a) and N_2 (b) atmosphere at 280°C.

3.3 Thermal Stability

The main influences on the thermal stability of poly(ethylene terephthalate) are hydrolysis, thermal-oxidation and random chain scission (homolysis) (Zimmermann, 1984). Additionally, changes by polymerisation mechanisms such as ester- and transesterification and cross-linking can occur during thermal treatment. The observation of these mechanisms is a fundamental task in understanding the melt behavior.

3.3.1 The Impact of Atmosphere

The surrounding atmosphere involved was always considered in studies of poly(ethylene terephthalate) in the melt state. Marshall and Todd (1953) compared the degradation effect in N_2 to various oxygen contents. Regardless of the atmosphere, all measured melt viscosities declined linearly on a half logarithmic plot, but more pronounced with increasing oxygen concentration. Thermal-oxidative degradation is a very determining process during melt processing, due to the reactivity of oxygen and the generation of peroxides (Johnson and Morrison, 1996). Figure 3.2 (a) shows the change of the storage modulus G' with time for the grades investigated. It has to be mentioned that G' is also representative for G'', which is not plotted here, but behaves qualitatively similar. The initial level of modulus corresponds to the specification of the producer (see Section 3.1).

Table 3.3: Intrinsic viscosity and molar mass calculated with Mark-Houwink equation.

	$[\eta]$ $[dl/g]^2$		M_v $[kg/mol]$		M_{n_v} $[kg/mol]^3$
H-PET	1.045	± 0.0083	63.6	± 0.8	31.8
L-PET	0.844	± 0.0025	45.3	± 0.2	22.6
l-PET	0.824	± 0.0131	43.6	± 1.1	21.8

Additionally, solution viscosity measurements were conducted to obtain the molar mass. The whole procedure and analysis is described in Chapter 6. At this point, it should be sufficient to mention that the Mark-Houwink parameters $a = 0.630$ and $K = 0.0985 ml.g^{-1}$ are based on absolute measurement (MALS), which were obtained by PET standards. The results in Table 3.3 agree with Berkowitz (1984) and reveal the same intrinsic viscosity relation as in Table 3.1. However, since the solvent hexafluoroisopropanol used in this study act more as a theta or even as a good solvent, the viscosity is higher. The calculated molar mass values are $63.5k$, $45.2k$ and $43.5k$ for H-PET, L-PET and l-PET, respectively, and exhibit a standard deviation below 3%. Since all grades possess the same structure, a high molar mass leads to long relaxation times and to high values of G' at constant frequency, as for H-PET. All three grades in Figure 3.2 (a) undergo initially a substantial reduction of elasticity. The decrease continues to a minimum, which occurs for the low molar mass PET between 60 and $100 min$ and for H-PET at $300 min$ at different duration, but at comparable levels of storage modulus. This decay of melt elasticity was observed by many authors as will be demonstrated in the following. The common way to achieve reliable viscoelastic data is to perform the experiment under an inert atmosphere. Therefore already Marshall determined melt viscosities in nitrogen and observed a lower degradation rate. However, the viscoelasticity of the PET investigated increases with time in N_2 surrounding. In Figure 3.2 (b) an immediate enhancement of G' to a maximum at around $100 min$ can be seen. The most obvious explanation is that the chains in air atmosaphere undergo a reduction of molar mass, and an enhancement in nitrogen. Both alterations occurred affect the mobility of the polymer. Mours and Winter (1994) described changes regarding the mobility, no matter if introduced by changes in molar mass, connectivity between molecules or aggregation, as mutation. Table 3.4 displays the *mutation factor*, i.e. the ratio of minimal or maximum value of G' to the initial value. The initial differences between the grades (83 to $1260 Pa$) are almost compensated during the measurement of G' in N_2 atmosphere, reflected by the maximum value (between 2240 and $5220 Pa$). Although

[2]Solvent: hexafluoroisopropanol at $35°C$

[3]Assuming PDI=2 (Rieckmann and Völker (2004))

Table 3.4: Mutation factor relating minimum to maximum value from thermal stability test for H-, L-, and l-PET.

	air			N_2		
	Initial G' [Pa]	Min or max G' [Pa]	Mutation factor [-]	Initial G' [Pa]	Min or max G' [Pa]	Mutation factor [-]
H-PET	601 ±61	99.0 ±45.5	0.16	1260 ±140	5220 ±160	4
L-PET	62.0 ±2.9	33.5 ±2.8	0.54	141 ±7	2560 ±240	18
l-PET	36.7 ±2.1	27.5 ±3.2	0.75	83.0 ±3.5	2240 ±60	27

the general tendency holds for all grades, individual changes of the different grades occur. H-PET reveals a mutation factor of 4 in nitrogen while G' is reduced in air to 16% (6.25-fold) of the initial value. The low molar mass grade l-PET behaves in a different way resulting in a 27-fold enhancement of G' in N_2 but maintaining 75% of G' in air atmosphere. This ratios were obtained at the order of $100min$ thermal exposure which is neither an appropriate duration for processing nor rheological characterization, but it gives already a hint to a first property which dictates the melt behavior: high molar mass PET is more stable in nitrogen and less stable in air surroundings than low molar mass.

Nevertheless the instability in N_2 surrounding is rather unusual. For its understanding it is worth to briefly review how rheologically based work on poly(ethylene terephthalate) developed since the time of Marshall. Buxbaum (1968) compared the thermal scission of PET observed by different authors. He described the degradation kinetics based on melt or intrinsic viscosities and emphasized the accelerating impact of temperature. Although Utracki et al. (1982) conducted their experiments regarding degradation in air atmosphere, they mentioned that the behavior in nitrogen was not different. In the following years, the decrease of viscosity is the only documented behavior (Kim et al., 1990; Seo and Cloyd, 1991), even in inert atmosphere. Additionally Tate and Narusawa (1996) quantified the degradation derived from COOH concentration and revealed a higher degradation rate when a specimen possesses a higher molar mass. Guenther and Baird (1996) observed a reduction of the complex viscosity in air by 35% but by 9% in nitrogen at $290°C$ during $5min$. Hatzikiriakos et al. (1997) were able to shift subsequently conducted frequency sweeps by a linear factor to a reference measurement, which was assumed to be

unaffected. However, two years later Paci and La Mantia (1998) reported the opposite, an increasing molar mass during kneading PET in a torque rheometer under N_2. They concluded that either a trans- or an esterification proceeded. Although articles were still published on decreasing viscosities in nitrogen (Incarnato et al., 2000; Dhavalikar et al., 2003; Tharmapuram and Jabarin, 2003), Assadi et al. observed an increase of the complex viscosity at a low rate in nitrogen of a processed PET. Based on these results, Nait-Ali et al. (2011) derived a kinetic model, and concluded that small doses of oxygen during the measurement lead to cross-linking. In the following years, published data revealed small increases of melt viscosities (Forsythe et al., 2006; Coltelli et al., 2007; Daver et al., 2008). In 2010, Souza et al. found a drastic increase of melt viscosity at $\omega = 1 rad/s$ by analyzing the impact of drying. Recently Härth et al. (2015) described the reaction kinetics of the build-up process at the same angular frequency as a function of temperature. It seems that somehow the thermally induced degradation of poly(ethylene terephthalate) changed in the past 60 years. The initially observed strong decrease of viscosity reduced with time and muted into a viscosity enhancement currently observed at low shear rates and frequencies.

Definitely, the production of PET progressed and improved in the last decades, although the initial materials are still the same. The requirements on stable products increased, not least, due to the wide application of PET in food packaging. In particular the beginning of the solid state polycondensation and the need for specific and antimony free catalysts go along with the observed enhancement. It is also noticeable that all the enhancements were measured at low frequencies or rates, e.g. by torque rheometer.

Besides the degree of polymerization, the grades investigated differ in the chemical synthesis route. Poly(ethylene terephthalate) from TPA is known to have a higher DEG content than PET produced from DMT (Scheirs and Long, 2004). As can be seen from Table 3.1, l-PET has the highest DEG concentration and with an additional SSP it diminishes to lower values than observed for H-PET, although the behavior of DEG in SSP is not fully understood (Wu et al., 1997). An affect of DEG, on thermal degradation of PET in nitrogen, is not known. Hence the progression in nitrogen should be independent on DEG. However, an influence on thermal-oxidative degradation was observed, based on concentrations of DEG which were four times higher than in the PET investigated (Zimmermann, 1984). By examining the l-PET data in air atmosphere a small bump is prominent. This TPA based PET reveals that the reduction in G' is split into a first relatively stable region and a second stronger decline starting from $40 min$, until an increase at very long times dominates. Since the degradation rate is lower at the beginning, an effect of DEG can be neglected at these low concentrations. However, an explanation for the two different reduction

rates of l-PET can be given by the two catalysts used. Compared to H- and L-PET, the TPA based l-PET needs a different combination of catalysts for the ester- and the transesterification. Their interaction can emerge a lower degradation rate, before the reaction is terminated and a stronger decrease occurs.

A second reason could be the end groups. A coupling of two PET chains by a transesterification would consume two hydroxyl and an esterification each a COOH and a OH end group(s) (Rieckmann and Völker, 2004). With this general rule a beneficial tendency considering a polycondensation with higher amount of hydroxyl end groups can be inferred. From the M_v and an assumed $PDI = 2$ as typical for poly(ethylene terephthalate)[4] (Awaja and Pavel, 2005) a number-average molar mass $M_{v/n}$ based on the intrinsic viscosity yields a carboxyl group amount per two possible end groups of 0.79, 0.61 and 0.54 for H-, L- and l-PET, respectively. In other words, the theoretical hydroxyl end group content of 1.46 per molecule in l-PET is the largest[5]. Since comparable more OH groups are consumed during polycondensation, a SSP treatment increases the concentration of COOH end groups (Wu et al., 1997) as reflected in H-PET. A second positive effect of OH-groups is a reactivity with vinyl end groups (Zimmermann, 1984) which are generated by thermal-oxidative degradation. Although no enlargement from their reaction can be expected, the molar mass maintains on average. However, comparing the initial value of l-PET in air to G' after $40min$ a deviation of only 12% occurs. A reason for this low degradation can be seen by, either the catalyst combination and, or the OH end group concentration which act as an "active" stabilizer.

The initial idea of the thermal stability measurement is to define a scope for reliable rheological measurements. By using a 5% deviation rule the response of the grades at $280°C$ vary from $60s$ to $400s$, which is not a sufficient duration for rheological practice. Furthermore, by comparing the initial G' data for each grade from Table 3.4 or in Figure 3.2, a fundamentally different modulus can be observed. This leads to the conclusion that the structure of the polymer is changed significantly before the start of measurement.

3.3.2 Zero-Loading Time

Usually, rheological data as viscosity or moduli are plotted in a logarithmic diagram, since the changes exceeds decades, due to the temperature, shear rate or frequency variation. However, this can hide actual differences, in particular on a half logarithmic graph. The results from the thermal stability measurement

[4] As demonstrated in Chapter 6, the SSP leads to a broadening of PDI of H-PET due to diffusion. Additionally, the MALS weight-average molar mass is slightly higher than the Mark-Houwink based value. Since l-PET and l-PET were not fractionated, $PDI = 2$ and M_v were used for the sake of homogeneity.

[5] Both end groups of TPA are COOH groups and since l-PET exhibits the lowest amount of COOH per mol the TPA conversion into BHET seemed to be terminated.

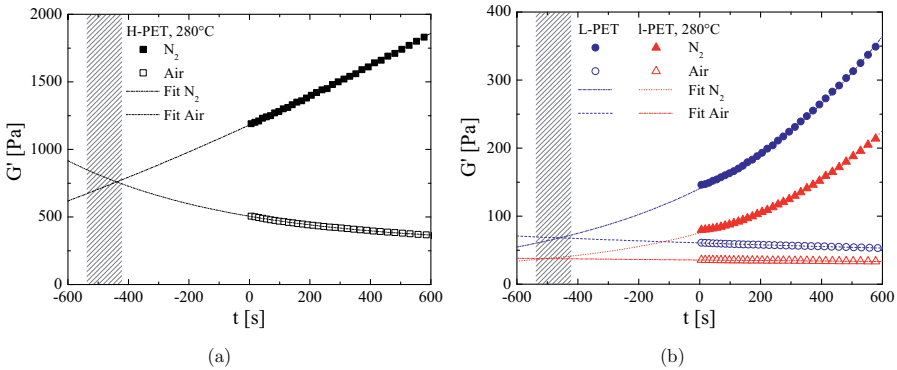

(a) (b)

Figure 3.3: Zero-loading time by comparison of air (empty) and N_2 (solid) atmosphere for H-PET (square) (a) L-PET (circle) and l-PET (triangle) (b) with fitting at 280°C (Kruse et al., 2013).

are shown in Figure 3.3 with linear scale. To get an insight of the initial state of the PET investigated, the two atmospheres are compared for each grade in one diagram.

The sample with the high molar mass H-PET in Figure 3.3 (a) features a twofold difference of the storage modulus between air and nitrogen at the beginning of measurement at $t = 0$. Since the structure of the PET changed before the measurement, the time axis is extended to negative values to include the actual loading time, which is marked by the transverse striped area[6]. The storage modulus was fitted to extrapolate the initial condition of the poly(ethylene terephthalate) at the loading time (Kruse et al., 2013). The evolution of the storage modulus was fitted by an exponential functions. The time scope was limited to $600s$, which avoids complexity due to second order kinetics from side products. Otherwise, a prevailing thermal degradation (N_2) or cross-linking (air) counteracts with time. The first order equation used is as follows (Kruse and Wagner, 2016):

$$G'(t) = A + Be^{\frac{t}{\tau}} \tag{3.2}$$

$$G'(t = 0) = A + B \tag{3.3}$$

with t as time and τ as time constant. The constant prefactor A is required to consider chain specimens which are not active, i.e. either the corresponding end groups do not participate the polycondensation or the chains are not attacked by radical scission. B represents the chains which participate the progression

[6]The loading time was always recorded and took between 7-9min. Subsequently, the routine was modified to handle also the high viscous PET produced, which decreased the time to 5-6min.

either by enhancement or reduction of the molar mass. The interceptions of the extrapolated data in 3.3 (a) and (b) reveal the initial storage modulus at zero loading time for H-PET, L-PET, and l-PET. It has to be mentioned that the sample conditions, between loading and start of the measurement are not homogeneous. The oven temperature drops since the sample has to be placed and trimmed, oxygen is in contact during the trimming of the sample although employing nitrogen, and small water residuals inside the sample or air atmosphere affect the reactions. Particularly, the hydrolysis is a fast reaction (Scheirs and Long, 2004) which will be terminated in a few minutes, if the water content is low (Seo and Cloyd, 1991). The time constant in Equation 3.2 gives information about the reaction speed. In case of an enhancement of G' due to esterfication and transesterfication in nitrogen at a low rate, τ possesses high values and the storage modulus would increase slowly. A fast reduction in air atmosphere is reflected by a negative and small τ. Table 3.5 compares the different kinetics of the grades investigated for both atmospheres at $280°C$. The results confirm the conclusions from the mutation number. The lowest molar mass l-PET exhibits the highest time constant in air, and hence the lowest degradation rate, while H-PET exhibits a small τ and a fast reduction. The effect in nitrogen is vice versa, the high molar mass H-PET polymerizes with the lowest rate expressed by the highest time constant. l-PET posses the highest reactivity as also illustrated in Figure 3.2 (b) and correlates with the end group analysis. A simple rule could be that a poly(ethylene terephthalate) with high amount of OH end groups is less stable in nitrogen since the condensation reaction is not terminated. A very high molar mass PET with saturated end group reactivity is more stable in an inert atmosphere.

The comparison of factor A and B gives an idea about chain specimens which are not affected by the reaction (A), and which participate actively in the reaction (B). However, such model parameters underlie the limitations of their ideal assumptions. The negative value of A for H-PET results from an almost linear increase from the start of recording, e.g. since an exponential start-up occurred already during the loading time.

Table 3.5: Time-constant τ and factor A and B from exponential fitting for H-, L-, and l-PET.

	air			N_2		
	$\tau[s]$	$A[Pa]$	$B[Pa]$	$\tau[s]$	$A[Pa]$	$B[Pa]$
H-PET	-550	295	210	3190	-2101	3282
L-PET	-2120	30	31	630	1	140
l-PET	-3200	23	13	460	18	57

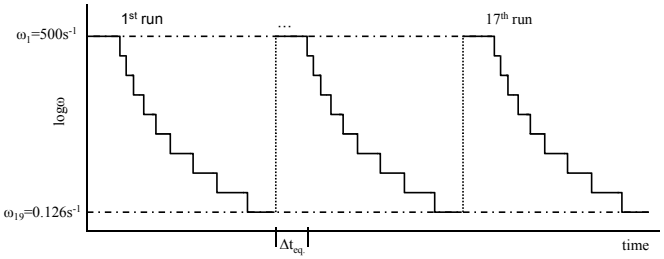

Figure 3.4: TRMS data splitting of the angular frequency over elapsed time of 17 frequency sweep runs.

The evolution of viscosity, storage or loss modulus with time, due to inert and oxidative atmosphere, temperature and water content, were studied by different authors (Buxbaum, 1968; Seo and Cloyd, 1991; Assadi et al.; Härth et al., 2015). The two common ways describing mutations of PET melt properties, assume either a large number of model parameters or a simplification of the kinetics. However, since the structural changes due to a polycondensation and degradation act on the molar mass and potentially on the polydispersity, the flow variations should be analyzed in a wide frequency range.

3.3.3 Time-Resolved Mechanical Spectroscopy

In regards of rheology of PET, Hatzikiriakos et al. published an hitherto outstanding article in 1997. Beside dynamic and non-linear measurements and the constitutive description via a Phan-Tien-Tanner equation, they derived a degradation shift factor valid for the whole frequency range. However, they observed a reduction of moduli in a nitrogen environment and assumed the first frequency sweep to be unaffected. Therefore they referred to the so-called time-resolved mechanical spectroscopy (TRMS), which was established by Mours and Winter (1994). This method does not include mutations which occur before the measurement as emphasized in Section 3.3.2, but alterations during the measurement can be analyzed. This allows investigations of the reliability of each recorded frequency, and the observation of a frequency spectrum at a fixed time, as demonstrated in the following. Already in 1988 Winter et al. presented a mutation number N_{mu} (Equation 3.5) to relate changes of any property to a specific time. In 1994 they introduced the TRMS with the addition of a mutation time λ_{mu} (Equation 3.4) which can be understood as the reciprocal normalized

rate of alteration of a molecular property g.

$$\lambda_{mu} = \left[\frac{1}{g}\frac{\partial g}{\partial t}\right]^{-1} \tag{3.4}$$

$$N_{mu} = \frac{\Delta t}{\lambda_{mu}} \tag{3.5}$$

Analogous to the Deborah number, the time of observation can be related to the measurement time, which is of the order of a wave period $\Delta t = 2\pi\omega$. The property of interest is the loss or storage modulus, $g = G'$ or $g = G''$, leading to a λ'_{mu} and λ''_{mu}.

The data used for the TRMS originated from subsequently conducted frequency sweeps on H-PET. Since the described changes for the PET grades investigated underlie fast changes, the two lowest frequencies 0.05 and $0.0792 s^{-1}$ were omitted. This reduces the duration of a single run from approximately 24 to $11 min$ and a higher resolution can be achieved. Starting from the highest ω and with an equilibrium time of $2 min$ between the runs, a rapid and reliable data collection was realized and repeated 16 times. Subsequently, the measured data were analyzed by the software *IRIS* (Winter and Mours, 2006), which splits the 17 runs by their 19 different angular frequencies and relates them to the corresponding time elapsed, as sketched in Figure 3.4. In fact, this method is a thermal stability measurement over all angular frequencies with a recording rate of approximately $13 min^{-1}$ and a duration of $212 min$. The change of G' is more sensitive compared to G'', which generally is less pronounced or even delayed (see Appendices). In particular if $\delta \to \pi/2$, a sinusoidal function converges to 1 and the loss modulus converges to the reduced stress as denoted in Equation 3.7, even an elastic response still exists. In contrast, a cosine function as Equation 3.6 is at its inflection point, and small variations of δ lead to large variations in G'. Therefore, the storage modulus, analyzed with care, can be a precise indicator at high viscous behavior.

$$G' = \frac{\tau_0}{\gamma_0} cos\delta \tag{3.6}$$

$$G'' = \frac{\tau_0}{\gamma_0} sin\delta \tag{3.7}$$

$$tan\delta = \frac{G''}{G'} \tag{3.8}$$

TRMS in Air Atmosphere

In Figure 3.5, the evolution of G' in air at (a) $265°C$ and (b) $288°C$ is illustrated. The two graphs represent the behavior at low and high temperatures and the results at $272°C$ and $280°C$ (Appendices) can be seen as intermediate states.

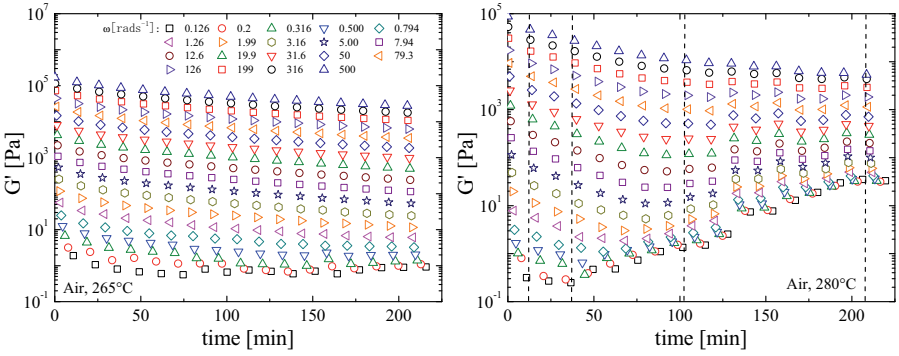

Figure 3.5: TRMS of the storage modulus G' for H-PET at (a) $265°C$ and (b) $288°C$ in air atmosphere. Dashed lines denote the state after the 1^{st}, 3^{rd}, 8^{th} and 16^{th} sampling.

The reduction of G' in air occurs at $265°C$ over the whole angular frequency range. The reduction follows an exponential evolution as described in Chapter 3.3. However, at higher temperature or, in terms of Arrhenius, reaction rate, the modulus starts to increase at low ω in Figure 3.5 (b). Thermo-oxidative degradation of poly(ethylene terephthalate) is known to occur after the initiation of a hydrogen peroxide on the methyl group. This homolytic scission leads to carbon and oxygen radicals and carboxyl and vinyl ester end groups. Chain scission induced by radicals reduces the molar mass (Madras and McCoy, 1997). However, the secondary reactions and arising side products can lead to network formation. Assadi et al. observed a cross-linking of PET and reported on a consumption of the O_2 molecules by small doses of oxygen in a nitrogen atmosphere and relates this cross-linking mainly to alkyl radicals. The competition of both scission and polymerization and their evidence has been established by rhelogical methods. In this context the contributions of Rolón-Garrido has to be emphasized who studied thermal, thermo-oxidative and photoinitiated degradations on polyolefins. He found an alternating process of a scission reaction and the formation of LCB up to cross-linking and verified his results by dynamic shear, elongation and absolute molecular measurements [Rolón-Garrido 2013; 2014; 2015].

Since the storage modulus reaches very low values, the reliability of the data needs to be verified. The lowest measured data presented are still two magnitudes above the minimal detectable torque. Since $tan\delta = \pi/2$ is not defined for $G' = 0$ (cf. Equation 3.8) a loss angle of 90° varies with the transducer resolution for pure viscous behavior. The scattering at low frequencies represent a G'

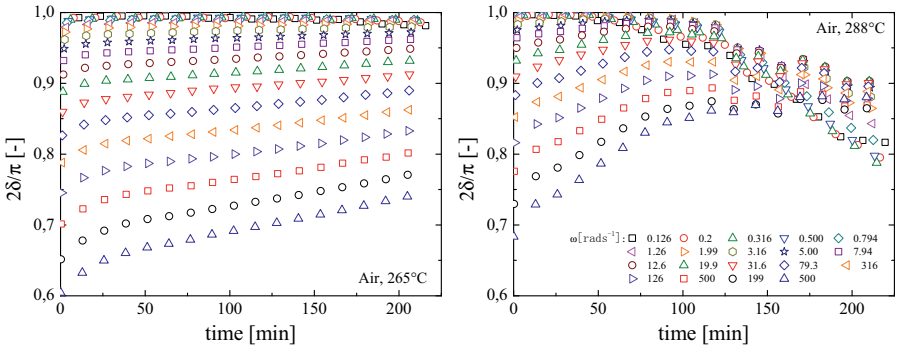

Figure 3.6: TRMS of the loss angle for H-PET at (a) $265°C$ and (b) $288°C$ in air atmosphere.

converging to zero, where the material approaches the behavior of a Newtonian liquid. This can be noted from the phase shift converging to $\pi/2$ in Figure 3.6.

The initial degradation rate in air atmosphere is independent of the angular frequency as can be noted from the parallel negative slope in Figure 3.5 and 3.12. Whereas, at $288°C$, the reduction of G' is followed by an enhancement, which can be detected at first at low frequencies, i.e. at long relaxation times, and leads to a plateau of G' at low frequencies. The approach to the gelling point is expressed by the convergence of all frequencies to a single loss modulus at high times in Figure 3.6 (b) (Winter and Chambon, 1986; Chambon and Winter, 1987). The impact of both degradation and cross-linking leads to large changes of the viscosity. Figure 3.7 illustrates the evolution of the complex viscosity with time in air at $265°C$ (a) and $288°C$ (b). Since the molecular changes occur during the measurement, TRMS was employed to correct the data. By smoothing the frequencies over time, a calculated G' and G'' for all ω at a fixed time can be obtained. With this, a snapshot of the whole frequency spectrum is realized, as illustrated by the dashed lines in Figure 3.5 (b). The plotted times of 11, 36, 113 and $201 min$ represent the actual state after the 1^{st}, 3^{rd}, 8^{th} and 16^{th} measurement. Since *IRIS* does not extrapolate the fittings to the start of the measurement, the modulus G'_0 was calculated as (Kruse and

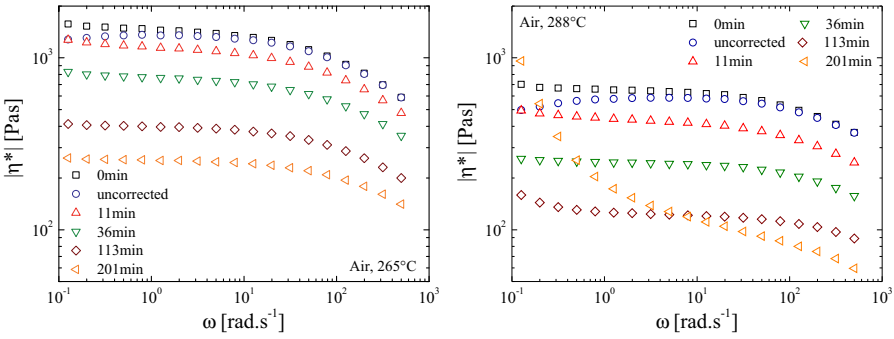

(a) (b)

Figure 3.7: TRMS of the complex viscosity for H-PET at (a) $265°C$ and (b) $288°C$in air atmosphere, based on calculations after the 1^{st}, 3^{rd}, 8^{th} and 16^{th} reading.

Wagner, 2016):

$$m_{1,2} = \frac{dlogG'}{dt} \tag{3.9}$$

$$\approx \frac{logG'_2 - logG'_1}{\Delta t_{1,2}} \tag{3.10}$$

$$logG'_0 = logG'_1 - m_{1,2}t_1 \tag{3.11}$$

with the slope $m_{1,2}$ between G'_1 and G'_2 at run 1 and 2 with time $\Delta t_{1,2} = t_2 - t_1$, respectively.

The complex viscosity based on the calculated G'_0 and G''_0 is denoted with $0min$ in Figure 3.7 (a) and overlaps with the *uncorrected* first frequency sweep measurement at high ω. However, at low frequencies the degradation is expressed as a reduction of the *non-corrected* data and overlaps with the first snapshot at $11min$. All following viscosities are shifted vertical to lower values with degradation time (Hatzikiriakos et al., 1997). Neither the range of the Newtonian plateau nor the slope of shear thinning behavior changes significantly. Usually, the shear thinning behavior is less pronounced when lowering the molar mass (Ferry, 1980). The response at high frequencies represents the chemical consistence of the polymer, since it originates from small segments, or even the primary covalent bonds of the macromolecule. Since the shift is solely vertical, it can be concluded that the emerging scission products, e.g. oligomeric chains and other degradation side products, act as plasticizer. The dilution effect leads to a lower viscosity with increasing degradation time.

This agrees also with the complex viscosities measured at $288°C$. Due to the higher temperature, the absolute value is lower and the degradation rate

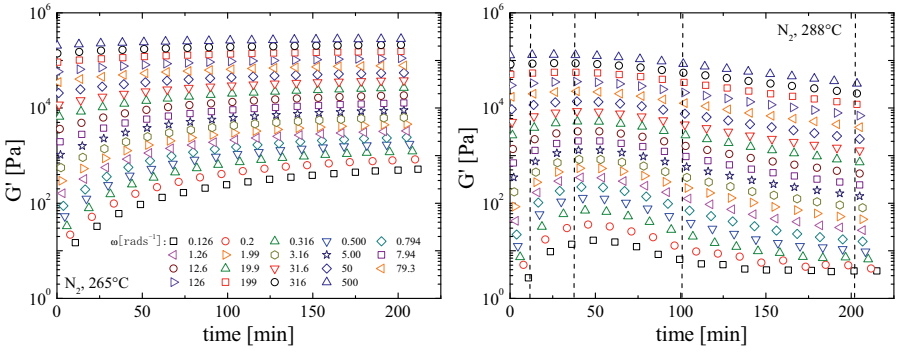

Figure 3.8: TRMS of the storage modulus G' for H-PET at (a) $265°C$ and (b) $288°C$ in nitrogen atmosphere at deformation of 1%. Dashed lines denote the state after the 1^{st}, 3^{rd}, 8^{th} and 16^{th} reading.

is higher, reflected in larger vertical shift. Furthermore, a strong increase of viscosity at low frequencies is detected at $201min$, indicating the existence of a yield stress. Obviously, cross-linking induced by oxygen, leads to a network, which can be first detected at low frequencies. This tendency is also reflected in the former snapshots, suggesting high molecular specimens at low frequencies.

TRMS in Nitrogen Atmosphere

The results in nitrogen atmosphere in Figure 3.8 illustrate the increase of molar mass. As seen in Figure 3.8 (a), an asymptotic increase of G' is more pronounced at low frequencies. A prevailing thermal degradation cannot be observed at $265°C$ during the experimental time. The data at $288°C$ in Figure 3.8 (b) possess a large enhancement which depends on the angular frequency, but also decreases due to thermal degradation with time.

The complex viscosity illustrates the build up of the molecular structure. The extrapolated data at $0min$ show the lowest values at $265°C$ in Figure 3.9 (a). The *uncorrected* recordings show the enhancement during the measurement at low frequencies. At $288°C$ in Figure 3.9 (b), the increase of molar mass is noticeable until $36min$. It can be seen that a more pronounced shear thinning effect occurs. Concurrently, the Newtonian plateau is shifted to lower frequencies and higher values with time due to the build-up of molar mass. At high frequencies, the convergence of viscosities indicates again the constant chemical structure on short length scales. This effect was also observed by a comparison of the three different grades investigated in Figure (3.16). At $288°C$ after the viscosity has reached maximum values at $36min$, the viscosity are shifted downwards verti-

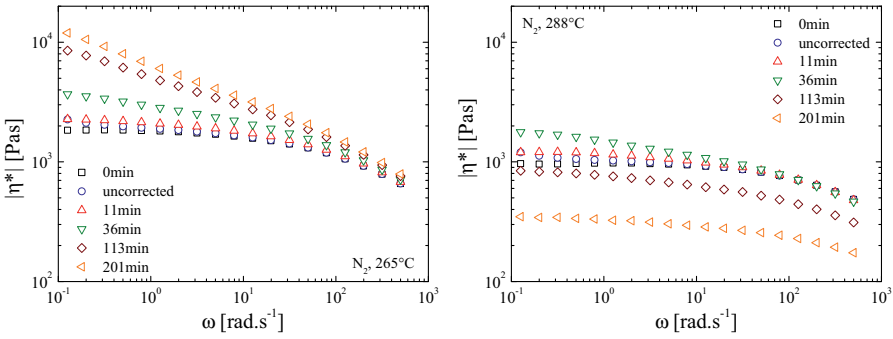

Figure 3.9: TRMS of the complex viscosity for H-PET at (a) $265°C$ and (b) $288°C$ in nitrogen atmosphere at strain of 1%, based on calculations after the 1^{st}, 3^{rd}, 8^{th} and 16^{th} reading.

cally at 113 and $201min$, as observed for thermo-oxidative degradation. It can be concluded that the *plasticizer effect* occurs at thermal and thermo-oxidative degradation, and the 3.4 power law for the relation between zero-shear viscosity and molar mass needs to be analyzed with care.

An modification of the measurement routine was applied to analyze the origin of enhancement in viscosity. In Figure 3.10 (a), the usual loading procedure is illustrated at $280°C$, which includes an opening of the oven at melt temperature and trimming at $280°C$. The preparation, as seen in Figure 3.10 (b), were conducted without any opening and trimming after the sample was loaded. As a consequence, the viscosity is slightly higher due to additional friction betwen rim and plate. The comparison of the enhancement of complex viscosity reveals a larger value for the trimmed sample at $113min$. Beside the mentioned possible cross-linking induced by oxygen, the diffusivity of the side products from the polycondensation should be considered. Due to the enlarged rim, these products, e.g. ethylene glycol, cannot evaporate from the interface. At the perimeter, the highest contribution to the torque is created and a reversible condensation would have large influence on the polymer viscosity. Therefore, the rim size and its barrier function should also be considered, which can affect the measurement.

The side products of the polycondensation and degradation possess a further impact on the measurement. The strain for the TRMS trials needed to be adjusted to 1% in nitrogen atmosphere, since a strain of 10% leads to apparent slipping at long measurement times. In Figure 3.10 (c), a strain of 10% leads to a decrease of viscosity at high frequencies. An amplitude sweep over the same duration reveals only a small decrease of non-linearity as reported in

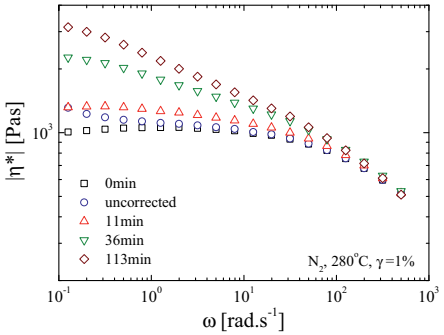

(a)

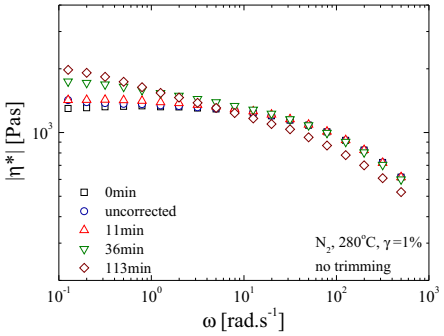

(b)

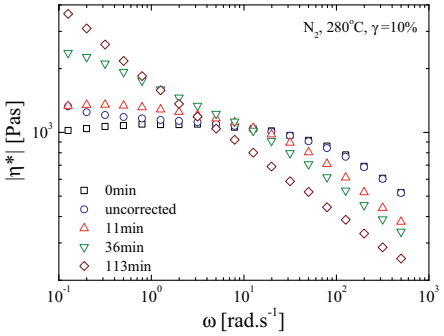

(c)

Figure 3.10: Comparison of TRMS of complex viscosity for H-PET on trimmed sample (a), non-trimmed sample (b), both with $\gamma_0 = 1\%$, and at $\gamma_0 = 10\%$ (c) in nitrogen atmosphere at $280°C$, based on calculations after the 1^{st}, 3^{rd}, 8^{th} and 16^{th} reading.

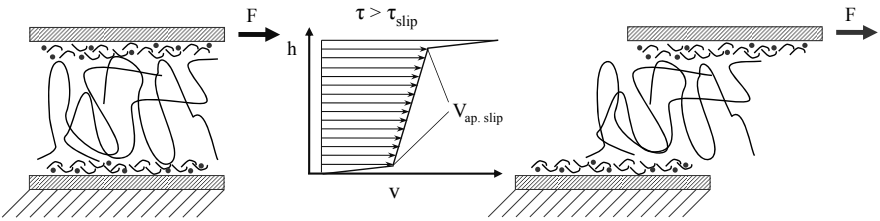

Figure 3.11: Illustrations of oligomeric layer, leading to apparent slipping of the polymer melt at critical stress with a corresponding velocity profile.

Section 3.2. High frequencies result in high stresses, and as soon the stress exceeds the adhesion force, the polymer will start to slip on the confining plates. This phenomena was observed for the three PET investigated at the highest frequencies, but only after a certain time in nitrogen atmosphere, e.g. when starting the measurement from the lowest frequency. The side products such as ethylene glycol or diethylene glycol possess a high polarity. Due to diffusion, low molar mass species deposit on the metal plates, which promotes an apparent slipping of the polymer. As illustrated in Figure 3.11, apparent slip leads to an accelerated velocity at the interphase. This was also confirmed by an easy peel when removing the sample after the test, and a white powder which deposited on the rheometer housing. The reduction of the strain amplitude to 1% leads to a reduction of the shear stress and slipping is avoided. For the sake of clarity, measurements with different gap size would be required.

These overall changes at low frequencies for polycondensed polymers in nitrogen where also observed by Filippone et al. (2015) for polyamide. They reported on a similar trend at low frequencies over time by TRMS. Ibar et al. (2015) analyzed a comparable frequency sweep evolution for polycarbonate.

The increase and decrease of viscosity during thermal and thermo-oxidative conditions can be quantified by the slope m'' of G'' between the first two runs used for the correction. Since $[\lambda_{mu}]^{-1} \propto m$, an accelerated reactivity or mutation is represented by higher or more negative values in Figure 3.12. The TRMS analysis reveals a higher polycondensation rate with higher temperatures and with larger impact on low frequencies, before a degradation similar to the thermo-oxidative behavior occurs ($288°C$ is not plotted since it overlaps with the lower temperatures). An enlarged rim suppresses the enhancement, as reflected in reaction rate (non trimmed). The high frequencies are not affected, since the chemical structure remains. The degradation effect in air is governed by a *plasticizer effect* and also larger at high temperatures, as can been noted from more negative m'' values.

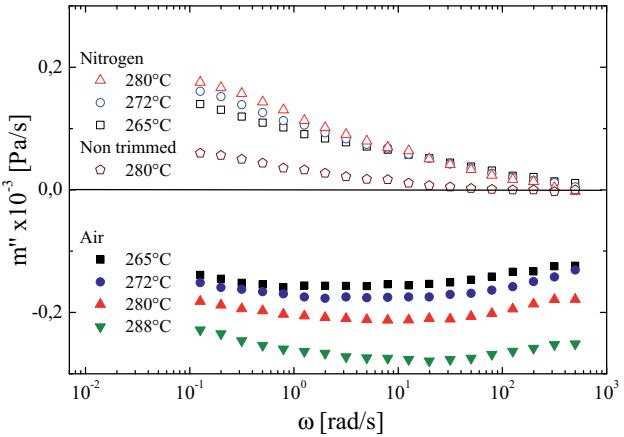

Figure 3.12: Comparison of alteration in air and nitrogen, expressed by slope m'' of loss modulus between the first and second reading at temperature $265°C$, $272°C$, $280°C$ and $288°C$. The results of $288°C$ in nitrogen atmosphere are omitted for the sake of clarity, due to overlapping with the lower temperatures.

3.4 The Shear Viscosity of PET

The analyses presented in Section 3.3 give an insight of the alterations during the measurements and to the behavior during processing. Both zero-loading time and TRMS are sophisticated procedures, nonetheless, their awareness is crucial for the validation of common measurement techniques. In the following, linear dynamic and steady rotational and capillary shear flow measurements are analyzed and compared.

3.4.1 Linear Viscoelastic Analysis

The extend and speed of the observed molecular changes emphasize the demand on a detailed knowledge of the sample preparation and experimental mode used. The impact on the viscoelastic response were investigated with variations of atmosphere (air or nitrogen), preparation of the sample (pellets or compression molded plate in air and nitrogen) and the frequency mode (increasing from $0.05s^{-1}$ to $500s^{-1}$ or decreasing from $500s^{-1}$ to $0.05s^{-1}$. Figure 3.13 (a) illustrates a frequency sweep in nitrogen at $280°C$ for H-PET pellets starting from $\omega = 500s^{-1}$ (solid symbols) and a subsequent second run from $0.05s^{-1}$ (empty symbols). The increase of the complex viscosity is mostly pronounced at low ω, where the measurement time increases, and accompanied in the second run from $\omega = 0.05s^{-1}$ by a stronger shear thinning behavior. The findings originate

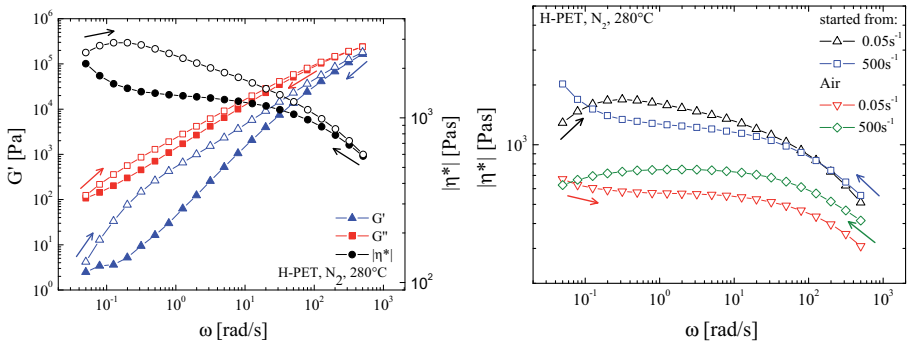

Figure 3.13: Storage and loss modulus and complex dynamic viscosity for run 1 (solid) and run 2 (empty) (a) and dynamic viscosity in air and nitrogen atmosphere at 280°C for H-PET pellets measured by a decreasing and increasing run (b).

from both moduli, which possess higher values in the second run. In particular in the first run, G' demonstrates the approximation to a plateau modulus G_N^0 at high frequencies and a terminal regime in the middle section. The formation of high molecular specimens with time increases the storage moduli at low frequencies and continues in the second run, subsequently. The increasing run continues with a less steeper slope in the middle section compared to the first run, which reflects a broader shear thinning behavior. The origin of non-Newtonian behavior are entanglements, which are increased by higher molar mass, a broadening of polydispersity and the formation of long chain branches (Dealy and Larson, 2006) and should be considered.

Figure 3.13 (b) reveals the influence of the frequency sweep mode started from $\omega = 0.05s^{-1}$ or $500s^{-1}$ and atmosphere on the complex viscosity of H-PET at 280°C. Both variations can be noticed significantly at long measurement times at low frequencies expressed as upturn or downturn. The substantial changes before the measurements are also expressed, since the air and nitrogen frequency sweep measurements do not overlap at the same modes. The comparison of both atmospheres demonstrate again that in air degradation leads to a linear vertical downward shift, by neglecting the opposed reduction at low ω. The structure seems to be the same, whereas in nitrogen the Newtonian plateau is shifted to smaller frequencies. At this point, it should be mentioned that these effects are intrinsic material properties, but they can be accelerated by the measurement technique. Degradation reactions are known to occur with a threefold rate in a closed system (Zimmermann, 1984) and the barrier function of surrounding material was already discussed.

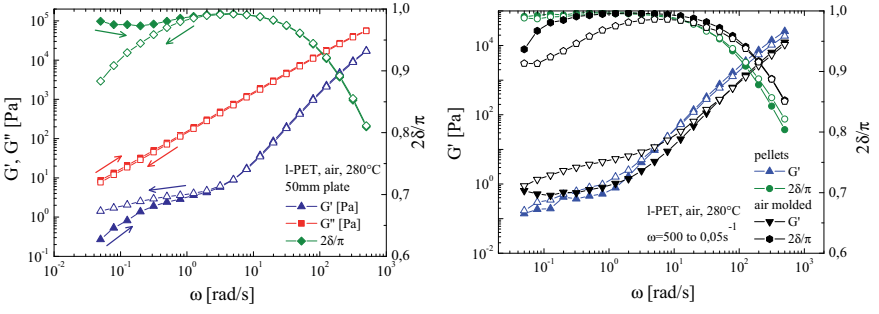

Figure 3.14: Storage (triangle) and loss modulus (square) and loss angle (diamond) in air atmosphere at 280°C for l-PET pellets measured by 50 mm parallel plate geometry (a) and comparison of virgin pellets with compression molded sheets in air atmosphere (b), for run 1 (solid) and run 2 (empty).

However, the analysis of the complex viscosity has to be done with care, since it is based on the sum of storage and loss moduli. By observing G' in air atmosphere from Figure 3.14 (a) a higher value from the second run (empty symbols) can be noticed, although a degradation to lower viscosities is dominant, as can be seen from the G'' data. This experiment was conducted with a $50mm$ parallel plate geometry which leads to tenfold higher torque on neat l-PET pellets. The distinct detection of the loss angle at low frequencies represents an enhanced elastic behavior during the second run, e.g. due to cross-linking. This is also obvious by comparing G' and δ of neat pellets with samples which were compression molded in air atmosphere, as can be seen in Figure 3.14 (b). In general, the molded samples behave more viscous, as can be noted from a lower storage modulus and higher loss angle at high frequencies, due to degradation occurring during processing. At low frequencies the modulus increases from the first to the second run and the phase shift reaches lower values. The induced oxygen and further radicals lead to an ongoing enhancement of molar mass during measurement.

The dominating drastic viscosity reduction due to compression molding in air is illustrated in 3.15 (a). The measurement was conducted in inert atmosphere starting from high frequencies. The duration of compression molding in air atmosphere is $4min$. The comparison with molding in a nitrogen surrounding reveals a negligible change of complex viscosity although the processing time is $10min$. In contrast to solid state polycondensation the molar mass seems to be unaffected and an increase of viscosity did not occur in the N_2 mold. Actually the results of H-PET lead to a reduction of $|\eta^*|$, but still much less than the

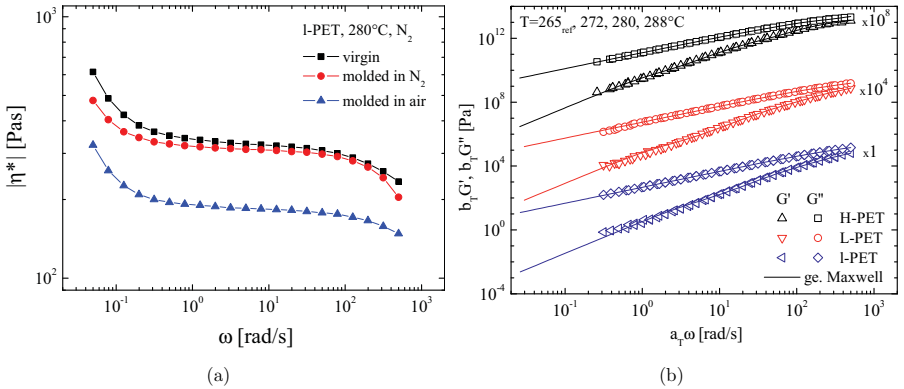

Figure 3.15: Comparison of preparation method of virgin pellets, compression molded sheets in nitrogen and air atmosphere (a) and master curve of G' and G" with generalized Maxwell model for H-, L-, and l-PET compression molded sheets in nitrogen atmosphere.

compression molded sample in air. The impact of the diffusivity of the side products seem to influence the compression processing, as observed in Section 3.3.3. Since the squeezed melt remains for minutes inside the inert mold, a balance between condensation and reversible reaction occurs, as a consequence of the small volume to free surface ratio.

Despite small changes during the sample preparation, the compression molding in inert atmosphere reduces the loading time of samples. Since samples for non-linear measurements need to be processed in stripes, another advantage is the comparison of material with the same thermal history. The huge impact of atmosphere, temperature, preparation method, loading time and initial molar mass on the thermal stability prevent a simple concept of analyzing poly(ethylene terephthalate). For example, most of the results in air atmosphere evolve less alternations and a well defined terminal region. On contrary, for the sake of chain extension and achieving high molar masses, or employing other additives, the use of a nitrogen environment is to prefer.

Master Curve

One aim of a frequency sweep is to achieve a wide range of the frequency spectrum. This is due to the fact that data at low ω allows the analysis of the long relaxation time behavior and the zero-shear viscosity, while data of high ω can be related to processing conditions as injection molding. A master curve of different temperatures merged to one reference temperature allows to observe the properties at very short and long relaxation times.

As illustrated in Chapter 3.3.3, the storage and loss moduli of the PET investi-

gated converges to a terminal regime, but are counteracted by the enhancement effect in nitrogen atmosphere. The applied procedure to achieve a master curve consists of first recording all frequencies, starting from the highest, and, subsequently, discard data for each temperature, which deflect from an approach to a terminal behavior, and finally merge to superposition. The time-temperature superposition of G' and G'' for H-PET, L-PET and l-PET is confirmed in Figure 3.15 (b). The data are shifted vertically for the sake of clarity. The plotted generalized Maxwell model shows good agreement with the experimental data and includes the lowest measured frequencies which had to be erased. The discrete relaxation spectra and η_0 based on the algorithm of Baumgaertel and Winter (1989), assuming a Cox-Merz rule, and the flow activation energy E_A in Table 3.6 were calculated by the software IRIS. Additionally, the shift factors a_T and b_T for a reference temperature $265°C$ are included. The vertical shift factor is comparably low and should be seen as a result of experimental artifacts, and not as a consequence of non-linear density changes with temperature (Dealy and Larson, 2006; Rubinstein and Colby, 2003). The linear PET can be described as rheologically simple. A comparison of the three PET grades in Figure 3.16 (a) emphasizes the differences in complex viscosity. The level of the Newtonian plateau reflects the respective high molar mass of H-PET, which also shows the most pronounced shear thinning behavior.

The superposition clearly demonstrates the reliability of the measurement and a well developed Newtonian plateau. Without the introduced procedure, the calculated zero-shear viscosity would be 8% for the high and 17% for the low molar mass PET above the presented values. The activation energy of flow derived from the Arrhenius-type relation in Figure 3.16 (b) of H-PET ($65 kJ.mol^{-1}K^{-1}$) is above that of L-PET ($54 kJ.mol^{-1}K^{-1}$) expressed by the steeper slope and corresponds to a possible higher entanglement density of H-PET. The value of l-PET ($68 kJ.mol^{-1}K^{-1}$) is comparable to the high molar mass sample, although its molar mass is in the range of L-PET. The different synthesis route could be an explanation, but in general an over-interpretation has to avoided, since experimental deviations especially at the highest temperatures have to be considered. Overall the observed activation energies are in good agreement with Hatzikiriakos et al. who measured between 48 and $67 kJ.mol^{-1}K^{-1}$, and (Utracki et al., 1982) and Wang et al. who observed 38 to 46 and $84 kJ.mol^{-1}K^{-1}$ for linear PET, respectively.

3.4.2 Steady Shear Flow

The response of the material during dynamic or steady shear flow measurements deviates crucially, since the deformation in the oscillatory mode is small and disentanglement can be neglected, whereas in steady shear orientation and disentanglement determine shear thinning. On the other hand, dynamic ex-

Table 3.6: Discrete relaxation moduli and times, zero-shear viscosity at reference temperature $265°C$, flow activation energy and shift factors for $272°C$, $280°C$, and $288°C$ on compression molded PET sheets.

H-PET		L-PET		l-PET	
$\eta_0 = 1260Pas$		$\eta_0 = 560Pas$		$\eta_0 = 470Pas$	
$g_i(Pa)$	$\lambda_i(s)$	$g_i(Pa)$	$\lambda_i(s)$	$g_i(Pa)$	$\lambda_i(s)$
1.06×10^9	3.92×10^{-1}	6.05×10^9	2.06×10^{-2}	6.12×10^8	4.00×10^{-1}
9.83×10^7	5.82×10^0	1.87×10^8	8.89×10^{-1}	5.24×10^7	2.84×10^0
4.65×10^6	4.91×10^1	5.07×10^7	3.67×10^0	5.54×10^6	1.20×10^1
4.92×10^4	7.72×10^2	3.64×10^6	2.02×10^1	3.87×10^4	2.33×10^2
		1.91×10^4	5.58×10^2		
$E_A = 65.4kJ.mol^{-1}K^{-1}$		$E_A = 54.9kJ.mol^{-1}K^{-1}$		$E_A = 68.3kJ.mol^{-1}K^{-1}$	
$loga_T(-)$	$logb_T(-)$	$loga_T(-)$	$logb_T(-)$	$loga_T(-)$	$logb_T(-)$
-0.082	-0.008	-0.057	0.008	-0.106	-0.047
-0.119	-0.001	-0.123	0.033	-0.202	-0.013
-0.284	0.005	-0.227	-0.011	-0.279	-0.032

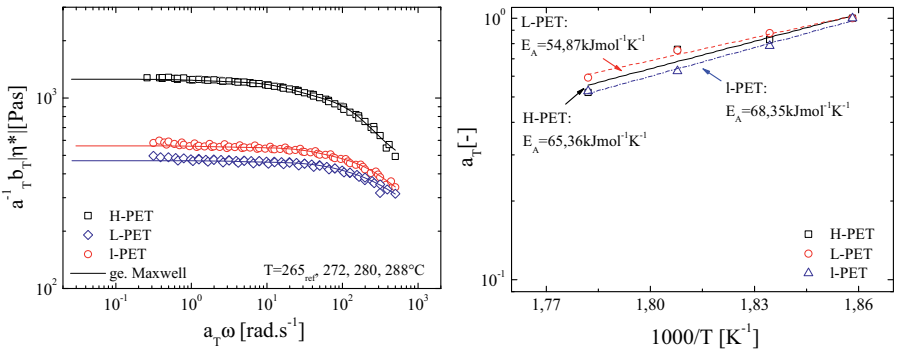

(a) (b)

Figure 3.16: Comparison of master curve of complex viscosity (a) and flow activation energy (b) of virgin, H-, L-, and l-PET compression molded in nitrogen atmosphere at reference temperature $265°C$.

periments depend also on the number of entanglements, since the rubber-like liquid behavior can be seen as a network acting at high frequencies where dissipation becomes a minor aspect (Ferry, 1980). The major advantage of steady capillary shear flow is the comfortable handling and the direct applicability to polymer processing, where high shear rates occur, e.g. injection molding (Macosko, 1994). This section relates steady with dynamic viscosity for a validation of the Cox-Merz rule. Before, a correction of the recorded capillary data is conducted to achieve true values.

Entrance Pressure Drop Correction
The flow behavior in a capillary can by described in cylindrical coordinates and with the following assumptions:

- Fully developed, steady, isothermal, laminar flow.
- No velocity components in the r and θ directions.
- No slip at the walls, i.e. $v_z = 0$.
- Incombressibility and no pressure dependence of viscosity.

Based on these assumptions the stress τ_{rz} along the radius r in the z-direction of a die and a pressure gradient $\partial p/\partial z$ can be expressed with the equation of motion (Macosko, 1994):

$$0 = \frac{\partial p}{\partial z} + \frac{1}{r}\frac{\partial (r\tau_{rz})}{\partial r} \tag{3.12}$$

With a constant pressure drop p_c over the capillary length L and integration, the shear stress results in:

$$\tau_{rz} = \frac{r}{2}\frac{p_c}{L} \tag{3.13}$$

The stress at the capillary wall $r = R$ is than given as:

$$(\tau_{rz})_{r=R} = \tau_w = \frac{R}{2}\frac{p_c}{L} \tag{3.14}$$

Before a flow converging from a barrel into a capillary is fully developed, a contribution of extensional deformation occurs (Cogswell, 1981). Unfortunately the small diameter of a capillary inhibits the installation of a pressure transducer, which is commonly above the entrance of the die[7]. In 1957, Bagley introduced a correction method which allows to obtain the real viscosity by the use of different L/R ratios. The idea he had was to increase the shear stress but keep the entrance pressure drop constant with a fixed radius. By an extrapolation over constant shear rates the intersection with the x-axis leads to

[7]By employing a slit die the actual pressure can be measured.

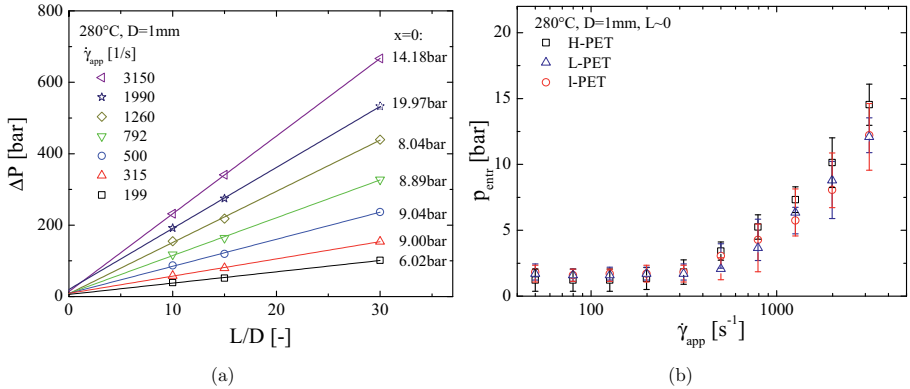

Figure 3.17: Comparison of Bagley correction with three dies for H-PET (a) and entrance pressure of an orifice die for H-, L-, and l-PET (b) at different shear rates.

an effective die length. In Figure 3.17 (a) the results of seven different apparent shear rates $\dot{\gamma}_{app}$ over die lengths of 10, 15 and 30mm diameter of 1mm at 280°C are shown. Since the shear stress is directly proportional to both, the ratio of the pressure drop in the die $p_c = p_0 - p_L$ (p_0 at $z = 0$) and the effective length, a correction can be also conducted on the entrance pressure drop p_{entr}. The corresponding values from a linear regression at $x = 0$ reveal a convergence to a single pressure drop for the low shear rates. Only $\dot{\gamma}_{app}$ 1990 and 3150s^{-1} lead to higher values.

The aforementioned assumptions emphasize the need of incompressibility and a fully developed flow. The latter is supported in particular by the capillary length. On the other hand, the increased flow resistance could either induce pressure effects on the free volume or a locally increased temperature due to dissipation, which leads to higher and lower pressure values, respectively (Aho and Syrjälä, 2008). Therefore, Laun and Schuch (1989) used a polynomial fit to extrapolate the entrance pressure drop. Indeed Hatzikiriakos et al. (1997) succeeded in obtaining reliable data for poly(ethylene terephthalate) by a quadratic extrapolation. Whereas, Aho and Syrjälä (2008) demonstrated that the preferred procedure can vary. A polynomial fit lead to higher p_{entr} (Kim and Dealy, 2001) which can be threefold higher than the present data. Since the values of the 30mm die overlap with the fitting, the linear prediction is reliable and only the discrepancy of the highest shear rates can be explained by non-linear pressure effects. This is confirmed by results with an orifice die.

In 1972, Cogswell reported on a zero-length die to directly measure the amount of extensional contribution (cf. Section 2.4). The die geometry plays a significant role as reported by Kim and Dealy (2001). They concluded that the

actual L/D ratio should be below 0.5 and the entrance angle above 90°. Also the exit of the die is of interest, since an enhanced extrudate swelling at high $\dot{\gamma}$ leads to sticking at a concave enlargement and an increased exit pressure (Aho and Syrjälä, 2008). To avoid these possible error sources, an orifice die with an entrance angle of 180°, a L/D ratio of 0.25 and an exit angle $< 20°$ were manufactured. Figure 3.17 (b) illustrates the p_{entr} of H-PET, L-PET and l-PET of four measurements including the standard deviation. The results were recorded with a 1000*bar* pressure transducer which was calibrated with a *Dynasco PPS 1200* and the accuracy is reflected by the error bars. The high molar mass PET possesses higher values compared to the grades with the lower molar mass, but all three exhibit increasing values at shear rates larger than $500 s^{-1}$. In comparison with the entrance pressure drop achieved from the Bagley correction the orifice data are lower, which reveals that no wall sticking at the exit influence the measurement of the orifice die. In generally, the data are in the same order of magnitude, and the orifice die is to prefer, since it reduces the effort. However, the contribution to the total pressure drop is approximately 2% and can be neglected for the linear PET (Utracki et al., 1982).

Weissenberg-Rabinowitsch Correction
Even if the impact of entrance pressure drop correction to the real viscosity is a minor aspect, a correction of the non linearity of the shear rate should be considered, since a non uniform shear flow will occur, if the fluid is forced through a gap (Han, 2007). These observations were first made by Hagen (1839) and Poiseiulle (1840), who realized that the velocity of a fluid through a channel is at its maximum at the center and the velocity gradient or shear rate is 0, which reaches the highest value at the wall, $\mathrm{d}v_z/\mathrm{d}r = \dot{\gamma}_w$ (Macosko, 1994). The volumetric flow rate can be expressed as (Münstedt and Schwarzl, 2014):

$$Q = 2\pi \int_0^R v_z(r) r \, \mathrm{d}r \tag{3.15}$$

Assuming non-slip condition, the velocity at the wall becomes $v_z(r = R) = 0$ and integration by parts leads to:

$$Q = -\pi \int_0^R r^2 \frac{\mathrm{d}v_z}{\mathrm{d}r} \, \mathrm{d}r \tag{3.16}$$

Based on a Newtonian flow behavior:

$$\tau_{rz} = \eta \, \dot{\gamma}_{rz} \tag{3.17}$$

the shear rate with Equation 3.13 and 3.17 becomes

$$\dot{\gamma}_{rz} = \frac{\partial v_z}{\partial r} = \frac{r}{2\eta} \frac{p_c}{L} \tag{3.18}$$

and by substitution of the differential equation in 3.16 the integration can be conducted and after rearranging the shear rate at the wall becomes:

$$\dot{\gamma}_w = \frac{4\,Q}{\pi\,R^3} \tag{3.19}$$

An integration of Equation 3.18 with respect to the velocity describes a parabolic profile over the radius. And since the viscosity depends on the shear rate, a profile of the latter would be unknown for a non-Newtonian liquid. A possible shear thinnig would increase the shear rate at the wall. The Weissenberg-Rabinowitsch correction provides a method to include this effect (Rabinowitsch, 1929). With $\tau_{rz}/\tau_w = r/R$ Equation 3.16 can be formulated as:

$$Q = \frac{\pi\,R^3}{\tau_w^3} \int_0^{\tau_w} \tau_{rz}^2\,\dot{\gamma}_{rz}\,(\tau_{rz})\,\mathrm{d}\tau_{rz} \tag{3.20}$$

After integration with respect to $\mathrm{d}\tau_{rz}$ and rearranging, the shear rate at the wall is:

$$\dot{\gamma}_w = -\frac{Q}{\pi r^3}\left(3 + \frac{\mathrm{d}lg\,Q}{\mathrm{d}lg\,\tau_w}\right) \tag{3.21}$$

With the apparent shear rate $\dot{\gamma}_{app} = \dot{\gamma}_w$ and Equation 3.19, the correction with the true shear stress results in:

$$\dot{\gamma}_w = \dot{\gamma}_{app}\left(\frac{3}{4} + \frac{1}{4}\,\frac{\mathrm{d}lg\,\dot{\gamma}_{app}}{\mathrm{d}lg\,\tau_w}\right) \tag{3.22}$$

A discrete analysis was conducted from $\dot{\gamma}_{app}$ and τ_w at each measured point n, with the initial condition $\dot{\gamma}_{app} = \tau_w = 0$ and an extrapolation of an additional high rate with

$$\dot{\gamma}_n = \dot{\gamma}_{n-1}\frac{Q_n}{Q_{n-1}} \tag{3.23}$$

In Figure 3.18 (a) the effect of both corrections is demonstrated. In particular the impact of the shear rate correction with increasing shear thinning effect is noticeable.

Cox-Merz Rule

The empirical Cox-Merz rule relates linear to nonlinear viscoelastic data (Cox and Merz, 1958). The assumption that the shear rate and frequency affect the viscosity in the same way (see Equation 2.76) is verified in Figure 3.18 (b). The dynamic data originate from a frequency sweep in air atmosphere starting from the highest frequency by discarding the 5 lowest frequencies which are affected by substantial degradation. The capillary data were recorded from the lowest shear rate to avoid unfinished relaxation processes. The plotted data begin at approximately $80s^{-1}$ depending on the extent of the correction. At first glance,

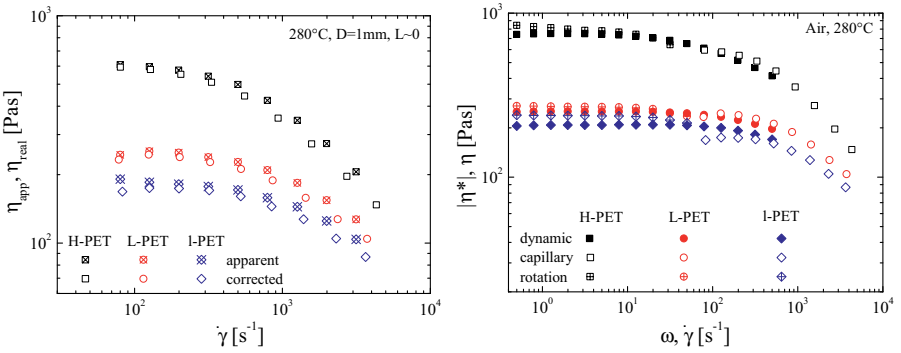

Figure 3.18: Comparison apparent and true shear flow viscosity (a) and complex and steady flow viscosity (b) for H-, L-, and l-PET in air atmosphere.

the data show fair agreement in both shear thinning behavior and absolute value of the viscosity.

Whereas by a more thorough examination, deviations from a linear plateau are obvious, e.g. for H-PET and l-PET. It has to be mentioned that the loading procedure of both techniques differs not only in time (a capillary measurement can last up to $10min$ from the loading to the beginning of recording) but also by atmospheric conditions, since a degradation rate can be up to threefold higher in a closed system for PET. On contrast, Assadi et al. reported on a consumption of oxygen and enhancement of molar mass, when the oxygen content is limited. These conditions are comparable to the capillary loading procedure, where after compression the melt is sealed. A further critical aspect is the diameter of the capillary since the viscosity is direct proportional to the fourth power of the radius:

$$\eta_{app} = \frac{\pi R^4 p_c}{8 Q L} \tag{3.24}$$

small deviations in the radius drastically changes the absolute value.

Since measurements at low shear rates in capillary flow are limited due to limits of the sensitivity of pressure transducer, and higher frequencies exceed the physical limits of an oscillatory device, the overlap of data is small. Additionally, rotational experiments by a cone and plate geometry with an angle of 4° were conducted. The experiments started from $0.05s^{-1}$ to ensure steady relaxation conditions, and possible edge fracture and centrifugal forces are avoided.

The results demonstrate the reduction of viscosity during the measurement and a cross-over with the dynamic data, which started from high frequencies.

However, the comparison of the three employed techniques should be done with care. All three methods have different degradation histories, which cannot be standardized due to intrinsic requirements of each method. In total, a strong correlation of the shear rate and frequency dependence support a Cox-Merz relationship, in particular, since deviations up to 25% were observed (Ferry, 1980; Dealy and Larson, 2006). The result is in agreement with Hatzikiriakos et al. (1997) and (Utracki et al., 1982), who observed a Cox-Merz behavior.

3.5 Conclusions

Three PET grades produced by different synthesis routes, which can be distinguished by molar mass and concentration of functional end groups, were investigated in regards of thermal and thermo-oxidative degradation and preparation.

The thermal stability investigations exhibit a degradation mechanism and a reduction of the storage modulus in air atmosphere, and an enhancement of the moduli in nitrogen atmosphere, due to polycondensation. With time, the degradation reaction in air atmosphere is prevailed by an increase of the moduli, due to a cross-linking induced by oxygen. The enhancement reaction in nitrogen atmosphere is counteracted by a thermal degradation.

A time constant, which is based on an exponential function, revealed for all PET grades in both atmospheres relations between stability and polymer properties. High molar mass PET is more stable in nitrogen and less stable in air environment than low molar mass PET, and vice versa. This findings correlate to the OH end group concentration and a related reactivity.

The different degradation effects can be analyzed by means of time-resolved mechanical spectroscopy (TRMS) and a correction of the storage and loss modulus of poly(ethylene terephthalate), allowing an observation at a fixed time. Both thermal and thermo-oxidative degradation lead to small molecules which act as plasticizer.

Besides a vertical shift of the complex viscosity/frequency curve, severe cross-linking leading to a yield stress was observed by degradation in air. On the other hand, in nitrogen, polycondensation increases the molar mass, the viscosity and the shear thinning regime.

Diffusion of the side products was found to influence the enhancement of the moduli and complex viscosity and to promote slipping. Additionally, a barrier function of surrounding material during the rheological measurements leads to the conclusion that the diffusion and the volume to free surface ratio plays a crucial role for the enhancement.

This findings were confirmed by the compression molding preparation in air and nitrogen atmosphere. A routine for a reliable master curve was established. Differences between dynamic, rotational and capillary shear flow were found due

to the differences in the experimental protocols used, but revealed to be small enough to conclude the approximate validity of the Cox-Merz relation. The contribution of stretching during a converging flow can be neglected for linear PET.

4 Reactive Extrusion of PET

Reactive processing of polymers has been of increasing interest for science and processing in the recent decades. In 1992, Xanthos published a book on polymerization, polymer modification, and blend compatibilization conducted in a continuous extrusion process. More recently Cassagnau et al. (2007) reviewed current work and highlighted also the higher efficiency of this technique, e.g. due to an omission of solvent and a reduced residence time. Their report includes the impact of mixing and diffusion processes on the reaction, and emphasizes the advantage of a twin screw extruder. Typical applications are grafting or functionalization of polymers and even bulk polymerization of lactams or urethans.

The modification of PET mostly aims at a chain lengthening by an application of a chain extender. Depending on the functionality of the coupling agent, long linear and even LCB molecules can be expected. Concurrently, Cassagnau et al. mentioned the negative aspects of the extrusion, due to possible thermal degradation and other side reactions. Consequently this chapter reports, at first, on the extruder settings and their correlation to a possible emerge of degradation of solely poly(ethylene terephthalate). Subsequently, the three chain extenders (PMDA, TGDDM, and TPP) will be introduced and characterized at different concentrations applied by means of a preliminary batch test. With awareness of the extrusion findings and the batch results, the reactive extrusion by means of different chain extenders is described.

4.1 Extruder Configuration

For the sake of thorough mixing, a *Leistritz* intermeshing twin co-rotating extruder with a screw diameter of $34mm$ and a L/D of 34 were used, fulfilling industrial requirements. As displayed in Figure 4.1 the temperature profile varies from 240 to $290°C$. The two stage degassing twin screw consists of a set of two conveying, transition and metering zones. After the first kneading elements and barrier flights, a degassing vent is assembled, allowing the installation of a vacuum pump or a second hopper (zone 4). At that point, the polymer is already in the melt state at $270°C$, followed by a second more extensive compression and metering zone, including further kneading elements. The throughput of $1250g/h \pm 5\%$ was realized with a weight controlled feeder. Two

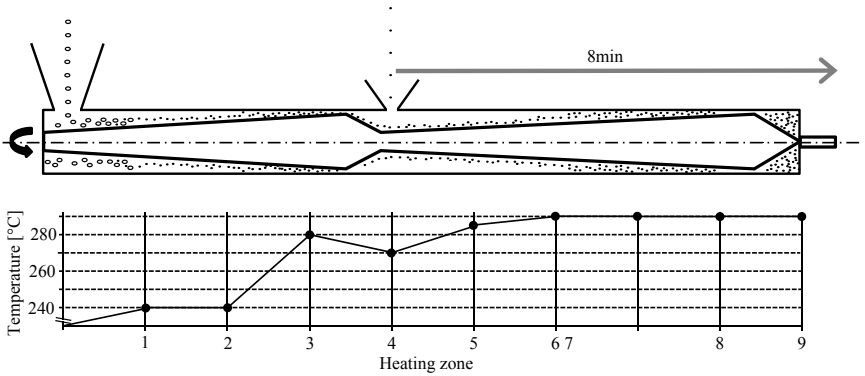

Figure 4.1: Co-rotating twin-screw extruder with set of two conveying, transition and metering zones, two feeding sections, and respective temperature profile.

dies with three horizontal circular outlets of $1mm$ and $1.4mm$ were assembled. The small diameter enables a quick quenching of the strand and a withdraw of even highly viscous material. Additionally, this setting minimizes degradation after extrusion, since the thin filaments were immediately conveyed through a water bath, and pelletized subsequently.

Usually, investigations on the processing of polymers are conducted at laboratory scale. Since poly(ethylene terephthalate) undergoes substantial changes during its processing (Daver et al., 2008), researchers often use inert conditions, especially when applying reactive processing (Cardi et al., 1993; Härth et al., 2015). However, susceptible material is still processed under environmental atmosphere, due to low costs and stable processing conditions. The intention of the present work is to investigate the effect of reactive extrusion at large scale and to examine industrial processing. Therefore, to study the impact of extrusion under thermo-oxidative and inert environment, the atmospheric conditions at zone 4 were assembled as closed, open (plotted) and degassed systems, which was realized by a vacuum pump. Besides the vent settings, the shear conditions were varied by different screw rotations rates (40, 100, 200 and $250rpm$). During the extrusion, the online pressure was recorded by a $150bar$ *Dynisco MDA* transducer at the die entrance. The residence time of $8min$ from the vent and $11min$ in total were adjusted to realize thoroughly mixing and sufficient reaction time, as will be described in Section 4.3.2. The pellets were dried at $130°C$ for $7d$ in a vacuum oven before application.

4.2 Degradation of PET During Extrusion

The main consequences of degradation are a change of viscosity, embrittlement and yellowing (Colin and Verdu, 2006). In particular the change of viscosity and the reaction of even pure PET during extrusion should be analyzed by taken into account the results from Chapter 3. As demonstrated, molecular changes during thermal treatment can lead to decomposition, but also to further polycondensation or cross-linking in inert environment. Correlating these results to the extruder process, the die and the hopper section are in direct contact to oxygen (Zone 1, 9 and eventually 4), whereas inert condition can be assumed in a filled barrel (Colin and Verdu, 2006; Assadi et al.).

4.2.1 Variations of Atmosphere

Figure 4.2 (a) shows the apparent steady shear viscosity of L-PET at different ventilation conditions measured in air atmosphere. The unprocessed reference exhibits the highest viscosity, and a continuous reduction from the degassed to the closed and open setting can be noted. A similar tendency is prominent when analyzing the complex viscosity Figure 4.2(b) measured in nitrogen atmosphere. The viscosity differs due to the different atmospheres provided during the experiments, which leads to either decrease or increase of viscosity. Additionally, the relations between curves are shifted. The processed material still exhibits a polymerization during the oscillatory test as reflected by an increase of $|\eta^*|$ at low frequencies (the frequency sweep starts from the highest angular frequency). This enhancement is slightly more pronounced on the graphs representing the closed and open setting compared to the degassed setting. Additionally, the reactivity of the extruded grades has a second outcome, the emerge of gaseous side products. The occurrence of bubbles during the measurement can reduce the detected complex viscosity. The extent of this effect varies between the two measurement techniques, which the relative shift of graphs may indicates. Due to the low viscosity of the PET and the strong pressure drop by the vacuum pump, a constant air stream from the hopper (zone 1) to the vent (zone 4) appeared during the degassing. Therefore the degassing leads to an extraction of side products but also to a supply of oxygen. The shift of the apparent and complex viscosity curve is not purely vertical, furthermore a reduced shear thinning regime can be noted. The diluting effect from oligomeric side products is still prominent, but a reduction of the molar mass also influences the flow behavior.

The zero viscosity allows a quantitative comparison of the material and represents the Newtonian plateau (Ferry, 1980). Unfortunately, the enhancement during the measurement counteracts a terminal behavior in Figure 4.2 (b). Therefore the complex viscosity at angular frequency of $3.15s^{-1}$ was chosen as

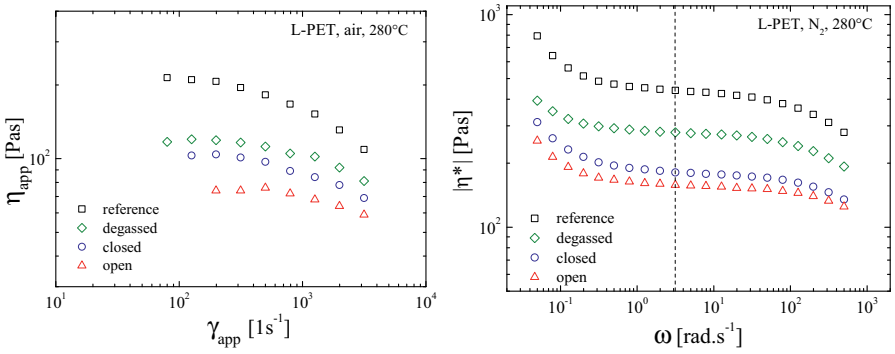

Figure 4.2: Degradation of L-PET extruded analyzed by the apparent steady shear viscosity in air (a) and dynamic shear viscosity in N_2 (b) atmosphere at 280°C.

representative in Figure 4.3 (a), since it is both in sufficient distance to the shear thinning slope and the enhancement at low frequencies. The plotted data reflect the degradation progressed. By degassing, the viscosity decreases to 66% of the initial value (reference). The difference of the extend of degradation between a closed (44%) and an open vent (38%) is small. Although the polymer is without direct contact to air in the filled barrel for several minutes, a molecular reduction and the vertical dilution effect is prominent for all cases, expressed as viscosity drop, and clearly dominates over concurrent polycondensation. Since the oligomers act as plasticizer, the 3.4 power law should be analyzed with care for such degraded PET. As mentioned, the degassing provides additional air and a distinction between thermal and thermo-oxidative decomposition cannot be drawn. The comparison between the degassed system and the closed and open settings indicates a lower degradation for degassing, due to the removal of the side products and residual water molecules. The same behavior can be distinguished from the online measurement of melt pressure, denoted as p_{ext}.

Based on the measured pressure, the apparent melt viscosity during extrusion can be calculated by Equation 3.13, 3.19 and 3.24. The calculation is based on a simplification, assuming a block flow in the transition zone between screw and die, and hence unified flow conditions in the three horizontal capillaries with length of $L = 20mm$. The volumetric throughput can be calculated by the mass throughput and the molar melt volume V_l at $563K$ ($290°C$), which can be achieved by means of the group contribution approach and the Simah

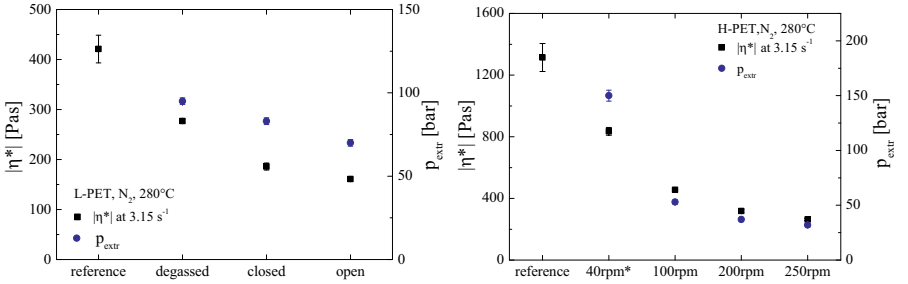

Figure 4.3: Comparison of complex viscosity at $\omega = 3.15s^{-1}$ in nitrogen atmosphere and extrusion pressure at different ventilation on L-PET (a) and different rotational speeds for H-PET (b) at 280°C.

and Boyer model (Simha and Boyer, 1962; van Krevelen, 1976):

$$V_l\,(563) = V_g\,(298) + E_g\,(T_g - 298) + E_l\,(563 - T_g) \tag{4.1}$$
$$= 143.2 + 4.2 \cdot 10^{-2} \cdot 55 + 9.4 \cdot 10^{-2} \cdot 210 \tag{4.2}$$
$$= 165.3 \quad cm^3/mol \tag{4.3}$$

with a molar volume $V_g = 143cm^3.mol^{-1}$ at $298K$ of an amorphous PET and a molar thermal expansivity E_g and E_l in the glassy and liquid state in $cm^3.molK^{-1}$. With a mean $T_g = 353K$ and molar mass of the monomer $M_m = 192.2g.mol^{-1}$, the melt density ρ_l at $290°C$ is:

$$\rho_l\,(563) = \frac{M_m}{V_l(298)} = 1.163 \quad kg/cm^3 \tag{4.4}$$

and the volumetric throughput is $Q = 1.075cm^3.min^{-1}$, as a sum of the three outlets. Taking into account that the actual flow is not a block profile, the flow in the die possesses shear thinning behavior and the extrusion temperature is $10°C$ higher than in Figure 4.2 (a), the results in Table 4.1 for L-PET are in reasonable agreement with the viscosity at the corresponding shear rates from the capillary rheometer.

Badia et al. (2009) repeatedly extruded virgin PET by a twin screw extruder and found an increase of fluidity with each extrusion. After the fifth extrusion the material was too brittle to allow probing in solid state. Likely Assadi et al. found a limit of four extrusion cycles, but besides scission, they found a vast gelling of the polymer, inhibiting a further processing. Different to Badia et al., they used post consumer PET which is known to have impurities as PVC residuals (Scheirs, 1998). Compared to the present long residence time and

Table 4.1: Online apparent shear rate, shear stress and viscosities during extrusion at 290°C for L-PET and H-PET using two different dies calculated from online pressure measurements.

	$\dot{\gamma}_{ext}$ $[s^{-1}]$	p_{ext} $[bar]$	τ_{ext} $[Pa]$	η_{ext} $[Pas]$
	L-PET (1mm die)			
degassed	1013	95±2	39600	39.0
closed	1013	83±2	34600	34.1
open	1013	70±2	29100	28.7
	H-PET (1.4mm die)			
40rpm*	768	> 150	87500	113.9
100rpm	369	53±2	30900	83.7
200rpm	369	37±2	21600	58.4
250rpm	369	32±2	18700	50.5

omitting of inert conditions, the degradation is in common scope. An effect of gelation on the extrusion could not be observed.

The apparent extrusion shear rate of $1013s^{-1}$, based on a die diameter of $1mm$, is in an order of magnitude which can induce shear degradation. The following chain extended PETs were produced with a $1.4mm$ die to be suitable for higher viscosities. This decreases the absolute pressure value and the shear rate to $369s^{-1}$, as can be seen by the right columns in Table 4.1. However, during extrusion the shear degradation in the die is less severe than caused mechanical degradation by the screw flights.

4.2.2 Shear Degradation

Janssen (1998) described the interaction of processing parameters presented in Figure 4.4. Although the scheme is to demonstrate the correlations in reactive processing, it can be used to elucidate degradation effects.

The contribution from the screw revolution rate to shear degradation originates from higher mechanical energy introduction by shearing the molecules at the wall and by the intermeshing of the screw flights. A second direct consequence results from locally increased temperature. An enhanced friction contribution at the flights and the barrel leads to a thermal decomposition, in particular, at large scale extrusion (Janssen, 1998). The effect inside the die is neglected for the present analysis, since the throughput is constant for 100, 200 and $250rpm$ and a constant shear rate is given for the same diameter.

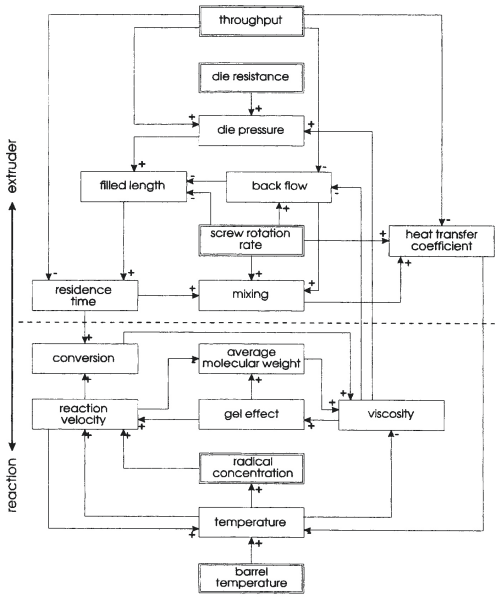

Figure 4.4: Sketch of extrusion interaction from Janssen (1998).

As denoted in Figure 4.3 (b), the complex viscosity and online pressure decreases with higher rotational speed. The reliability of angular frequency $3.15s^{-1}$ as representative for a zero-shear viscosity was analyzed by a comparison. A master curve, based on the method presented in Section 3.4.1 for pure H-PET pellets (non compression molded in N_2 atmosphere, not presented), leads to a zero-shear viscosity of $1280Pas$ at $280°C$ and agrees with the reference presented in the diagram ($1310Pas$). The results at $40rpm$ need to be analyzed with care, since they were conducted with a throughput of $2.6kg.h^{-1}$ and a vacuum pump. With this setting, the combination of the high viscosity of H-PET and an increased filling allows a pure degassing at the vent, without an additional air stream. The negative effect of the setting is an overfeeding of the barrel, which leads to unstable processing conditions. Further, the pressure transducer reached its maximum and froze at $150bar$. The plotted extrusion value can only be taken as qualitatively. Although this setting ensures excellent condition to avoid degradation (low rpm and vacuum), a significant decrease in the complex viscosity is depicted in Figure 4.3 (b). An expected compensation by a transesterification does not occur. This confirms the observed lower molar mass enhancement by a restricted diffusion, as in the case of enlarged sample rim in Chapter 3.3.3. Despite the applied vacuum, the side products cannot evaporate in the *sealed* filled barrel and a balance between polycondensation and reversible reaction emerges. The extend of this nearly non thermal-oxidative

degradation is comparable to the L-PET reduction at thermo-oxidative conditions with the degassing setting (64% vs. 66%). Further, by comparing the degradation of $100rpm$ with the same L-PET setting (open) from the tests with various atmospheres, a similar reduction of H-PET and L-PET can be observed (35% vs. 38%). Poly(ethylene terephthalate) with high viscosity degrades to the same extend as low viscous PET during processing. Since the degradation effect in the rheometer experiment was more pronounced on H-PET, it can be concluded that the degradation induced by mechanical energy and local temperature plays a crucial role. Besides the *plasticizer effect*, the impact of molar mass reduction or a narrowing of polydispersity is gained, as can be inferred from the changed shear thinning behavior. Unfortunately, no published melt viscosity reduction could be found on the impact on PET extrusion. Cardi et al. (1993) reported a reduction of the intrinsic viscosity of 9% on virgin and recycled PET in a single screw extruder during $3min$ under nitrogen. Applying such a reduction on the IV of the present H-PET, would lead to a decrease of the M_v by 14% from $63.6kg.mol^{-1}$to $54.7kg.mol^{-1}$. By applying the 3.4 power law, an assumed zero viscosity of $1310Pas$ would be reduced to 60% ($790Pas$). As mentioned before, the power law has to be analyzed with care of degraded PET, since an extra contribution to the reduction is expected by oligomers. However, the reduction is even larger than the observed reduction with degassing system in this study, although the residence time is longer.

The die radius of $1.4mm$ for H-PET was adjusted to handle an increased viscosity of chain extended material. This compensates the higher flow resistance of H-PET and consequently the shear stress is in the same order of magnitude for both grades, as can be seen in Table 4.1. The observed comparable degradation of the L-PET (open) and H-PET at $100rpm$ is independent of the a shear degradation inside the die, it occurs already inside the barrel.

A further contribution, to the enhanced degradation with respect to rotational speed, can emerge from stronger mixing of melt and oxygen. The screw in the conveying zone is less filled due to the higher rate, and the stirring effect is enhanced. Additionally, a shear induced reaction can participate in an oxidative degradation (Colin and Verdu, 2006). However, the degradation process is not solely initiated be external excitation, e.g. oxygen and temperature, but also from intrinsic properties, as the occurring of side products. Different stabilizers are known to suppress the thermal degradation and the emerge of acetaldehyde (Awaja and Pavel, 2005). Antioxidants inhibiting an auto-accelerated decomposition by hydroperoxide (Colin and Verdu, 2006). The amount of contained stabilizers for the present grades is not known. The hydrolysis effect was minimized by the drying but still influences the processing. Since the feeding of dried pellets last up to $30min$, surface moisture can depose in the hopper. Also the environmental air supplies water which makes the hydrolysis a determining aspect.

Based on the results, a rotational speed of $100rpm$ were chosen for the reactive processing, since it enables a thoroughly mixing, high throughput by large filled length and minimum of degradation. Since the effect of the vacuum pump was comparable low, not at least due to the very long drying period, and not applicable on low viscous grades, no degassing system was applied. A second reason for the open setting is the processing of a chain extender, which needed to be added in the melt state, due to its different properties, which will be introduced in the next section.

4.3 Reactive Processing of PET

Reactive extrusion of PET is employed to either compound impact modifiers or, as in this study, to induce long and branched molecules. To achieve a LCB structure, multifunctional chain extenders were chosen which possess different reactivity with regards to the end groups of the PET backbone. A stable reaction is a fundamental task for a successful chain extending and depends on the chain extender reaction, the conversion and the filled length of the co-rotating extruder (Janssen, 1998) (cf. Figure 4.4).

4.3.1 Chain Extenders

The main requirement of an additive, acting as coupling agent, is the reactivity. Actually, any molecule with at least two functional end groups can be used as chain extender. However, the generation of undesirable side products limits the choice.

A second restriction is the reactivity of the polymer chain. The end groups of PET consist of either a carboxyl or hydroxyl group, which reduces the amount of possible chain extender. Common chain extenders for polyesters are cyclic anhydride (Incarnato et al., 2000; Daver et al., 2008), epoxide (Bikiaris and Karayannidis, 1995, 1996), oxazoline (Karayannidis and Psalida, 2000; Inata and Matsumura, 1985, 1986, 1987), and isocyanate (Raffa et al., 2012; Zhang et al., 2009) based molecules.

Pyromellitic Dianhydride (PMDA)
The tetra-functional pyromellitic dianhydride was chosen to form LCB molecules. The PMDA used was supplied by *abcr* (Germany) as white powder. The melting point is at $\approx 286°C$ and the molar mass is $218 g.mol^{-1}$. As seen in Figure 4.5, the alcohol end group of the PET reacts with the chain extender (Awaja et al., 2004) and leads to possible water molecules. A transesterfication should be also considered, which is independent of the PET end groups (Incarnato et al., 2000). The applied concentration published varies between $0.08 wt.\%$ and

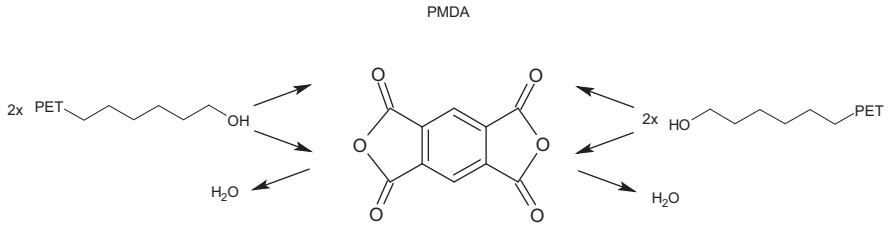

Figure 4.5: Tetra-functional chain extender PMDA reacting with four hydroxyl end groups of PET would lead to two water molecules.

Table 4.2: Stoichiometric chain extender concentrations in weight percentage for one chain extender reacting with four or three PET molecules, respectively.

	PMDA	TGDDM	TPP
Functionality	4	4	3
Preferred reactant	OH	COOH	both
	Concentration [wt.%]		
H-PET	0.21	0.26	0.65
L-PET	0.33	0.29	0.91
l-PET	0.36	0.26	0.95

1.00$wt.\%$ (Daver et al., 2008; Coccorullo et al., 2009; Incarnato et al., 2000). In particular, the optimum of PMDA concentration added were different, with respect to a maximum in viscosity or molar mass without gelation. Depending on the grade or the processing conditions, the maximum concentration was found at 0.3$wt\%$ (Härth et al., 2015) in a lab-extruder under nitrogen. The same concentration resulted in gelation conducted by industrial scale experiments under air (Daver et al., 2008). However, Incarnato et al. (2000), for example, were able to add 0.5$wt.\%$ without gelling.

The stoichiometric concentration can be calculated by the number-average molar mass, functionality of chain extender and the preferred end group. In Table 4.2 the theoretical concentration is depicted by assuming a reaction of one chain extender with four PET chains. If the tetra-functional coupling agents react only with two chains, the twofold concentration would be necessary.

The calculation assumes that the molar mass is not affected by degradation during processing. Since a reduction of molar mass and a change of end groups occurs dynamically, the molar mass of both the neat and extruded PET cannot describe the reaction kinetics sufficiently. Therefore a broad variation of chain

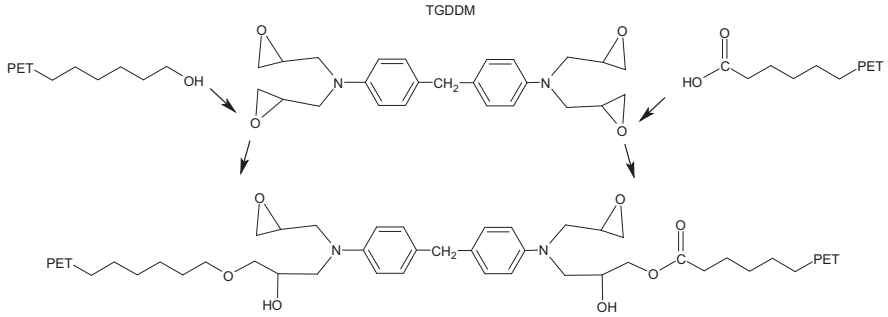

Figure 4.6: Tetra-functional chain extender TGDDM reacting with caboxyl and hydroxyl end groups of PET, e.g. to a linear macromolecule.

extender concentrations were chosen (0.15, 0.3, 0.4, 0.5, 0.65, 0.8, and 1.2$wt.\%$).

Tetraglycidyl Diamino Diphenyl Methane (TGDDM)
The reaction of the epoxy-based tetraglycidyl diamino diphenyl methane (TGDDM) is a polyaddition (Xanthos et al., 2004). The reported stoichiometric values are based on a COOH coupling, since the tetra-functional chain extender possesses higher reactivity with the carboxyl group. Additionally, a coupling with OH is also assumed to occur at long reaction times (Japon et al., 2000a), as it can be seen in Figure 4.6, and even random branching reaction at the backbone should be considered. TGDDM was supplied by *Huntsman* as highly viscous liquid and possesses a molar mass of $422 g.mol^{-1}$. The addition was realized by a heated syringe pump to lower the viscosity and apply a continuous feeding during extrusion. The concentrations were 0.06, 0.12, 0.31, and $0.61 wt.\%$.

Triphenyl Phosphite (TPP)
The tri-functional triphenyl phosphite (TPP) is a condensing agent, which can lead to the separation of phenyl. Figure 4.7 only represents the coupling of the chain ends, but the actual chain extension is rather complex. The reaction is assumed to start with a consumption of OH groups, before a chain extension occurs from the COOH ends. Both are essential for the chain lengthening (Aharoni et al., 1986). The molar mass of the viscous liquid (*abcr*) is $422 g.mol^{-1}$. Based on Table 4.2 and reported concentration up to $2.5 wt.\%$, the applied concentrations were 0.5, 1, 2, and $3 wt.\%$.

To study the concentrations of interest and the adjustment of the extruder setting on more detail, preliminary tests were conducted. The batch experi-

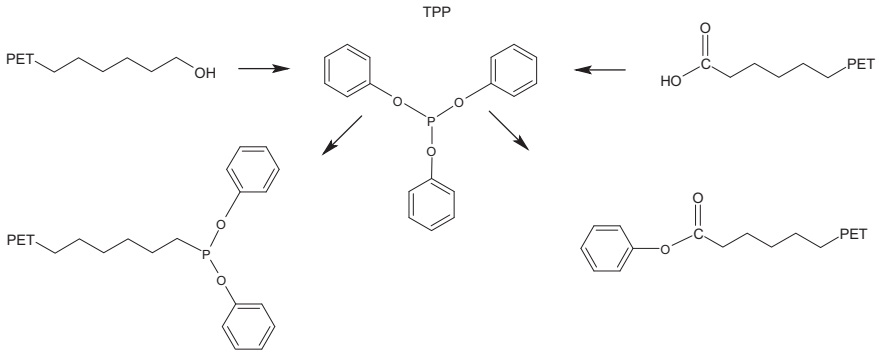

Figure 4.7: Tri-functional chain extender TPP reacting with caboxyl and hydroxyl end groups of PET.

ments give an insight into the reaction kinetics, thus giving guidelines for the continuous reactive extrusion.

4.3.2 Preliminary Results

The experiments were conducted on a *Brabender PL2000* internal batch mixer with a heating chamber of $60cm^2$, two rotors and a torque transducer. Besides the torque, the melt temperature was recorded. The applied temperature was $270°C$ and the rotational speed $60rpm$. This setting was verified by variations betwen $255°C$ and $285°C$, and $40rpm$ and $80rpm$. The load was $30g$ for PMDA and $36g$ for TGDDM and TPP, which increases the torque response. At least three trials were conducted for PMDA and TPP and two for TGDDM. The torque measured by the kneader can be seen as simplified measure of viscosity, as long as different effects during the measurement are considered, e.g. temperature and shear rate changes.

As seen in Figure 4.8 (a), after adding the neat PET the solid granules start to melt and stick to the rotor, reflected by a sharp increase (not fully displayed) and subsequent decrease. The level of torque can be correlated with the molar mass from H-PET to l-PET. A continuous reduction can be noted and attributed to the thermo-oxidative degradation.

The kneader promotes the degradation effect, since it stirs air into the melt. To recall, the low viscosity is not only an effect of lower molar mass generated by scission, but also of dilution by small molecules. A slipping between melt and blade is excluded, since the viscosity and the shear stress is too low and the thermal-oxidative reactions enhance polymer adhesion. The transverse stripped area marks the melting of the polymer. Since a constant degradation

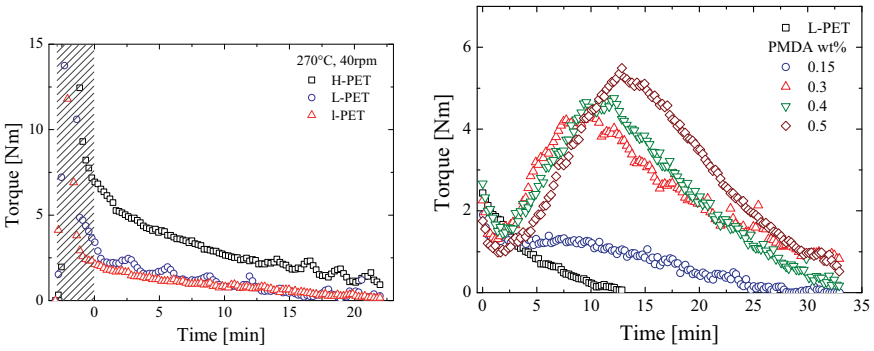

(a) (b)

Figure 4.8: Comparison of torque over time for neat l-, L- and H-PET (a) and for L-PET with different PMDA concentrations (b) at 270°C.

of polymer occurs during kneading, the melt phase (2-4min) was assumed from the change of slopes, denoted as 0min.

Pyromellitic Dianhydride (PMDA)
The addition of PMDA to the PET grades investigated lead to an increase of torque depending on the chain extender concentration. Figure 4.8 (b) shows at first a reduction of L-PET due to melting and degradation, which is counteracted subsequently by the chain extender from 2min. 0.15$wt.\%$ PMDA lead to a compensation of the degradation effect before the degradation prevails, as can be distinguished by the reference. Concentrations of 0.3, 0.4, and 0.5$wt.\%$ PMDA lead to a drastic increase of torque, followed by a maximum at around 7.5 to 12min and a continuous reduction. The linear difference between the peak level reflects a remaining reactive potential for higher concentrations. The slope of the graphs indicate no difference in reaction rate. The shift to longer reaction times with higher concentration, as was also observed by Incarnato et al. (2000), is assumed to originate from the feeding of the powder. Since the hopper of the chamber is small, the PMDA added remains at first at the surface and tends to phase separation. This poor and delayed dispersion inhibits also the application of 1$wt\%$. Therefore, the feeding during extrusion was conducted permanently and the metering zone was set to 290°C, ensuring PMDA to be above melting temperature.

Tetraglycidyl Diamino Diphenyl Methane (TGDDM)
The results of TGDDM in Figure 4.9 illustrate a chain extension by an increase of melt resistance, which depends on the concentration of the additive. l-, L- and H-PET in (a), (b) and (c) possesses a higher reaction rate as a result of

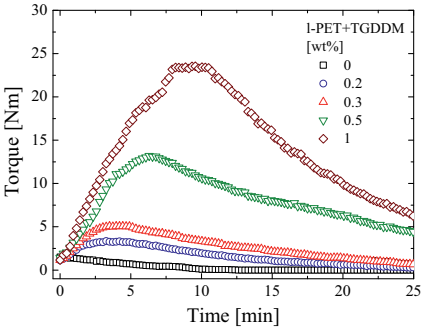

(a)

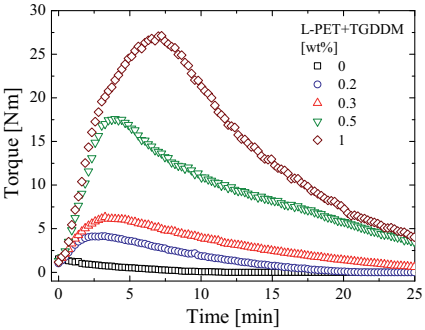

(b)

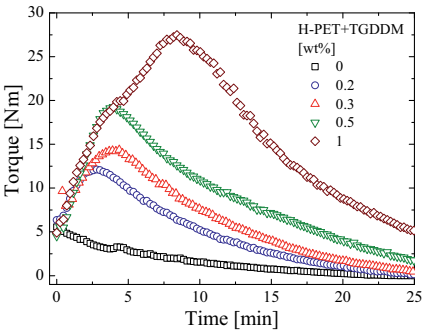

(c)

Figure 4.9: Comparison of l-, L- and H-PET in torque rheometer (a) and L-PET with different TGDDM concentrations (b) at 270°C.

higher chain extender concentration, as reflected by the variations of the slope. The slope indicates also a faster reaction for H- and L-PET which have a higher carboxyl concentration. From the graph of $1wt.\%$ in all plots, a second reaction starting at $5min$, can be noticed. Possible sources are a delayed homopolymerization of the chain extender (Japon et al., 2000b), and a reaction of OH groups or newly emerged COOH groups, from the degradation process with remaining chain extenders at longer mixing times. The maximum are between 4 and $6min$ neglecting the highest concentration. The absolute increase in melt resistance corresponds to the initial molar mass and the carboxyl group concentration. Comparing each concentration in Figure 4.9 (a), (b), and (c), H-PET has the highest and l-PET the lowest response. However, the reduced enhancement, with respect to the initial value, is for H-PET the lowest (factor 3.5) and for L-PET (factor 11) the highest at $0.5wt\%$. l-PET increases by factor 8.5, although it has a low potential due to the lower COOH concentration compared to the other grades.

Triphenyl Phosphite (TPP)
Figure 4.10 (a), (b) and (c) illustrate the torque rheometer diagrams of l-, L- and H-PET. The compounding of PET with TPP leads to an increased torque with higher concentration of TPP by a concurrent increase of reaction rate. Again, the reaction rate is the highest for H-PET. The prediction of the reaction kinetic assumes at first OH consumption, which would be terminated at first for H-PET, followed by the chain lengthening by thermal excitation (Aharoni et al., 1986). By examining the temperature dependence during the reaction, as depicted in Figure 4.10 (d), an almost similar curve compared to the torque can be noted. From the reference measurement it can be seen that the melt temperature is higher than the temperature measured at the chamber housing ($270°C$). The control of temperature leads to a sinusoidal graph which is also reflected as viscosity/temperature dependence in the torque signal. Since the temperature curve of the reference is horizontal, the increase of the chain extended samples originates either from an exothermic reaction, or a higher dissipation contribution due to extended molecules. The chain coupling via TPP is a condensation reaction, and side products are generated during reaction. This implies that these products need to be removed to prevent a reversible reaction. Indeed, the side products evaporate during processing, leading to highly toxic steam consisting of different phosphite derivatives. As can be seen in Figure 4.10, a higher TPP concentration leads not only to higher enhancement, but also a more intense degradation during processing. Tests on samples produced show a strong reduction of viscosity within a few days, which is even faster during drying at $130°C$. Due to the toxicity and unstable behavior, no further reactive extrusion experiments with TPP were conducted.

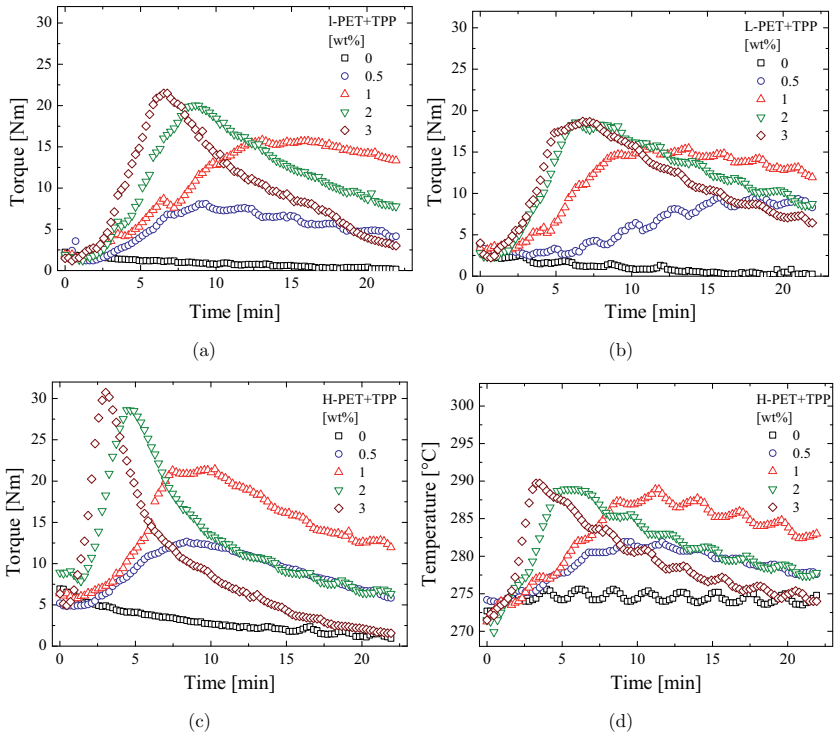

Figure 4.10: Comparison of l-, L- and H-PET in torque rheometer (a), (b), and (c) and the temperature evolution of H-PET with different TPP concentrations (d) at 270°C.

The impact of rotational speed was probed on all chain extenders. The speed of 40rpm leads to a slower reaction than 60 and 80rpm, which possessed negligible differences in conversion rate. This shows that the efficiency of reaction depends on the mixing to a certain maximum. Besides an expected coupling between the agent and main chain, a homopolymerization of the chain extender needs to be taken into account (Japon et al., 2000a). A higher functionality and cross-linking tendency would emerge, which makes the dispersion of the additive a crucial necessity.

4.3.3 Chain Extension with Twin Screw Extruder

PMDA and TGDDM were added continuously at extruder zone 4, ensuring melt state for all materials. As shown by the batch experiments, a thorough, but also moderate mixing facilitates the reaction and therefore a rotational speed

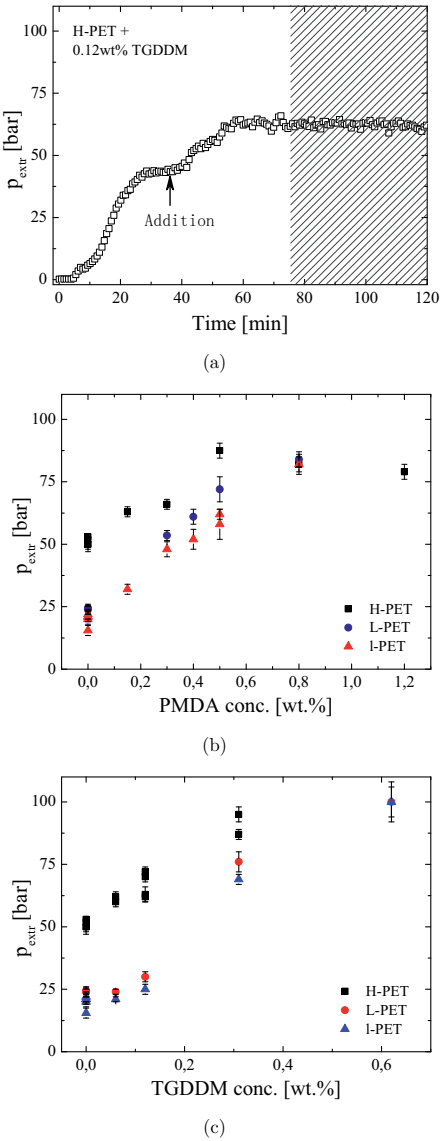

Figure 4.11: Extruder pressure vs. time for H-PET and addition of $0.12wt\%$ of TGDDM at approximately $40min$ (a) and extruder pressure of different PMDA (b) and TGDDM (c) concentrations.

of $100rpm$ was chosen. This ensures a sufficient mixing and conversion, due to a residence time of $8{:}30min$ (Xanthos et al., 2004) (cf. Figure 4.4). The applied reaction time is inferred from the results obtained from the torque rheometer. It was chosen to conduct equal processing conditions for both coupling agents. Since the processing conditions of the extruder and batch mixer differ, a direct comparison of the operation parameter is not possible.

In Figure 4.11 (a) a reactive extrusion of H-PET with $0.12wt.\%$ TGDDM is illustrated. The first increase reflects the filling of the extruder, and the first plateau the approach of steady processing conditions of neat material. Subsequently the chain extender is added, resulting in a further increase of the online pressure. The second steady plateau shows the successful reactive extrusion, which originates from the increased viscosity of the reacted material, which is used for further investigations (transverse striped). The average of the processing pressure as a function of chain extender content can be seen by Figure 4.11 (b) for PMDA and Figure 4.11 (c) for TGDDM. The error bars reflect the plateau scattering seen in Figure 4.11 (a). All grades possess a linear increase of extrusion pressure depending on the chain extender concentration. For PMDA, a plateau or even a reduction starts from $0.5wt.\%$, and at $0.8wt.\%$ all grades overlap in a single point. Such a plateau or an approach to a single melt pressure, regardless of the PET grade, cannot be observed for TGDDM. The addition of $0.62wt.\%$ TGDDM led to a highly elastic material, which could not be removed, and led to a blockage of the extruder conveying. This grade is not considered further. The occurrence of stable processing conditions is a slow process, as can be seen in Figure 4.11 (a). In particular, industrial scale processing needs to avoid disturbances which could result in thermal, hydrodynamic or chemical instabilities. Therefore, temperature, pressure and flow rate are the variables that need to be controlled. Unfortunately, as found in Section 4.3.2, the exothermic reaction and higher dissipation energy lead to an increase of melt temperature. This was also seen by the extruder experiments, by an increase of the barrel temperature to $320°C$, depending on chain extender concentration. Since a strong degradation was obtained, an additional cooling device improved the processing. The graphs display only produced materials which were investigated by rheological tests.

DSC measurements on chain extended samples reveal a constant glass transition temperature and almost constant melt temperature, which was slightly affected by degradation products.

Based on the online pressure and a constant shear rate, the apparent viscosity for all PET with $0.8wt\%$ PMDA, as calculated in Chapter 3.3.1, is around $130Pas$ from an initial viscosity of 81, 38, and $31Pas$ for the H-, L-, and l-PET, respectively. This seems to be a fair increase for the two low molar mass materials, but the high molar mass H-PET is less than two times higher. Especially by realizing the vast reduction during processing, the enhancement

seems to be small. However, since the extrusion shear rate is in the shear thinning regime, the viscosity needs to be analyzed over a wide shear rate and angular frequency spectrum, respectively.

4.4 Conclusion

The results of extruded H-PET and L-PET with variations of the vent setting and mechanical induced shearing exhibit a dominating degradation regardless of the extruder setting. Even with a degassing and thorough drying, an occurring polycondensation inside the filled barrel is in balance with the reversible reaction, and no increase of viscosity can be expected. However, if oligomeric side products would be removed, e.g. by fractionation, higher viscosity and melt strength can be expected.

Degradation without degassing leads to around 40% of the initial viscosity. Besides an dilution of oligomeric side products (plasticizer effect), a strong influence of mechanical induced degradation accompanied by a locally increased temperature was observed. This was reflected by changes of the shear thinning behavior, which originates in either a molar mass reduction or in narrowing of polydispersity. The main degradation mechanism was identified as a consequence of shearing. The impact of thermo-oxidative degradation is comparable small to shear and pure thermal contributions. This emphasizes the need of a twin screw extruder with moderate shear conditions, which is known to induce less energy into the material compared to a single screw extruder.

The reactive processing was preliminary conducted in a torque rheometer. The batch experiment revealed a dependence of the chain extender employed and the corresponding PET end group reactivity, which leads to the conclusion that a tailored dose is necessary for PET and chain extender combinations.

However, the three PET grades show a successful increase of viscosity with pyromellitic dianhydride (PMDA) and tetraglycidyl diamino diphenyl methane (TGDDM). This was confirmed by reactive extrusion with the twin-screw extruder, and an online measurement of an increasing and stable pressure. From the batch experiments it was found that triphenyl phosphite (TPP) is not a useful chain extender due to rapid degradation and toxicity.

5 Rheological Characterization of Branched PET

The linear viscoelastic behavior of a polymer is controlled by the structure of the chain and is used in this study to analyze the molecular characteristics. The first part of this chapter covers the analysis by means of dynamic shear rheology. Due to different applied temperatures, a wide range of the storage and loss modulus, complex viscosity and phase angle allows a precise study of molar mass, molar mass distribution and branching. Further, the non-linear behavior gives a deeper and secured insight of the molecular architecture, e.g. the long-chain branching (Wagner et al., 2005; Lohse et al., 2002). Finally, the experimentally determined linear behavior and the non-linear behavior are modeled by a constitutive equation. The molecular stretch function model considers the orientation and the stretch of the molecule, which is expressed by the parameter f^2_{max}. The branching of the molecule is represented by β (Wagner et al., 2004), and correlations between intrinsic molecular features and the macroscopic material response can be shown.

5.1 Linear Viscoelasticity

The linear viscoelastic characterization is widely used in polymer science and can lead to information about the molecular topology (Wood-Adams et al., 2000). It was shown that based on G' and G'', prediction of the molar mass distribution can be achieved (Van Ruymbeke et al., 2002; Kheirandish, 2005). The analysis of the loss angle leads to an insight of the branched (Trinkle and Friedrich, 2001; Rolón-Garrido, 2014) and gel-like content (Winter and Chambon, 1986; Chambon and Winter, 1987; Rolón-Garrido, 2014).

5.1.1 Dynamic Moduli and Viscosity

The master curves of the storage and loss modulus shifted to a reference temperature $265°C$ can be seen in Figure 5.1 for all PET grades and four different concentrations of PMDA. The well overlapped data measured at four different temperatures demonstrate the superposition, and the solid line represents the calculated generalized Maxwell model. Due to either condensation reaction or

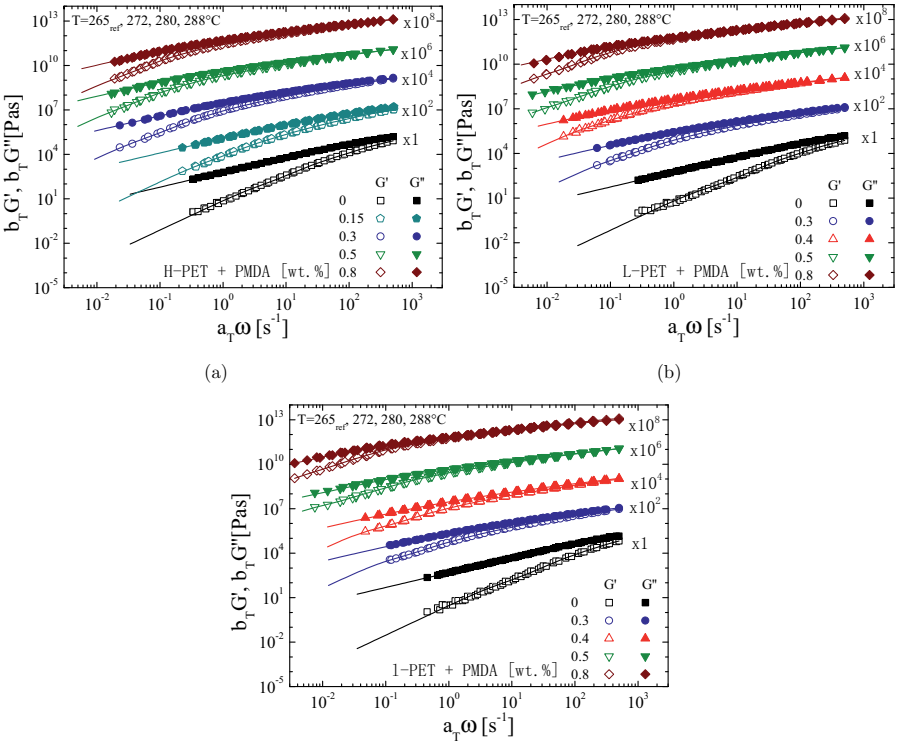

Figure 5.1: Comparison of time-temperature superposition of storage and loss modulus and calculations from general Maxwell model for H-PET (a), L-PET (b) and l-PET (c) with different concentrations of PMDA.

thermal degradation, differing data were discarded following the procedure described in Section 3.4. This is reflected by the predictions which expand to lower frequencies compared to the measured values. For the sake of clarity, the data of each concentration is shifted by a factor. All graphs include a processed reference data set (0%) and 0.3, 0.5, and 0.8$wt.$%. Additionally, 0.15$wt.$% PMDA was added to H-PET Figure 5.1 (a), and 0.4$wt.$% to L-PET Figure 5.1 (b) and l-PET Figure 5.1 (c), respectively. All grades exhibit a flattening of G' and G'' with increasing chain extender content. The onset to the terminal regime is shifted to lower frequencies and the approach is outside of the experimental window. Consequently, the cross-point of the moduli vanishes into a tapered narrowing over a long frequency range. Especially the two highest concentrations in each graph exhibit a gel-like behavior at short relaxation times, which is indicated by parallel moduli (Chambon and Winter, 1987). This behavior can be attributed mostly to the increasing storage moduli, due to higher entropic elasticity from a chain lengthening. Although branching should be included into the consideration, a clear distinction cannot be drawn, since possible broadening of the MMD and increase of molar mass influence the moduli and inhibits a straight forward analysis of G' and G''.

The effect of 0.06, 0.12, and 0.31$wt.$% TGDDM added to H-PET in Figure 5.2 (a) and l-PET in Figure 5.2 (b) is qualitatively similar to the chain extending with PMDA. Nevertheless, the parallel evolution for 0.31$wt.$% is observed for both grades and more prominent compared to the samples with PMDA. Consequently, the predicted transition to a terminal regime at low frequencies is speculative for 0.31$wt.$% TGDDM. Additionally, the difference between the extent of prediction and the non-discarded data are larger for TGDDM than for PMDA. This is due to a stronger ongoing reaction during the dynamic measurement, as was already observed from high reactivity during the batch test reported in Section 4.3.2. Both moduli increase with chain extender concentration, but the increased molar mass leads to a more pronounced elastic response (cf. Section 5.1.3) and a higher complex relaxation modulus (cf. Equation 2.68).

The calculated discrete relaxation modes, shift factors, zero-shear viscosity, and activation energy of flow are reported in the Table 5.1, 5.2, and 5.3.

A more lucid comparison of the chain extended PET data is given by plotting the master curve of the complex viscosity. The efficient application of chain extender can be noted in Figure 5.3 (a) for H-PET. With increasing PMDA concentration both the shear thinning behavior and the Newtonian plateau increase in a similar way, as was observed for neat PET due to an enhancement of molar mass during the measurement in Section 3.3.3. All graphs converge at high frequencies, reflecting the same chemical consistency. The largest contribution to an increased zero-shear viscosity originates from the molar mass

Table 5.1: Discrete relaxation moduli and times, zero viscosity at reference temperature $265°C$, flow activation energy and shift factors for 272, 280, and $288°C$ of chain extended H-PET.

H-PET with 0%		0.06% TGDDM		0.12% TGDDM		0.12% TGDDM	
$\eta_0 = 616 Pas$		$\eta_0 = 1207 Pas$		$\eta_0 = 3354 Pas$		$\eta_0 = 21866 Pas$	
$g_i(Pa)$	$\lambda_i(s)$	$g_i(Pa)$	$\lambda_i(s)$	$g_i(Pa)$	$\lambda_i(s)$	$g_i(Pa)$	$\lambda_i(s)$
5.29×10^5	5.57×10^{-4}	6.05×10^5	4.80×10^{-4}	5.04×10^5	6.97×10^{-4}	4.10×10^6	3.51×10^{-5}
4.80×10^4	4.32×10^{-3}	7.23×10^4	3.87×10^{-3}	6.52×10^4	6.17×10^{-3}	1.07×10^5	2.28×10^{-3}
3.87×10^6	2.46×10^{-2}	1.41×10^4	1.67×10^{-2}	1.57×10^4	3.22×10^{-2}	3.09×10^4	1.05×10^{-2}
4.42×10^4	3.1×10^{-1}	3.06×10^3	6.78×10^{-2}	4.00×10^3	1.54×10^{-1}	1.39×10^4	4.21×10^{-2}
	4.57×10^2	3.03×10^{-1}	9.02×10^2	7.59×10^-1	5.25×10^3	1.73×10^{-1}	
	2.40×10^1	2.35×10^0	1.44×10^2	5.59×10^0	2.23×10^3	6.33×10^{-1}	
						1.09×10^3	2.27×10^0
						4.28×10^2	7.34×10^0
						2.01×10^2	4.79×10^1
$E_A = 44.3 kJ.mol^{-1}K^{-1}$		$E_A = 63.1 kJ.mol^{-1}K^{-1}$		$E_A = 111.5 kJ.mol^{-1}K^{-1}$		$E_A = 254.1 kJ.mol^{-1}K^{-1}$	
$loga_T(-)$	$logb_T(-)$	$loga_T(-)$	$logb_T(-)$	$loga_T(-)$	$logb_T(-)$	$loga_T(-)$	$logb_T(-)$
-0.093	-0.058	-0.250	-0.094	-0.273	-0.112	-0.149	-0.031
-0.173	-0.064	-0.250	-0.030	-0.434	-0.150	-0.430	-0.138
-0.174	-0.057	-0.263	-0.034	-0.360	-0.075	-0.952	-0.372
0.15% PMDA		0.3% PMDA		0.5% PMDA		0.8% PMDA	
$\eta_0 = 1274 Pas$		$\eta_0 = 4100 Pas$		$\eta_0 = 8589 Pas$		$\eta_0 = 10592 Pas$	
$g_i(Pa)$	$\lambda_i(s)$	$g_i(Pa)$	$\lambda_i(s)$	$g_i(Pa)$	$\lambda_i(s)$	$g_i(Pa)$	$\lambda_i(s)$
5.20×10^5	5.30×10^{-4}	3.95×10^5	7.34×10^{-4}	3.42×10^5	6.39×10^{-4}	4.48×10^5	4.61×10^{-4}
6.35×10^4	3.93×10^{-3}	5.98×10^4	6.09×10^{-3}	5.90×10^4	5.10×10^{-3}	6.93×10^4	4.40×10^{-3}
1.57×10^4	1.65×10^{-2}	2.06×10^4	2.85×10^{-2}	2.56×10^4	2.48×10^{-2}	2.96×10^4	2.10×10^{-2}
3.94×10^3	6.26×10^{-2}	6.91×10^3	1.30×10^{-1}	9.77×10^3	1.14×10^{-1}	1.21×10^4	9.35×10^{-2}
6.49×10^2	2.58×10^{-1}	1.81×10^3	5.87×10^{-1}	3.64×10^3	4.94×10^{-1}	5.07×10^3	4.08×10^{-1}
2.15×10^1	1.87×10^0	2.87×10^2	2.46×10^0	1.18×10^3	2.03×10^0	1.78×10^3	1.75×10^0
	6.04×10^0	2.30×10^1	2.27×10^2	7.22×10^0	4.37×10^2	6.41×10^0	
				5.61×10^0	5.15×10^1	6.61×10^0	5.93×10^1
$E_A = 88.7 kJ.mol^{-1}K^{-1}$		$E_A = 179.7 kJ.mol^{-1}K^{-1}$		$E_A = 227.7 kJ.mol^{-1}K^{-1}$		$E_A = 238.5 kJ.mol^{-1}K^{-1}$	
$loga_T(-)$	$logb_T(-)$	$loga_T(-)$	$logb_T(-)$	$loga_T(-)$	$logb_T(-)$	$loga_T(-)$	$logb_T(-)$
0.013	0.019	-0.161	-0.059	-0.419	-0.163	-0.311	-0.137
-0.127	-0.024	-0.487	-0.143	-0.669	-0.279	-0.619	-0.177
-0.343	-0.068	-0.738	-0.250	-1.005	-0.340	-0.940	-0.281

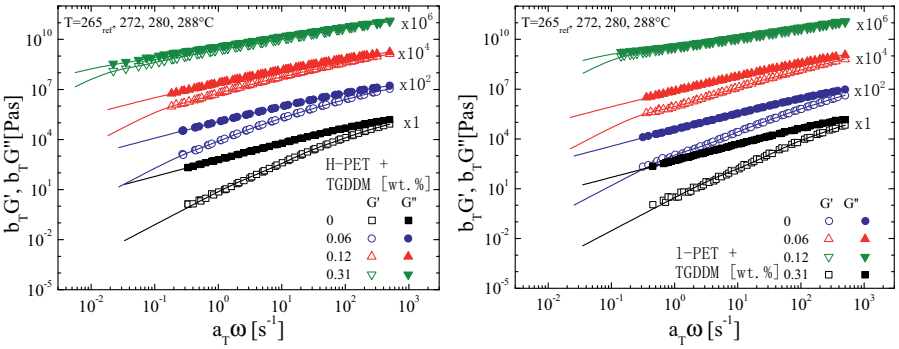

(a) (b)

Figure 5.2: Comparison of time-temperature superposition of storage and loss modulus and calculations from general Maxwell model (solid line) for H-PET (a) and l-PET (b) with different concentrations of TGDDM.

Table 5.2: Discrete relaxation moduli and times, zero viscosity at reference temperature 265°C, flow activation energy and shift factors for 272, 280, and 288°C of chain extended L-PET.

L-PET with 0%		0.06% TGDDM		0.12% TGDDM		0.31% TGDDM	
$\eta_0 = 558 Pas$		-		-		-	
$g_i(Pa)$	$\lambda_i(s)$						
6.62×10^5	4.00×10^{-4}						
6.19×10^4	3.20×10^{-3}						
5.10×10^3	1.67×10^{-2}						
3.70×10^1	3.59×10^{-1}						
$E_A = 55.3 kJ.mol^{-1}K^{-1}$							
$loga_T(-)$	$logb_T(-)$						
-0.063	-						
-0.149	-						
-0.217	-						

0.3% PMDA		0.4% PMDA		0.5% PMDA		0.8% PMDA	
$\eta_0 = 3697 Pas$		$\eta_0 = 9507 Pas$		$\eta_0 = 15118 Pas$		$\eta_0 = 23012 Pas$	
$g_i(Pa)$	$\lambda_i(s)$	$g_i(Pa)$	$\lambda_i(s)$	$g_i(Pa)$	$\lambda_i(s)$	$g_i(Pa)$	$\lambda_i(s)$
4.56×10^5	4.97×10^{-4}	1.78×10^6	9.04×10^{-5}	4.20×10^5	5.22×10^{-4}	4.87×10^5	3.54×10^{-4}
6.22×10^4	4.78×10^{-3}	8.62×10^4	3.39×10^{-3}	6.66×10^4	5.57×10^{-3}	6.74×10^4	5.14×10^{-3}
2.05×10^4	2.25×10^{-2}	2.98×10^4	1.66×10^{-2}	2.72×10^4	2.92×10^{-2}	2.85×10^4	2.95×10^{-2}
7.43×10^3	9.66×10^{-2}	1.29×10^4	6.70×10^{-2}	1.10×10^4	1.50×10^{-1}	1.16×10^4	1.58×10^{-1}
2.24×10^3	4.06×10^{-1}	5.54×10^3	2.74×10^{-1}	4.27×10^3	7.27×10^{-1}	4.91×10^3	8.03×10^{-1}
4.64×10^2	1.60×10^0	2.07×10^3	1.11×10^0	1.48×10^3	3.37×10^0	1.96×10^3	3.86×10^0
3.28×10^1	1.04×10^1	6.04×10^2	4.14×10^0	2.00×10^2	1.36×10^1	4.49×10^2	1.39×10^1
		5.99×10^1	2.33×10^1	1.20×10^1	1.08×10^2	1.47×10^1	1.41×10^2
$E_A = 128.1 kJ.mol^{-1}K^{-1}$		$E_A = 211.7.3 kJ.mol^{-1}K^{-1}$		$E_A = 229.0 kJ.mol^{-1}K^{-1}$		$E_A = 275.6 kJ.mol^{-1}K^{-1}$	
$loga_T(-)$	$logb_T(-)$	$loga_T(-)$	$logb_T(-)$	$loga_T(-)$	$logb_T(-)$	$loga_T(-)$	$logb_T(-)$
-0.118	-0.006	-0.387	-0.133	-0.337	-0.075	-0.367	-0.089
-0.292	-0.061	-0.692	-0.225	-0.596	-0.155	-0.713	-0.194
-0.510	-0.134	-0.841	-0.277	-0.932	-0.255	-1.109	-0.296

Table 5.3: Discrete relaxation moduli and times, zero viscosity at reference temperature $265°C$, flow activation energy and shift factors for 272, 280, and $288°C$ of chain extended l-PET.

l-PET with 0%		0.06% TGDDM		0.12% TGDDM		0.12% TGDDM	
$\eta_0 = 485Pas$		$\eta_0 = 367Pas$		$\eta_0 = 881Pas$		$\eta_0 = 15922Pas$	
$g_i(Pa)$	$\lambda_i(s)$	$g_i(Pa)$	$\lambda_i(s)$	$g_i(Pa)$	$\lambda_i(s)$	$g_i(Pa)$	$\lambda_i(s)$
3.75×10^5	5.72×10^{-4}	5.43×10^6	1.98×10^{-5}	3.93×10^5	6.17×10^{-4}	4.26×10^6	3.41×10^{-5}
7.37×10^4	3.19×10^{-3}	8.00×10^4	1.74×10^{-3}	2.75×10^4	6.52×10^{-3}	9.57×10^4	2.40×10^{-3}
2.63×10^2	1.03×10^{-1}	6.81×10^3	1.03×10^{-2}	4.24×10^3	4.04×10^{-2}	2.37×10^4	1.03×10^{-2}
		6.08×10^2	5.72×10^{-2}	5.19×10^2	5.12×10^{-1}	8.99×10^3	2.78×10^{-2}
		1.84×10^1	8.32×10^{-1}	5.48×10^1	2.93×10^0	6.86×10^3	6.96×10^{-2}
						4.06×10^3	2.46×10^{-1}
						2.30×10^3	1.06×10^0
						1.71×10^3	6.52×10^0
$E_A = 37,1kJ.mol^{-1}K^{-1}$		$E_A = 69.2kJ.mol^{-1}K^{-1}$		$E_A = 89.0kJ.mol^{-1}K^{-1}$		$E_A = 36.7kJ.mol^{-1}K^{-1}$	
$loga_T(-)$	$logb_T(-)$	$loga_T(-)$	$logb_T(-)$	$loga_T(-)$	$logb_T(-)$	$loga_T(-)$	$logb_T(-)$
-0.041	0.024	-0.115	-0.024	-0.144	-0.006	-0.095	0.050
-0.076	0.085	-0.171	-0.024	-0.278	-0.054	-0.147	0.053
-0.153	0.128	-0.289	-0.030	-0.351	-0.048	-0.147	0.189

0.3% PMDA		0.4% PMDA		0.5% PMDA		0.8% PMDA	
$\eta_0 = 2875Pas$		$\eta_0 = 4975Pas$		$\eta_0 = 13806Pas$		$\eta_0 = 34620Pas$	
$g_i(Pa)$	$\lambda_i(s)$	$g_i(Pa)$	$\lambda_i(s)$	$g_i(Pa)$	$\lambda_i(s)$	$g_i(Pa)$	$\lambda_i(s)$
6.07×10^5	2.50×10^{-4}	3.86×10^5	5.01×10^{-4}	3.39×10^5	6.06×10^{-4}	2.82×10^6	4.85×10^{-5}
7.21×10^4	2.79×10^{-2}	5.43×10^4	4.83×10^{-3}	5.57×10^4	5.71×10^{-3}	7.62×10^4	3.82×10^{-3}
2.54×10^4	1.27×10^{-3}	2.00×10^4	2.35×10^{-2}	2.31×10^4	3.03×10^{-2}	3.32×10^4	2.14×10^{-2}
8.97×10^3	6.06×10^{-3}	7.40×10^3	1.14×10^{-1}	8.92×10^3	1.61×10^{-1}	1.39×10^4	1.00×10^{-1}
2.50×10^3	2.79×10^{-1}	2.28×10^3	5.39×10^{-1}	3.27×10^3	8.15×10^{-1}	6.87×10^3	4.39×10^{-1}
4.91×10^2	4.91×10^0	4.84×10^2	2.33×10^0	1.03×10^3	3.83×10^0	3.28×10^3	1.94×10^0
3.97×10^1	9.29×10^0	4.43×10^1	1.93×10^1	1.09×10^2	1.99×10^1	1.56×10^3	8.02×10^0
				1.42×10^1	1.67×10^2	1.79×10^2	3.41×10^1
						1.90×10^1	2.18×10^2
$E_A = 144.1kJ.mol^{-1}K^{-1}$		$E_A = 152.8kJ.mol^{-1}K^{-1}$		$E_A = 245.0kJ.mol^{-1}K^{-1}$		$E_A = 285.8kJ.mol^{-1}K^{-1}$	
$loga_T(-)$	$logb_T(-)$	$loga_T(-)$	$logb_T(-)$	$loga_T(-)$	$logb_T(-)$	$loga_T(-)$	$logb_T(-)$
-0.233	-0.076	-0.231	-0.073	-0.369	-0.152	-0.416	-0.105
-0.332	-0.107	-0.398	-0.129	-0.571	-0.212	-0.792	-0.193
-0.608	-0.193	-0.624	-0.187	-1.022	-0.329	-1.145	-0.300

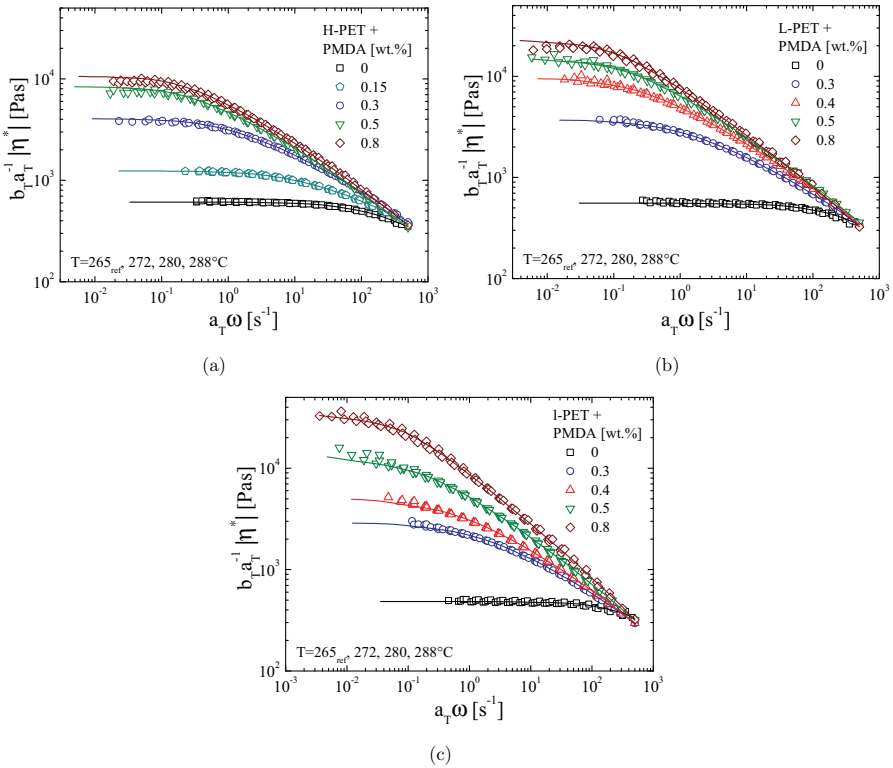

Figure 5.3: Comparison of master curves of complex viscosity and calculations from general Maxwell model (solid line) for H-PET (a), L-PET (b) and l-PET (c) with different concentrations of PMDA.

Table 5.4: End group probabilities and density at $23°C$ for H-, L-, and l-PET.

	H-PET	L-PET	l-PET
	Probability of end group [-]		
OH	0.605	0.695	0.730
COOH	0.395	0.305	0.270
	Probability of end group combination [-]		
OH-OH	0.366	0.483	0.533
COOH-COOH	0.156	0.093	0.073
OH-COOH	0.478	0.424	0.394
Density $\left[g.cm^{-3}\right]$	1.355 $\pm$0.040	1.395 $\pm$0.012	1.401 $\pm$0.018

(Ferry, 1980). However, an extended shear thinning behavior is directly related to an increased entanglement density, which increases with molar mass, MMD and, in particular, LCB (Vega et al., 2002). The difference between $0.5wt.\%$ and $0.8wt.\%$ is small, indicating apparently the approach of a terminated chain extension reaction between PMDA and H-PET. A comparison of 0.3, 0.5 and $0.8wt.\%$ with L-PET Figure 5.3 (b) and l-PET Figure 5.3 (c) illustrates a higher efficiency for higher concentration compared to H-PET. In particular, l-PET shows a substantial increased complex viscosity between $0.5wt.\%$ and $0.8wt.\%$ for PMDA.

These findings correlate with the preferred OH end group reactivity of PMDA and the highest concentration of alcohol groups for l-PET, and lowest for H-PET (Table 5.4), respectively. By comparing the low frequency region of the grades, L-PET and l-PET reveal the highest absolute values of complex viscosity and the Newtonian plateau is not captured fully in the experimental window.

The impact of TGDDM on H-PET (a) and l-PET (b) can be seen in Figure 5.4. The successful reaction can be noticed from the reference and an increased viscosity for $0.06wt.\%$ and $0.12wt.\%$ TGDDM in both graphs, which again merge at high frequencies despite $0.06wt.\%$ added to l-PET. However, the addition of $0.31wt.\%$ TGDDM leads to a vast shear thinning behavior, which can also include a yield stress at low frequencies, in contrast to the prediction illustrated. This effect is largely prominent for l-PET indicating an up-turn, although it possesses the lowest concentration of COOH end group, which should be preferred by TGDDM. This leads to the conclusion that an excess supply of TGDDM leads to cross-linking, which can be supported by a homopolymerization and a subsequently increased functionality. Since the initial end group concentration plays a minor role, the COOH groups, which emerge during processing from degradation, facilitate a reaction with the epoxy based chain ex-

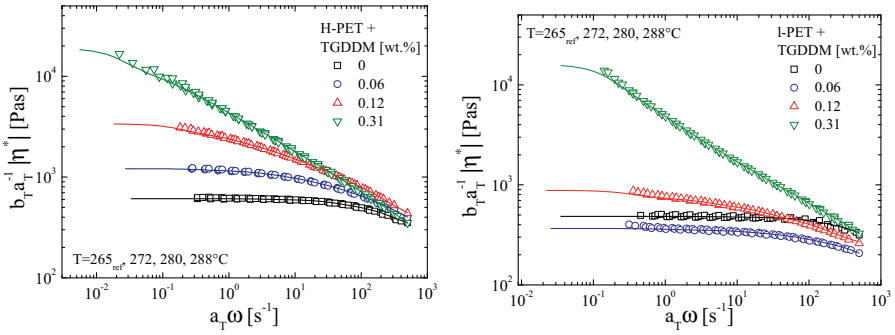

Figure 5.4: Comparison of master curves of complex viscosity and fitting by general Maxwell model (solid line) for H-PET (a) and l-PET (b) with different concentrations of TGDDM.

tender. Further, it should be considered that the high reactive epoxy group leads to bondings at the backbone, due to thermo-oxidative induced radicals. However, the lack of a Newtonian plateau can also originate from the ongoing reaction during the measurement, since the distinction between enhancement, thermal stability and thermal degradation is more sophisticated compared to PMDA. Nevertheless, the linear viscoelastic behavior of the samples with high TGDDM concentrations shows large similarities with hyperbranched PET (Kil et al., 2003).

Both, the increase and flattening of the storage and loss modulus, can be found in the literature for PMDA (Daver et al., 2008; Incarnato et al., 2000; Yilmazer et al., 2000; Forsythe et al., 2006) and TGDDM (Japon et al., 2001). Additionally, the broader shear thinning behavior and convergence at high frequencies of the complex viscosity were found for different molar masses of PET (Rosu et al., 2000; Coccorullo et al., 2009; Härth et al., 2014) and also for polyolefins (Wood-Adams et al., 2000; Lohse et al., 2002).

5.1.2 Zero-Shear Viscosity and Flow Activation Energy

The quantitative comparison of non-Newtonian liquids with different molecular architecture is complicated due to the dependence on flow rate. Therefore, the viscosity at zero-shear rate can be used for a comparison, since it is proportional to a power-law to the molar mass of the molecule (cf. Section 2.3.2). Degradation and the impact on the viscosity is comparable for all PET grades and chain extender combinations examined, since the reactive extrusion process was similar for all samples.

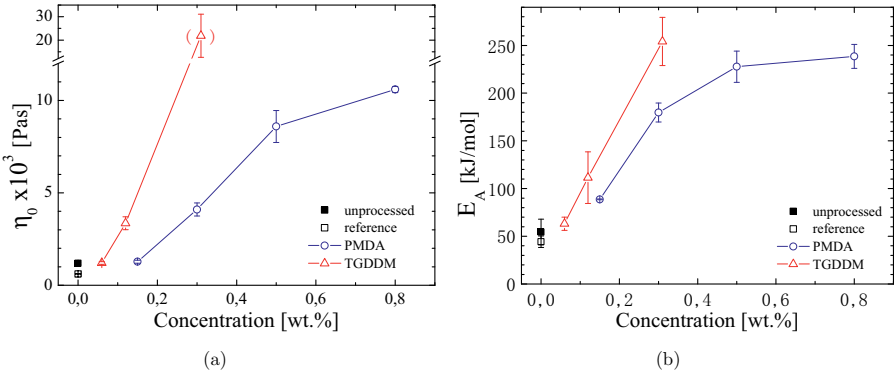

Figure 5.5: Comparison of different concentrations of PMDA and TGDDM by zero-shear viscosity at $265°C$ (a) and flow activation energy (b) for H-PET in nitrogen atmosphere.

The actual measurement of low shear rate behavior is complicated due to physical and thermal stability limitations, but, with the extrapolated predictions (Baumgaertel and Winter, 1989) and a valid Cox-Merz rule (cf. Section 5.2.1), η_0 can be inferred from the dynamic measurements. In Figure 5.5 (a), the reference sample reflects the degradation by extrusion by comparison with the neat unprocessed specimen of H-PET and $0wt.\%$ PMDA. The addition of PMDA leads at first to a compensation of the initial zero-shear viscosity ($0.15wt.\%$), and increases linearly with higher concentrations to an alluded asymptote. The efficiency of TGDDM is also demonstrated. The highest concentration is denoted by parenthesis, since a Newtonian plateau was not observed and the value represents only a tendency (note the interrupted y-axis in Figure 5.5 (a)). An absolute comparison of both chain extender concentrations cannot be conducted by the representation, since the addition depends on the corresponding molar masses[1]. The flow activation energy in 5.5 (b) exhibits a similar trend as η_0, which consists of a sigmoidal shape for PMDA and a gradual increase for TGDDM. The main influence on the activation energy is the friction of the molecule. Since the chemical consistence is almost unaffected, the drastic increase to a fivefold higher E_A is caused by LCB. Large branches are known to affect the flow energy to a larger extent than solely molar mass and MMD (Lohse et al., 2002; van Gurp and Palmen, 1998).

The efficiency of the chain extension is compared in Figure 5.6 for all PET grades and both chain extenders. Figure 5.6 (a) shows an increasing zero-shear viscosity with PMDA concentration. The initial highest viscosity of H-PET

[1]In Section 4.3.1 it was demonstrated that both stoichiometric maximum are around $0.3wt.\%$, with respect to the grade.

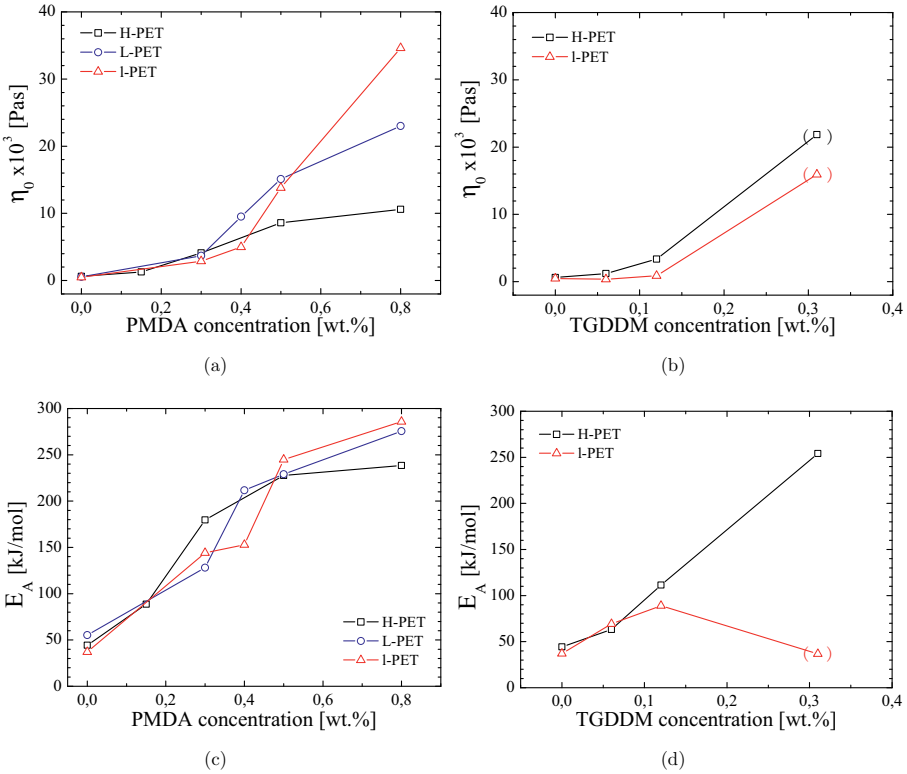

Figure 5.6: Comparison of zero shear viscosity of PMDA (a), TGDDM (b) at $265°C$, and activation energy of flow of PMDA (c) and TGDDM (d) with H-PET, L-PET, and l-PET in nitrogen atmosphere.

is compensated with increasing chain extender addition, and the former lowest molar mass grade, l-PET, exhibits the highest value at 0.8%. As seen, this result agrees directly with the initial OH end group concentration of the three grades investigated. TGDDM in Figure 5.6 (b) reacts preferable with the carboxyl group of the PET molecule, leading to a higher increase for H-PET compared to l-PET. The values at 0.31% are not reliable quantitatively, as discussed. The analysis of the activation energy of PMDA in Figure 5.6 (c) and TGDDM in Figure 5.6 (d) reveals a linear progression with chain extender concentration, despite an observed saturation tendency for H-PET and PMDA. The nearly direct proportional higher flow resistance indicates a branching occurring from the lowest addition of chain extender. Since linear polymers show a constant activation energy regardless of molar mass (Lohse et al., 2002), the increase proofs an ongoing branching. The highest concentration of TGDDM with l-PET should not be included into the discussion. As can be noticed from Figure 5.2, G' and G'' are almost horizontal and overlap. The gel-like behavior leads to a time and temperature invariant response, and the shift factor and the activation energy cannot be determined accurately.

5.1.3 The Loss Angle

The loss angle describes the phase shift between the strain and the stress during an oscillating excitation. The material can be categorized into solid-like or liquid-like. An alternative method was introduced by van Gurp and Palmen, who analyzed the phase shift with respect to the complex modulus (van Gurp and Palmen, 1998). This allows a frequency independent analysis, and a linear monodisperse polymer is represented by a terminal viscous behavior at low modulus and a steep decay of the loss angle at large values of the complex relaxation modulus. In Figure 5.7 such a behavior is depicted by all reference data, which possess a similar polydispersity and therefore the same shape of curve. The decrease at high modulus would continue to a minimum, which reflects the plateau modulus G_N^0, if more data would be available (Trinkle and Friedrich, 2001). A broadening of the molar mass distribution leads to a flattening of the curve as for $0.15wt.\%$ PMDA in Figure 5.7 (a) or for $0.06wt.\%$ TGDDM in Figure 5.7 (d) and Figure 5.7 (e). Since the topology influences both properties, δ and $|G^*|$, a branched structure leads to an even more pronounced flattening, and will lead to an extra bump, if the LCB character dominates the behavior (Trinkle et al., 2002). Schulze et al. (2005) analytically derived classifications of topology from the curve and Lohse et al. (2002) could distinguish between a star and a comb polymer. In simple terms the characterization follows a deflection at high $|G^*|$ near the linear behavior for a star, and a more distant bump at low $|G^*|$ for long comb-like side arms. The present results do not allow a clear distinction, but the observed emerging bump is clearly a second dominating re-

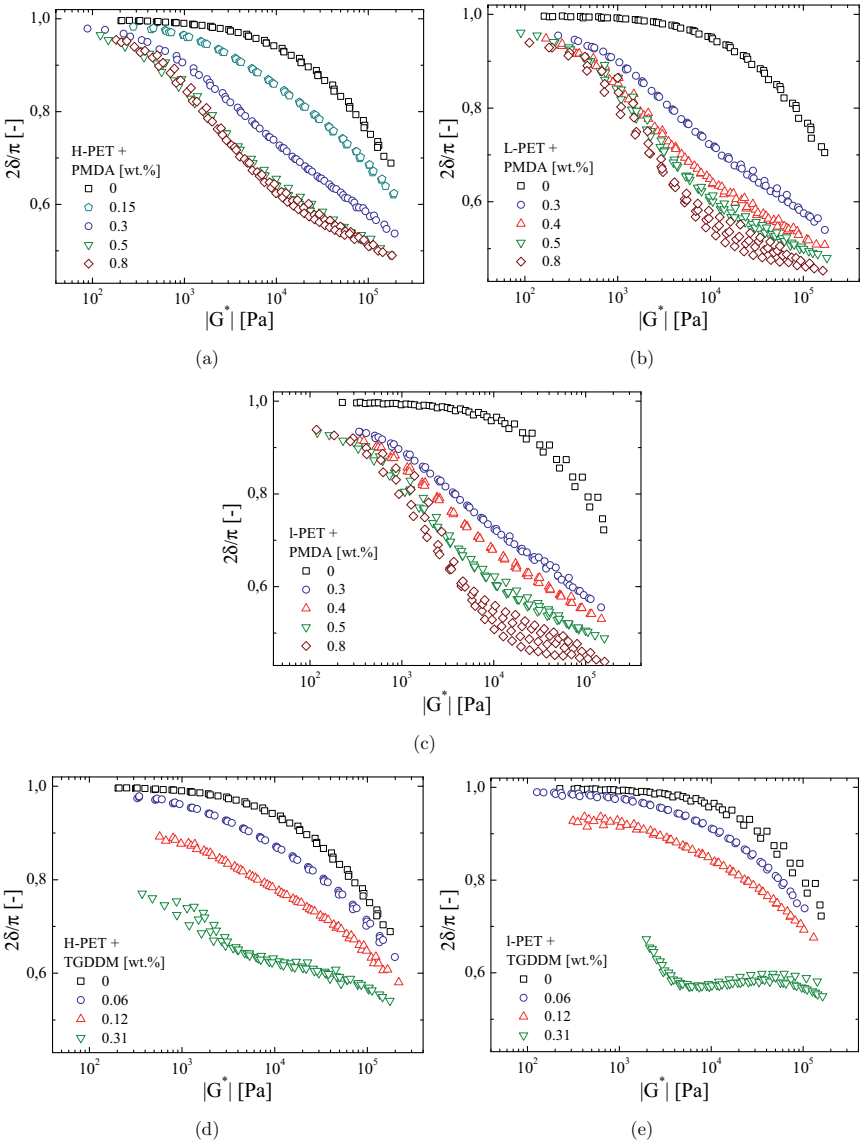

Figure 5.7: Comparison of reduced phase angle and complex relaxation modulus of H-PET, L-PET, and l-PET with different concentrations of PMDA (a), (b), and (c), and H-PET and l-PET with different concentrations of TGDDM (d) and (e).

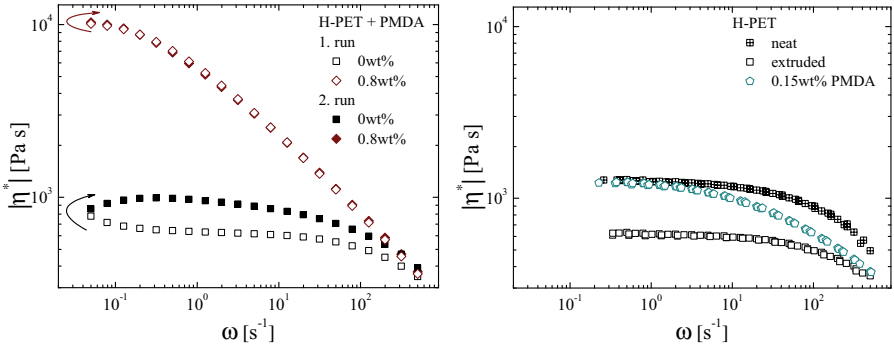

Figure 5.8: Thermal stability demonstrated on H-PET with 0.8*wt.*% PMDA during frequency sweep measurements (a) and compensation of degradation and viscosity loss at low frequencies by PMDA addition (b).

laxation process, which increases with higher concentrations of chain extender. This tendency can be observed for PMDA, where larger side arms of H-PET in 5.7(a) are noticeable at lower modulus. The size of the bump and the adjacent location to the potential maximum of the complex modulus for L-PET (Figure 5.7 (b)) and l-PET (Figure 5.7 (c)), indicates more branches per molecule, which seem to be shorter and more packed. The indication of possible star-like formation cannot be inferred. The graphs representing the highest TGDDM concentration reveal a largely pronounced branching behavior. In particular, the l-PET sample with 0.31*wt.*% in Figure 5.7 (e) shows a large bump which is in reasonable distance to the plateau value, indicating a dominating second relaxation time from large branched side arms (Lohse et al., 2002; Trinkle et al., 2002).

A further feature of the van Gurp-Palmen plot is the analysis of the time-temperature superposition. Since $tan\delta$ is the ratio of loss and storage modulus (cf. Equation 3.8), the temperature shift factors vanish and the graph is temperature invariant. Since the shift factor b_T is related to the free volume of the molecules, a non-linear temperature dependence temperature leads to deflections, as can be seen at high concentrations. L-PET and l-PET show a high complexity and thus a strong branching. This thermo-rheological complex behavior is typical for LCB material blended with linear chains (van Gurp and Palmen, 1998).

In comparison to the analysis of the online extrusion pressure in Section 4.3.2, the increase of the complex viscosity and zero-shear viscosity from the reference to chain extended samples is much higher. The strong shear thinning behavior

induced by both chain extenders reduces the extrusion pressure significantly.

As demonstrated, a polycondensation reaction can occur in neat PET. Since a transesterification consumes a hydroxyl group, a saturation of the functional group leads to stable polymer. Thus, less data need to be discarded from the measurement and the polymer is thermal stable, as can be seen in Figure 5.8 (a). The neat PET measured from the highest to the lowest frequency exhibit the enhancement of molar mass and viscosity at low frequencies, which continues in the second run from low to high frequencies. The PMDA treated H-PET is thermal stable since both runs overlap.

A further application of low concentrations of chain extender is demonstrated in Figure 5.8 (b). To overcome the degradation due to processing which decreases the low shear rate behavior, chain extender can be added and facilitates the processability at high rates (Rosu et al., 2000).

The samples with PMDA revealed not only a thermal stability during the measurement, additionally, the drying at $130°C$ could endure more than a week before a degradation occurred. The long time stability was proved after 6 month under environmental conditions. The stability of TGDDM was significantly lower.

5.2 Non-Linear Viscoelasticity

The linear viscoelastic measurements reveal a strong increase of the molar mass and clear indications of a branched structure of the chain extended PET. Nevertheless, non-linear analysis should be employed for a distinct and quantitative detection of branches (Dealy and Larson, 2006). The main non-linear influences were found to be disentanglement (Wagner, 1976) and the stretch of molecules, which is promoted by branching in elongational flow (Wagner et al., 2000). Consequently, this section considers non-linear shear flow at steady state and simple elongational flow. The application of the MSF model enables to quantify the experimental data.

5.2.1 Steady Shear Flow Viscosity

Disentanglement usually causes the non-linearity in shear flow, which occurs at large strains or high rates. However, if the shear flow is not purely simple, a second contribution emerges from elongation, e.g. during a converging flow as in the case of extrusion or injection molding. Therefore, LCB should also influence the non-linear shear behavior in a converging flow (Cogswell, 1978). The capillary measurements were conducted at $280°C$ with an additional orifice die as described in Section 3.2. Indeed, the negligible entrance pressure drop measured for the linear grade, increased to 20% of the total pressure at the

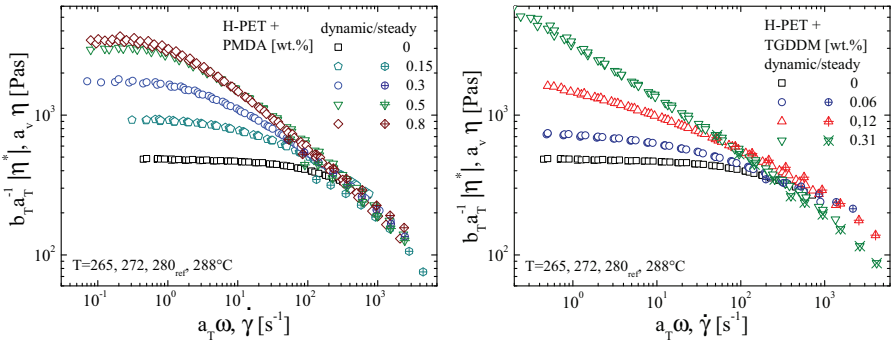

Figure 5.9: Comparison of master curves of complex viscosity and shifted steady state capillary flow viscosity of H-PET with PMDA (a) and TGDDM (b).

highest shear rates, and the Bagley and Rabinowitsch correction are an unavoidable necessity. The elongational contribution was extracted and analyzed from the shear flow as was introduced in Section 2 (Cogswell, 1981). Reliable correlations to simple elongation were found by this method (Aho et al., 2010), but the absolute correctness of the Cogswell analysis can be doubted (Mitsoulis et al., 1998). For the present study, it should be sufficient to mention that the entrance pressure drop and the Bagley correction increases with chain extender concentration, but the amount of derived elongational flow data is too small for a discussion. The corrected shear flow curve is illustrated in Figure 5.9 for H-PET with PMDA (a) and TGDDM (b). It was found that degradation in the capillary rheometer is different from degradation in the oscillatory rheometer, due to different atmospheres (air vs. nitrogen) and diffusion conditions. Since the thermo-oxidative degradation causes as a vertical downward shift (cf. Section 3.3.3), the steady shear data were multiplied by a shift factor $a_v = 1.2$. As seen, the Cox-Merz relation is found to be valid to a certain extent, and the shifting leads to an overlap of the steady flow with the dynamic data (Rosu et al., 2000). A single shift factor leads to good agreement for all modified PET samples. Nevertheless, the Cox-Merz validity should be considered with care for the branched structure.

5.2.2 Experimental Conditions for Sentmanat Extensional Rheometer

The uniaxial elongation experiments were conducted with a *Sentmanat Extensional Rheometer* (SER) which can be attached to the rheometer described in Section 3.2. The surrounding atmosphere was nitrogen at $265°C$. The SER tool consists of two counter-rotating drums with gauge L_0 and radius R, and the Hencky rate is given by means of the rotation rate Ω as:

$$\dot{\varepsilon}_H = \frac{2\Omega R}{L_0} \tag{5.1}$$

The applied elongation rates were 8, 5, 3, 2, 1, 0.5, 0.3, 0.2, 0.1, $0.05s^{-1}$, whereas the reliability of the lowest rates depends on a sufficient high viscosity of the proceeded samples. The time dependent extensional viscosity for uniaxial elongation η_E^+ is the ratio of the tensile stress $\sigma_{xx}(t)$ and the elongation rate:

$$\eta_E^+(t) = \frac{\sigma_{xx}(t)}{\dot{\varepsilon}_H} = \frac{F(t)}{\dot{\varepsilon}_H A(t)} \tag{5.2}$$

The stress can be expressed by the force $F(t)$, which can be detected as torque acting on the drums, and the cross-section area $A(t)$. The cross-section A_0 decays with the Hencky strain as:

$$A(t) = A_0 \exp[-\dot{\varepsilon}_H t] \tag{5.3}$$

Since the sample geometry is measured at room temperature A_{RT}, a density correction is necessary (Sentmanat, 2004):

$$A_0 = A_{RT} \left(\frac{\rho_s}{\rho_l}\right)^{\frac{2}{3}} \tag{5.4}$$

with the densities ρ_s at solid and ρ_l at melt state. The density at room temperature was measured by a Mohr-Westphal balance based on Archimedes principle. The measured densities in Table 5.4 reflect an average of at least 10 measurements. The samples were obtained of different concentrations and sheet locations of each PET grade and revealed no variation of density. The branching does not influence the density, but the higher molar mass between the branching points of H-PET shows an impact on the folding of lamellae. The crystallization behavior is slower for large molecules, and the lower density of the H-PET samples is caused by the longer relaxation times.

The melt density at $265°C$ can be calculated according to Equation 4.1 and 4.4 leading to $\rho_l(538) = 1.178 g.cm^{-3}$. The correction is based on the recorded temperature at the corresponding stresses, which was in a range of $0.3°C$ after

$2min$ of melting. The SER tool is limited to zero shear viscosities above $10^4 Pas$ (Sentmanat, 2004) due to the horizontal arrangement of the sample. Since the lowest concentrations of chain extender possess lower viscosities, a modification of the measurement protocol by a pretension was applied (Aho and Syrjälä, 2008). However, even a very low pretension leads to a large stretching of the sample and a reduced measured Hencky strain. The impact of prestretching was found to be below 5% at the highest strains and was neglected for the present results. The sagging of the low viscous specimens was compensated during the first phase of testing, as could be distinguished by different slopes of the elongational viscosity start-up. Due to the polarity and adhesion forces of the grades, the specimens were attached without clamps.

5.2.3 Uniaxial Elongation Viscosity

The results of simple extension of H-PET with different concentrations of PMDA are presented in Figure 5.10. An unprocessed H-PET is shown in Figure 5.10 (a) as reference, since the low viscosity of the extruded reference inhibit a testing. The non-linear measurement of neat linear PET without the support of a bearing surrounding, e.g. as provided by Meißener or Münstedt Rheometer (Macosko, 1994), is challenging, and the graph should be analyzed only qualitatively. From the two applied elongation rates, a horizontal evolution of the transient viscosity can be seen, which represents a fast achievement of the steady terminal regime. Although linear polymers with very high molar mass can reveal a strain hardening effect (Wagner et al., 2000), the present linear PET investigated shows no thickening behavior. A distinct, different behavior can be observed for the processed chain extended H-PET. From $0.3wt.\%$ Figure 5.10 (b) to $0.5wt.\%$ Figure 5.10 (c) an enlarged transient viscosity can be observed by a steeper start-up curve and a higher approach to a zero viscosity. A strain hardening effect is characterized by a remarkable increase of the elongation stress and from the linear viscoelastic start-up at high strains, which occurs in all samples produced. By a comparison of the slope and the gap between the highest achieved viscosity and the start-up curve, the strong impact of high PMDA concentration on the strain hardening effect is obvious. The difference between $0.5wt.\%$ and $0.8wt.\%$ Figure 5.10 (d) is low. The strain was limited to 4.5 due to geometrical limitations from full rotation of the SER tool. The grade with the lowest concentration in Figure 5.10 (b) leads to a ductile fracture, as indicated by a transition to a steady-state viscosity. In contrast, the high concentrations exhibit a cohesive fracture at high $\dot{\varepsilon}$, which emerged after wrapping of the sample and consequently cannot be analyzed here.

L-PET and l-PET with the addition of PMDA, as illustrated in Figure 5.11 and 5.12, demonstrate a gradual increased transient elongational viscosity and strain hardening as a function of chain extender concentration. Additionally

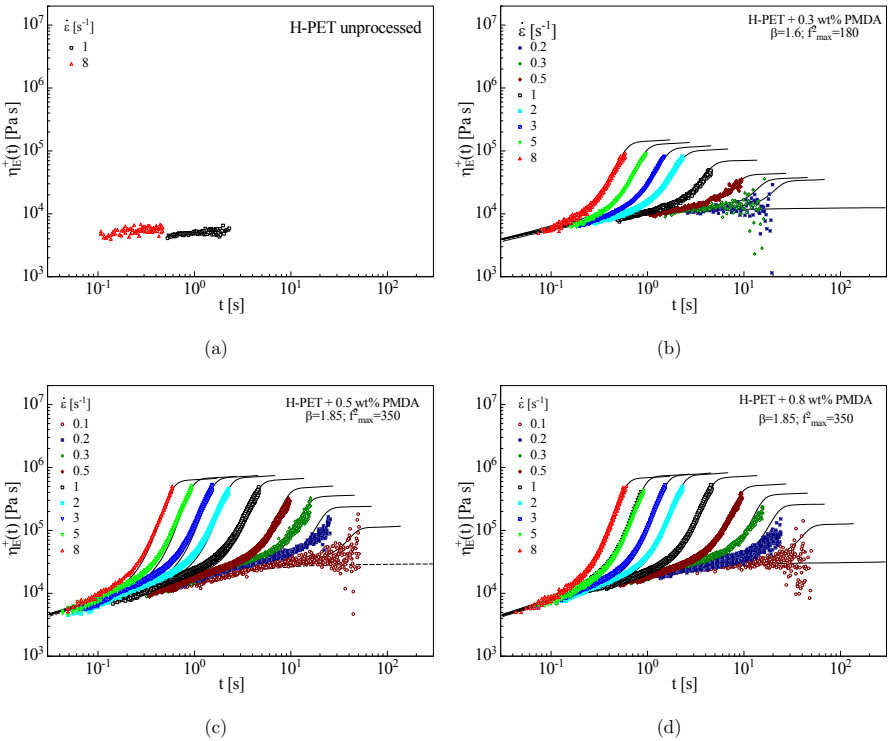

Figure 5.10: Transient uniaxial elongation viscosity for different elongation rates of unprocessed (a) and chain extended H-PET with 0.3*wt.*% (b), 0.5*wt.*% (c), and 0.8*wt.*% (d) PMDA. The solid line represents the prediction by the MSF model with the corresponding non-linear parameter β and f^2_{max}.

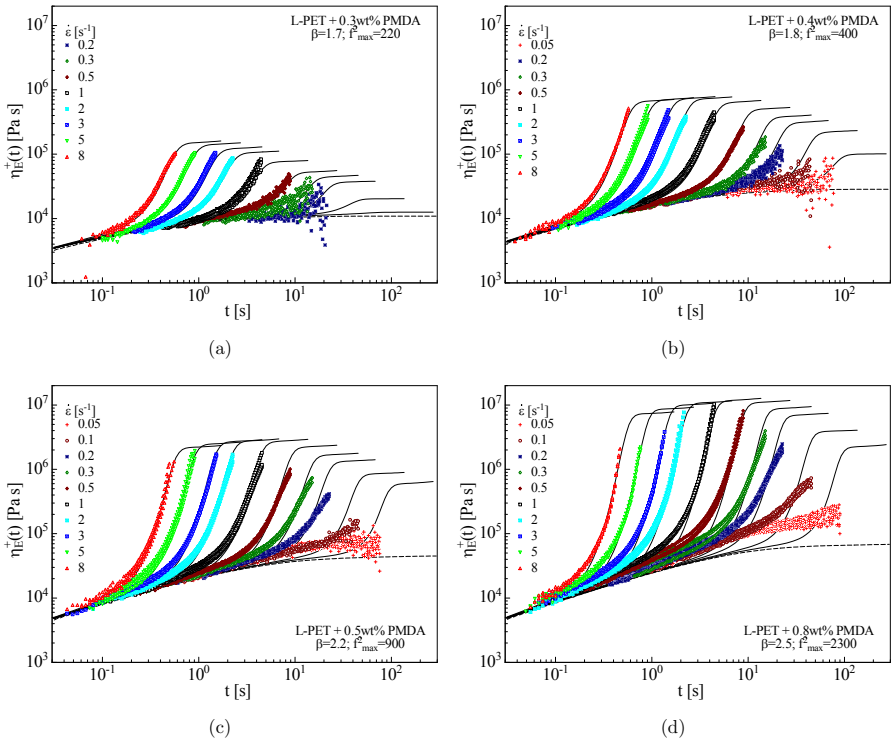

Figure 5.11: Transient uniaxial elongation viscosity for different elongation rates of chain extended L-PET with $0.3wt.\%$ (a), $0.4wt.\%$ (b), $0.5wt.\%$ (c), and $0.8wt.\%$ (d) PMDA. The solid line represents the prediction by the MSF model with the corresponding non-linear parameter β and f^2_{max}.

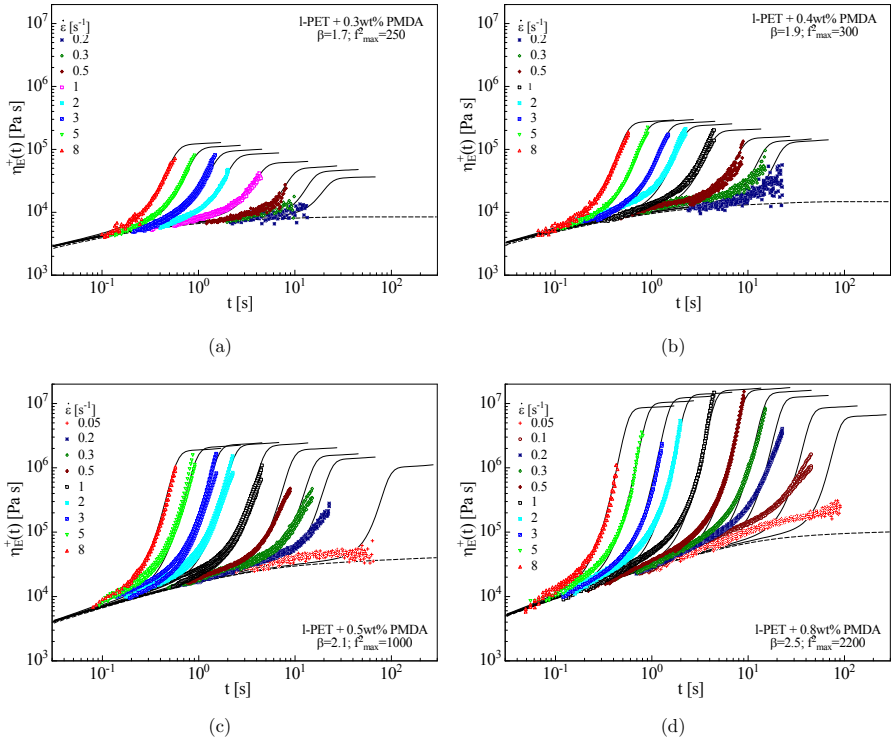

Figure 5.12: Transient uniaxial elongation viscosity for different elongation rates of chain extended l-PET with $0.3wt.\%$ (a), $0.4wt\%$ (b), $0.5wt.\%$ (c), and $0.8wt.\%$ (d) PMDA. The solid line represents the prediction by the MSF model with the corresponding non-linear parameter β and f^2_{max}.

to H-PET, $0.4wt.\%$ was applied on L-PET in Figure 5.11 (b) and l-PET in Figure 5.12 (b) and the linear grade was omitted in the presentation. Both low molar mass grades exhibit a clear distinction between $0.5wt.\%$ and $0.8wt.\%$ and indicate a higher efficiency of the high PMDA concentration. Consequently, $\dot{\varepsilon} = 0.05s^{-1}$ was operated successfully. A simple correlation between the transient elongation, transient shear η_S^+ and linear shear viscosity η_S is given by the Gleissle mirror relation (Gleissle, 1980; Leblans et al., 1985) and the Cox-Merz rule:

$$\eta_E^+(t) = 3\eta_S^+(t) = 3\eta_S(\dot{\omega}) \quad \text{for} \quad t = \frac{1}{\dot{\omega}} \tag{5.5}$$

Consequently, an extensive start-up behavior of samples with high chain extender concentration correlates directly with samples, which revealed the largest

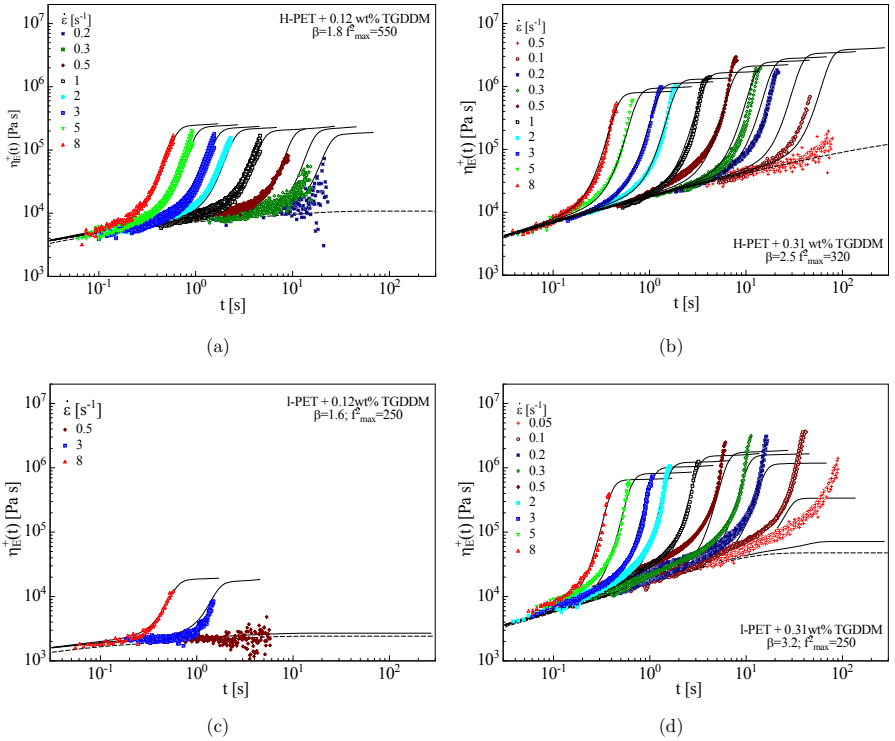

Figure 5.13: Transient uniaxial elongation viscosity for different elongation rates of chain extended H-PET with 0.12$wt.\%$ (a) and 0.31$wt.\%$ (b) TGDDM, and l-PET with 0.12$wt.\%$ (c) and 0.31$wt.\%$ (d) TGDDM. The solid line represents the prediction by the MSF model with the corresponding non-linear parameter β and f^2_{max}.

shear thinning phenomena in Section 5.1.1. As in the case of H-PET, the end of the measurement is governed either by the physical limitations of the tool, a ductile fracture at low strain rates or a cohesive fracture occurring at high elongation rates and chain extender concentrations. The fracture behavior analyzed quantitatively is discussed in the Section 5.17.

The uniaxial extensional behavior of 0.12$wt.\%$ and 0.31$wt.\%$ TGDDM is shown in Figure 5.13 for H-PET (a), (b) and l-PET (c), (d). All combinations lead to a strain hardening effect, which is more pronounced at increased concentration. The low molar mass l-PET reveals a low zero viscosity and an enhanced sagging using 0.12$wt.\%$ TGDDM, inhibiting an accurate testing, as can be seen in Figure 5.13 (c). This is in contrast to H-PET, which ensures

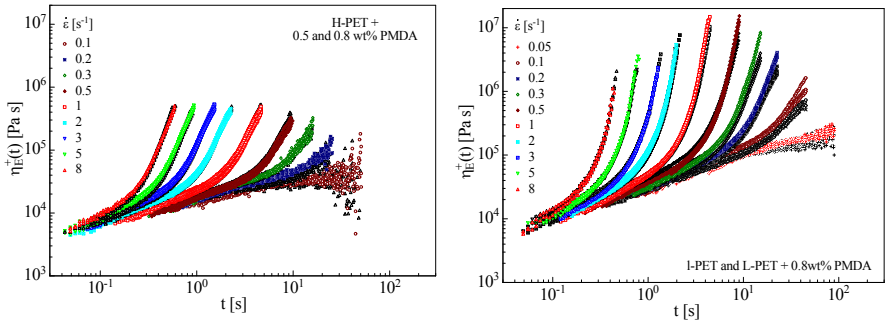

Figure 5.14: Non-linear comparison of H-PET with $0.5wt.\%$ (colored, prominent) and $0.8wt.\%$ (black, overlaid) (a), and L-PET (black, overlaid) and l-PET (colored, prominent) with $0.8wt.\%$ PMDA (b).

an improved analysis due to its higher zero-shear viscosity. Both high concentrations of chain extender reveal an extensive strain hardening and a cohesive fracture above elongation rates of $0.5s^{-1}$ and $0.2s^{-1}$ for H-PET and l-PET, respectively.

As was demonstrated by the batch tests and the linear viscoelastic analysis, H-PET tends to a saturation of the chain extension and branching effect, at high PMDA concentrations. As can be seen in Figure 5.14 (a), the transient elongational behavior of $0.5wt.\%$ and $0.8wt.\%$ is almost equal, which leads to the conclusion that the processing of the chain extended PET and the structure is very stable and reproducible. A similar conclusion can be drawn from the comparison of L-PET and l-PET with the same amount of PMDA. Although both grades can be distinguished by different OH end group concentration, which lead to different successful maximum PMDA addition, the initial molar mass of both is similar. Consequently, the addition of the same concentration leads to the same molecular structure and rheological behavior in Figure 5.14(b). This is valid as long the reaction of free OH end groups is not terminated for both grades.

The produced polymers are blends, which consists of linear and branched chains. The non-linear behavior is sensitive to the structure and the linear analysis obeys friction and molar mass correlations. Consequently, differences can be noted by the dynamic measurements, but a defined structure dominates the elongational behavior. It was found for LDPE and LLDPE blends that the elongation behavior is controlled by the LCB LDPE. A diluting by the linear PE can reduce the extent of stretch but not the strain hardening behavior (Kheirandish, 2005). Dekmezian et al. (2004) confirmed the dominating impact

of the concentration on the melt strength of LCB polymer blended with linear chains.

5.2.4 Application of the Molecular Stress Function Model

In Section 2.4 different constitutive equations were introduced which are capable to describe non-linear phenomena. The integral molecular stress function model is based on the tube model and possesses two essential molecular features to describe uniaxial elongation of branched polymers, which (i) include the stretch of the molecule and (ii) consider the LCB which participate in the stretching. The validity of the model was demonstrated on linear polyolefins [Wagner et al. (1998), branched polyolfins Wagner et al. (2000, 2001), branched polystyrene (Rolón-Garrido and Wagner, 2007), polydisperse polyisobutene (Wagner and Schaeffer, 1992), bran- ched poly(methyl methacrylate) (Ogura and Wagner; Ogura et al., 2015) and also partially gelled LDPE (Rolón-Garrido, 2014).

If the linear viscoelastic material function is known, i.e. the memory function (Equation 2.84), two parameters can sufficiently describe the non-linear behavior, which represents the maximal stored energy that occurred during stretching (f^2_{max}) and a measure of the branching (β). The modeled MSF data for the corresponding elongation rates are denoted as solid lines in Figure 5.10, 5.11, 5.12, and 5.13. The dashed line represents the transient zero viscosity. As can be noted from all simulated data, the experiments and the model are in very good agreement. A transition from the strain hardening into a flattening could be observed before the maximum strain was achieved, which is reflected by the f^2_{max} plateau. In case of cohesive rupture the transition was not observed for PMDA, opposed to the high elastic TGDDM modified PET, which reflected a transition. Even, if the occurred transition emerged from inhomogeneities of the TGDDM samples, the plateau was modeled for the material undergoing fracture, as a representative of the energy introduced to rupture.

The deviations between predictions and experimental data at low strain rates and high concentrations, e.g. for $0.8wt.\%$ in Figure 5.11 (d) and 5.12 (d) originate from insufficient terminal data from the linear viscoelastic analysis. Since the terminal regime is not described fully in the experimental window (cf. Section 5.3) the longest relaxation times are not included in the relaxation spectrum and memory function, respectively, and the behavior at long elongation times cannot be displayed. However, the strain hardening emerging during the start-up or at lower concentrations can be analyzed quantitatively by the two parameters.

Figure 5.15 (a) illustrates the evolution of f^2_{max} with increasing PMDA concentration. All three PET grades exhibit an increase of the parameter with higher concentration, representing an increased strain hardening behavior with chain extender concentration. As was observed before, H-PET shows an asymp-

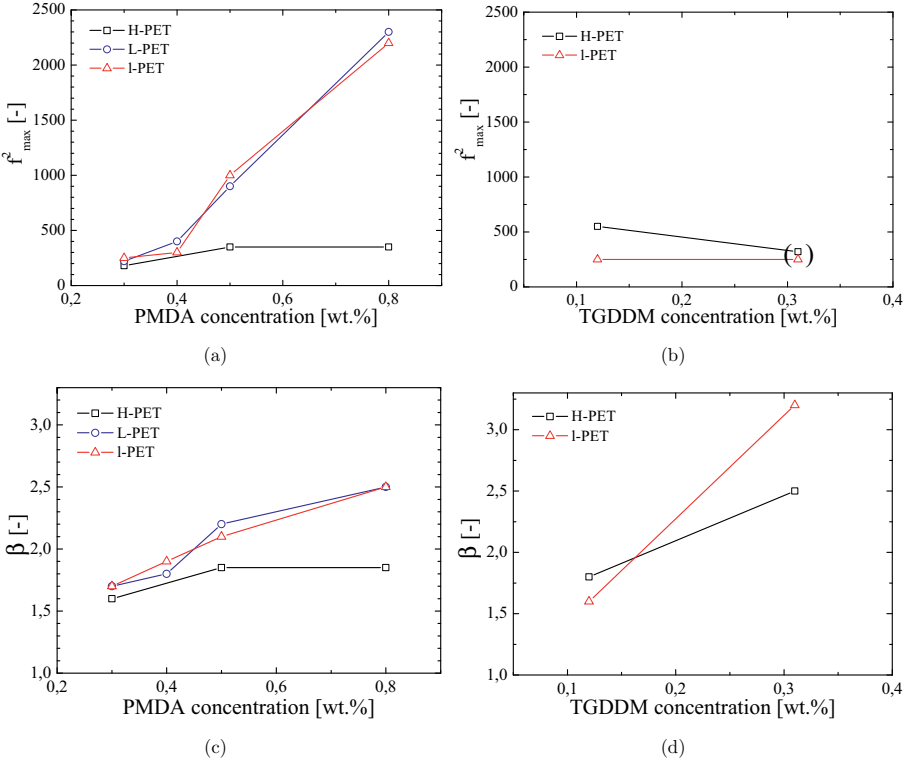

Figure 5.15: Non-linear parameter of MSF model f^2_{max} for H-PET, L-PET, and l-PET with PMDA (a) and for H-PET and l-PET with TGDDM (b), and β for H-PET, L-PET, and l-PET with PMDA (c) and for H-PET and l-PET with TGDDM (d).

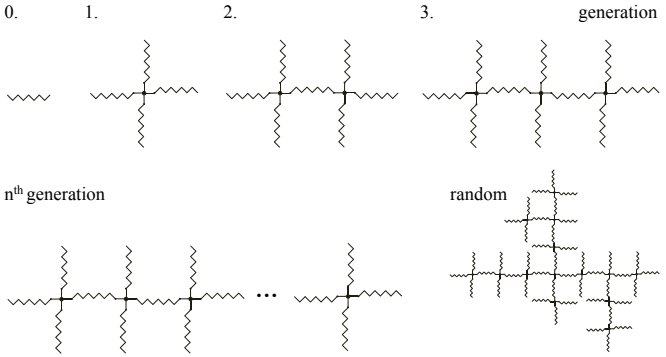

Figure 5.16: Possible structure due to tetra-functional chain extender.

totic behavior reflecting a similar structure. Remarkably, both low molar mass grades show a higher stretching at all concentrations as a result of higher molar mass and large amount of branched side arms. L-PET and l-PET possess a linear increase of f_{max}^2 and energy absorbance, before cohesive fracture at $0.8wt.\%$ occurred. It can be concluded that the stretch is largely supported by branching. Although the molar mass of H-PET is higher compared to L- and l-PET, the stretch is always lower. Consequently, stretching is not only enhanced by increased molar mass rather by the branching density. The results from $0.31wt.\%$ TGDDM addition in Figure 5.15 (b) are depicted in parenthesis due to the unique fracture as discussed in the next section. The lower value of l-PET compared to H-PET at $0.12wt.\%$ correlates with the higher reactivity of TGDDM and H-PET. The preferred reactivity of PMDA with the low viscous and high OH concentrated grades can be inferred from both parameter in Figure 5.15 (a) and (c). The evolution of β in Figure 5.15 (c) correlates with an increase of strain hardening effect at higher chain extender concentration, due to the occurrence of increased branching. It was shown that β can be related to the structure of a molecule with Equation 2.106, and M_n as the number-average molar mass of the entire branched molecule and $M_{n,bb}$ as the number-average molar mass of the backbone (Wagner, 2004).

$$\beta = \frac{M_n}{M_{n,bb}} \tag{2.106}$$

It was found for LDPE that β can be used to distinguish between a regular branching structure with a limiting value, and a random Cayley structure (Kheirandish, 2005). By considering an ideal reaction of one PMDA chain extender with four PET chains of equal length a star-like polymer would emerge, as can be noted from Figure 5.16. The chain growth depends on the functionality of both PET end groups. Only if a coupled chain possesses two OH

groups, a second PMDA molecule can be attached. Based on the calculated end group concentration (Table 4.2), the probability that H-PET contains two hydroxyl groups is around $\frac{1}{3}$ (Table 5.4), which would lead to a comb-like structure. Based on Equation 2.106 the limiting value of a comb structure with n_{CE} chain extender molecules can be expressed as:

$$\beta(n_{CE}) = \frac{3n_{CE}+1}{1+n_{CE}} \tag{5.6}$$

$$\lim_{n_{CE}\to\infty} \frac{3+\frac{1}{n_{CE}}}{1+\frac{1}{n_{CE}}} = 3 \qquad \forall \quad n_{CE} > 1 \tag{5.7}$$

Since star polymers are known to act as a linear polymer with comparable molar mass (Larson, 1988), the introduced progression is only valid for structures with more than one coupling agents. On contrast, the limiting value of a random polymer would diverge, since the probability to participate on the backbone decreases disproportional with chain extension. L-PET in Figure 5.15 (a) and l-PET in Figure 5.15 (c) are not converging in the experimental window. Additionally the probability of an attached PET chain with two OH groups is higher and thus a more random structure can be expected. Obviously, the idealized progression does not consider coupling of small oligomers, non-reacted ends or the blending effect of remaining linear chains. Nevertheless, from the evolution of H-PET and the almost identical behavior of L-PET and l-PET (cf. Figure 5.14) a defined structure can be expected from the elongational experiments. Since H-PET possesses a lower branching density and stretch ability at all concentrations, it can be stated that the length of side arms influence the strain hardening less than the branching density.

The epoxy based TGDDM needs to be analyzed with care, since only two different concentrations of TGDDM are available. However, remarkable is the increase of β of the less reactive l-PET by increased chain extender content, as can be seen in Figure 5.15 (d). At $0.06 wt.\%$, H-PET is able to bond more chain extender, which leads to more branching. On contrast, at high concentration the l-PET with less preferred COOH groups possesses a higher branching density. This leads to the conclusion that an extensive feeding of the epoxy-based coupling agent attacks also randomly at the backbone, bonds oligomers emerged with COOH end groups and homopolymerizes. Both lead to an inhomogeneous and locally concentrated, hyperbranched or dendrimer-like topology.

5.2.5 Fracture Behavior

The distinction, whether the fracture occurred was of brittle or ductile nature, was observed visually by camera for each measurement. Additionally, the fracture surface was investigated optically. Since a certain amount of fracture

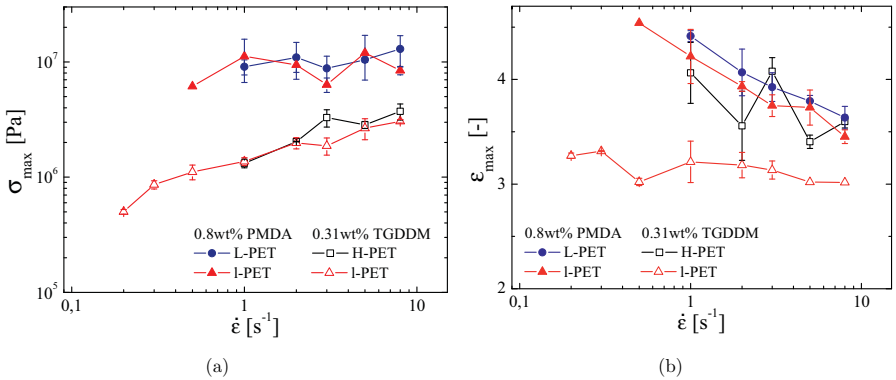

Figure 5.17: Comparison of stress (a) and strain (b) at break by variation of the strain rate for different PET grades with PMDA and TGDDM.

occurred after the geometrical limitations of the SER tool, or the distinction between ductile and inhomogeneity induced failure could not be made, the reported fractures in Figure 5.17 include only obvious cohesive rupture.

From the graphs of L-PET and l-PET with PMDA chain extender in Figure 5.17 (a) a constant stress at fracture can be observed in the experimental range. The corresponding maximum endurable stress of $10 MPa$ was reported before for LDPE (Rolón-Garrido and Wagner, 2014). Consequentl, a complete separation of the structure or even scission of the primary bonds can be expected. This behavior can also be seen in Figure 5.17 (b) representing the elongation at break, which decreases with higher strain rates. The stress is the restricting value for high molar mass and branched molecules achieved with PMDA. However, the TGDDM samples show a different behavior. In particular, l-PET reveals a constant strain at break in Figure 5.17 (b), which leads to the conclusion that the strain is the limiting value. As can be seen by the stress behavior, both TGDDM samples show an increasing stress with higher strain rates. Obviously, the high amount of network formation limits the strain. Due to relaxation at low rates, the stress is lower compared to the glassy behavior at high elongational rates. The H-PET sample in Figure 5.17 (b) can be seen as intermediate state, which can endure higher strains, since the polymer matrix is still participating in the stress absorption. Similar results were found on partially cross-linked LDPE (Rolón-Garrido and Wagner, 2014). The achieved amount of strain is in agreement with Japon et al. (2000a). They found a Hencky strain at fracture of 5.1 for linear PET with a Macosko type rheometer, which reveals that the present applied limit of 4.5 is close to rupture for the low chain extender concentrations. A strain of 4.2 and 3.9 for recycled and virgin PET was found for $0.3 wt.\%$ TGDDM, respectively. A decreasing maximum of

Table 5.5: Summery of rheological behavior of H-PET, L-PET, and l-PET and the different impact of both chain extenders. The evaluation from good to poor (++, +, ∘, -) considers a respective successful concentration, with respect to high melt strength and processability the grades produced.

		η_0	Strain hardening	ε_{max}	Gel-like	Stability	Apparent structure
H-PET	PMDA	+	+	++	++	++	comb-like
	TGDDM	+	+	∘	-	-	hyperbranched
L-PET	PMDA	++	++	+	+	++	tree-like
l-PET	PMDA	++	++	+	+	++	tree-like
	TGDDM	∘	++	-	-	-	hyperbranched

strain was also reported with chain extender concentration (Japon et al., 2001), as confirmed by the present analysis. A study by Kil et al. (2003) reported a maximum Hencky strain of 5.5 for linear PET.

5.3 Conclusions

It was shown that the chain extension with an industrial scale co-rotating twin-screw extruder leads to high molar mass and long-chain branched poly(ethylene terephthalate). The reactive processed PET grades with PMDA and TGDDM as employed chain extenders exhibit a fundamental different rheological behavior, which can be related to the initial molar mass and synthesis route of the virgin PETs. The processed grades possess a strongly increased dynamic and transient elongational viscosity, long-chain branching, strain hardening, and thermal stability as a function of chain extender concentration. The results were quantitatively analyzed by the molecular stress function model and the fracture behavior.

The dynamic linear viscoelastic analysis reveals an enlarged rubber-like transition, with a flattening of the loss moduls and even more pronounced storage modulus. Consequently, the shear thinning onset is shifted to higher viscosities and lower frequencies. A convergence of the complex viscosity at high frequencies is given for all modified grades investigated. The zero-shear viscosity is increased by two decades. Due to a preferred OH group reaction, PMDA and initial low molar mass PET (L-PET and l-PET) reacts to higher viscosities compared to initially high molar mass PET (H-PET).

The activation energy of flow shows strong indication of LCB for both chain

extenders applied. The analysis of the loss angle by the van Gurp-Palmen plot reveals a thermo-rheological complex material for high chain extender concentrations, in particular for L-PET and l-PET with PMDA. The results show a distinctly different behavior of the modified grades to the neat linear PET. The TGDDM specimens exhibit a large second relaxation process indicating extensive LCB or hyperbranching.

An additional stretch contribution was found by non-linear steady shear analysis. The degradation during the steady flow experiment was compensated by a vertical shift factor to fit steady and oscillatory data.

The uniaxial elongational measurements reveal an apparent saturation effect of PMDA processed with H-PET, and a defined and reproducible structure of such grades. L-PET and l-PET exhibit a similar structure consistency, but also a potential to higher branching and molar mass by higher PMDA concentration, as was confirmed by both non-linear MSF parameter β and f^2_{max}. Compared to H-PET, the both initially low molar mass grades show a higher molar mass and seem to have tree-like structure after reactive extrusion. The TGDDM samples reveal a correlation of chain extender effect and preferred reactivity with the COOH group at low concentrations. At high concentration, a random attack at the polymer backbone, a coupling of degraded chains with COOH end groups and a homopolymerization of the epoxy based coupling agent lead to a strong increase of β and thus, the strain hardening and branching density. The application of high $0.31 wt.\%$ TGDDM leads to a gel-like structure. The gel-like structure was also confirmed by the linear viscoelastic measurements. A comparison of linear and non-linear results reveals differences, apparently due to different sensitivity to the blend composition of linear and branched chains created. However, the creation of the structure was found to be reliable and similar, e.g. for L-PET and l-PET at $0.8 wt.\%$ PMDA, by non-linear measurements and the MSF model.

Fracture in elongational flow was found to be related to a limiting stress value of $10 MPa$ for PMDA treated L-PET and l-PET. In contrast, a limiting strain restricted the elongation of PET with TGDDM, which leads to the conclusion that a permanent covalent network governs the fracture for high TGDDM concentrations. Based on the results obtained, a qualitative evaluation with respect to high melt strength and processability of the grades is given in Table 5.5.

6 Molecular Characterization of Branched PET

The molecular determination of polymer chains includes the molar mass, molar mass distribution, and the size. These quantities influence largely the properties of the polymer, such as processability, melt viscosity, brittleness, glass transition temperature, and stress relaxation (Mori and Barth, 1999). The molecular analysis of the reactive processed PET is the objective of this chapter. The different average molar masses, the molar mass distribution, intrinsic viscosities, and radius of gyration are considered. However, the analysis of branched polymers is a challenging task. Although conclusions regarding LCB can be drawn from the fractionated molar mass and radius of gyration, a reliable certainty can only be achieved by the intrinsic viscosity and the hydrodynamic volume (Podzimek, 2011), as demonstrated in this chapter. Finally, the molecular characteristics observed are related to the rheological results.

6.1 Size-Exclusion Chromatography with Triple Detection

The combination of three different detectors allows an absolute measurement and the analysis of the structure of the polymer. Size-exclusion chromatography (SEC) is applied to a dilute polymer solution, which is forced at constant flow rate through a porous column. Due to diffusion processes, the polymer chains penetrate the voids provided by a gel. If no enthalpic interactions between polymer and column occur, small particles elute at long retention times and large molecules pass through fast. The spherical dimension of the molecule governs the separation. The hydrodynamic radius is based on the volume occupied by a molecule, which possesses the same intrinsic viscosity as a theoretical hard sphere. Hence, it is related to the diffusion coefficient (Equation 2.33), which leads to:

$$R_h = \left(\frac{3[\eta]M}{10\pi\mathcal{N}}\right)^{\frac{1}{3}} \tag{6.1}$$

with the intrinsic viscosity $[\eta]$, molar mass M, and Avogadro's number $\mathcal{N}$. After the sample is fractionated by the columns, it can be analyzed by detectors.

The concentration detector based on the refractive index is only sensitive to the amount of solute in the elute. The concentration c can be derived from the refractive index of the solvent n_o, sample n' and the solute n

$$n = n_0 + (n' - n_0)\, c \tag{6.2}$$

The differential refractive index increment dn/dc is a constant for a given solvent polymer combination, when the molar mass of the molecules is above a certain value[1]. The concentration signal from the differential refractive index detector (DRI) is essential for the light scattering measurement (Mori and Barth, 1999).

Based on the pair correlation function and the Debye structure function (cf. Section 2.1.2), the particle scattering function can be approximated at small angles as:

$$P(\theta) = 1 - \frac{\underline{q}^2(\theta) \left\langle R_g^2 \right\rangle}{3} \tag{6.3}$$

with R_g as radius of gyration and $\underline{q}(\theta)$ as scattering vector, which can be also expressed by the scattering angle $sin^2(\theta/2)$ (Equation 2.12). The Rayleigh ratio can be expressed as a function of the molar mass:

$$\frac{K^* c}{R(\theta)} = \frac{1}{MP(\theta)} + 2A_2 c + ... \tag{6.4}$$

with the optical constant K^*, the concentration c, and the molar mass M. The second viral coefficient A_2 can be neglected, if the concentration tends to zero. Equation 6.4 is known as Debye formalism, which deviates at high molar mass from the Zimm and Berry formalism (Podzimek, 2011). The optical constant depends on the refractive index of the solvent n_0, the differential refractive index increment dn/dc of the solution, and the wave length λ_0 and is given for vertically polarized light:

$$K^* = \frac{4\pi^2 n_0^2 (dn/dc)^2}{\mathcal{N} \lambda_0^2} \tag{6.5}$$

By extrapolation to zero concentration and scattering angle θ, the molar mass can be derived from the Rayleigh ratio (Kratochvil, 1972). The particle scattering function and the approach of Debye considers the spatial arrangement of the scattering centers and the emerging interference. The occurrence of an angular dependence of large particles measured by multi-angle light scattering (MALS) can be related to the radius of gyration, which is expressed as slope in the Zimm plot (cf. Figure 2.4) The molar mass in Equation 6.4 is correlated to the weight-average molar mass and R_g to the z-average radius, and whether the separation occurs precisely or not, both values are intrinsic values of the

[1] In average $1 kg.mol^{-1}$ for polymers.

Rayleigh scattering (Podzimek, 2011).

The viscosity detector is sensitive to the structure of the molecule, besides the concentration and the molar mass. The viscosity of a polymer in solution can be written as specific viscosity:

$$\eta_{sp} = \frac{\eta - \eta_0}{\eta_0} \tag{6.6}$$

with the viscosity of the solvent η_0 and of the sample η. The intrinsic viscosity is given at infinitesimal small concentration:

$$[\eta] = \lim_{c \to 0} \frac{\eta_{sp}}{c} \tag{6.7}$$

The specific viscosity can be measured online by a bridge viscometer with four capillaries. If one capillary possesses a higher resistance, the specific viscosity is given by the inlet pressure (IP) and the differential pressure (DP):

$$\eta_{sp} = \frac{4DP}{IP - 2DP} \tag{6.8}$$

6.1.1 Experimental Conditions for SEC

Size-exclusion chromatography measurements were conducted on H-PET samples with PMDA and TGDDM as chain extender with an Agilent GPC-PL 220. The separation was realized by a *PSS PFG linear XL* column with $7\mu m$ particle size and an equipped precolumn. The operation conditions for the columns, DRI ($\lambda = 890nm$), MALS (DAWN HELEOS 8+, Wyatt), and viscosity detector (PL-BV 400HT) were set to $35°C$ and flow rate of $0.5ml.min^{-1}$. The mobile phase was hexafluoroisopropanol (HFIP) with $0.05mol.l^{-1}$ potassium trifluoroacetate, to avoid agglomeration of the solute. A $6ml$ solution of each sample was prepared with a concentration of $2mg.ml^{-1}$ dissolved in HFIP for $12h$ and stirred gently. Each sample was injected tree times in total from two different solutions. The injected sample passed a $2\mu m$ in-line filter to sieve gel particles. Since the concentration was known, the recovery of the sample could be measured by the DRI detector and non-soluble contents could be determined (Rolón-Garrido et al., 2015). The recovery of 96% is in the experimental error for all samples, which leads to the result that no gel particles larger than $2\mu m$ occurred in any analyzed sample processed from H-PET and both chain extenders.

The DRI detector was calibrated based on H-PET and two PET standards (PSS) with M_w of $25kg.mol^{-1}$ and $74kg.mol^{-1}$, allowing the measurement of the concentration of any dissolved polymer under these conditions. Consequently, the refractive index increment can be calculated from the detector peak and

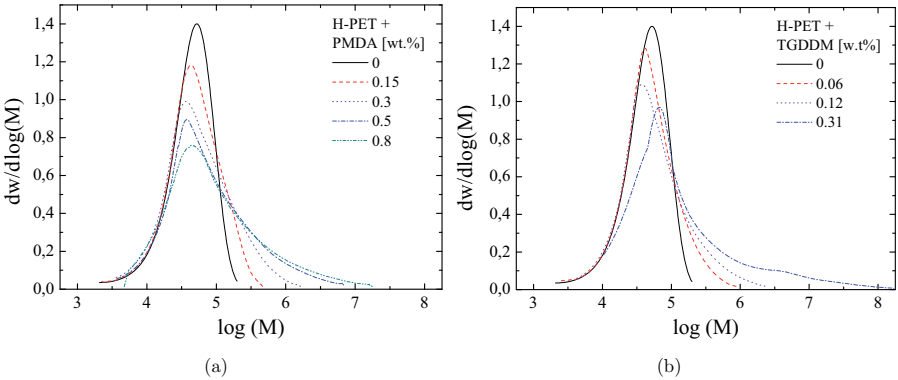

Figure 6.1: Weight differential molar mass distribution of H-PET with different concentration of PMDA (a) and TGDDM (b).

a known concentration. A dn/dc of $0.249 ml.g^{-1}$ with a standard deviation of 0.0041 was obtained from 7 different solutions of the two standards. The deviation from the literature value of $0.257 ml.g^{-1}$ (Berkowitz, 1983) can be explained by different temperatures and the salt added, and is in agreement with the variations seen for other polymer systems (Mori and Barth, 1999).

6.1.2 Molar Mass and Distribution of Branched PET

The weight differential molar mass distributions of extruded H-PET with PMDA (a) and TGDDM (b) chain extender can be seen in Figure 6.1. The reference in both graphs reflects a typical shape of a Schulz-Flory distribution for poly(ethylene terephthalate) (Rieckmann and Völker, 2004). The neat PET possesses a slightly higher molar mass compared to the molar mass based on intrinsic viscosity in Chapter 3. The degradation of neat PET in the extruder occurs as an entire shift of molar mass distribution to lower values (not plotted). The weight-average molar mass is reduced by 21% and the distribution is slightly more narrow, as can be seen in Table 6.1. This demonstrates the reduction of molar mass by shear degradation during extrusion.

The results for PMDA exhibit a constant slope of the low molar mass shoulder for all concentrations investigated. However, the high molar mass shoulder shows a gradual enhancement with increasing chain extender concentration, which reflects the increase of molar mass and MMD. Since the illustration is based on the weight fraction, a reaction of high molar mass molecules leads to a visible reduction of these specimens already at low PMDA concentration, reflected by a reduced height of the high molar mass shoulder. The amount of chains with low molar mass is relatively high and the corresponding shoulder

Table 6.1: SEC-MALS results.

	Conc. $[wt.\%]$	M_n $[kg.mol^{-1}]$	M_w $[kg.mol^{-1}]$	M_z $[kg.mol^{-1}]$	MMD $[-]$	IV $[dl.g^{-1}]$	R_g $[nm]$	R_h $[nm]$
virgin	0	26.7	66.7	110.1	2.51	1.05	19.8	13.2
processed	0	28.4	52.6	75.6	1.85	0.87	18.3	10.9
PMDA	0.15	31.6	69.4	205.5	2.12	0.92	20.8	14.0
	0.3	33.2	113.8	575.2	3.43	1.02	29.4	22.3
	0.5	38.0	276.9	2619	7.29	1.21	57.2	45.4
	0.8	39.5	484.5	6903	12.26	1.29	77.0	68.3
TGDDM	0.06	30.9	78.1	353.4	2.53	0.93	22.5	16.8
	0.12	34.4	133.6	1289	3.88	1.02	33.2	28.3
	0.31	54.8	1860	39908	34.09	1.43	158.1	136.7

exhibits a delayed behavior. The coupling of PET chains occurs over the whole range of molar mass. A similar tendency can be noted from the TGDDM treated samples in Figure 6.1 (b). However, the sample with $0.31wt.\%$ TGDDM can be distinguished from the lower concentrations, since it shows a clear shift of the peak. Large reduction of the small species exhibits numerous reactions, leading to an enlarged high molar mass tail with a small bump. This evolution of the MMD is comparable to observations of Japon et al. (2000a) (TGDDM) and (Härth et al., 2014) (PMDA), although in the latter case a bimodal distribution was obtained.

A quantitative analysis can be conducted by the molar mass averages in Figure 6.2 and Table 6.1. The number-average molar mass in Figure 6.2 (a) exhibits a gradual increase with concentration of both chain extenders employed, with an apparent asymptotic behavior for PMDA and a largely increased value for $0.31wt.\%$ TGDDM. It can be concluded that already small amounts of chain extender reduce the number of small molecules.

The weight-average Figure 6.2 (b) and z-average molar mass Figure 6.2 (c) exhibit an exponential increase for both chain extenders, and a large enhancement of the highest TGDDM concentration (M_z is three orders of magnitudes enlarged). Consequently, the molar mass distribution in Figure 6.2 (d) correlates with the weight-average, since the changes of M_n are relatively small. Based on a stoichiometric considerations, it can be concluded that already at small concentrations of chain extender, the number-average molar mass increases and the total number of chains decrease. By comparing the M_w and M_z values with the distribution of reference sample in Figure 6.1, it can be noted that all M_z and most of the M_w values of the chain extended grades are out of the scope

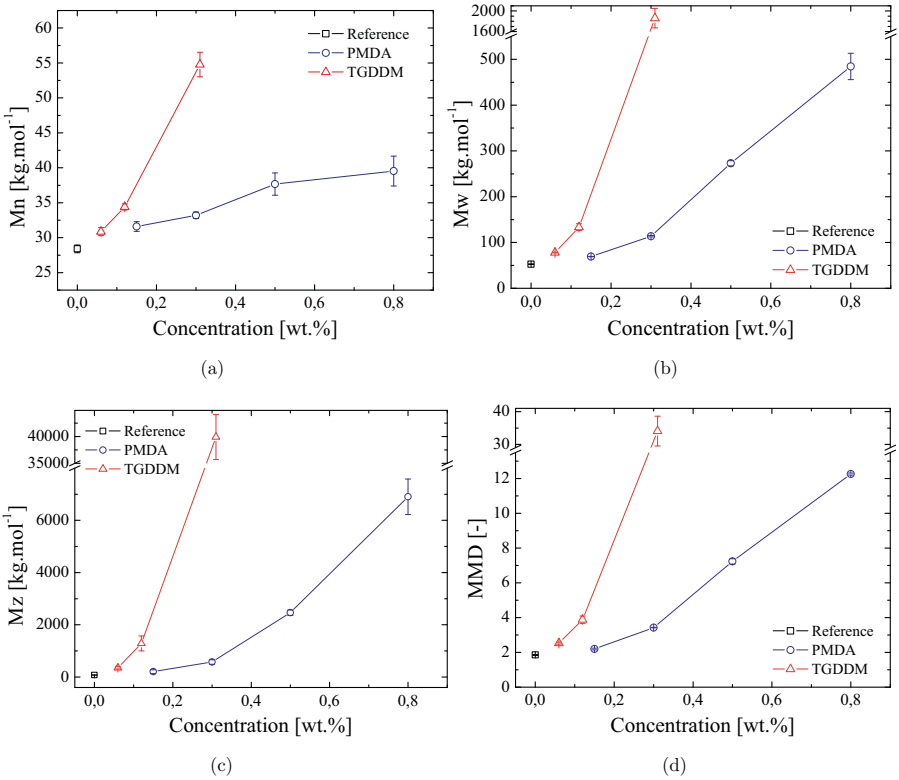

Figure 6.2: Number-average (a), weight-average (b), and z-average molar mass (c), and molar mass distribution (d) of H-PET with PMDA and TGDDM.

of the reference sample. These data reflect only the chain extended species and are unaffected by a blend with linear chains. The highest concentration of PMDA reflects a limited addition of chain extender by observing the M_n data, whereas $0.31 wt.\%$ TGDDM exhibits still reactivity. However, the effect on the weight-average and z-average differs. Since these quantities are not related to the number but to the molar mass of the molecules, only few couplings of large molecules can increase the values significantly.

6.1.3 Conformation of Branched PET

The intrinsic viscosity of H-PET with PMDA and TGDDM is presented in Figure 6.3 (a). The samples with the epoxy-based chain extender exhibit a linear increase with concentration, whereas the PMDA samples reflect an apparent sinusoidal shape. Since the samples were separated by the hydrodynamic radius followed by an absolute measurement, each specimen can be plotted as Mark-Houwink diagram. The corresponding parameter a, which reflects the slope of the logarithmic graph, is presented in Figure 6.3 (b). Additionally, Mark-Houwink parameters were evaluated for the PET standards, and lead to:

$$[\eta] = 0.0985\, M_w^{0.630} \tag{6.9}$$

which agrees with the extruded reference in the graph. The intrinsic viscosity is usually associated with the weight-average molar mass of a linear polymer (Podzimek, 2011). Since the temperature and solvent is the same, the decrease of the Mark-Houwink exponent with increasing chain extender concentration in Figure 6.3 (b) clearly demonstrates an increasing branching. In particular, the small difference between $0.5 wt.\%$ and $0.8 wt.\%$ PMDA reflects a similar conformation. The viscosity of non-entangled branched PET deviates from the Rouse relaxation times for linear polymers, e.g. due to an occurrence of excluded volume.

The radius of gyration can be seen in Figure 6.3 (c) for the grades investigated. The lowest PMDA concentration of $0.15 wt.\%$ exhibits almost no increase of the radius compared to the reference. Further, the radii of the higher concentrations increase significantly and linearly. The size of the lowest TGDDM concentration is also almost unchanged compared to the reference. The radius of gyration is related to the z-average of the fractionated specimen, which only reflects the reacted species, as demonstrated. Since low concentrations of chain extender change the size only slightly, although a large increase of molar mass was observed, a star-like shape can be concluded for these samples. On contrast to PMDA, the epoxy-based additive possesses an exponential eightfold higher R_g at the highest concentration. Both chain extenders, but in particular TGDDM, lead to vastly enlarged molecules at high concentrations. The detection of radii is limited to around $200 nm$, which is sufficient for the present

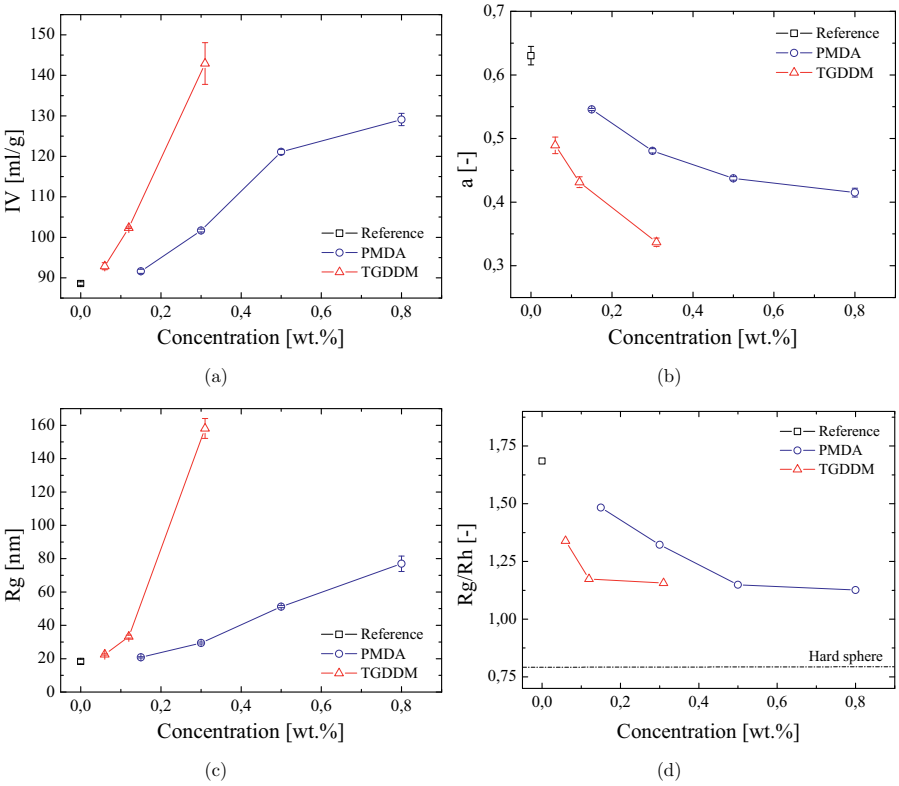

Figure 6.3: Intrinsic viscosity (a), Mark-Houwink exponent a (b), radius of gyration (c), and ratio of radius of gyration to hydrodynamic radius (d) of H-PET with PMDA and TGDDM.

species. Additionally, the evaluation routine needs to be modified for huge molecules. For $0.31wt.\%$ TGDDM, $0.5wt.\%$ and $0.8wt.\%$ PMDA, the analysis was changed from Zimm to Berry formalism (Podzimek, 2011). The comparison of the radius of gyration to the hydrodynamic radius gives an insight to the compactness of the molecule. Since R_h is related to a behavior of a hard sphere in solution, the theoretical ratio with the corresponding R_g is 0.77, as can be noted in Figure 6.3 (d). The ratio of a linear polymer with a MMD of 2 is rarely reported, and the measured value of 1.69 is in good agreement with theoretical predictions (Rubinstein and Colby, 2003). The lowering of the ratio describes an increased monomer density.

6.1.4 Coil Contraction

A further measure of the compactness and the impact of branching is given by the coil contraction factor (cf. Section 2.1.2). To emphasize again, the coil contraction factor based on the radius of gyration g is defined as:

$$g = \frac{\left\langle R^2_{g,br} \right\rangle}{\left\langle R^2_{g,lin} \right\rangle} \tag{2.16}$$

and the same quantity based on the intrinsic viscosity g' is defined as:

$$g' = \frac{[\eta_{br}]}{[\eta_{lin}]} \tag{2.20}$$

A conformation plot, i.e. the relation of molar mass to R_g in a logarithmic diagram, leads to a first-order exponential equation for a linear polymer, analogously to a Mark-Houwink expression. The conformation plot as representative for the standards and H-PET lead to (Podzimek, 2013):

$$R_{z,lin} = 0.0237\, M_z^{0.586} \tag{6.10}$$

With the corresponding molar mass from the chain extended samples, the coil contraction can be calculated, as can be seen in Figure 6.4 (a). The reference and its deviation from a theoretical value of 1 reflects the uncertainty of the power law, which is enlarged by the quadratic ratio. As can be seen for both chain extenders, the contraction significantly occurs already at low concentrations and both describe an asymptotic graph. This result was observed already on the R_g diagram, where a large increase of molar mass only leads to moderate enlargement of size. The contraction factor g' can be calculated with the Mark Houwink parameter and the corresponding M_w of the branched molecules. The results are given in Figure 6.4 (b), where the contraction and increased monomer density progress more moderately for PMDA,

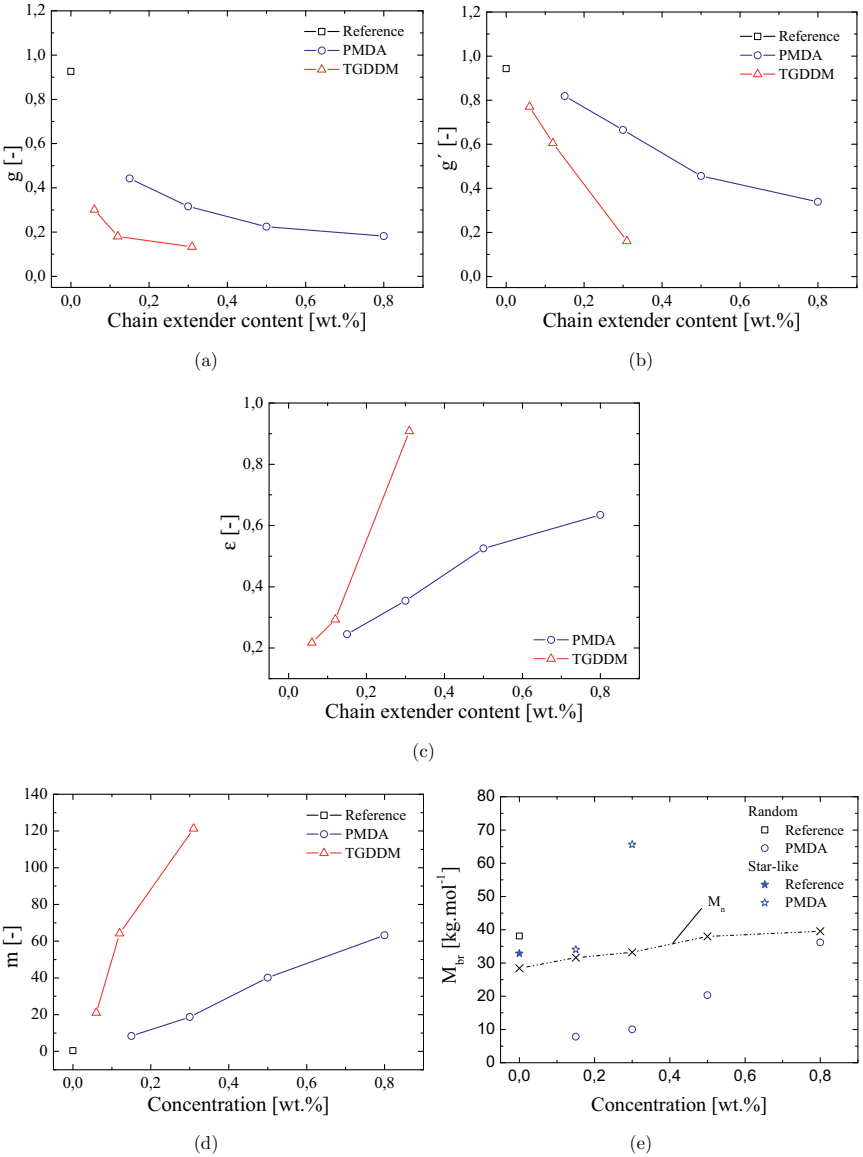

Figure 6.4: Coil contraction factor based on R_g (a), coil contraction factor based on $[\eta]$ (b), structure exponent ε (c), branch units m based on g_4 (d), and molar mass between branches (g_4) and star arms (g_s) (e) of H-PET with PMDA and TGDDM.

whereas TGDDM leads to an elevated compactness at $0.31 wt.\%$. The relation of both factors can lead to information about the structure (Berry, 1968; Radke and Müller, 2005; Rolón-Garrido et al., 2015):

$$g' = g^{\varepsilon} \tag{6.11}$$

The parameter ε is related to the drainability of the coil and is depicted in Figure 6.4 (c). Different values have been reported for ε, which depend on the solvent, molar mass, temperature, and branching. In general, a more comb-type structure was reported for values around 1, whereas star-like chains are much smaller. Clearly, the structure changes with addition of chain extender. Both coupling agents lead to an initially more star-like formation. The PMDA extended molecules seem to converge to a value around 0.7, whereas the TGDDM samples seem to diverge.

The difference in structure is even more emphasized when analyzing the branches per molecule m. The model presented by Zimm and Stockmayer (1949) allows calculating the amount of branch units from g. It has to be mentioned that not all possible branching points may have reacted with a respective large molecule in the range of M_n, since also non-reacted or ring reactions need to be considered. Nevertheless, a tetra-functional branching unit is assumed according to Equation 2.19. The solution of the non-linear equation was calculated with *Mathematica 5*. The branch points per molecule exhibit a linear enhancement with increasing concentration for PMDA in Figure 6.4 (d). The graph for TGDDM is also almost linear, but a higher amount of branches occurs. The random coupling at the backbone and homopolymerization of the chain extender lead to a large amount of branches. Even if the Zimm-Stockmayer model for g_4 should not be analyzed quantitatively for such undefined branching units, the effect is demonstrated. Furthermore, the branching density λ, i.e. the number of LCB per 1000 monomer units, can be calculated as Auhl et al. (2012):

$$\lambda = \frac{m}{M} M_m \cdot 1000 \tag{6.12}$$

Based on the branching frequency, the molar mass between two branch units M_{br} can be calculated. In Figure 6.4 (e) the molar mass between branches calculated with g_4 and the arm length for a star molecule with equal side arms g_s (Equation 2.17) are compared with the number-average molar mass of the PMDA samples. It can be seen that at low concentration, the star-like approach leads to a molar mass similar to M_n, whereas a tetra-functional unit describes the high concentrations precisely. The concentrations reflect a blend of star-like and random or comb-like structures. Hence, the numbers of branches presented in Figure 6.4 (d) are a qualitative measure at low concentrations. It can be concluded that PMDA leads to a controlled and defined structure, starting as a

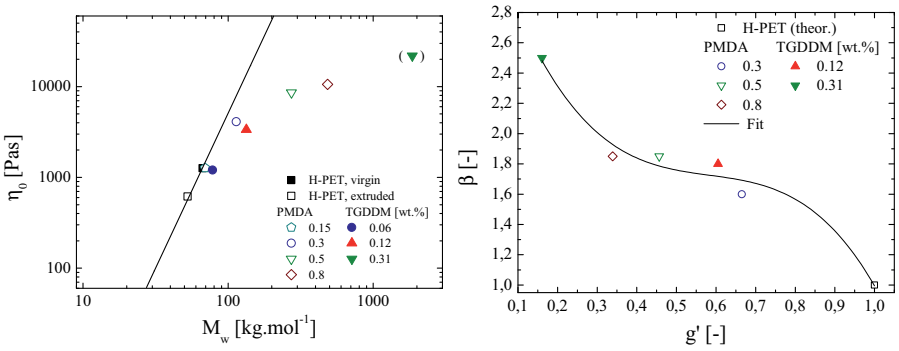

Figure 6.5: Comparison of the molar mass with zero-shear viscosity dependence with 3.4 power law denoted as solid line (a) and the coil contraction factor g' with parameter beta and polynomial fitting of 3^{rd} order (b) for H-PET with PMDA and TGDDM.

star-like conformation at low concentration and leading to a comb-like structure at high concentrations for H-PET.

6.2 Relation to Rheology

A fundamentally different rheological behavior can be observed for different structures of branched molecules in regards to linear, star-like, H-shape, comb-like, tree-like (Cayley) or irregular LCB arrangement (Auhl et al., 2004; Larson, 1999; McLeish and Milner, 1999). The main causes of the difference are related to mechanisms of polymer motion, which are reptation, primitive path fluctuation, constraint release, and the Rouse relaxation (Dealy and Larson, 2006).

As can be noted in Figure 6.5, the addition of different chain extenders and different chain extender concentrations reveals a distinctly different relation between molar mass and zero-shear viscosity. The solid line represents the 3.4 power law applied on the unprocessed H-PET. The extruded reference agrees with the predictions, which emphasizes the observed shear degradation during extrusion. The plasticizer effect is a minor aspect during extensive processing.

The sample with $0.15wt.\%$ PMDA is close to the virgin sample, although the Mark-Houwink parameter, the contraction factor and the radius of gyration clearly indicates a branched molecule. Since a regular star molecule would lead to a restricted primitive path fluctuation (McLeish and Milner, 1999) and enlarged relaxation time, such polymer would lead to higher η_0 at a constant molar mass. Therefore, the structure can be considered as star-like or H-shaped. This

observation holds also for $0.3wt.\%$, which deviates only slightly from the line predicted. Additionally, this grade revealed a largely increased viscosity during uniaxial elongation experiments, which clearly demonstrated the branching of this sample.

The samples with $0.5wt.\%$ and $0.8wt.\%$ exhibit a lower increase of relaxation times at high molar mass. Due to the structure, the molecules relax relatively fast relating to their molar mass. The molar mass of entanglements for PET is reported with $1450g.mol^{-1}$ (Fetters et al., 2007), which leads to 20 to 25 entanglements of a branched side arm with the observed M_n.

Both samples with $0.5wt.\%$ and $0.8wt.\%$ PMDA can be distinguished by their molecular properties like M_w and R_g, but the difference in intrinsic and dynamic viscosity is small, and the transient elongational viscosity reveals an equal behavior. As seen, the mentioned molecular properties represent only the reacted specimens, in contrast to the viscosity, which is influenced by the blend of branched and linear molecules. It was reported that non-linear behavior of a blend is dictated by the branched fraction (cf. Section 2.1.2), i.e. a few emerged highly branched molecules govern the behavior. The observed deviations between rheological asymptotic behavior and ongoing increase of molar mass and size reflect the sensitivity of rheology, in particular at elongational behavior, to the structure and density of entanglements. If both occur in a certain concentration, an enlarged molecule would have no effect on the flow behavior.

TGDDM exhibits a similar tendency of molar mass and zero-shear viscosity, but deviates more from the linear predictions. The random or tree-like branches govern the structure, as was also observed by the van Gurp-Palmen plot.

A comparison between the coil contraction factor g' and the non-linear parameter β from the MSF model is illustrated in Figure 6.5 (b). Starting from the theoretical value of 1 for a linear polymer, the PMDA treated samples exhibit an increase and a plateau of the branching parameter β with decreasing g', i.e. a higher branching density by a more compact coil. TGDDM behaves in a similar way, in particular the highly branched sample with $0.31wt.\%$ shows a high branching density at melt and diluted state.

6.3 Conclusions

The molecular analysis by SEC triple detection of H-PET reacted with PMDA and TGDDM reveals a strong increase of the average molar masses, polydispersity, radius of gyration, and hydrodynamic radius. The thermal and shear degradation of the reference sample during processing occurred over the whole molar mass distribution and led to a molar mass reduction of 21% and a more narrow distribution. No gel particles could be detected by a $2\mu m$ filter for the

samples investigated. A reaction over the whole molar mass range was observed by adding both chain extenders. The increase of molar mass exhibits an apparent saturation for PMDA based on the number-average, whereas M_w, M_z, and R_g increase linear or exponential for both chain extenders. M_w and M_z were shown to monitor the chain reacted specimen and being unaffected by the linear fraction.

The branching was confirmed by a decreasing Mark-Houwink exponent with increasing chain extender concentration, which was more pronounced for TGDDM samples. The Mark-Houwink parameters and a power law between molar mass and radius of gyration were determined for linear PET. A smaller coil contraction factor, i.e. a more compact structure, was achieved based on the radius of gyration compared to the contraction based on the intrinsic viscosity. Further, the exponent ε as indicator for the structure reveals a more star-like structure for low concentrations of both chain extenders. With increasing concentration, the structure changed to more comb-like for PMDA and random or hyperbranched for TGDDM.

The comparison to the rheological findings show deviations from the 3.4 viscosity versus molar mass power law. PMDA exhibits a star-like or H-shape structure at low concentrations and a regular random or comb-like structure at high concentrations. The branched polymer shows an increase of molar mass and size with high PMDA concentration, but the structure and the branching density is finite, which is reflected by an equal rheological behavior at high concentrations. TGDDM possesses a larger random tree-like or hyperbranched structure. The non-linear parameter β was found to correlate with the coil contraction factor and the branching density.

7 Conclusions

Industrial application and commercial use of poly(ethylene terephthalate) (PET) has increased in recent years, in spite of the fact that processing of the polymer is restricted by degradation and low viscosity, which are limiting factors for processes like film blowing, thermoforming, and recycling. The present work considers molecular changes during processing of commercial linear PET and provides solutions to benefit from the intrinsic reactivity of the molecule. Reactive processing of three multi-functional chain extenders leads to a long-chain branched (LCB) structure and highly improved elongational properties. Investigations were conducted with a commercial twin-screw extruder, which show that a successful polymer modification can be realized at industrial scale. The analysis of the polymer structure was mainly conducted by linear and non-linear rheology, size-exclusion chromatography (SEC) with light scattering (MALS), and modeling of the flow behavior with the molecular stress function (MSF) theory.

Three PET grades produced by different synthesis routes (H-PET and L-PET based on dimethyl terephthalate and l-PET on terephthalic acid) were investigated in regards of thermal and thermo-oxidative degradation. The three grades can be distinguished by molar mass (from high to low: H-, L-, l-PET) and concentration of functional carboxyl and hydroxyl end groups.

Thermal stability measurements with a parallel plate geometry in the linear viscoelastic regime were conducted. The measurements exhibit a degradation mechanism and a reduction of the storage modulus in air atmosphere, and an enhancement of the modulus in nitrogen atmosphere, due to polycondensation. At longer times, the degradation reaction in air atmosphere leads to an increase of the modulus, due to cross-linking induced by oxygen. The enhancement by reaction in nitrogen atmosphere is counteracted by thermal degradation (Kruse et al., 2013). Since both mechanisms occur already before the measurement during heating of the sample, the actual initial state of the polymer was reconstructed by a fitting to zero-loading time. The derived exponential function led to a time constant (Kruse and Wagner, 2016), which reveals clear relations between reactivity and polymer properties such as concentration of end groups, molar mass, and synthesis route for all PET grades in both atmospheres. High molar mass PET is more stable in nitrogen and less stable in air environment, and low molar mass PET is more stable in air but less stable in nitrogen atmo-

sphere. The different behavior can be traced back to the hydroxyl end group concentration, which possesses higher ester- and transesterification potential than carboxyl end groups.

The different degradation effects occurred in a rapid manner which could not be monitored sufficiently by *classical* thermal stability measurement. Consequently, further analysis by means of time-resolved mechanical spectroscopy (TRMS) at 265, 272, 280, and 288°C were necessary, allowing determination of moduli and complex viscosity at a fixed time and a wide range of angular frequencies. It was shown that both thermal and thermo-oxidative degradation lead to small molecules which act as plasticizer. Besides a vertical downward shift of the complex viscosity/frequency curve by degradation in air, severe and concurrent cross-linking was observed leading to a yield stress. On the other hand, in nitrogen atmosphere, polycondensation increases the molar mass, the viscosity and also the width of shear thinning regime.

Additionally, TRMS revealed a diffusion of the side products to the sample boundaries, which influences the determination of moduli and complex viscosity, and promotes apparent slipping (Kruse and Wagner, 2016). Degradation, diffusion, and cross-linking effects were also confirmed by samples prepared by compression molding in air and nitrogen atmosphere.

A routine for determination of reliable master curves was established for G' and G'' data. Small differences between dynamic, rotational and capillary shear flow measurements were found due to different experimental protocols used, but small enough to conclude that the Cox-Merz relation is valid. The contribution of stretching during converging die enttrance flow can be neglected for linear PET, as confirmed by Bagley correction and direct measurement of the entrance pressure loss by an orifice die.

The extrusion of neat PET with a Leistritz co-rotating twin-screw extruder was conducted to investigate the mechanisms of thermal and thermo-oxidative degradation, polycondensation and shear degradation on processing at industrial scale. The main degradation mechanism during extrusion was identified as a consequence of shearing. The impact of thermo-oxidative degradation is comparably small. This emphasizes the need of moderate shear conditions and the use of a twin-screw extruder for processing, which is known to induce less energy into the material compared to single screw systems.

Three different chain extenders were used to create LCB PET. Pyromellitic dianhydride (PMDA) is a tetra-functional chain extender possessing a preferred OH group reactivity, tetraglycidyl diamino diphenyl methane (TGDDM) is an epoxy-based tetra-functional chain extender which tends to a reaction with COOH groups, and triphenyl phosphite (TPP) is a tri-functional coupling agent and needs both groups for a successful application. The chain extension experiments were first conducted in a torque rheometer (*Brabender*). The

batch experiments revealed a correlation of the chain extender employed with the corresponding PET end group reactivity, which leads to the conclusion that the type and amount of chain extender necessary depends on the type of PET end group.

All three PET grades investigated showed a successful increase of viscosity both with PMDA and with TGDDM. This was confirmed by reactive extrusion with the twin-screw extruder, and online measurements showed an increasing and stable pressure. From the batch experiments it was found that TPP is not a useful chain extender due to rapid degradation and toxicity, and its application cannot be recommended.

The reactive extrusion of H-, L-, and l-PET with PMDA and TGDDM as chain extenders leads to high molar mass and long-chain branched poly(ethylene terephthalate). This was proven by a fundamentally different rheological behavior, which can be related to the initial molar mass and synthesis route of the virgin PETs. The processed grades show a strongly increasing dynamic and transient elongational viscosity, increasing strain hardening, and increasing thermal stability with increasing chain extender concentration.

The dynamic linear viscoelastic analysis revealed a broader spectrum of relaxation times due to large molecules generated. The zero-shear viscosity is increased by two decades and the shear thinning onset is shifted to lower frequencies. The activation energy of flow shows strong indication of LCB formation for both chain extenders. The analysis of the loss angle by the van Gurp-Palmen plot reveals a thermo-rheological complex material for high chain extender concentrations, in particular for L-PET and l-PET with PMDA. The TGDDM specimens exhibit a large second relaxation process indicating extensive LCB formation or hyperbranching.

The elongation measurements show a saturation effect for H-PET processed with PMDA, and a defined and reproducible structure of such saturated grades. L-PET and l-PET exhibit a similar structure consistency, but also a potential for higher branching and molar mass for higher PMDA concentrations. The MSF model predictions show good agreement with data measured, and allowed a quantitative analysis of the branching structure and of the stretch of the molecules by both non-linear MSF parameters, β and f^2_{max}. Compared to H-PET, the two initially low molar mass L-PET and l-PET show a higher molar mass and seem to have a tree-like structure after reactive extrusion. The TGDDM samples exhibit a dependence on concentration of COOH groups at low concentrations, while at high concentration side reactions such as homopolymerization of TGDDM and random attacks at the backbone of PET occur. The use of $0.31 wt.\%$ TGDDM leads to a gel-like structure, which was confirmed by the linear viscoelastic measurements. A comparison of linear and non-linear viscoelastic results reveals differences at high chain extender concen-

trations, apparently due to different sensitivity of both methods to the blend composition, consisting of linear and branched chains created. However, the LCB structure was found to be reproducible and similar, e.g. for L-PET and l-PET at $0.8wt.\%$ PMDA, by non-linear measurements and the MSF model.

The analysis of the fracture behavior in elongational flow revealed a limiting stress value of the order $10MPa$ for PMDA treated L-PET and l-PET. In contrast, a limiting strain restricted the elongation of PET with TGDDM, which leads to the conclusion that a permanent covalent network governs the fracture. These findings need to be considered for the potential application of the chain extender. TGDDM leads to a larger strain hardening, which e.g. facilitates blowing, but at high concentrations the same coupling agent would lead to a fracture of the film. PMDA extended PET can stand higher strains, in particular when reacted with high molar mass PET.

The molecular analysis by SEC triple detection of H-PET reacted with PMDA and TGDDM reveals a strong increase of the average molar masses, polydispersity, radius of gyration, and hydrodynamic radius, and confirms the molar mass increase observed by linear and non-linear rheological measurements. The thermal and shear degradation of the reference samples during processing with the twin-screw extruder occurred over the whole molar mass distribution and led to a molar mass reduction of 21% and a more narrow distribution. No gel particles could be detected by a $2\mu m$ filter for all samples. The increase of molar mass exhibits an apparent saturation for PMDA based on the number-average, whereas the weight-average, z-average, and the radius of gyration increase strongly with increasing chain extender concentrations.

The branching was confirmed by a decreasing Mark-Houwink exponent with increasing chain extender concentration, which was more pronounced for TGDDM samples and agrees with the observations by extensional rheological experiments. The Mark-Houwink relation between intrinsic viscosity and molar mass and a power law for the relation between radius of gyrations and molar mass were determined for linear PET. For LCB samples, a smaller coil contraction factor, i.e. a more compact structure, was found based on the radius of gyration compared to the contraction based on the intrinsic viscosity. Further, the exponent ε as indicator for the structure reveals a more star-like structure for low concentrations of both chain extenders. With increasing concentration, the structure changed to more comb-like for PMDA and random tree-like or hyperbranched for TGDDM.
The comparison between SEC-MALS and the rheological findings shows that the non-linear parameter β correlates with the coil contraction factor and that the 3.4 zero-shear viscosity versus molar mass power law is not valid for LCB PET. Interestingly, the branched polymer shows an increase of molar mass and radius of gyration at high PMDA concentration, in contrast to a saturation be-

havior for linear and non-linear viscoelastic properties like zero-shear viscosity and elongational strain hardening. Since the polydispersity increases strongly at these high PMDA concentrations, the light scattering data detects the absolute increase of the high molar mass specimens, which apparently have only a limited impact on the rheology. This demonstrates a limited sensitivity of rheology in this case to properties like weight-average molar mass and radius of gyration, but a high sensitivity to the type and concentration of LCB structure of the molecule. In other words, rheology may not tell us the absolute height of a building but rather its design.

The results presented reveal fundamental changes of the molecular structure during processing. The different mechanisms observed (plasticizer effect, oligomeric deposition, diffusion, shear degradation, thermal and thermo-oxidative degradation, polycondensation) emerge with different impact depending on the processing conditions (atmosphere, temperature, geometry, shear contribution, free surface, time). It was shown that custom-made polymer architectures can be achieved by reactive processing and by certain PET and chain extender combinations. Due to the pronounced shear thinning behavior of long-chain branched PET, a low energy consumption is expected for the processing at high shear rates, e.g. during injection molding or fiber spinning. The advantage of the branched structure and high molar mass can be beneficial for extrusion of profiles, for the stability of film blowing, and crack resistance of parts. The low molar mass grades with high OH end group concentration in combination with PMDA possess a high potential for LCB formation, and the full potential may not yet have been reached during this study. However, PMDA revealed to be an excellent coupling agent which induces reproducible structure, which are either star-like, comb-like, or tree-like depending on the added coupling agent concentration and OH concentration of the PET. Hence, foaming of such polymers can induce different pore structures and sizes. The LCB PET produced and investigated in this study extends the potential of poly(ethylene terephthalate) for new application fields.

Bibliography

S. M. Aharoni, C. E. Forbes, and W. B. Hammond. High-temperature reactions of hydroxyl and carboxyl PET chain end groups in the presence of aromatic phosphite. *Polymer*, 24(6):1281–1296, 1986. doi: 10.1002/pola.1986.080240614.

J. Aho and S. Syrjälä. Evaluation of different methods for determining the entrance pressure drop in capillary rheometry. *Applied Rheology*, 18(6):1–5, 2008.

J. Aho, V. H. Rolón-Garrido, S. Syrjälä, and M. H. Wagner. Extensional viscosity in uniaxial extension and contraction flowComparison of experimental methods and application of the molecular stress function model. *Journal of Non-Newtonian Fluid Mechanics*, 165(5-6):212–218, 2010. doi: 10.1016/j.jnnfm.2009.12.003.

R. Assadi, X. Colin, and J. Verdu. *Polymer*. doi: 10.1016/j.polymer.2004.04.029.

D. Auhl, J. Stange, H. Münstedt, , B. Krause, D. Voigt, A. Lederer, U. Lappan, and K. Lunkwitz. Long-chain branched polypropylenes by electron beam irradiation and their rheological properties. *Macromolecules*, 37(25):9465–9472, 2004. doi: 10.1021/ma030579w.

D. Auhl, F. J. Stadler, and H. Münstedt. Comparison of molecular structure and rheological properties of electron-beam- and gamma-irradiated polypropylene. *Macromolecules*, 45:2057–2065, 2012. doi: 10.1021/ma202265w.

F. Awaja and D. Pavel. Recycling of PET. *European Polymer Journal*, 41(7):1453–1477, 2005. doi: 10.1016/j.eurpolymj.2005.02.005.

F. Awaja, F. Daver, and E. Kosior. Recycled poly(ethylene terephthalate) chain extension by a reactive extrusion process. *Polymer Engineering & Science*, 44(8):1579–1587, 2004. doi: 10.1002/pen.20155.

J. D. Badia, F. Vilaplana, S. Karlsson, and A. Ribes-Greus. Thermal analysis as a quality tool for assessing the influence of thermo-mechanical degradation on recycled poly (ethylene terephthalate). *Polymer Testing*, 28(2):169–175, 2009. doi: 10.1016/j.polymertesting.2008.11.010.

E. B. Bagley. End corrections in the capillary flow of polyethylene. *Journal of Applied Physics*, 28(5):624–627, 1957. doi: 10.1063/1.1722814.

M. Baumgaertel and H. H. Winter. Determination of discrete relaxation and retardation time spectra from dynamic mechanical data. *Rheologica Acta*, 28 (6):511–519, 1989. doi: 10.1007/BF01332922.

S. A. Berkowitz. Specific Refractive Index Increment Measurements on Macromolecules Using a Waters R401 Differential Refractometer. *Journal of Liquid Chromatography*, 6(8):1359–1979, 1983. doi: 10.1080/01483918308064857.

S. A. Berkowitz. Viscosity-molecular weight relationships for poly (ethylene terephthalate) in hexafluoroisopropanol pentafluorophenol using SEC-LALLS. *Polymer*, 29(12):4353–4361, 1984. doi: 10.1002/app.1984.070291264.

G. C. Berry. Translational frictional constant of comb-branched polymers. *Journal of Polymer Science: Part a-2: Polymer Physics*, 6(8):1551–1554, 1968. doi: 10.1002/pol.1968.160060811.

G. C. Berry. Remarks on a relation among the intrinsic viscosity, the radius of gyration, and the translational friction coefficient. *Journal of Polymer Science: Part B: Polymer Physics*, 26(5):1137–1142, 1988. doi: 10.1002/polb.1988.090260517.

D. N. Bikiaris and G. P. Karayannidis. Chain extension of polyesters PET and PBT with N,N-bis(glycidyl ester) pyromellitimides.1. *Journal of Polymer Science: Part A: Polymer Chemistry*, 33(10):1705–1714, 1995. doi: 10.1002/pola.1995.080331017.

D. N. Bikiaris and G. P. Karayannidis. Chain extension of polyesters PET and PBT with two new diimidodiepoxides.2. *Journal of Polymer Science: Part A: Polymer Chemistry*, 34(7):1337–1342, 1996. doi: 10.1002/(SICI)1099-0518(199605)34:7⟨1337::AID-POLA22⟩3.0.CO;2-9.

R. B. Bird, R. C. Armstrong, and O. Hassager. *Dynamics of polymeric liquids, Volume 1: Fluid mechanics, 2nd Edition*. Wiley & Sons, Inc., New York, 1987. ISBN 9780471802457.

R. H. Boyd and P. J. Phillips. *The science of polymer molecules*. Cambridge University Press, Cambridge, 1996. ISBN 9780521565080.

F. Bueche. The viscoelastic properties of plastics. *Journal of Chemical Physics*, 22(4):603–609, 1954. doi: 10.1063/1.1740133.

L. H. Buxbaum. The degradation of poly(ethylene terephthalate). *Angewandte Chemie International Edition in English*, 7(3):182–190, 1968. doi: 10.1002/anie.196801821.

N. Cardi, R. Po, G. Giannotta, E. Occhiello, F. Garbassi, and G. Messina. Chain extension of recycled poly (ethylene terephthalate) with 2,2-bis(2-oxazoline). *Journal of Applied Polymer Science*, 50(9):1501–1509, 1993. doi: 10.1002/app.1993.070500903.

P. J. Carreau, D. C. R. D. Kee, and R. P. Chhabra. *Rheology of Polymeric Systems. Principles and Applications*. Hanser/Gardner Publications, Cincinnati, 1997. ISBN 9781569902189.

P. Cassagnau, V. Bounor-Legaré, and F. Fenouillot. Reactive processing of thermoplastic polymers: A review of the fundamental aspects. *Intern. Polymer Processing*, 22(3):218–258, 2007. doi: 10.3139/217.2032.

F. Chambon and H. H. Winter. Linear viscoelasticity at the gel point of a crosslinking PDMS with imbalanced stoichiometry. *Journal of Rheology*, 31 (8):683–697, 1987. doi: 10.1122/1.549955.

I. Coccorullo, L. Di Maio, S. Montesano, and L. Incarnato. Theoretical and experimental study of foaming process with chain extended recycled PET. *Polymer*, 3(2):84–96, 2009. doi: 10.3144/expresspolymlett.2009.12.

F. N. Cogswell. Converging flow of polymer melts in extrusion dies. *Polymer Engineering and Science*, 12(1):64–73, 1972. doi: 10.1002/pen.760120111.

F. N. Cogswell. Converging flow and stretching flow - Compilation. *Journal of Non-Newtonian Fluid Mechanics*, 4(1-2):23–38, 1978. doi: 10.1016/0377-0257(78)85004-6.

F. N. Cogswell. *Polymer Melt Rheology*. John Wiley & Sons, New York & Toronto, 1981. ISBN 9781855731981.

X. Colin and J. Verdu. Polymer degradation during processing. *Comptes Rendus Chimie*, 9(11-12):1380–1395, 2006. doi: 10.1016/j.crci.2006.06.004.

M. B. Coltelli, S. Bianchi, and M. Aglietto. Poly(ethylene terephthalate) (PET) degradation during the Zn catalysed transesterification with dibutyl maleate functionalized polyolefins. *Polymer*, 48(5):1276–1286, 2007. doi: 10.1016/j.polymer.2006.12.043.

J. M. G. Cowie and P. M. Toporowski. Dependence of glass temperature on molecular weight for poly alpha-methyl styrene. *European Polymer Journal*, 4(5):621–625, 1968. doi: 10.1016/0014-3057(68)90060-8.

W. P. Cox and E. H. Merz. Correlation of dynamic and steady flow viscosities. *Polymer*, 28(118):619–622, 1958. doi: 10.1002/pol.1958.1202811812.

F. Daver, R. Gupta, and E. Kosior. Rheological characterisation of recycled poly (ethylene terephthalate) modified by reactive extrusion. *Journal of Materials Processing Technology*, 204(1-3):397–402, 2008. doi: 10.1016/j.jmatprotec.2007.11.090.

J. Dealy and R. Larson. *Structure and rheology of molten polymers*. Hanser Publication, Munich, 1. edition, 2006. ISBN 9783446217713. doi: 10.3139/9783446412811.

A. H. Dekmezian, W. W. Q. Weng, C. A. Garcia-Franco, and E. J. Markel. Melt strength of blends of linear low density polyethylene and comb polymers. *Polymer*, 45:5635–5640, 2004. doi: 10.1016/j.polymer.2004.03.075.

R. Dhavalikar, M. Yamaguchi, and A. Xanthos. Molecular and Structural Analysis of a Triepoxide-Modified Poly (ethylene terephthalate) from Rheological Data. *Journal of Polymer Science: Part A: Polymer Chemistry*, 41(7):958–969, 2003. doi: 10.1002/pola.10641.

M. Doi. Explanation for the 3.4 power law for viscosity of polymeric liquids on the basis of the tube model. *Journal of Polymer Science Part B - Polymer Physics Edition*, 21(5):667–684, 1983. doi: 10.1002/pol.1983.180210501.

M. Doi and S. F. Edwards. Dynamics of concentrated polymer systems. 2. Molecular-motion under flow. *Journal of the Chemical Society - Faraday Transactions II*, 74(10):1802–1817, 1978. doi: 10.1039/F29787401802.

M. Doi and S. F. Edwards. *The theory of polymer dynamics*. Oxford University Press, 1986. ISBN 9780198520337.

A. Einstein. Motion of suspended particles on the kinetic theory. *Annalen der Physik*, 17(3):549–560, 1905.

J. D. Ferry. *Viscoelastic properties of polymers*. John Wiley & Sons, New York, 3. edition, 1980. ISBN 9780471048947.

L. J. Fetters, D. J. Lohse, and C. R. H. Chain dimensions and entanglement spacings. In J. E. Mark, editor, *Physical Properties of Polymers Handbook*, chapter 25, page 1076. Springer-Verlag, New York, 2. edition, 2007. doi: 10.1007/978-0-387-69002-5.

G. Filippone, S. C. Carroccio, R. Mendichi, L. Gioiella, N. T. Dintcheva, and C. Gambarotti. Time-resolved rheology as a tool to monitor the progress of

polymer degradation in the melt state - Part I: Thermal and thermo-oxidative degradation of polyamide 11. *Polymer*, 72:134–141, 2015. ISSN 0032-3861. doi: 10.1016/j.polymer.2015.06.059.

P. J. Flory. *Principles of Polymer Chemestry*. Cornell University Press Ltd, London, 8. (1971) edition, 1953. ISBN 9780801401343.

J. S. Forsythe, K. Cheah, D. R. Nisbet, R. K. Gupta, A. Lau, A. R. Donovan, M. S. O. Shea, and G. Moad. Rheological properties of high melt strength poly (ethylene terephthalate) formed by reactive extrusion. *Polymer*, 100(5): 3646–3652, 2006. doi: 10.1002/app.23166.

T. G. Fox and P. J. Flory. 2nd-order transition temperatures and related properties of polystyrene.I. Influence of molecular weight. *Journal of Applied Physics*, 21(6):581–591, 1950. doi: 10.1063/1.1699711.

C. Gabriel and H. Münstedt. Strain hardening of various polyolefins in uniaxial elongational flow. *Journal of Rheology*, 47(3):619–630, 2003. doi: 10.1122/1.1567752.

P. G. D. Gennes. Reptation of a polymer chain in the presence of fixed obstacles. *Journal of Chemical Physics*, 55(2):572–578, 1971. doi: 10.1063/1.1675789.

W. Gleissle. A simple relation combining transient zero shear viscosity with pseudoplastic flow behavior. *Journal of Rheology*, 24(6):919–920, 1980.

J. W. Goodwin and R. W. Hughes. *Rheology for chemists: An introduction*. The Royal Society of Chemistry, Cambridge, 2000. ISBN 9780854046164.

M. S. Green and A. V. Tobolsky. A new approach to the theory of relaxing polymeric media. *Journal of Chemical Physics*, 14(2):80–92, 1946. doi: 10.1063/1.1724109.

G. K. Guenther and D. G. Baird. Rheology of a textured fluid consisting of poly(ethylene terephthalate) and nylon 6,6. *Journal of Applied Polymer Science*, 59(5):845–859, 1996. doi: 10.1002/(SICI)1097-4628(19960131)59:5⟨845::AID-APP11⟩3.0.CO;2-L.

C. D. Han. *Rheology and processing of polymeric materials - Volume I polymer rheology*. Oxford University Press, 2007. ISBN 9780195187823.

M. Härth, J. Kaschta, and D. W. Schubert. Shear and elongational flow properties of long-chain branched poly(ethylene terephthalates) and correlations to their molecular structure. *Macromolecules*, 47(13):4471–4478, 2014. doi: 10.1021/ma5002657.

M. Härth, J. Kaschta, and D. W. Schubert. Rheological study of the reaction kinetics in a poly (ethylene terephthalate) melt. *Polymer Degradation and Stability*, 120:70–75, 2015. doi: 10.1016/j.polymdegradstab.2015.06.001.

S. G. Hatzikiriakos, G. Heffner, D. Vlassopoulos, and K. Christodoulou. Rheological characterization of polyethylene terephthalate resins using a multimode Phan-Tien-Tanner constitutive relation. *Rheologica acta*, 36(5):568–578, 1997. doi: 10.1007/BF00368134.

P. Haupt. *Continuum mechanics and theory of materials*. Berlin Heidelberg, Berlin Heidelberg, 2002. ISBN 9783540431114. doi: 10.1007/978-3-662-04775-0.

W. Hu. *Polymer physics a molecular approach*. Springer-Verlag, Wien, 1 edition, 2013. ISBN 9783709117538. doi: 10.1007/978-3-7091-0670-9.

J. P. Ibar, Z. Zhang, Z. M. Li, and A. Santamaria. Investigation of the dynamic rheological properties of a polycarbonate melt presenting solid-like characteristics and a departure from pure liquid newtonian behavior at long relaxation times. *Journal of Macromolecular Science, Part B: Physics*, 54(6):649–710, 2015. doi: 10.1080/00222348.2015.1029411.

H. Inata and S. Matsumura. Chain extenders for polyesters. I. Addition-type chain extenders reactive with carboxyl end groups of polyesters. *Journal of Applied Polymer Science*, 30(8):3325–3337, 1985. doi: 10.1002/app.1985.070300815.

H. Inata and S. Matsumura. Chain extenders for polyesters. III. Addition-type nitrogen-containing chain extenders reactive with hydroxyl end groups of polyesters. *Journal of Applied Polymer Science*, 32(4):4581–4594, 1986. doi: 10.1002/app.1986.070320423.

H. Inata and S. Matsumura. Chain extenders for polyesters. IV. Properties of the polyesters chain-extended by 2,2-bis(2-oxazoline). *Journal of Applied Polymer Science*, 33(8):3069–3079, 1987. doi: 10.1002/app.1987.070330838.

L. Incarnato, P. Scarfato, L. D. Maio, and D. Acierno. Structure and rheology of recycled PET modified by reactive extrusion. *Polymer*, 41(18):6825–6831, 2000. doi: 10.1016/S0032-3861(00)00032-X.

L. P. B. M. Janssen. On the stability of reactive extrusion. *Polymer Engineering and Science*, 38(12):2010–2019, 1998. doi: 10.1002/pen.10370.

S. Japon, L. Boogh, Y. Leterrier, and J. A. E. Månson. Reactive processing of poly(ethylene terephthalate) modified with multifunctional epoxy-based

additives. *Polymer*, 41(15):5809–5818, 2000a. doi: 10.1016/S0032-3861(99)00768-5.

S. Japon, Y. Leterrier, and J. A. E. Månson. Recycling of poly(ethylene terephthalate) into closed-cell foams. *Polymer Engineering and Science*, 40(8):1942–1952, 2000b. doi: 10.1002/pen.11326.

S. Japon, A. Luciani, Q. T. Nguyen, Y. Leterrier, and J. A. E. Månson. Molecular characterization and rheological properties of modified poly(ethylene terephthalate) obtained by reactive extrusion. *Polymer Engineering and Science*, 41(8):1299–1309, 2001. doi: 10.1002/pen.10830.

R. T. Johnson and E. J. Morrison. Thermal scission and cross-linking during polyethylene melt. In R. L. Clough, N. C. Billingham, and K. T. Gillen, editors, *Polymer Durability - Degradation, Stabiliazion, and Lifetime Prediction*, chapter 39, page 728. American Chemical Society, Washington DC, advances i edition, 1996. ISBN 9780841231344.

G. P. Karayannidis and E. A. Psalida. Chain extension of recycled poly(ethylene terephthalate) with 2,2'-(1,4-phenylene)bis(2-oxazoline). *Journal of Applied Polymer Science*, 77(10):2206–2211, 2000. doi: 10.1002/1097-4628(20000906)77:10⟨2206::AID-APP14⟩3.0.CO;2-D.

G. P. Karayannidis, D. E. Kokkalas, and D. N. Bikiaris. Solid-state polycondensation of poly(ethylene terephthalate) recycled from postconsumer soft-drink bottles.1. *Journal of Applied Polymer Science*, 50(12):2135–2142, 1993. doi: 10.1002/app.1993.070501213.

G. P. Karayannidis, D. E. Kokkalas, and D. N. Bikiaris. Solid-state polycodensation of poly(ethylene-terephthalate) recycled from postconsumer soft-drink bottles.2. *Journal of Applied Polymer Science*, 56(3):405–410, 1995. doi: 10.1002/app.1995.070560311.

S. Kheirandish. *Constitutive Equations for Linear and Long-Chain-Branched Polymer Melts*. PhD thesis, Berlin, 2005.

S. B. Kil, T. Augros, Y. Leterrier, J. A. E. Manson, A. Christel, and C. Borer. Rheological properties of hyperbranched polymer/poly(ethylene terephthalate) reactive blends. *Polymer Engineering and Science*, 43(2):329–343, 2003. doi: 10.1002/pen.10028.

B. K. Kim, H. M. Jeong, and Y. H. Lee. Melt rheology of poly(ethylene terephthalate), polyarylate, and their blends. *Journal of Applied Polymer Science*, 40(11-12):1805–1818, 1990. doi: 10.1002/app.1990.070401101.

S. Kim and J. M. Dealy. Design of an orifice die to measure entrance pressure drop. *Journal of Rheology*, 45(6):1413–14–19, 2001. doi: 10.1122/1.1410374.

P. Kratochvil. Particle Scattering Function. In M. B. Huglin, editor, *Light Scattering from Polymer Solutions*, chapter 7, pages 333–384. Academic Press, London and New York, 1972. ISBN 0123610508.

M. Kruse and M. H. Wagner. Time-resolved rheometry of poly(ethylene terephthalate) during thermal and thermo-oxidative degradation. *Rheologica Acta*, 55(10):789–800, 2016. doi: 10.1007/s00397-016-0955-2.

M. Kruse, V. H. Rolón-Garrido, and M. H. Wagner. Rheological characterization of degradation and polycondensation of poly(ethylene terephthalate) melt in air and in nitrogen. *AIP Conference Proceedings*, 1526:216–229, 2013. doi: 10.1063/1.4802616.

W. Kuhn. Shape of fibre-forming molecules in solutions. *Kolloid Zeitschrift*, 68:2–15, 1934. doi: 10.1007/BF01451681.

R. G. Larson. *Constitutive equations for polymer melts and solutions*. Butterworth-Heinemann, Boston, 1988. ISBN 9780409901191.

R. G. Larson. *The structure and rheology of complex fluids*. Oxford University Press, New York & Oxford, 1999. ISBN 9780195121971.

H. M. Laun and H. Schuch. Transient Elongational Viscosities and Drawability of Polymer Melts. *Journal of Rheology*, 33(1):119–175, 1989. doi: 10.1122/1.550058.

P. J. R. Leblans, J. Sampers, and H. C. Booij. The mirror relations and nonlinear viscoelasticity of polymer melts. *Rheologica Acta*, 24(2):152–158, 1985. doi: 10.1007/BF01333243.

M. D. Lechner, K. Gehrke, and E. H. Nordmeier. *Makromolekulare Chemie: Ein Lehrbuch für Chemiker, Physiker, Materialwissenschaftler und Verfahrenstechniker*. Springer Spektrum, Berlin Heidelberg, 5. edition, 2014. ISBN 364241768X. doi: 10.1007/978-3-7643-8891-1.

D. C. Leigh. *Nonlinear continuum mechanics*. McGraw-Hill Education - Europe, New York, 1968. ISBN 9780070370852.

A. S. Lodge. A network theory of flow birefringence and stress in concentrated polymer solutions. *Trans. Faraday Soc.*, 52:120–130, 1956. doi: 10.1039/tf9565200120.

D. J. Lohse, S. T. Milner, L. J. Fetters, M. Xenidou, N. Hadjichristidis, R. A. Mendelson, C. A. García-Franco, and M. K. Lyon. Well-defined, model long chain branched polyethylene. 2. Melt rheological behavior. *Macromolecules*, 35(8):3066–3075, 2002. doi: 10.1021/ma0117559.

Y. Ma, U. S. Agarwal, D. J. Sikkema, and P. J. Lemstra. Solid-state polymerization of PET: influence of nitrogen sweep and high vacuum. *Polymer*, 44 (15):4085–4096, 2003. doi: 10.1016/S0032-3861(03)00408-7.

C. W. Macosko. *Rheology: Principles, Measurements, and Applications*. John Wiley & Sons, Poughkeepsie, NY, 1994. ISBN 9780471185758.

G. Madras and B. J. McCoy. Oxidative degradation kinetics of polystyrene in solution. *Chemical Engineering Science*, 52(16):2707–2713, 1997. doi: 10.1016/S0009-2509(97)00091-2.

G. Marrucci and N. Grizzuti. The free energy function relaxation of the Doi-Edwards theory: Analysis of the instabilities in stress. *Journal of Rheology*, 27(5):433–450, 1983. doi: 10.1122/1.549715.

I. Marshall and A. Todd. The thermal degradation of polyethylene terephthalate. *Transaction of the Faraday Society*, 49:67–78, 1953. doi: 10.1039/tf9534900067.

J. E. McIntyre. The historical development of polyesters. In J Scheirs and T. E. Long, editors, *Modern polyesters: chemistry and technology of polyesters and copolyesters*, chapter 1, pages 3–28. John Wiley & Sons Ltd, Chichester, 2003. doi: 10.1002/0470090685.ch1.

T. C. B. McLeish and S. T. Milner. Entangled dynamics and melt flow of branched polymers. *Advances in Polymer Science*, 143:195–256, 1999.

E. Mitsoulis, S. G. Hatzikiriakos, K. Christodoulou, and D. Vlassopoulos. Sensitivity analysis of the Bagley correction to shear and extensional rheology. *Rheologica Acta*, 37(5):438–448, 1998. doi: 10.1007/s003970050131.

S. Mori and H. G. Barth. *Size exclusion chromatography*. Springer, Berlin Heidelberg, 1999. ISBN 9783642084935.

M. Mours and H. H. Winter. Time-resolved rheometry. *Rheologica Acta*, 33(5): 385–397, 1994. doi: 10.1007/BF00366581.

H. Münstedt. Dependence of the elongational behavior of polystyrene melts on molecular weight and molecular weight distribution. *Journal of Rheology*, 24 (6):847–867, 1980. doi: 10.1122/1.549587.

H. Münstedt and D. Auhl. Rheological measuring techniques and their relevance for the molecular characterization of polymers. *Journal of Non-Newtonian Fluid Mechanics*, 128(1):62–69, 2005. doi: 10.1016/j.jnnfm.2005.03.011.

H. Münstedt and F. R. Schwarzl. *Deformation and flow of polymeric materials*. Springer-Verlag, Berlin Heidelberg, 2014. ISBN 9783642554087. doi: 10.1007/978-3-642-55409-4.

H. Münstedt, S. Kurzbeck, and J. Stange. Importance of elongational properties of polymer melts for film blowing and thermoforming. *Polymer Engineering and Science*, 46(9):1190–1195, 2006. doi: 10.1002/pen.20588.

L. K. Nait-Ali, X. Colin, and A. Bergeret. Kinetic analysis and modelling of PET macromolecular changes during its mechanical recycling by extrusion. *Polymer Degradation and Stability*, 96(2):236–246, 2011. doi: 10.1016/j.polymdegradstab.2010.11.004.

E. Narimissa and M. H. Wagner. A hierarchical multimode molecular stress function model for linear polymer melts in extensional flows. *Journal of Rheology*, 60(4):625–636, 2016a. doi: 10.1122/1.4953442.

E. Narimissa and M. H. Wagner. From linear viscoelasticity to elongational flow of polydisperse linear and branched polymer melts: The hierarchical multi-mode molecular stress function model. *Polymer*, in press(-):–, 2016b.

K. Ogura and M. H. Wagner. *Rheologica Acta*.

K. Ogura, K. Morioka, Y. Tsujii, S. Y. Hsu, and M. H. Wagner. Uniaxial extensional flow behavior of comb-shaped poly(methyl methacrylate). *Journal of Polymer Science*, 54(7):637–645, 2015. doi: 10.1007/s00397-013-0714-6.

M. Paci and F. P. La Mantia. Competition between degradation and chain extension during processing of reclaimed poly(ethylene terephthalate). *Polymer Degradation and Stability*, 61(3):417–420, 1998. doi: 10.1016/S0141-3910(97)00227-9.

N. Phan-Thien. *Understanding viscoelasticity*. Springer-Verlag Berlin Heidelberg, Berlin Heidelberg, 2002. ISBN 9783662107041. doi: 10.1007/978-3-662-10704-1.

Plastics Europe. Plastics the facts 2014/2015 An analysis of European plastics production, demand and waste data. Technical report, 2015.

S. Podzimek. *Light scattering, size exclusion chromatography and asymmetric flow field flow fractionation: Powerful tools for the characterization of polymers, proteins and nanoparticles*. John Wiley & Sons, 2011, Hoboken, New Jersey, 2011. ISBN 9780470386170.

S. Podzimek. Importance of multi-angle light scattering in polyolefin characterization. *Macromolecular Symposia*, 330(1):81–91, 2013. doi: 10.1002/masy.201300014.

B. Rabinowitsch. Viscosity and elasticity of sols. *Zeitschrift fur Physikalische Chemie A*, 145(1):1–26, 1929.

W. Radke and A. H. E. Müller. Synthesis and characterization of comb-shaped polymers by SEC with on-line light scattering and viscometry detection. *Macromolecules*, 38(9):3949–3960, 2005. doi: 10.1021/ma047799+.

P. Raffa, M. B. Coltelli, S. Savi, S. Bianchi, and V. Castelvetro. Chain extension and branching of poly(ethylene terephthalate) (PET) with di- and multifunctional epoxy or isocyanate additives: An experimental and modelling study. *Reactive and Functional Polymers*, 72(1):50–60, 2012. ISSN 1381-5148. doi: 10.1016/j.reactfunctpolym.2011.10.007.

A. Ravve. *Principles of Polymer Chemistry*. Springer, New York, 3. edition, 2012. doi: 10.1007/978-1-4614-2212-9.

T. Rieckmann and S. Völker. Poly(ethylene Terephthalate) Polymerization Mechanism, Catalysis, Kinetics, Mass Transfer and Reactor Design. In J. Scheirs, editor, *Modern Polyesters: Chemistry and Technology of Polyesters and Copolyesters*, pages 31–116. John Wiley & Sons Ltd, Chichester, 1. edition, 2004. doi: 10.1002/0470090685.ch2.

V. H. Rolón-Garrido. The molecular stress function (MSF) model in rheology. *Rheologica Acta*, 53:663–700, 2014. doi: 10.1007/s00397-014-0787-x.

V. H. Rolón-Garrido and M. H. Wagner. The MSF model: relation of nonlinear parameters to molecular structure of long-chain branched polymer melts. *Rheologica Acta*, 46(5):583–593, 2007. doi: 10.1007/s00397-006-0136-9.

V. H. Rolón-Garrido and M. H. Wagner. The damping function in rheology. *Rheologica Acta*, 48(3):245–284, 2009. doi: 10.1007/s00397-008-0308-x.

V. H. Rolón-garrido and M. H. Wagner. Linear and non-linear rheological characterization of photo-oxidative degraded LDPE. *Polymer Degradation and Stability*, 99:136–145, 2014. doi: 10.1016/j.polymdegradstab.2013.11.014.

V. H. Rolón-Garrido and M. H. Wagner. Elongational rheology and cohesive fracture of photo-oxidated LDPE. *Journal of Rheology*, 58(1):199–222, 2014. doi: 10.1122/1.4853395.

V. H. Rolón-Garrido, M. Zatloukal, and M. H. Wagner. Increase of long-chain branching by thermo-oxidative treatment of LDPE: Chromatographic, spectroscopic, and rheological evidence. *Journal of Rheology*, 57(1):105–129, 2013. doi: 10.1122/1.4763567.

V. H. Rolón-Garrido, M. Kruse, and M. H. Wagner. Size exclusion chromatography of photo-oxidated LDPE by triple detection and its relation to rheological behavior. *Polymer Degradation and Stability*, 111:46–54, 2015. doi: 10.1016/j.polymdegradstab.2014.10.022.

R. F. Rosu, R. A. Shanks, and S. N. Bhattacharya. Dynamic rheology of branched poly (ethylene terephthalate). *Polymer International*, 49(2):203–208, 2000. doi: 10.1002/(SICI)1097-0126(200002)49:2⟨203::AID-PI329⟩3.0.CO;2-Q.

P. E. Rouse. A theory of the linear viscoelastic properties of dilute solutions of coiling polymers. *Chemical Physics*, 21(7):1272–1280, 1953. doi: 10.1063/1.1699180.

M. Rubinstein and R. H. Colby. *Polymer physics*. Oxford University Press, Oxford, New York, 1. edition, 2003. ISBN 9780198520597.

J. Scheirs. Recycling of PET. In J. Scheirs, editor, *Polymer recycling science, technology and applications*, chapter 4, page 614. John Wiley & Sons, Chichester, 1. edition, 1998. ISBN 9780471970545.

J. Scheirs. Additives for the modification of poly (ethylene terephthalate) to produce engineering-grade polymers. In L. T. E. Scheirs, J, editor, *Modern polyesters: chemistry and technology of polyesters and copolyesters*, chapter 14, pages 495–541. John Wiley & Sons Ltd, Chichester, 1. edition, 2004. ISBN 0471498564. doi: 10.1002/0470090685.ch14.

J. Scheirs and T. E. Long. *Modern polyesters : chemistry and technology of polyesters and copolyesters*. John Wiley & Sons Ltd, Chichester, 2004. ISBN 9780471498568. doi: 10.1002/0470090685.

D. Schulze, T. Roths, and C. Friderich. Classification of model topologies using the delta versus G* plot. *Rheologica Acta*, 44:485–494, 2005. doi: 10.1007/s00397-004-0429-9.

F. R. Schwarzl. Numerical calculation of stress relaxation modulus from dynamic data for linear viscoelastic material. *Rheologica Acta*, 14(7):581–590, 1975. doi: 10.1007/BF01520809.

M. L. Sentmanat. Miniature universal testing platform: from extensional melt rheology to solid-state deformation behavior. *Rheologica Acta*, 43(6):657–669, 2004. doi: 10.1007/s00397-004-0405-4.

K. S. Seo and J. D. Cloyd. Kinetics of hydrolysis and thermal degradation of polyester melts. *Journal of Applied Polymer Science*, 42(3):845–850, 1991. doi: 10.1002/app.1991.070420330.

R. Simha and R. F. Boyer. On a general relation involving the glass temperature and coefficients of expansion of polymers. *Journal of Chemical Physics*, 37 (5):1003–1007, 1962. doi: 10.1063/1.1733201.

A. M. C. Souza, D. S. Lepretre, N. R. Demarquette, M. F. Lacrampe, and P. Krawczak. Influence of water content, time, and temperature on the rheological behavior of polyethylene terephtalate. *Journal of Applied Polymer Science*, 116(6):3525–3533, 2010. doi: 10.1002/app.31885.

G. Strobl. *The physics of polymers*. Springer-Verlag, Berlin, Heidelberg, 3. edition, 2007. ISBN 9783540252788. doi: 10.1007/978-3-540-68411-4.

S. Tate and H. Narusawa. Thermal degradation and melt viscosity of ultra-high-molecular-weight poly(ethylene terephthalate). *Science*, 37(9):1583–1587, 1996. doi: 10.1016/0032-3861(96)83706-2.

S. R. Tharmapuram and S. A. Jabarin. Processing characteristics of PET/PEN Blends, Part 2: rheology and degradation kinetics. *Advances in Polymer Technologypolymer*, 22(2):147–154, 2003. doi: 10.1002/adv.10045.

T. Toda, H. Yoshida, and F. Koushi. Structure and molecular motion changes poly (ethylene terephthalate) induced by annealing under dry and wet conditions. *Polymer*, 36(4):699–706, 1995. doi: 10.1016/0032-3861(95)93097-6.

S. Trinkle and C. Friedrich. Van Gurp-Palmen-plot: a way to characterize polydispersity of linear polymers. *Rheologica Acta*, 40(4):322–328, 2001. doi: 10.1007/s003970000137.

S. Trinkle, P. Walter, and C. Friedrich. Van Gurp-Palmen plot II - classification of long chain branched polymers by their topology. *Rheologica Acta*, 41(1-2): 103–113, 2002. doi: 10.1007/s003970200010.

L. A. Utracki, A. M. Catani, G. L. Bata, M. R. Kamal, and V. Tan. Melt rheology of blends of semicrystalline polymers. I. Degradation and viscosity of poly(ethylene terephthalate)polyamide-6,6 mixtures. *Journal of Applied Polymer Science*, 27(6):1913–1931, 1982. doi: 10.1002/app.1982.070270606.

M. van Gurp and J. Palmen. Time-temperature superposition for polymeric blends. *Rheology Bulletin*, 67:5–8, 1998.

D. W. van Krevelen. *Properties of polymers*. Elsevier Science, Amsterdam, Oxford, 2. edition, 1976. ISBN 9780444414670.

D. W. van Krevelen and K. te Nijenhuis. *Properties of polymers*. Elsevier Science, 4. edition, 2009. ISBN 9780080548197.

E. Van Ruymbeke, R. Keunings, and C. Bailly. Determination of the molecular weight distribution of entangled linear polymers from linear viscoelasticity data. *Journal of Non-Newtonian Fluid Mechanics*, 105(2-3):153–175, 2002. doi: 10.1016/S0377-0257(02)00080-0.

J. Vega, M. Aguilar, J. Peón, D. Pastor, and J. Martínez-Salazar. Effect of long chain branching on linear-viscoelastic melt properties of polyolefins. *e-Polymers*, 2(1):624–685, 2002. doi: 10.1515/epoly.2002.2.1.624.

M. H. Wagner. Analysis of time-dependent non-linear stress-growth data for shear and elongational flow of a low-density branched polyethylene melt. *Rheologica Acta*, 15(2):136–142, 1976. doi: 10.1007/BF01517505.

M. H. Wagner. A constitutive analysis of uniaxial elongational flow data of a low-density polyethylene melt. *Journal of Non-Newtonian Fluid Mechanics*, 4(1-2):39–55, 1978. doi: 10.1016/0377-0257(78)85005-8.

M. H. Wagner. Quantitative analysis of melt elongational behavior of LLDPE/LDPE blends. *Rheologica Acta*, (2):198–218, 2004. doi: 10.1007/s00397-004-0400-9.

M. H. Wagner. Modeling nonlinear rheology of polydisperse polymer melts. *International Journal of Applied Mechanics and Engineering*, 11(2):255–267, 2006.

M. H. Wagner and K. Geiger. The role of the orientation tensor in the rheology of flexible polymers. *Macromolecular Theory and Simulations*, 6(4):703–711, 1997. doi: 10.1002/mats.1997.040060402.

M. H. Wagner and J. Schaeffer. Nonlinear strain measures for general biaxial extension of polymer melts. *Journal of Rheology*, 36(1):1–26, 1992. doi: 10.1122/1.550338.

M. H. Wagner and J. Schaeffer. Rubbers and polymer melts: Universal aspects of nonlinear stress-strain relations. *Journal of Rheology*, 37(4):643–661, 1993. doi: 10.1122/1.550388.

M. H. Wagner, H. Bastian, P. Ehrecke, M. Kraft, P. Hachmann, and J. Meissner. Nonlinear viscoelastic characterization of a linear polyethylene (HDPE) melt in rotational and irrotational flows. *Journal of Non-Newtonian Fluid Mechanics*, 79(2-3):283–296, 1998. doi: 10.1016/S0377-0257(98)00112-8.

M. H. Wagner, H. Bastian, P. Hachmann, J. Meissner, S. Kurzbeck, H. Münstedt, and F. Langouche. The strain-hardening behaviour of linear and long-chain-branched polyolefin melts in extensional flows. *Rheologica Acta*, 39(2): 97–109, 2000. doi: 10.1007/s003970050010.

M. H. Wagner, P. Rubio, and H. Bastian. The molecular stress function model for polydisperse polymer melts with dissipative convective constraint release. *Journal of Rheology*, 45(6):1387–1412, 2001. doi: 10.1122/1.1413503.

M. H. Wagner, M. Yamaguchi, and M. Takahashi. Quantitative assessment of strain hardening of low-density polyethylene melts by the molecular stress function model. *Journal of Rheology*, 47(3):779–793, 2003. doi: 10.1122/1.1562155.

M. H. Wagner, J. Hepperle, and H. Münstedt. Relating rheology and molecular structure of model branched polystyrene melts by molecular stress. *Journal of Rheology*, 48(3):489–503, 2004. doi: 10.1122/1.1687786.

M. H. Wagner, S. Kheirandish, K. Koyama, A. Nishioka, A. Minegishi, and T. Takahashi. Modeling strain hardening of polydisperse polystyrene melts by molecular stress function theory. *Rheologica Acta*, 44(3):235–243, 2005. doi: 10.1007/s00397-004-0402-7.

J. S. Wang, R. S. Porter, and J. Wang. On the viscosity-temperature behavior of polymer melts. *Rheologica Acta*, 34(5):496–503, 1995. doi: 10.1007/BF00396562.

H. H. Winter and F. Chambon. Analysis of linear viscoelasticity of a crosslinking polymer at the gel point. *Journal of Rheology*, 30(2):367–382, 1986. doi: 10.1122/1.549853.

H. H. Winter and M. Mours. The cyber infrastructure initiative for rheology. *Rheologica Acta*, 45(4):331–338, 2006. doi: 10.1007/s00397-005-0041-7.

H. H. Winter, P. Morganelli, and F. Chambon. Stoichiometry effects on rheology of model polyurethanes at the gel point. *Macromolecules*, 21(2):532–535, 1988. doi: 10.1021/ma00180a048.

P. M. Wood-Adams, J. M. Dealy, W. A. DeGroot, and D. O. Redwine. Effect of molecular structure on the linear viscoelastic behavior of polyethylene. *Macromolecules*, 33(20):7489–7499, 2000. doi: 10.1021/ma991533z.

D. Wu, F. Chen, R. Li, and Y. Shi. Reaction kinetics and simulations for solid-state polymerization of poly(ethylene terephthalate). *Macromolecules*, 30(22):6737–6742, 1997. doi: 10.1021/ma9612541.

M. Xanthos. *Reactive extrusion*. Oxford University Press, Munich, 1992. ISBN 9780195209518.

M. Xanthos, C. Wan, R. Dhavalikar, G. P. Karayannidis, and D. N. Bikiaris. Identification of rheological and structural characteristics of foamable poly(ethylene terephthalate) by reactive extrusion. *Polymer International*, 53:1161–1168, 2004. doi: 10.1002/pi.1526.

U. Yilmazer, M. Xanthos, G. Bayram, and V. Tan. Viscoelastic characteristics of chain extended/branched and linear polyethylene terephthalate resins. *Journal Of Applied Polymer Science*, 75(11):1371–1377, 2000. doi: 10.1002/(SICI)1097-4628(20000314)75:11⟨1371::AID-APP8⟩3.0.CO;2-5.

Y. Zhang, W. H. Cuo, H. S. Zhang, and C. F. Wu. Influence of chain extension on the compatibilization and properties of recycled poly(ethylene terephthalate)/linear low density polyethylene blends. *Polymer Degradation and Stability*, 94(7), 2009. doi: 10.1016/j.polymdegradstab.2009.03.010.

B. H. Zimm. Apparatus and methods for measurement and interpretation of the angular variation of light scattering; preliminary results on polystyrene solutions. *The Journal of Chemical Physics*, 16(12):1099–1116, 1948. doi: 10.1063/1.1746740.

B. H. Zimm and R. W. Kilb. Dynamics of branched polymer molecules in dilute solution. *Journal of Polymer Science*, 37(131):19–42, 1959. doi: 10.1002/pol.1959.1203713102.

B. H. Zimm and W. Stockmayer. The dimensions of chain molecules containing branches and rings. *Journal of Chemical Physics*, 17(12):1301–1314, 1949. doi: 10.1063/1.1747157.

H. Zimmermann. Degradation and stabilisation of polyesters. In N. Grassie, editor, *Developments in Poly Degradation Vol 5*, chapter 3, pages 79–119. Applied Science Publishers, London and New York, 1984. ISBN 9789401080323. doi: 10.1007/978-94-009-3425-2.

Nomenclature

Latin symbols

Symbol	Description
A	factor of non-active specimens
a	tube diameter
a_0	tube diameter at equilibrium
A_2	second viral coefficient
A_{RT}	cross section area at room temperature
a_T	horizontal time-temperature shift factor
a_v	vertical degradation shift factor
$A(t)$	time dependent cross section area
B	factor of active specimens
b	length of chain segment and
b_b	length of bond
$\underline{b}_i$	vector of chain segment i
b_k	length of Kuhn segment
b_T	vertical time-temperature shift factor
$\underline{\underline{C}}$	Cauchy tensor
c	concentration
c_i	concentration fraction
$c.m.$	center of mass
$\underline{\underline{C}}_{t,t'}(t,t')$	relative Cauchy tensor
$\underline{\underline{C}}^{-1}_{t,t'}(t,t')$	relative Finger tensor
C_∞	characteristic ratio
D	diffusion coefficient
$\underline{\underline{D}}$	deformation rate tensor
d	distance
dn/dc	differential refractive index increment

E	Youngs modulus
E_A	flow activation energy
E_g, E_l	glassy and liquid molar thermal expansivity
F	Helmholtz free energy
f	number of arms of star molecule
f^2_{max}	maximum of storable energy from chain stretch (MSF)
f_e	energy contribution to the force
f_s	entropy contribution to the force
$F(t)$	time dependent force
$\underline{\underline{F}}_{t,t'}(t,t')$	relative deformation gradient tensor
$\underline{\underline{F}}^{-1}_{t,t'}(t,t')$	relative inverse deformation gradient tensor
$\underline{f}$	force
$f(t,t')$	stretch of tube
G	shear modulus
g, g'	coil contraction factor based on R_g and $[\eta]$
G_e	equilibrium modulus of cross-link network
G^0_N	plateau value of network entanglements
g_s, g_3, g_4	numerical coil contraction factor of star, tri-, tetra-functional branch units
$G'(\omega)$	storage modulus
$G''(\omega)$	loss modulus
$G(t)$	relaxation modulus
$g(r)$	pair correlation function
$\|G^*\|$	absolute value of complex shear modulus
$h(I_1, I_2)$	damping function
$H(\lambda)$	continuous relaxation spectrum
I_0	intensity of incident light
I_1, I_2	first and second invariant
$I(\underline{q})$	intensity of scattering light
$J(t)$	compliance
K	constant (e.g. 3.4 power law, Mark-Houwink, Fox-Flory)
$\underline{K}$	retractive force of an ideal chain

k	Boltzmann constant
K^*	optical constant
$\left\lvert \underline{K}_{eq} \right\rvert$	equilibrium force
$\underline{k}_f$	wave vector of scattered light
$\underline{k}_i$	incident plane wave vector
l	length
l_0	gauge
l'	past length
m	number of monomers and degree of branching
M_{br}	molar mass between branch units
M_c	critical molar mass
M_e	molar mass of entanglements
M_n	number-average molar mass
$M_{n,br}$	number-average molar mass of branched molecule
M_m	molar mass of monomer
M_w	weight-average molar mass
M_z	z-average molar mass
m', m''	slope of G' and G'' from TRMS
$m(t-t')$	memory function
N	number of segments, beads, and bonds, and refractive index of the solute
$\underline{n}$	normal vector
n_{CE}	number of chain extender molecules
n_i	number fraction
N_{mu}	mutation number
n_0	refractive index of the solvent
n'	refractive index of sample
$\mathcal{N}$	Avogadro's number
P	survival probability
P_c	pressure drop in capillary
P_{extr}	online extruder pressure
P_O	pressure drop at orifice die

$P(\theta)$	particle scattering function
Q	volumetric flow
$\underline{q}$	scattering vector
R	radius at wall
$\underline{R}$	end-to-end vector
r	radius
$\underline{r}_i$	local vector
R_{max}	length of fully expanded chain
R_g	radius of gyration
R_h	hydrodynamic radius
R_z	z-average radius of gyration
R_0	end-to-end distance of an ideal
$R(\theta)$, $R(\underline{q})$	Rayleigh ratio
$\langle R^2 \rangle$	mean square end-to-end distance
S	entropy
S	strain measure
$\underline{\underline{S}}$	orientation tensor
$\underline{\underline{S}}_{DE}^{IA}$	Doi-Edward independent alignment assumption orientation tensor
$\underline{\underline{S}}_{MSF}$	MSF orientation tensor
T	temperature
T_g	glass transition temperature
$T_{g,\infty}$	glass transition temperature with infinite molar mass
U	internal energy
$\underline{u}, \underline{u}'$	undeformed and deformed orientation vector
V	volume and molar volume
v	strand density
$\underline{v}$	velocity vector
v_e	entanglement density
V_g, V_l	glassy and liquid molar volume
$\underline{\underline{W}}$	rotation deformation or vorticity tensor
w_{MSF}	free energy of segment

w_i	weight fraction
$\underline{x}$	deformed state
$\underline{x}_0$	relaxed state

Greek symbols

Symbol	**Description**
β	MSF branching factor
$\dot{\gamma}_{app}$	apparent shear rate
$\dot{\gamma}_w$	shear rate at wall
$\dot{\gamma}(dt)$	shear rate
$\gamma(t,t')$	shear deformation
δ	phase angle, loss angle
ε	strain and structure correlation exponent
ε_E	engineering strain
$\dot{\varepsilon}$	strain rate
ζ	friction coefficient
η	viscosity
η_E	elongation viscosity
$\eta_E^+(t,\dot{\varepsilon})$	transient uniaxial elongation viscosity
$\eta_S^+(t)$	transient shear viscosity
η_{sp}	specific viscosity
η_0	zero-shear viscosity
$[\eta]$	intrinsic viscosity
$\lvert\eta^*\rvert$	absolute value of complex viscosity
θ	scattering angle
$\underline{\underline{\kappa}}$	velocity gradient tensor
λ	relaxation time and branching frequency
λ_{mu}	mutation time
λ_i, g_i	discrete relaxation spectrum
$\lambda_i(t,t')$	strain, extensional ratio
λ_0	wave length
ρ	density

ρ_l	melt density
ρ_s	solid density
σ	stress
$\underline{\underline{\sigma}}$	stress tensor
σ_{ij}	components of stress tensor
σ_{xx}	tensile stress
τ	reaction time constant
τ_d	disengagement time
τ_R	Rouse relaxation time
τ_w	shear stress at wall
$\Psi(\underline{R})$	Gaussian probability of end-to-end vector
ω	angular frequency
$\underline{\nabla v}$	velocity gradient tensor

Abbreviations

Symbol	**Description**
BHET	bis(2-hydroxyethyl) terephthalate
CR	constraint release
COOH	carboxyl group
DEG	diethylene glycol
DMT	dimethyl terephthalate
DP	differential pressure
DRI	differential refractive index
HFIP	hexafluoroisopropanol
H-PET	high molar mass PET based on dimethyl terephthalate
IP	inlet pressure
IV	intrinsic viscosity
K-BKZ	Kaye-Bernstein, Kearsley and Zapas (equation)
LCB	long-chain branching
L-PET	low molar mass PET based on dimethyl terephthalate
l-PET	low molar mass PET based on purifed terephthalic acid
MALS	multi-angle light scattering

MEG	monoethylene glycol
MMD	molar mass distribution
MSF	molecular stress function
OH	hydroxyl group
PET	poly(ethylene terephthalate)
PDI	polydispersity index
PMDA	pyromellitic dianhydride
SEC	size-exclusion chromatography
SSP	solid-state polycondensation
TGDDM	tetraglycidyl diamino diphenyl methane
TPA	purifed terephthalic acid
TPP	triphenyl phosphite
TRMS	time-resolved mechanical spectroscopy
WLF	Williams-Landel-Ferry (equation)

Appendices

Results from Time-Resolved Mechanical Spectroscopy

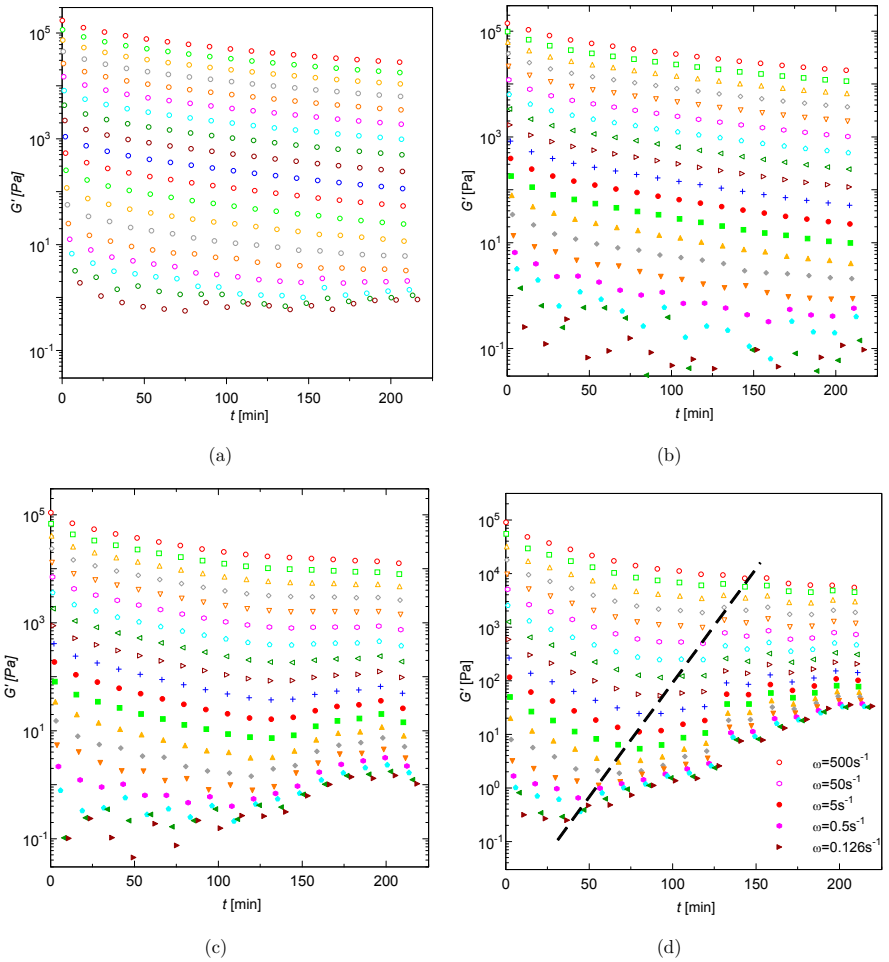

Figure 7.1: TRMS of G' for H-PET at 265°C (a), 272°C (b), 280°C (c), and 288°C (d) in air atmosphere.

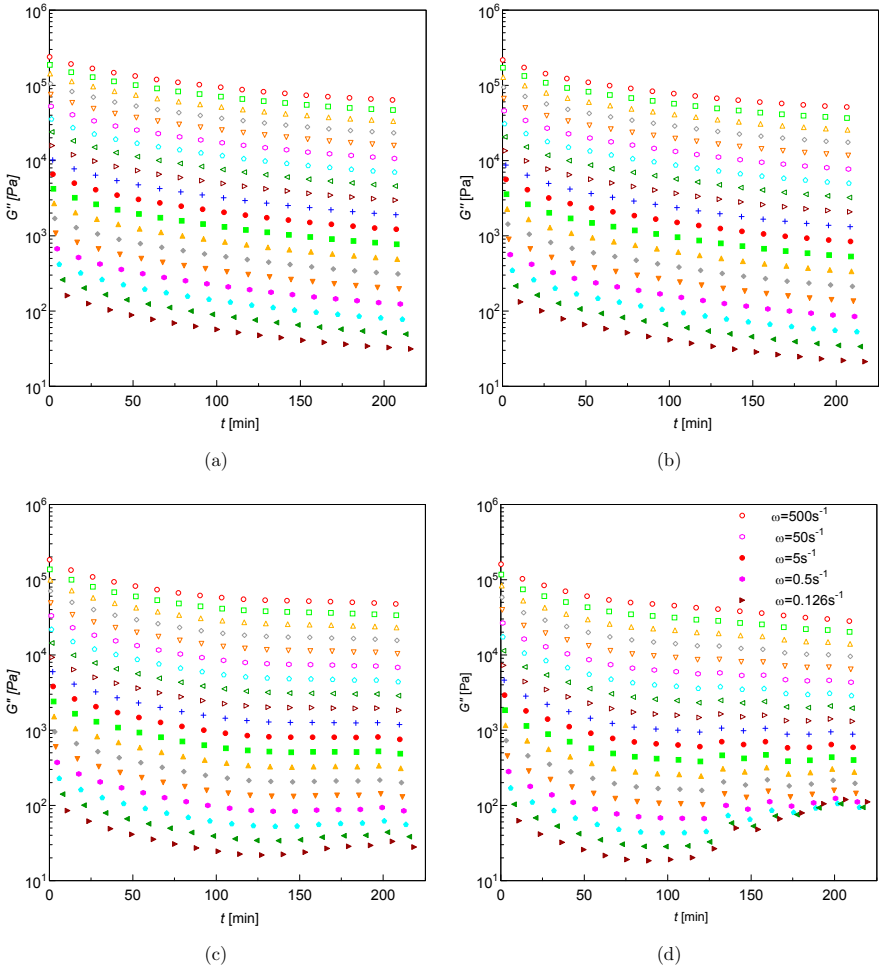

Figure 7.2: TRMS of G'' for H-PET at 265°C (a), 272°C (b), 280°C (c), and 288°C (d) in air atmosphere.

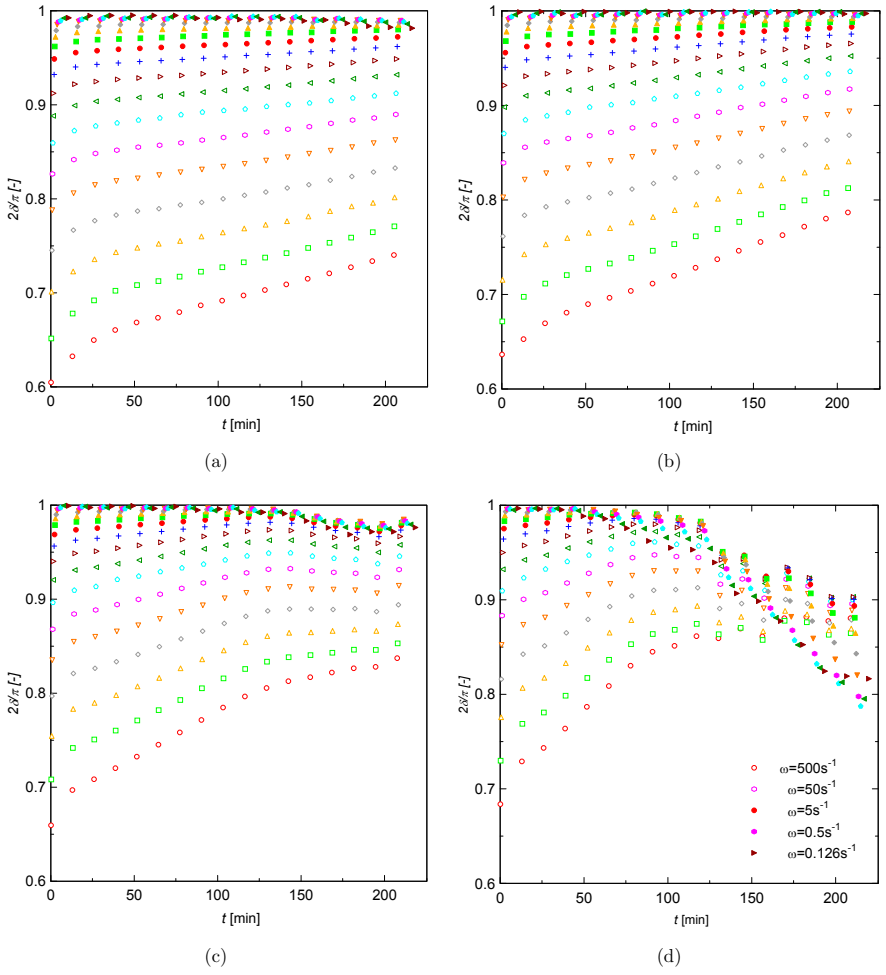

Figure 7.3: TRMS of δ for H-PET at 265°C (a), 272°C (b), 280°C (c), and 288°C (d) in air atmosphere.

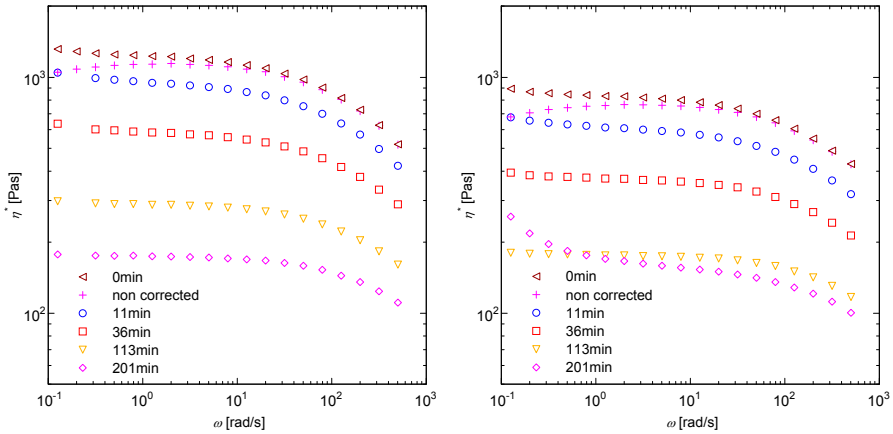

(a) (b)

Figure 7.4: TRMS of complex viscosity for H-PET at $272°C$ (a) and $280°C$ (b) in air atmosphere .

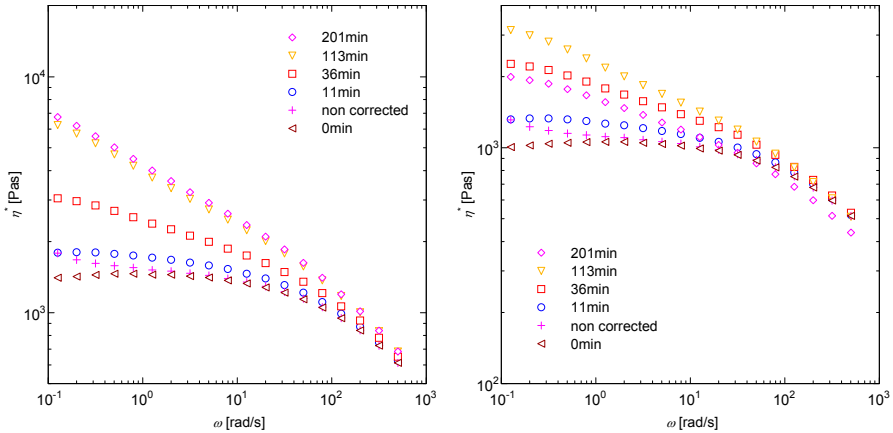

(a) (b)

Figure 7.5: TRMS of complex viscosity for H-PET at $272°C$ (a) and $280°C$ at deformation of 1% in nitrogen atmosphere.

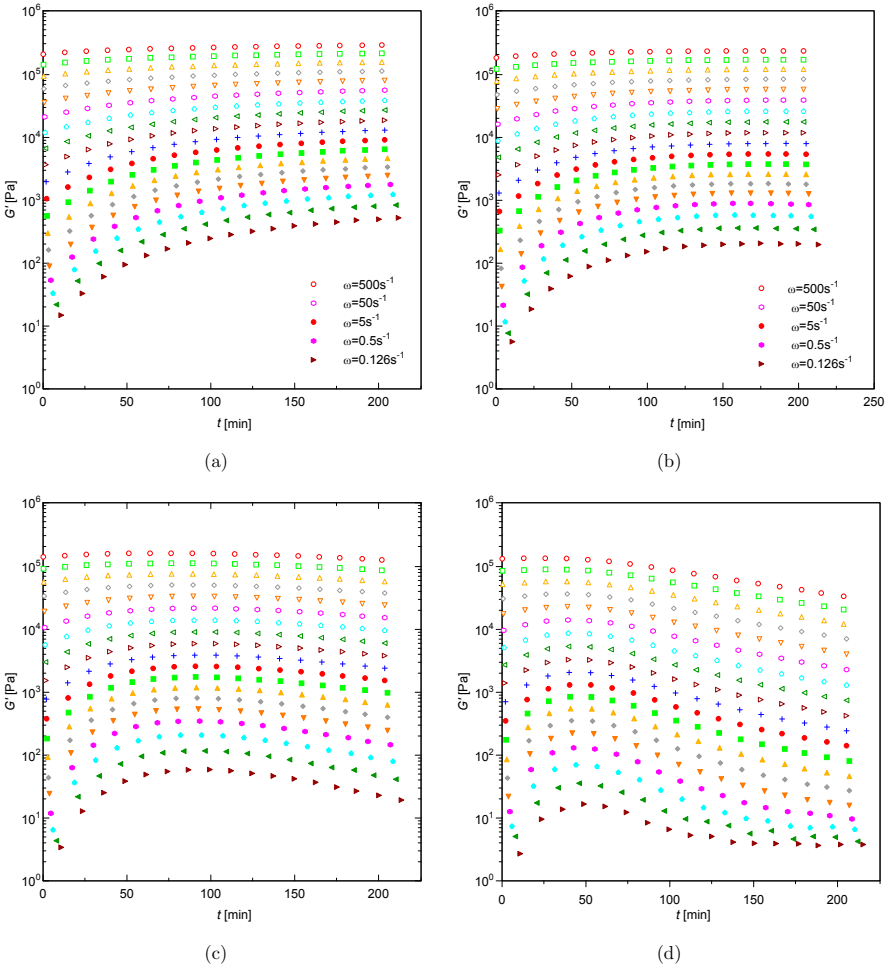

Figure 7.6: TRMS of G' for H-PET at 265°C (a), 272°C (b), 280°C (c), and 288°C (d) at deformation of 1% in nitrogen atmosphere.

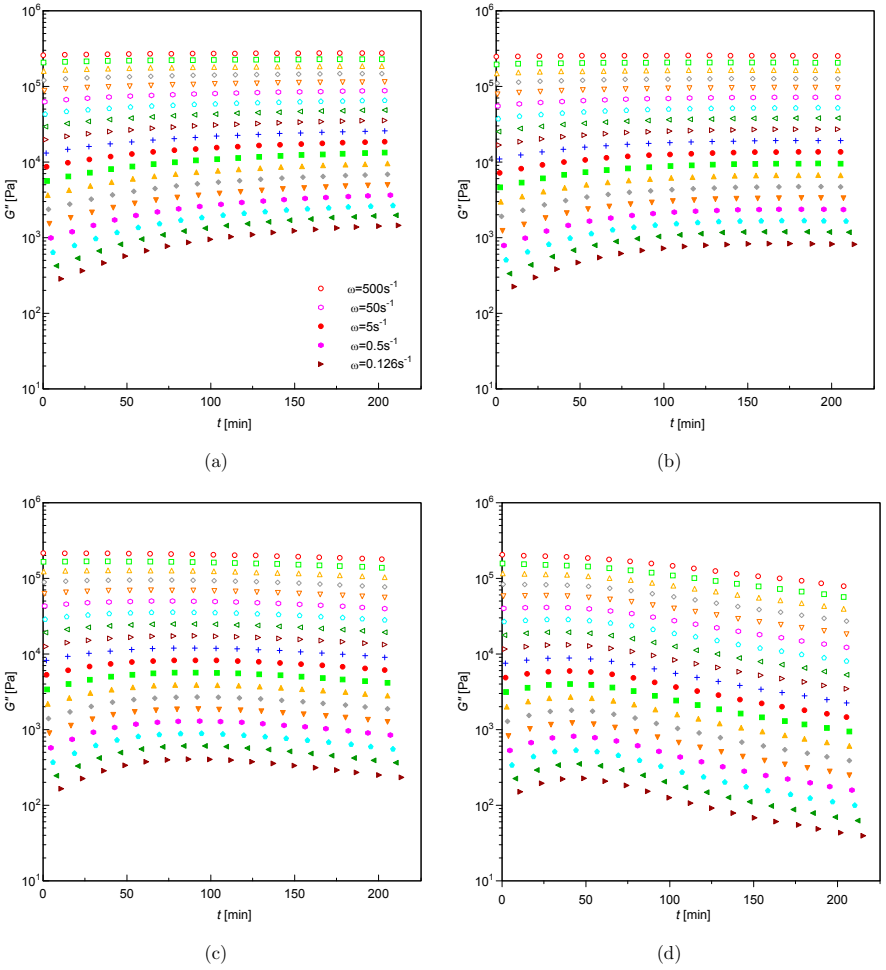

Figure 7.7: TRMS of G'' for H-PET at 265°C (a), 272°C (b), 280°C (c), and 288°C (d) at deformation of 1% in nitrogen atmosphere.

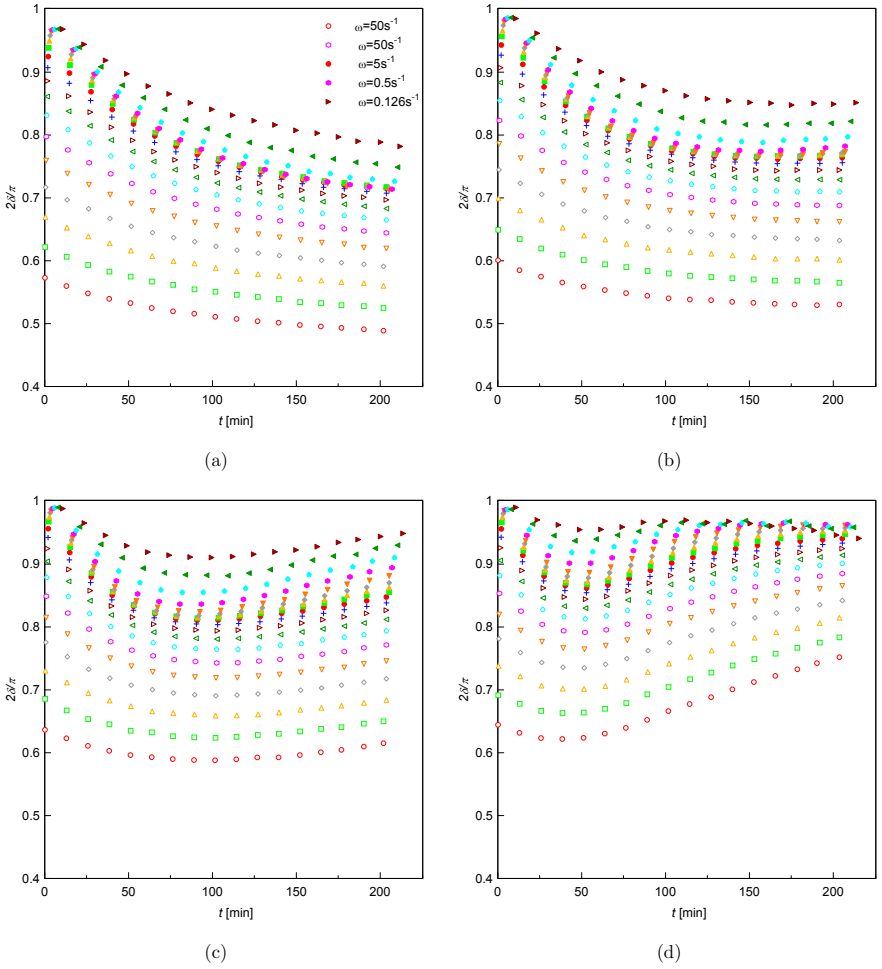

Figure 7.8: TRMS of δ for H-PET at 265°C (a), 272°C (b), 280°C (c), and 288°C (d) at deformation of 1% in nitrogen atmosphere.

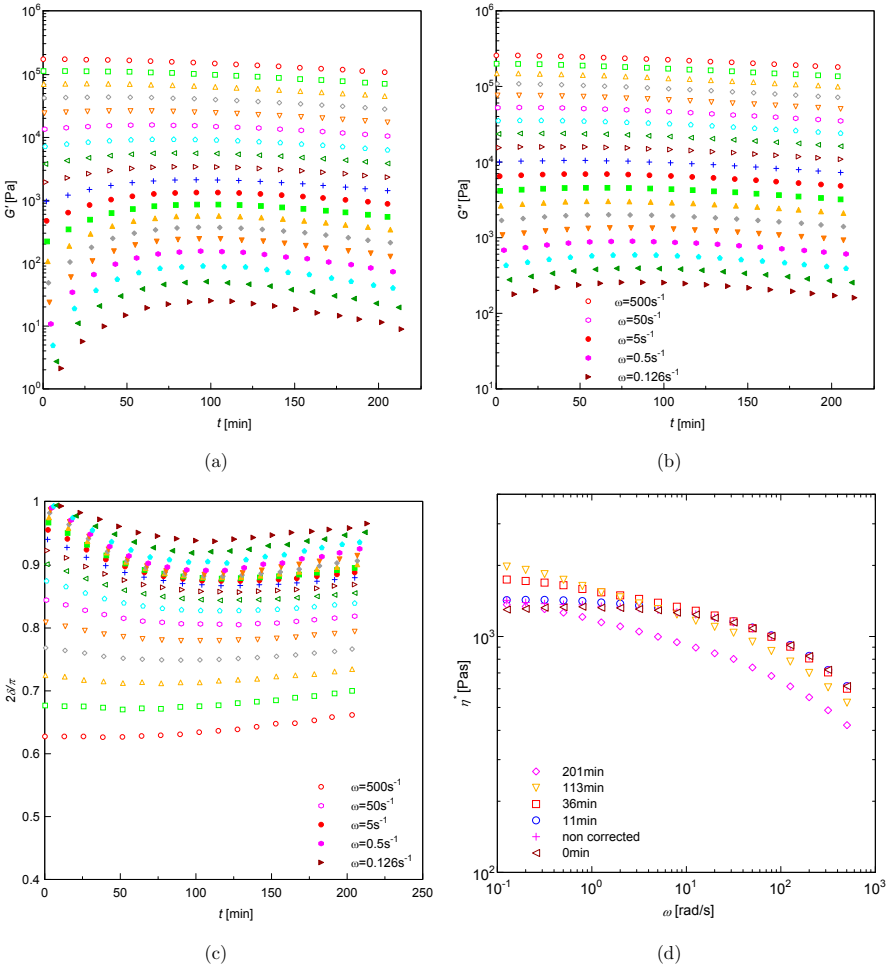

Figure 7.9: TRMS of G' (a), G'' (b), δ (c), and complex viscosity (d) at deformation of 1% of non trimmed in nitrogen atmosphere for H-PET

Schriftenreihe Kunststoff-Forschung
der Technischen Universität Berlin
Herausgegeben von Helmut Käufer
ISSN 0174-4003

01: Biangardi, Harald J.: Bestimmung der Orientierung und molekularen Ordnung in Polymeren. - 1980. - 145 S.
ISBN **3-7983-0737-7** vergriffen

02: Kristukat, Peter: Verhalten von teilkristallinen Thermoplasten beim Pressrecken und dabei erreichbare Eigenschaften von POM. - 1980. - 137 S.
ISBN**3-7983-0738-5** vergriffen

03: Arnold, Gerhart: Pressrecken zum Einbringen orientierter Bereiche für Konstruktionsteile aus teilkristallinen Thermoplasten. - 1980. - 140 S.
ISBN **3-7983-0739-3** vergriffen

04: Käufer, Helmut; Burr, August; Hüppe, Reinhard u.a.: Wissenschaftliche Arbeiten und Einrichtung der Kunststofftechnik. - 1980. - 118 S.
ISBN **3-7983-0740-4** vergriffen

05: Hofbauer, Lothar: Entwicklung einer Kalanderausformtheorie und beispielhafte technische und wirtschaftliche Erprobung an PVC-Folien. - 1981. - 210 S.
ISBN **3-7983-0750-4** vergriffen

06: Jitschin, Michael: Entwicklung eines Konstruktionskatalogs mit Lösungssammlungen schnappbarer Form- und Kraftschlussverbindungen an Kunststoffteilen und beispielhafte Anwendungen. - 1981. - 129 S.
ISBN **3-7983-0763-6** vergriffen

07: Zapf, Wolfgang: Verhalten und Beurteilung stoßbelasteter Kunststoffbauteile. - 1981. - 127 S.
ISBN **3-7983-0764-4** vergriffen

08: Naranjo-Carvajal, Alberto; Burr, August: Abkühlungsbeschreibung bei Thermoplasten im Spritzgieß-Prozess durch Kombinierung experimenteller und rechnerischer Methoden in FORTRAN IV. - 1981. - 49 S.
ISBN **3-7983-0771-7** vergriffen

09: Rautenberg, Lutz: Walzgereckte Thermoplastplatten, ihre Technologie, Eigenschaften und Strukturen. - 1982. - 205 S.
ISBN **3-7983-0810-1** vergriffen

10: Burr, August: Spritzgießpressrecken thermoplastischer Formteile am Beispiel von Zahnrädern aus Polyoximethylen. - 1983. - 148 S.
ISBN **3-7983-0811-X** vergriffen

11: Käufer, Helmut; Huppe, Reinhard; Mähler, Dieter u.a.: Anwendungstechnische Arbeiten aus der Polymertechnik. - 1983. - 123 S.
ISBN **3-7983-0835-7** vergriffen

12: Käufer, Helmut; Thomssen, Udo u.a.: Verarbeitungstechnische und konstruktive Arbeiten aus der Polymertechnik. - 1983. - 127 S.
ISBN **3-7983-0938-8** vergriffen

13: Käufer, Helmut; Fischer, Klaus D.; u.a.: Erarbeitung von Beurteilungsverfahren für angeklebte Fassaden-Verkleidung. - 1984. - 90 S.
ISBN **3-7983-0965-5** vergriffen

14: Woite, Bernd F.: Beitrag zur Dimensionierung statisch und stoßartig belasteter Platten und Sandwichplatten aus Thermoplasten. - 1984. - 275 S.
ISBN **3-7983-0966-3** vergriffen

15: Thomssen, Udo: Gestaltung gewölbter Körper am Beispiel spritzgegossener Halbkugelschalen aus Thermoplasten. - 1984. - 186 S.
ISBN **3-7983-1033-5** vergriffen

16: Hüppe, Reinhard: Sensoreinsatz zur direkten, kontinuierlichen Erfassung und Regelung von Produkteigenschaften beim Spritzgießen. - 1985. - 252 S.
ISBN **3-7983-1034-3** vergriffen

17: Lemke, Hans-Jürgen: Qualitätsabhängige Regelung und Überwachung des Spritzgießprozesses mittels Rechnereinsatz. - 1985. - 190 S.
ISBN **3-7983-1063-7** vergriffen

18: Fischer, Klaus-Dieter: Stahl-Thermoplast-Leichtbauträger in wirtschaftlicher recycling-freundlicher Verbundkonstruktion mit Belastungs- und Anwendungsanalyse. - 1986. - 173 S.
ISBN **3-7983-1111-0** vergriffen

19: Bonau, Hugo: Recycling von Alt-Thermoplasten mit Aufwertung für gezielte Anwendungen am Beispiel von Polypropylen. - 1988. - 126 S.
ISBN **3-7983-1112-9** vergriffen

20: Fischer, Hans-Joachim: Versteifungswirkung gewölbter Flächen am Beispiel von Halbkugelschalen aus faserverstärkten Kunststoffen. - 1989. - 186 S.
ISBN **3-7983-1238-9** vergriffen

21: Münnich, Janos: Prozessorientierte Untersuchungen zum Walzpreßrecken von teilkristallinen Thermoplasten. - 1989. - 142 S.
ISBN **3-7983-1285-0** vergriffen

22: Kipfelsberger, Christian: Fertigung und Schrumpfverhalten spritzgießpressgereckter Flachstäbe und Folgerungen für Schrumpfteile. - 1989. - 174 S.
ISBN **978-3-7983-1286-9** vergriffen

23: Jahnke, Joachim: Federelemente aus eigenverstärkten Thermoplasten, ihre Optimierung und Herstellung. - 1989. - 196 S.
ISBN **978-3-7983-1287-7** vergriffen

24: Frey, Gerhard: Eigenverstärken des Gesamtvolumens von komplexen Bauteilen aus teilkristallinen Thermoplasten durch Umformen. - 1990. - 180 S.
ISBN **978-3-7983-1288-5** vergriffen

25: Leyrer, Karl-Hans: Verfahrensentwicklung für dickwandige, eigenverstärkte Präzisionsformteile (Thermoplastische Zahnräder). - 1990. - 170 S.
ISBN **978-3-7983-1355-5** vergriffen

26: Tiemann, Uwe: Plastographie von teikristallinen Thermoplasten am Beispiel von Polypropylen-Recyclaten. - 1990. - 124 S.
ISBN **978-3-7983-1356-3** vergriffen

27: Mokrani, Gerhard: Kontinuierliches Walzpressrecken eigenverstärkter Thermoplastbleche. - 1991. - 166 S.
ISBN **978-3-7983-1426-8** vergriffen

28: Elsner, Helmut: Grundlegende Untersuchungen an Kunststoff-Metall-Klebungen als Basis einer Entwicklungsmethodik. - 1991. - 133 S.
ISBN **978-3-7983-1436-5** vergriffen

29: Chemnitius, Reiner: Das wissensbasierte CAD-System ICX zur Entwicklung von Kunststoff-Klebeverbindungen. - 1991. - 183 S.
ISBN **978-3-7983-1437-3** vergriffen

30: Voßhenrich, Bruno: Verarbeitung flüssigkristalliner Thermoplaste zu hochfesten technischen Teilen. - 1991. - 162 S.
ISBN **978-3-7983-1454-3** vergriffen

31: Piotter, Volker: Flüssigkristalline Thermoplaste und Blends verarbeitet zu optimal eigenverstärkten Teilen. - 1994. - 158 S.
ISBN **978-3-7983-1552-3** vergriffen

32: Heschke, Peer: Demontage von Klebverbindungen für eine praktikablere Instandhaltung und ein optimier-tes Recycling. - 1995. - 160 S., zahlr. graph. Darst., 29 Fotos, z.T. farbig.
ISBN **978-3-7983-1663-8** EUR **2,60**

33: Karras, Wolf: Differenzierte Aufbereitung zum wirtschaftlichen Recycling von Polyolefinen. - 1996. - 204 S., zahlr. graph. Darst. u. Fotos.
ISBN **978-3-7983-1671-3** EUR **2,60**

34: Kämmler, Georg: Fixierzeitmodulierte Präzisionseinstellung von Kunststoffgleitlagern. - 1996. - 172 S., zahlr. graph. Darst.
ISBN-13: **978-3-7983-1679-9** EUR **2,60**

35: Xing, Zhijie: Verarbeitung, Struktur und Eigenschaften von hochgefüllten teilkristallinen Thermoplasten. - 1996. - 152 S., zahlr. Fotos, z.T. farbig.
ISBN **978-3-7983-1675-1** EUR **2,60**

36: Quast, Oliver von: Universelle Methode zur Dehalogenierung von Thermoplasten. - 1996. - 197 S., zahlr. graph. Darst.
ISBN **978-3-7983-1689-8** EUR **2,60**

37: Weinlein, Roger: Vergleichende Umweltanalyse von Thermoplast-Bauteilen aus Recyclat und Neuware. - 1996. - 224 S., 20 Fotos, zahlr. graph. Darst.
ISBN **978-3-7983-1697-3** EUR **2,60**

38: Martin, Jan: Kunststoff und Holz als Werkstoffe für den Baubereich - ein technischer Vergleich. - 1996. - 140 S., zahlr. graph. Darst.
ISBN **978-3-7983-1704-8** EUR **2,60**

39: Wagenblast, Joachim: Verfahrens- und maschinentechnische Verbesserungen bei der Verarbeitung von Thermoplasten mit Schneckenmaschinen. - 1997. - 188 S., 3 Photos, zahlr. graph. Darst.
ISBN **978-3-7983-1718-5** EUR **2,60**

40: Zoll, Günther B.: Entwicklung von Kunststoffprodukten mit systemtechnischen Methoden. - 1997. - 170 S., zahlr. graph. Darst. u. Tab.
ISBN **978-3-7983-1729-1** EUR **2,60**

41: Siebert, Martin: Entfärben von Thermoplasten beim Recycling über Lösen. - 1997. - 140 S., zahlr. graph. Darst., 13 Fotos.
ISBN **978-3-7983-1723-9** EUR **2,60**

42: Giese, Dagmar: Recycling über Lösen von Elastomeren und faserverstärkten Thermoplasten. Konzeption einer Technikumsversuchsanlage. - 1998. - 160 S., 33 S. Anh., zahlr. graph. Darst. u. Fotos.
ISBN **978-3-7983-1770-3** EUR **2,60**

43: Bongers, Alexander: Polymere Implantate durch spezielle Oberflächenfibrillierung. - 1997. - 132 S., graph. Darst.
ISBN **978-3-7983-1756-7** EUR **2,60**

44: Sambale, Harald: Recycling von Thermoplasten durch Direktverarbeitung von Lösungen. - 1999. - 120 S., Abb.
ISBN **978-3-7983-1797-0** EUR **2,60**

45: Tief, Kerstin: Variable Kalkulationsmethodik zur Analyse von Kunststoffrecyclingverfahren anhand von wirtschaftlichen und umweltrelevanten Kriterien. - 1998. - 206 S., zahlr. graph. Darst. u. Tab.
ISBN **978-3-7983-1777-2** EUR **2,60**

46: Bosewitz, Stefan: Kapselungstechnik zur Optimierung der Aufstellung von Anlagen am Beispiel Recycling über Lösen. - 1999. - 192 S., Abb.
ISBN **978-3-7983-1807-6** EUR **2,60**

47: Shaik-El-Eid, Sliman: Biokompatibilität und Zellzahlbestimmung von Fibroblasten auf integralen und normalen Polymerimplantaten. - 1998. - 132 S., graph. Darst. u. Tab.
ISBN **978-3-7983-1788-8** EUR **2,60**

48: Klein, Frank: Verfahrensentwicklung, Werkstoffeigenschaften und Wirtschaftlichkeitsbetrachtung für das Kunststoffrecycling über Lösen von Mischthermoplasten. - 1999. - 152 S.
ISBN **978-3-7983-1811-3** EUR **2,60**

49: Kaya, Yasar: Kunststoffanwendungen bei der Entwicklung extrakorporaler Medikalprodukte und Implantate. - 1999. - 152 S.
ISBN **978-3-7983-1795-6** EUR **2,60**

50: Karras, Wolf; Bosewitz, Stefan; Weinlein, Roger; Tief, Kerstin; Seifert, Daniel; Glandorf, T.: Vergleichende Normierende Betrachtung bei der Verwertung von Abfällen aus Kunststoffverkaufsverpackungen. - 1999. - 200 S.
ISBN **978-3-7983-1817-5** EUR **2,60**

51: Müller, Thomas: Polymere Implantate mit Formgedächtnis am Beispiel von Stents. - 2000. - V, 128 S.
ISBN **978-3-7983-1843-4** EUR **2,60**

52: Bedekar, Aravind: Verbund von polymeren Zahnwurzelimplantaten mit Knochen. - 2001. - 184 S.
ISBN **978-3-7983-1844-1** EUR **2,60**

53: Seifert, Daniel: Quantitative Analyse von Polyolefinblends zur Prozeßregelung einer Recyclingsanlage. - 2002. - 125 S.
ISBN **978-3-7983-1898-4** EUR **2,60**

54: Käufer, Helmut: Highlights unbekannt? Kunststoffe. Trilogie der Kunststofftechnik [1]. - 2001. - 120 S.
ISBN **978-3-7983-1874-8** EUR **2,60**

55: Ziesche, Bernhard Dieter: Dimensionierung von großen Rechteckbehältern aus Thermoplasten. - 2003. - 168 S.
ISBN **978-3-7983-1899-1** EUR **7,90**

Schriftenreihe Kunststoff-Forschung
Hrsg.: Univ.-Prof. Dr. Manfred Wagner,
Fachgebiet: Werkstoffwissenschaften und -technologien
Fakultät: Prozesswissenschaften der Technischen Universität Berlin
ISSN 0174-4003
1. 1980. ff.

56: John, Ingo: Beurteilung von vernetztem UHMWPE hinsichtlich seiner Eignung als Implantatwerkstoff für Hüftgelenksschalen. - 2003. - 124 S.
ISBN **978-3-7983-1934-9** EUR **7,90**

57: Käufer, Helmut: Highlights - unbekannt? Kunststoff-Entstehung. Trilogie der Kunststofftechnik [2]. - 2004. - 154 S., zahlr. farb. Abb.
ISBN **978-3-7983-1929-5** EUR **8,90**

58: Zygalsky, Frank: Herstellung und Charakterisierung von oxidischen hochtemperatursupraleitenden dünnen Filmen aus Polymer-Metall-Precursoren. - 2004. - 111 S., zahlr. Tab. u. Abb.
ISBN **978-3-7983-1946-2** EUR **7,90**

59: Yu, Erkang: Herstellung und Charakterisierung von Blends aus technischen und hochtemperaturbeständigen Thermoplasten. - 2004. - 104 S.
ISBN **978-3-7983-1947-9** EUR **7,90**

60: Wache, Hans-Martin: Optimierung des Memory-Verhaltens von Kunststoffen am Beispiel eines polymeren Stents. - 2004. - IV, 116 S.
ISBN **978-3-7983-1954-7** EUR **7,90**

61: Prockat, Jan: Developing Large Structural Parts for Railway Application using a Fibre Reinforced Polymer Design. - 2005. - XII, 139 S.
ISBN **978-3-7983-1955-4** EUR **19,90**

62: Tartakowska, Diana Joanna: Degradationskinetik von medizinisch relevanten bioabbaubaren Copolymeren unter statischen und dynamischen Bedingungen. - 2005. - 123 S.
ISBN **978-3-7983-1967-7** EUR **18,90**

63: Hentrich, Axel: Herstellung von polymeren Stents als Drug Delivery Systeme durch Tauchen aus der Polymerlösung. - 2005. - III, 139 S.
ISBN **978-3-7983-1975-2** EUR **19,90**

64: Kabaha, Eiad: Kleinprüfstäbe zur Charakterisierung der mechanischen Eigenschaften thermoplastischer Polymere. - 2005. - 151 S.
ISBN **978-3-7983-1980-6** EUR **18,90**

65: Käufer, Helmut: Highlights - unbekannt? Kunststoff-Zukunft. Trilogie der Kunststofftechnik [3]. - 2006. - 158 S., zahlr. farb. Abb.
ISBN **978-3-7983-2018-5** EUR **18,90**

66: Kheirandish, Saeid: Constitutive Equations for Linear and Long-Chain-Branched Polymer Melts. - 2005. - IV, 186 S.
ISBN **978-3-7983-1997-4** EUR **17,90**

67: Hetschel, Martin: Abformung von Nanostrukturen im Spritzgießverfahren zur Erzeugung von Antireflexoberflächen. - 2005. - 132 S.
ISBN **978-3-7983-2003-1** EUR **16,90**

68: Rolón Garrido, Víctor Hugo: Molecular Structure and Constitutive Modelling of Polymer Melts. - 2007. - VII, 147 S.
ISBN **978-3-7983-2064-2** EUR **17,90**

69: Müller, Marco: Thermoplastische Elastomere als neuartige Additive für die Kunststoffverarbeitung. - 2009. - 161 S., zahlr. Abb.
ISBN **978-3-7983-2172-4** EUR **19,90**

70: Navarro Gonzáles, Manuel: Rheology and engineering parameters of bitumen modified with polyolefins, elastomers and reactive polymers. - 2010. - VIII, 187 S., zahlr. Abb. u. Tab.
ISBN **978-3-7983-2229-1** EUR **21,90**

71: Kübler, Michael: Verfahrensentwicklung zur Herstellung gebrauchsbständiger kleinststrukturierter Kunststoffbauteile. - 2010. - XVIII, 136 S., zahlr. Abb.
ISBN **978-3-7983-2270-7** EUR **12,90**

72: Schubert, Mario: Biopolymere als definierte Permeationsschicht für aktive Lebensmittelverpackungen. - 2010. - 180 S., zahlr. Tab. u. Abb.
ISBN **978-3-7983-2271-4** EUR **20,90**

73: Akier, Amer H.: Untersuchungen zum Materialverhalten von Rapsstroh-Polypropylen Compounds. - 2011. - XII, 93 S., zahlr. Tab. u. Abb.
ISBN **978-3-7983-2309-4** (online)
ISBN **978-3-7983-2308-7** (print) EUR **11,90**

74: Greger, Marcus: Entwicklung einer verstellbaren Dispergierringtechnik für Planetwalzenextruder. - 2012. - 136 S., zahlr. Abb.
ISBN **978-3-7983-2386-5** (print) EUR **23,90**

75: Kismet, Yilmaz: Entwicklung eines Verfahrens für die Verwertung von Pulverlackrecyclaten. - 2012. - 164 S., zahlr. Abb.
ISBN **978-3-7983-2480-0** (online)
ISBN **978-3-7983-2479-4** (print) EUR **12,90**

76: Himmel, Tobias: Über die Wirkung thermoplastischer Elastomere als Additive zur Unterdrückung des sharkskin-Effekts. - 2013. - VIII, 119 S. zahlr. Abb.
ISBN: **978-3-7983-2515-9** (online)
ISBN**: 978-3-7983-2514-2** (print) EUR **12,00**

77: Kurz, Alexander: Rheologische Untersuchungen zum Einfluss des TBPMN-Netzwerkes auf die scherinduzierte Kristallisation von Polypropylen. - 2013. - VIII, 149 S., zahlr. Abb.
ISBN **978-3-7983-2643-9** (online)
ISBN **978-3-7983-2642-2** (print) EUR **12,90**

78: Taufertshöfer, Thomas: Einfluss der Verfahrenstechnik eines Planetwalzenextruders auf die elektrische Leitfähigkeit rußgefüllter Polyolefine. - 2014. - VII, 147 S., zahlr. Abb.
ISBN **978-3-7983-2690-3** (online)
ISBN **978-3-7983-2689-7** (print) EUR **12,00**

79: Scheuerle, Volker: Verbesserung der Haltbarkeit von Dokumenten mit Hilfe polymerer Schichten. - 2014. - 176 S., zahlr. Abb.
ISBN **978-3-7983-2680-4** (online)
ISBN **978-3-7983-2679-8** (print) EUR **18,00**

80: Mohammed, Nabilah Adel: Rheology, Processing and Properties of Polymer Nanocomposites Based on POSS and Boehmite. - 2014. - 225 S., zahlr. Abb.
ISBN **978-3-7983-2681-1** (online)

Universitätsverlag der TU Berlin

ISBN 978-3-7983-2891-4 (print)
ISBN 978-3-7983-2892-1 (online)